Springer Series in Materials Science 189

Francisco Javier Manjon
Ion Tiginyanu
Veaceslav Ursaki *Editors*

Pressure-Induced Phase Transitions in AB_2X_4 Chalcogenide Compounds

Springer

Springer Series in Materials Science

Volume 189

For further volumes:
http://www.springer.com/series/856

The Springer Series in Materials Science covers the complete spectrum of materials physics, including fundamental principles, physical properties, materials theory and design. Recognizing the increasing importance of materials science in future device technologies, the book titles in this series reflect the state-of-the-art in understanding and controlling the structure and properties of all important classes of materials.

Francisco Javier Manjon · Ion Tiginyanu
Veaceslav Ursaki
Editors

Pressure-Induced Phase Transitions in AB_2X_4 Chalcogenide Compounds

Springer

Editors
Francisco Javier Manjon
Instituto de Diseño para
Polytechnic University of Valencia
Valencia
Spain

Veaceslav Ursaki
Institute of Applied Physics
Chişinău
Moldova

Ion Tiginyanu
Academy of Sciences of Moldova
Chişinău
Moldova

ISSN 0933-033X
ISSN 2196-2812 (electronic)
ISBN 978-3-642-40366-8
ISBN 978-3-642-40367-5 (eBook)
DOI 10.1007/978-3-642-40367-5
Springer Heidelberg New York Dordrecht London

Library of Congress Control Number: 2013953646

Printed on acid-free paper

Springer is part of Springer Science+Business Media (www.springer.com)

Preface

There is a vast number of compounds with AB_2X_4 stoichiometry, where A and B refer to cations and X corresponds to the anion, depending on the cation and anion valences to fit the octet rule. They include: (i) $A^{II}B_2^{III}X_4^{VI}$ compounds, like $MgAl_2O_4$, $ZnGa_2S_4$, $CdIn_2Se_4$, and $HgTl_2Te_4$; (ii) $A_2^{I}B^{VI}X_4^{VI}$ compounds, like Li_2SO_4, Na_2SeO_4, K_2TeO_4, Tl_2CrO_4, Li_2WO_4, Cs_2MoS_4, and K_2WS_4; (iii) $A_2^{II}B^{IV}X_4^{VI}$ compounds, like Mg_2SiO_4, Fe_2GeS_4, Ba_2SnS_4, and Pb_2SiSe_4; and (iv) $A_2^{I}B^{II}X_4^{VII}$ compounds, like Na_2BeF_4, K_2CoCl_4, Cs_2CuCl_4, K_2PdBr_4, and Rb_2MnI_4.

All these families of AB_2X_4 compounds have one thing in common; i.e., they have an unbalanced number of cations (3) and anions (4) per formula unit. Therefore, from the point of view of structural phase transitions, these compounds are prone to suffer order-disorder processes under different conditions of pressure and temperature where cations may get mixed with vacancies at cation sites to fulfil the requirements of high-symmetry structures.

In particular, $A^{II}B_2^{III}X_4^{VI}$ chalcogenides is a vast family of compounds that crystallize at ambient conditions in a great variety of structures. However, they can be classified into three main groups: (i) compounds crystallizing in the spinel or related structures; (ii) compounds crystallizing in tetrahedrally coordinated structures, derived from the diamond and zinc-blende structures with ordered vacancies in the unit cell, and known as adamantine-type ordered-vacancy compounds (OVCs); and (iii) other compounds crystallizing in structures not related to those of spinel or to those of OVCs, e.g. layered materials. Usually, oxides belong to the first group, selenides and tellurides to the second group, and sulphides are in the borderline between the two first groups and belong either to the first, to the second or to the third group.

The big number of $A^{II}B_2^{III}X_4^{VI}$ chalcogenides includes compounds with very different properties and with a wide interest ranging from Geophysics, like spinel-related compounds, to many technological applications. The study of the properties of $A^{II}B_2^{III}X_4^{VI}$ chalcogenide compounds under high pressures and of their pressure-induced phase transitions can help to understand the properties of these compounds and the relationship between their properties and their structures which can have profound implications in many fields.

In this book we are going to review the main results obtained in the study of $A^{II}B_2^{III}X_4^{VI}$ chalcogenide compounds at high pressures to date, paying special attention to the pressure-induced phase transitions. We will see that $A^{II}B_2^{III}X_4^{VI}$ chalcogenide compounds are complex materials that crystallize in different structures or with different degree of disorder depending on the crystal growth conditions. Therefore, the growth conditions determine the properties of the materials and their pressure dependence. We will see how high pressure studies show that the different structures of these compounds at ambient conditions in the three main groups stated above, despite not being considered similar or related in the past, bear a strong relationship between them. Furthermore, we will see that high pressure studies in the last years, despite being insufficient yet, will allow in the next future to establish a systematics of the temperature- and pressure-induced phase transitions in the complex family of $A^{II}B_2^{III}X_4^{VI}$ compounds. We hope the present work will promote future works for a better understanding of the structure and properties of these interesting, and still not well studied, materials.

The present book is organised as follows: after the first chapter, written by V. Ursaki and I. Tiginyanu and devoted to the description of the structure and properties of $A^{II}B_2^{III}X_4^{VI}$ chalcogenide compounds at ambient conditions and which serves as introduction and motivation for the studies at high pressures, the book is divided into three parts. In the first part, written by D. Errandonea, D. Santamaría Pérez, J. Ruiz-Fuertes, P. Rodríguez-Hernández and A. Muñoz, different high-pressure studies on indium thiospinel AIn_2S_4 family and spinel-structured oxides are review with the focus on X-ray diffraction and Raman studies in oxospinels and angle-dispersive X-ray diffraction, Raman and optical absorption measurements in thiospinel. The effects of pressure in the spinel structure are described discussing facts like bulk and polyhedral compressibility, cation size and cation substitution. The effects of pressure on the phase stabilities and transformation pathways of spinel-type semiconductors, as well as on their vibrational and electronic properties are also discussed. Finally, we will present a general overview which hopefully will contribute to achieve a better understanding of the behaviour of thiospinels and selenospinels under compression. The experimental data are accompanied by an overview of the theoretical work done from first principles on the structural, elastic, electronic and vibrational properties of spinels under pressure as well as pressure-induced post-spinel phases.

The second part is written by F. J. Manjón, R. I. Vilaplana, O. Gomis Hilario, A. Muñoz and M. Fuentes-Cabrera it being devoted to the experimental and theoretical studies of ordered-vacancy compounds at high pressures. An overview of the effects of pressure on the crystalline structure and physical properties of sulphur-based and selenium-based ordered-vacancy compounds of the $A^{II}B_2^{III}X_4^{VI}$ family is presented. Recent X-ray diffraction and Raman spectroscopy studies are presented with a main focus on the discussion of pressure-induced phase transitions and their inherent cation and cation-vacancy disordering processes.

The experimental data are supported by ab initio calculations within the Density Funtional Theory and the Density Functional Perturbation Theory of electronic, dynamical, and elastic properties of defect chalcopyrite, defect stannite and pseudo-cubic chalcopyrite structures of AB_2X_4 (X = S and Se) compound under hydrostatic pressures.

The third part, written by V. V. Ursaki and I. M. Tiginyanu, deals with the few studies devoted to other $A^{II}B_2^{III}X_4^{VI}$ chalcogenides with structures different from those of spinels and ordered-vacancy compounds on the instance of layered $A^{II}InGaS_4$ crystals with Cd, Zn, and Mg as A^{II} cations as well as on the instance of the Zn–Al–S system which provides an initial wurtzite structure in addition to the spinel structure. It is also shown that quaternary solid solutions $ZnAl_{2(1-x)}Ga_{2x}S_4$ obtained by adding gallium atoms to the system demonstrate a systematics of phase transitions different from that inherent to $A^{II}B_2^{III}X_4^{VI}$ compounds with chalcopyrite, stannite and spinel structure.

Finally, an epilogue with some final remarks is presented.

Valencia, Spain — Francisco Javier Manjon
Chisinau, Moldova — Ion Tiginyanu
Veaceslav Ursaki

Contents

Contributors

Daniel Errandonea Universitat de València, Valencia, Spain

M. Fuentes-Cabrera Oak Ridge National Laboratory, Computer Science and Mathematics Division, Center for Nanophase Materials Science, Oak Ridge, TN 37831, USA

Óscar Gomis Hilario Centro de Tecnologías Físicas: Acústica, Materiales y Astrofísica, MALTA Consolider Team, Universitat Politècnica de València, 46022 València, Spain

Francisco Javier Manjón Instituto de Diseño para la Fabricación y Producción Automatizada, MALTA Consolider Team, Universitat Politècnica de València, 46022 València, Spain

A. Muñoz Departamento de Física Fundamental II, Instituto de Materiales y Nanotecnología, Universidad de La Laguna, La Laguna, Tenerife, Spain

David Santamaría Pérez Universidad Complutense de Madrid, Madrid, Spain

P. Rodríguez-Hernández Departamento de Física Fundamental II, Instituto de Materiales y Nanotecnología, Universidad de La Laguna, La Laguna, Tenerife, Spain

Javier Ruiz-Fuertes Harvard University, Cambridge, USA

I. M. Tiginyanu Institute of Applied Physics and Institute of Electronic Engineering and Nanotechnologies, Academy of Sciences of Moldova, Chisinau, Moldova

V. V. Ursaki Institute of Applied Physics and Institute of Electronic Engineering and Nanotechnologies, Academy of Sciences of Moldova, Chisinau, Moldova

Rosario Isabel Vilaplana Centro de Tecnologías Físicas: Acústica, Materiales y Astrofísica, MALTA Consolider Team, Universitat Politècnica de València, 46022 València, Spain

Chapter 1
Relation of $A^{II}B_2^{III}X_4^{VI}$ Compounds to Other Materials, Their Properties and Applications (Instead of Introduction)

V. V. Ursaki and I. M. Tiginyanu

Abstract This chapter provides a review of $A^{II}B_2^{III}X_4^{VI}$ compounds as a class of materials in a wide family of ternary compounds. The origin and the place of these materials in the hierarchy of ternary compounds are presented. The technological methods for the growth of these compounds are analyzed and the procedures for obtaining larger crystals for practical applications are evidenced. The crystal structure and the energy band structure are discussed in terms of the production of spinel, layered, or tetragonal structure according to the number of octahedral and tetrahedral cationic sites. The "ordered-vacancy compounds" are analyzed taking into account different degrees of possible disorder. The relationship of the electronic band structures of these compounds with the band structure of their parent chalcopyrite compounds $A^{I}B^{III}X_2^{VI}$ and their grand parent $A^{II}B^{VI}$ compounds is clarified. The influence of the crystallographic structure upon the energy band structure is evidenced by comparing crystal modifications with different space groups. Optical, radiative, and vibrational properties are discussed and the energy level scheme explaining the extrinsic optical properties of $A^{II}B_2^{III}X_4^{VI}$ semiconductors is presented. It is shown that a source of interest in $A^{II}B_2^{III}X_4^{VI}$ compounds is their crystal structures derived from the diamond type, but modified to accommodate three or more atoms of different sizes, allowing additional symmetries and thus an increase in the selection of electro-optic, acousto-optic, and non-linear materials for device applications. Another source of interest related to the variety of $A^{II}B_2^{III}X_4^{VI}$ crystal structures comes from their importance for the investigation of the role of structure and composition in a response to the applied pressure.

V. V. Ursaki (✉)
Institute of Applied Physics, Academy of Sciences of Moldova, Chisinau, Moldova
e-mail: ursaki@yahoo.com

I. M. Tiginyanu
Institute of Electronic Engineering and Nanotechnologies, Academy of Sciences of Moldova, Chisinau, Moldova
e-mail: tiginyanu@gmail.com

F. J. Manjón et al. (eds.), *Pressure-Induced Phase Transitions in AB_2X_4 Chalcogenide Compounds*, Springer Series in Materials Science 189,
DOI: 10.1007/978-3-642-40367-5_1, © Springer-Verlag Berlin Heidelberg 2014

Keywords Ternary compounds · Crystal growth · Crystal structure · Energy band structure · Optical, radiative, and vibrational properties · Hydrostatic pressure, Phase transitions.

1.1 $A^{II}B_2^{III}X_4^{VI}$ Compounds Among Other Ternary and Multinary Compounds

$A^{II}B_2^{III}X_4^{VI}$ compounds represent a class of materials in a wide family of ternary compounds. The hierarchy of ternary compounds originates from binaries. Particularly, 245_2 compouns are derived from 35 by replacing two atoms of the third column by one of the second and one of the fourth, and the 136_2 are derived from 26's by replacing two atoms of the second column by one atom of the first column and one of the third [1–3]. Shay and coworkers [4] have shown that the quasi-cubic model of band structure is very adequate to derive the band structure of 245_2 from the band structure of 35's. Similarly, the band structure of 136_2 can be derived from the 26, if provision is made for the additional perturbation due to the d-band of the monovalent atom.

The scientific team led by Goryunova [5] made significant contribution to the field of ternaries, particularly by the observation of optical nonlinear properties [6] and the demonstration of laser action in a ternary compound [7]. Later, Chemla, Kupecek Robertson and Smith [8] demonstrated phase-matched second harmonic generation in a chalcopyrite crystal.

$A^{II}B_2^{III}X_4^{VI}$ compounds are also treated as a result of pseudobinary $AX + B_2X_3$ join. The B_2X_3 compounds have generally a defective tetrahedral structure with some exceptions like In_2S_3, which has a spinel structure. In this pseudobinary join with a 50 % molar composition one has AB_2X_4 compounds. Within the integer molar ratios one may found also $AX + 2B_2X_3 = AB_4X_7$ compounds with a 33 % molar composition, and $2AX + B_2X_3 = A_2B_2X_5$ with a 66 % molar composition.

Similarly to most of the ternary compounds, a significant part of $A^{II}B_2^{III}X_4^{VI}$ compounds have tetrahedral structures with fourfold coordination determined by the electronic valence of the atoms [9, 10]. In a tetrahedral structure each atom has four nearest neighbours which form a more or less regular tetrahedron. Two nearest neighbours are bonded by the overlap of two valence electrons' wave functions [3]. This overlapping of sp_3 hybrids accounts for the cohesive energy like in purely covalent crystals, like diamond, silicon and germanium. In contrast to normal tetrahedral structures, $A^{II}B_2^{III}X_4^{VI}$ compounds have bond defect tetrahedral structures in which some atomic sites are empty. Around such a vacant site there are electron lone pairs. All the tetrahedral compounds including those with normal tetrahedral structures and those with bond defect tetrahedral structures belong to the class of adamantine structures in which there are no anion–anion and cation–cation bonds. Among these many of them have the so-called chalcopyrite structure.

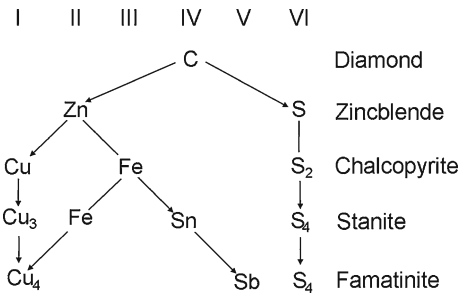

Fig. 1.1 Grimm–Sommerfeld splitting diagram for tetrahedral structures

Tetrahedral complex structures of binary, ternary and quaternary compounds are obtainable from diamond structure by Grimn–Sommerfeld splitting of an atom pair into two different atoms from other groups of the periodic system, while keeping the valence electron number per atom constant as shown in the splitting diagram in Fig. 1.1. All these compounds have the normal tetrahedral structure with different arrangements of the cations in the cationic sublattice.

The Grimm–Sonunerfeld rule can be extended to the defect tetrahedral structures by assigning to a vacancy a zero valent atom. By introducing vacancies into the Grimm–Sommerfeld splitting procedure, one may obtain different defective structures containing one or more vacancy per unit cell [11].

From two formula units of the chalcopyrite parent $A^IB^{III}X^{VI}_2$ compound, for instance $2CuInSe_2$, by replacing the $2A^I$ atoms by an A^{II} atom and a vacancy □, an $A^{II}B^{III}_2\square X^{VI}_4$ defect chalcopyrite structure is obtained, for instance $ZnIn_2\square Se_4$.

From the stannite parent $A^I_2B^{II}C^{IV}X^{VI}_4$ compound, for instance Cu_2FeSnS_4, by replacing the C atom by a vacancy □, and the four X^{VI} atoms by four X^{VII} atoms, an $A^I_2B^{II}\square X^{VII}_4$ defect stannite structure is obtained, for instance $Ag_2Hg\square I_4$.

From the famatinite parent $A^I_3B^VX^{VI}_4$ compound, for instance Cu_3SbS_4, by replacing the three A^I atoms by an A^{III} atom and two vacancies (2□), an $A^{III}B^V\square_2X^{VI}_4$ defect famatinite structure is obtained, for instance $InP\square_2S_4$.

Not all the structures show ordered cationic sublattices: in some cases some disorder has been proposed to interpret the experimental data (Fig. 1.2). With different degree of disorder, $I\bar{4}$ defect chalcopyrite, $I\bar{4}2m$ defect famatinite, or partially cation disordered (vacancies not involved in disorder) centered tetragonal structures are obtained.

As one can see from Fig. 1.2, the "defect chalcopyrite" (or thiogallate) structure (Fig. 1.2d) can be derived from chalcopyrite (Fig. 1.2a) by removing alternately one base-centered and four corner cations of the chalcopyrite structure.

The "defect famatinite" (or "defect stannite") structure of Fig. 1.2e can be derived similarly from famatinite (Fig. 1.2b).

As in substitutional adamantine compounds, in the "ordered-vacancy compounds" (OVC's) OVC's each cation is coordinated by four nearest-neighbor anions. However, the anions are coordinated by two cations of one type, one of a different type, and one vacancy. Many $A^{II}B^{III}_2C^{VI}_4$ compounds can be found in both defect

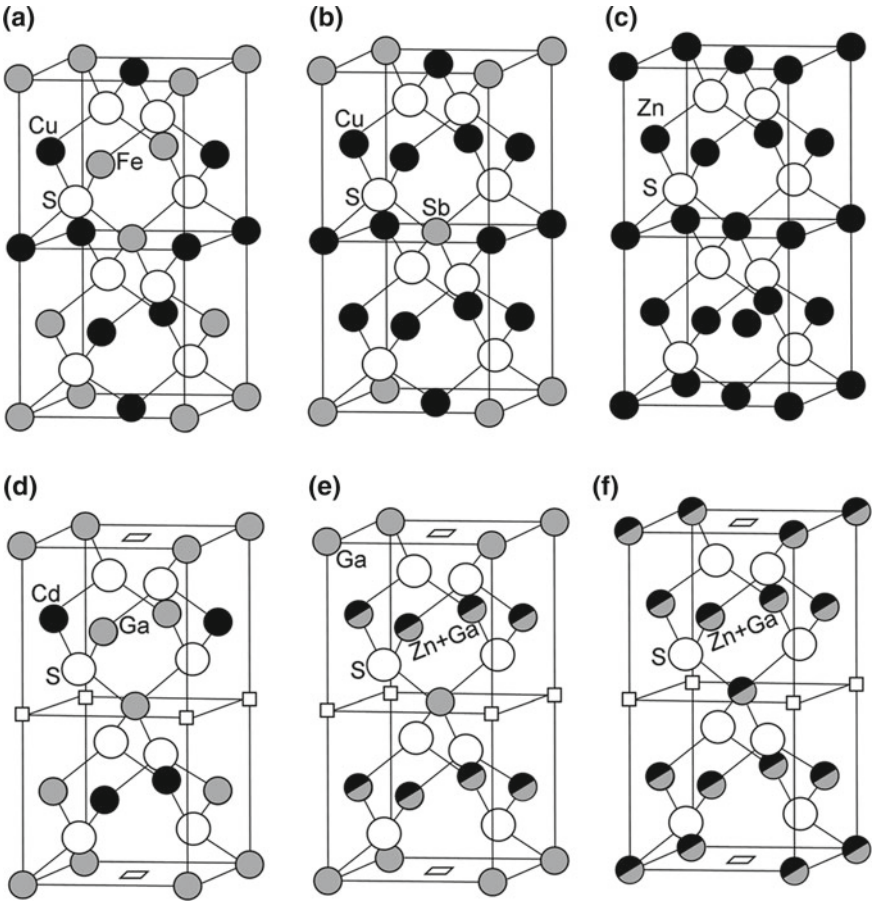

Fig. 1.2 Ordered and disordered defective structures. **a** Chalcopyrite $1\bar{4}2d$. **b** Famatinite $1\bar{4}2m$. **c** Zinc blende $F\bar{4}3m$. **d** Defect chalcopyrite (thiogallate $1\bar{4}$). **e** Defect famatinite (defect stannite $1\bar{4}2m$). **f** Partially cation-disordered (centered tetragonal)

chalcopyrite and defect famatinite structures. The defect famatinite structures differ from the defect chalcopyrite in that the face centered B^{III} and A^{II} cations are randomly distributed (disordered), i.e., Ga and Zn cations in Fig. 1.2e. Further disorder in the cation sublattice by involving also the B^{III} cations (for instance Ga ions in Fig. 1.2f) in the disordering process leads to the production of a defective centered tetragonal structure. This structure (Fig. 1.2f) can be derived from zinc blende (Fig. 1.2c) by removing alternately one base-centered and four corner cations of the zinc blende structure.

The crystal structure of α-$CdIn_2Se_4$ (Fig. 1.3, left) was attributed by Hahn et al. to the space group $P\bar{4}2m$ [12]. Different degrees of cation disorder can also be found in this compound. A rather accurate structure determination of $CdIn_2Se_4$ with electron

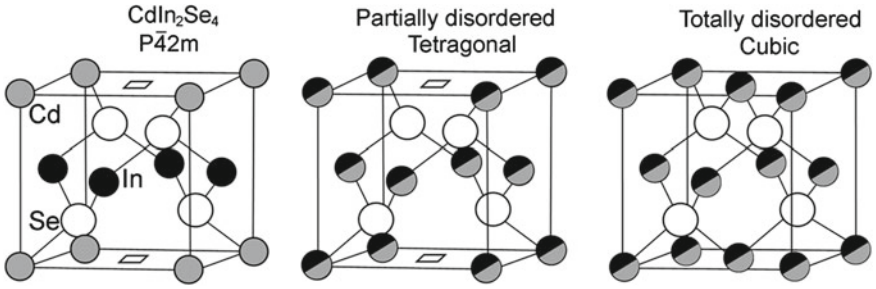

Fig. 1.3 Disordered defective tetrahedral structures: filled cation sublattice disorder (*middle*); complete cation sublattice disorder involving vacancies (*right*)

microscopy revealed that different degrees of order or different structures coexist within this compond [11], as shown in Fig. 1.3. If also vacancies are disordered, e.g., $HgGa_2Te_4$ at room temperature [13] or $CdGa_2Se_4$ at high temperature [14], a disordered cubic zinc blende structure is obtained (Fig. 1.3, right).

In the zincblende structure each S atom is at the center of a tetrahedron with four Zn atoms at each corner. The four bonds have all the same length and are symmetrically equivalent in space making a very well known angle of 109°45′. When two Zn atoms are replaced in the chalcopyrite structure by Cu and the two other Zn atoms are replaced by Fe the four bonds are no longer identical: the distance between S and Cu is not exactly equal to the distance between S and Fe [1]. In other words, the tetrahedron is no longer regular but is slightly deformed along the two-fold axis. However this distortion in most compounds is not very large and the orbitals remain very close to sp, hybrids. Therefore, the lattice period c is not exactly equal to $2a$. This is characterized by a dimensionless parameter: which takes into account the dilatation or the compression along the z-axis.

$$\delta = 2 - \frac{c}{a} \tag{1.1}$$

On the other hand, the displacement of the S atoms due to bonds' length difference is alternatively along the +x and the −x axis and along the +y and −y axis. If x is the actual position of the S atom in the cell, this displacement is measured by the dimensionless parameter

$$\sigma = \left| \frac{4x}{a} - 1 \right|. \tag{1.2}$$

Many of the physical properties of the chalcopyrite crystals depend to some extent on the values of δ and σ.

Similarly to other ternary compounds, apart from tetrahedral structures, $A^{II}B_2^{III}X_4^{VI}$ compounds can be obtained in other structures. It is known that many ternary compounds are not of the chalcopyrite structure. There are examples where the actual structure is slightly different from the chalcopyrite. Many tetrahedral ternary

compounds have a structure very different from chalcopyrite. More precisely, they often display a particular structure which is derived from wurtzite much in the same way chalcopyrite is derived from sphalerite. Moreover, several ternary compounds are not tetrahedrally coordinated but have a sixfold or an eightfold coordination [3].

As concerns $A^{II}B_2^{III}X_4^{VI}$ compounds, according to the number of octahedral (Ω) and tetrahedral (τ) cationic sites, one has spinel ($2\Omega + 1\,\tau$), layered ($1\Omega + 2\,\tau$) and tetragonal structures ($3\,\tau$) as shown in Fig. 1.4 [11, 15].

If tetrahedral coordination prevails, one has deffective structures; in the presence of octahedral coordination, the four non-bonding orbitals are arranged in planes, and the compound is characterized by easy cleavage along these planes which interact via vander Waals forces (layered compounds). If all the sites are tetrahedrally coordinated, the non-bonding orbitals originate point defects (vacancies) arranged in a more or less ordered tridimensional array (defect chalcopyrite).

The primitive unit cell of a $A^{II}B_2^{III}X_4^{VI}$ spinel is shown in Fig. 1.5. The elementary cell of the $A^{II}B_2^{III}X_4^{VI}$ spinel-type compounds consists of 8 formula units. X^{VI} ions create a close-packed arrangement with 64 tetrahedral and 32 octahedral interstices per cell. In an ideal spinel structure, A^{II} atoms occupy eight tetrahedral sites of T_d symmetry and B^{III} atoms are situated in 16 octahedral sites of D_{3d} symmetry; whereas X atoms occupy C_3v sites [4].

In real spinel structures, the distribution of the cations is not ideal, and the cations are sometimes disordered on their sites. The disordering of cations is described by means of the normality index λ. This parameter leads to a more general formula $A_\lambda B_{1-\lambda}(A_{1-\lambda}B_{1+\lambda})$ which describes the occupation of the tetrahedral (octahedral) positions in the lattice. The value of the normality index $\lambda = 1$ describes an ideal spinel structure, while $\lambda = 0$ corresponds to an inverse spinel structure. Thus, for the "inverse" spinel, a half of the trivalent (B) ions are located in the tetrahedral position; the other part of B and A ions is usually statistically distributed between the octahedral positions. A totally stochastic distribution on cations is obtained with the value $\lambda = 1/3$.

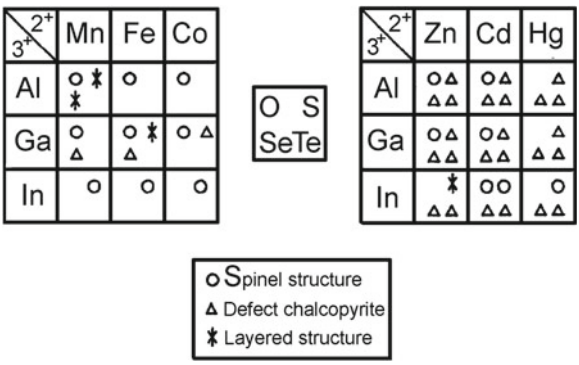

Fig. 1.4 Structures of $A^{II}B_2^{III}X_4^{VI}$ compounds. Reprinted with permission from Razzetti et al. [11]. © 1987, Elsevier

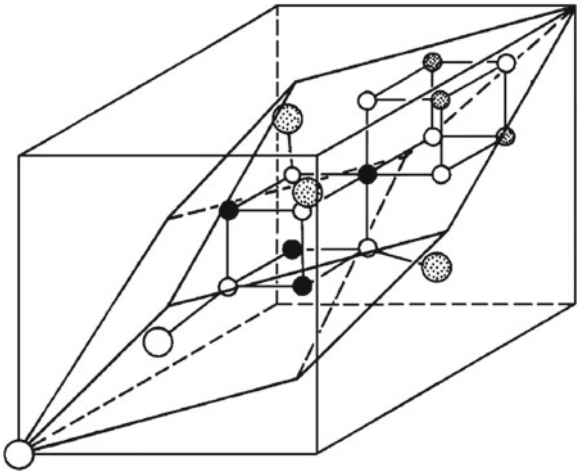

Fig. 1.5 Crystal structure of spinel. *Large open* and *large flecked circles* are A^{II} ions, *full* and *small flecked circles* are B^{III} ions and *small open circles* are X ions. The *flecked circles* are outside the primitive unit cell

Razzetti et al. noticed that layered phases appear for compositions intermediate between spinel and tetragonal structures [15]. It was assumed that all these layered structures, characterized by two tetrahedral ($2\,\tau$) and one octahedral (1Ω) cation coordinations, are intermediate between the spinels and the thiogallates

$$\begin{aligned} &AB_2X_4 - AB_2OX_4 - AB_2\square X_4 \\ &(2\Omega + 1\,\tau) - (1\Omega + 2\,\tau) - (3\,\tau). \end{aligned}$$

As concerns the degree of cation and vacancies ordering, a number of possible order-disorder transitions were identified by Bernard and Zunger [16]. Two levels of disorder were considered in the system. In the "stage-I disorder" two cations A and B in AB_2X_4 compounds mutually substitute for one another. This leads in both the defect famatinite (Fig. 1.2e) and the defect chalcopyrite (Fig. 1.2d) OVC's to the same partially cation-disordered phase (Fig. 1.2f), whereas in the structure with the space group $P\bar{4}2m$ such as α-$CdIn_2Se_4$ a pseudocubic structure results after stage-I disorder (Fig. 1.3). The impossibility to determine unequivocally whether $ZnGa_2S_4$, $ZnGa_2Se_4$, $ZnGa_2Te_4$, $ZnA1_2Te_4$, $CdA1_2Te_4$, $HgA1_2Te_4$, and $HgGa_2Te_4$ are ordered in the defect famatinite or in the defect chalcopyrite phase was explained by the fact that both defect famatinite and defect chalcopyrite disorder into the same structure.

In "stage II" disorder both of the two cation types and the vacancy disorder mutually. This results in the formation of the disordered zinc-blende-like phase from either of the partially (cation) disordered phases. It was suggested that ten OVC's disorder into this zinc blende phase: $ZnAl_2Se_4$, $ZnAl_2Te_4$, $ZnGa_2S_4$, $ZnGa_2Se_4$, $ZnGa_2Te_4$, $ZnIn_2Te_4$, $CdA1_2Te_4$, $CdGa_2Se_4$, $HgA1_2Te_4$, and $HgGa_2Te_4$

[16]. Direct order-disorder transformations into this zinc-blende phase were observed by Mocharnyuk et al. [14] for $(CdGa_2Se_4)_x(CdIn_2Se_4)_{1-x}$ alloys. It was concluded that only the disordered phase is observed, if the transition temperature T_c is lower than the crystal growth temperature, this being the case for $HgGa_2Te_4$ exhibiting only zinc-blende-type diffraction peaks.

It was assumed that order-disorder transformations are more prevalent (and occur at lower T_c's) in the ordered-vacancy $A^{II}B^{III}_2X^{VI}_4$ compounds, as compared to ternary chalcopyrites $A^{I}B^{III}C^{VI}$ and pnictides $A^{II}B^{IV}C^{V}$, since the difference in the valence of the disordering atoms A and B is two in chalcopyrites and pnictides, while the A–B valence difference is but one in $A^{II}B^{III}_2X^{VI}_4$ compounds. Therefore, disordering is energetically less costly, and the material properties of OVC's (structural parameters, band gap, transport properties) may depend sensitively on growth temperature and on the growth and quenching rates, as these control the extent to which a (partial or complete) disorder or multiple phase coexistence is "frozen into" the sample. Two further cation-vacancy disorder reactions were suggested to exist in AB_2X_4 compounds in addition to stage I and stage II disorder: disordering of the A atom alone on the vacancy site, or disordering of the eight atom on the vacancy site.

In the system $Cd(Ga_xIn_{1-x})_2Se_4$ the order-disorder transition temperature is a function of composition and the order collapse is tied to the disordering of the vacancy sublattice which leads to a disordered sphalerite structure [11, 14], as shown by the phase diagram of this alloy system (Fig. 1.6). In addition, there is some evidence of a second order phase transition at lower temperatures in $CdGa_2Se_4$. Similar transitions were observed for other families of alloys, and they are clearly connected to a disordering of the cation sublattice. This means that the structures shown in Figs. 1.2 and 1.3 which are observed in different compounds at room temperature could be obtained from one compound just as a function of temperature.

It was shown that the order–disorder transition with increasing temperature can take place only in the chalcopyrites with axial ratio $c/a > 1.95$ [17]. Compounds with $c/a < 1.95$ remain in the ordered chalcopyrite structure all the way up to the melting point. Apart from that, the order-disorder behavior and the tetragonal distortion δ

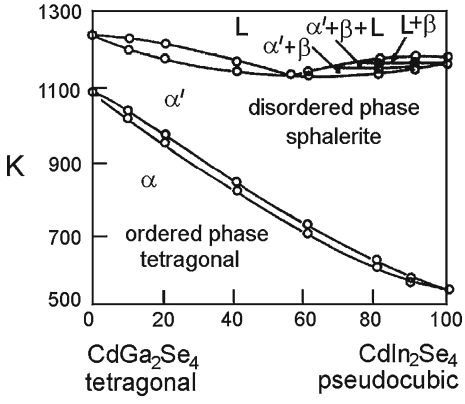

Fig. 1.6 The phase diagram of the $Cd(Ga_xIn_{1-x})_2Se_4$ alloy. Reprinted with permission Razzetti et al. [11]. © 1987, Elsevier

Table 1.1 The tetragonal distortion δ and difference $\Delta\chi_{AB}$ in electronegativity between the A–X and B–X bonds for the $A^{II}B_2^{III}X_4^{VI}$ materials

Compound	$\Delta\chi_{AB}$	δ
$CdGa_2S_4$	0.124	0.17
$CdGa_2Se_4$	0.118	0.13
$ZnGa_2S_4$	0.042	0.04
$ZnGa_2Se_4$	0.040	0

of the chalcopyrite compounds ABX_2 can be described in terms of the difference in electronegativity $\Delta\chi_{AB}$ between the A–C and B–X bonds [17]. Chalcopyrites with $\Delta\chi_{AB} < 0.09$ exhibit an order-disorder solid state transition, whereas the chalcopyrites with $\Delta\chi_{AB} > 0.09$ remain in the ordered chalcopyrite structure up to their melting point. The tetragonal distortion δ and the difference in electronegativity for the $A^{II}B_2^{III}X_4^{VI}$ materials under consideration are presented in Table 1.1. As one can see from the table, the materials with $\Delta\chi_{AB} < 0.09$ and $\delta < 0.05$($ZnGa_2S_4$ and $ZnGa_2Se_4$) crystallize as DF whereas the compounds with $\Delta\chi_{AB} > 0.09$ and $\delta > 0.05$ ($CdGa_2S_4$ and $CdGa_2Se_4$) crystallize as DC.

On the other hand, the temperature-induced order-disorder transitions were investigated in $A^{II}B_2^{III}X_4^{VI}$ compounds [18–20]. In analyzing these data it was observed that the lower the δ the higher the temperature of the order-disorder transition. However, unlike chalcopyrites, in DC $A^{II}B_2^{III}X_4^{VI}$ compounds the order-disorder transitions with temperature can occur in materials with $\delta > 0.05$ as well. This different behavior can be explained by the presence of stoichiometric vacancies in the DC phase.

The microscopic dielectric theory of Phillips and Van-Vechten [21] pr ovides a basis for understanding the structural trends of semiconductors. In Table 1.2 we summarize the homopolar energy gap E_h and ionic energy C for most of the $A^{I}B^{III}X_2^{VI}$ CP compounds [22, 23] as well as for $A^{II}B_2^{III}X_4^{VI}$ DC compounds [24]. The values of E_h and C for $A^{II}B_2^{III}X_4^{VI}$ compounds were calculated from

$$E_h = (E_{h,AX} + 2E_{h,BX})/3 \tag{1.3}$$

and

$$C = (C_{AX} + 2C_{BX})/3, \tag{1.4}$$

while the average energy gaps from

$$E_g^2 = E_h^2 + C^2. \tag{1.5}$$

The ionic effective charges are also important parameters characterizing the lattice, dynamical, electronic or optical properties of solids and are directly related to the concept of ionicity [25].

Several kinds of effective charges have been introduced. Static and dynamical charges, local and nonlocal contribution to the effective charges have been extensively

Table 1.2 The homopolar (E_h), ionic (C) and average (E_g) energy gap for ABX_2 and AB_2X_4 compounds. All energies are in eV units

Compound	E_h	C	E_g
ABX_2			
$CuAlS_2$	5.078	8.161	9.612
$CuAlSe_2$	4.490	7.300	8.570
$CuAlTe_2$	3.789	6.257	7.315
$CuGaS_2$	4.795	7.679	9.053
$CuGaSe_2$	4.254	6.955	8.153
$CuGaTe_2$	3.713	6.141	7.176
$CuInS_2$	4.207	6.711	7.921
$CuInSe_2$	4.133	6.900	8.043
$CuInTe_2$	3.463	5.298	6.329
$AgAlS_2$	4.605	7.630	8.912
$AgAlSe_2$	4.118	6.887	8.024
$AgAlTe_2$	3.469	5.970	6.905
$AgGaS_2$	4.529	7.495	8.757
$AgGaSe_2$	4.050	6.820	7.932
$AgGaTe_2$	3.447	5.983	6.905
$AgInS_2$	4.138	7.222	8.323
$AgInSe_2$	3.705	6.520	7.499
$AgInTe_2$	3.171	5.656	6.484
AB_2X_4			
$CdAl_2S_4$	4.679	5.831	7.476
$CdGa_2S_4$	4.638	5.789	7.420
$CdGa_2Se_4$	5.071	6.015	7.867
$ZnGa_2S_4$	4.177	5.269	6.720
$ZnGa_2Se_4$	4.477	5.400	7.015

studied. The static ionic charge is based on the electronegativity of the ions and is influenced by the symmetry of the surrounding atoms. The dynamic ionic charge is, on the other hand, induced by the lattice vibrations.

The transverse effective charge e_T^*, directly related to the TO–LO splitting, is given, in cubic binary systems with one optic mode, by

$$e_{T^2}^* = \varepsilon_\infty \varepsilon_V \mu v(\omega_{\mathrm{LO}}^2 - \omega_{\mathrm{TO}}^2) \tag{1.6}$$

where $\varepsilon_\propto$ is the high frequency dielectric constant, ε_v is the vacuum dielectric constant, μ is the reduced mass of the ion pair, v is the volume occupied by a chemical formula unit and ω_{LO} ω_{TO} are the LO–TO splitted frequencies of the optic mode.

More often, a Szigeti effective charge e_S^* is used, simply related to e_T^* by

$$e_S^* = \frac{3e_T^*}{\varepsilon_\infty + 2} \tag{1.7}$$

When the dielectric constant is >5, indicating that the LO–TO splitting is due in part to the polarizability of the ions, the Szigeti effective charge should be used for studying ionicity effects.

Wakamura and Arai [26] found an empirical relationship between the normalized Szigeti effective charge and $\varepsilon_\infty - 1$ in binary and ternary compounds, expressed by

$$\varepsilon_\infty - 1 = \frac{2}{x + x^2} \tag{1.8}$$

where $x = e_S^*/Z_{eff} \cdot e$, and Z_{eff} is the effective chemical valency of the ion.

The data related to the normalized Szigeti effective charge for a series of compounds are presented in Fig. 1.7. It was suggested that the applicability of (1.8) to a greater number of compounds may be supported intensely, as most points show a small scatter from the curve. In the correlation, the relatively large scatter for some

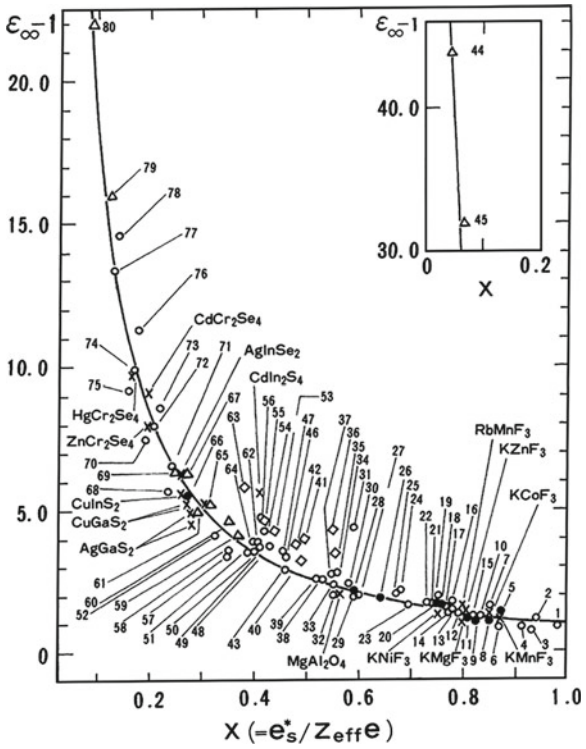

Fig. 1.7 Relationship between the effective charge normalized by the effective chemical valency, $e_S^*/Z_{eff} \cdot e$, and $\varepsilon_\infty - 1$. □: the $3d$- or $4f$-electron compounds. Δ: the values calculated from e_i^*. •: the compounds of types AX_2, and A_2X and ammonium halides. ○: other binary compounds. x: ternary compounds, the correspondence between the compound and the number is listed in Table 1.3 of Wakamura and Arai [26]. The *solid line* shows the relation of $\varepsilon_\infty - 1 = 2.0/(x + x^2)$. Reprinted with permission. © 1981, American Physical Society

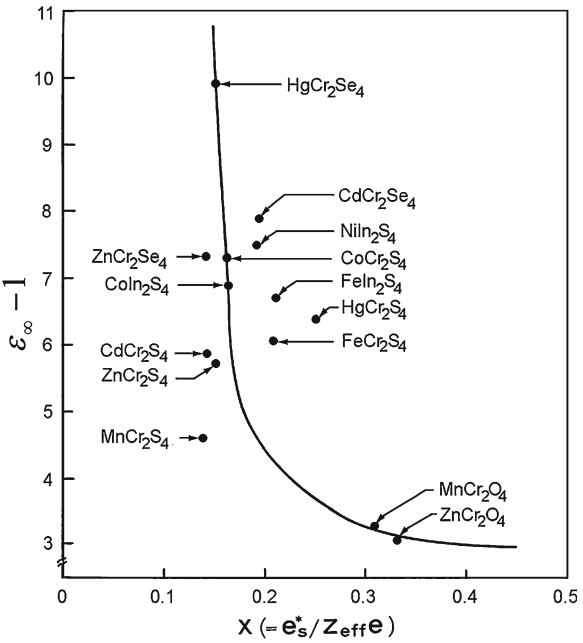

Fig. 1.8 Relationship between the effective charge normalized by the effective chemical valency, $e^*_S/Z_{eff}\cdot e$, and $\varepsilon_\infty - 1$ for ternary chalcogenide spinels. Reprinted with permission from Kushwaha and Kushwaha [27]. © 2005, Creative Commons

compounds was explained by the *d*- or *f*-electron effect on the dielectric constant ε_∞ and by the screening and the anisotropic effects on the effective charge.

The empirical relationship between the normalized Szigeti effective charge and the dielectric constant ε_∞ for ternary chalcogenide spinels (Fig. 1.8) was analyzed by Kushwaha [27]. It was found that the charge of the cation is related directly to ε_∞ in compounds composed of two kinds of anions. From this analysis it was deduced that the ionicity increases in the order oxide > sulphide > selenide, indium compounds > cromium compounds, normal spinel > inverse spinel.

Lottici and co-workers [25] found that ionic effective charges of defect chalcopyrite crystals deduced from the LO–TO phonon frequencies in a "nearly cubic" approximation and hypothizing equal normalized effective charges of the cations fit also this empirical relationship between the normalized Szigeti effective charge and the dielectric constant ε_∞. Some scatter from this relationship for defect chalcopyrite compounds was attributed to the anisotropy of the crystals which induces different averages with respect to a cubic surrounding.

1.2 Crystal Growth

It was shown that most ternary oxides can be prepared by sintering the finely powdered, binary constituents in air and crystals are usually grown by pulling from a melt or by cooling a solution of the oxides in a suitable molten-salt solvent (flux) [28]. The synthesis of nonoxidic chalcogenides is aggravated by their oxidizability. It has to be carried out in vacuum or in a protective atmosphere. The chalcogenide layers which form on the metal surfaces in the initial stage of crystal growth can prevent diffusive completion of the reaction. This may lead to excessive pressures upon further heating. These difficulties can be overcome by adding small amounts of halogens to the reaction mixture. The halogen acts as mineralizer, breaking-up non-reactive surface films. This mineralizing action of small halogen additions often drastically cuts down the reaction times and allows syntheses at considerably reduced temperatures as compared to pure systems. The product of the crystal growth is determined by the existence of the so-called subsolidus phases which form by peritectic or solid–solid reactions. Figure 1.9 shows a section of a hypothetical, pseudobinary system [28, 29] in which three ternary compounds exist. Only AB_2X_4 is obtainable from a stoichiometric melt. Solution growth of AB_6X_{10} is problematic and $A_2B_2X_5$ only forms by a solid–solid reaction. All three compounds can however easily be synthesized from the proper mixtures of the elements at low temperatures (e.g., along the 700° line indicated in Fig. 1.9) by the halogen method, i.e., by participation of a reactive vapour phase.

Growth from liquid phases has been successful in certain cases. Melt growth of chalcopyrite-type compounds by the Bridgman method has been reported by several authors. Particularly, the molten sulfides of arsenic, As_2S_3 and As_2S_5 and their mixtures can dissolve sizeable amounts of In_2S_3, they being good solvents even for ternaries such as $ZnIn_2S_4$ and $CdIn_2S_4$ [30]. Chalcopyrites have been grown also from liquid indium [31]. However, the growth from the vapour (either by sublimation or by chemical transport) is the most promising method for many ternary chalcogenides [28, 32]. Both sublimation and chemical transport can be carried out in open (flow) systems and in closed systems, usually sealed quartz vessels, the latter being preferred for bulk crystal growth on an experimental scale. The stationary, sealed ampoule, placed in a temperature gradient [28, 33], is the simplest device for vapour growth (Fig. 1.10). The upper temperature limit attainable is about 250 and 2,000 °C with transparent sapphire tubing.

In most cases, the halogenes I_2, Br_2, or Cl_2, are the preferred transporting agents. However, in some cases, the presence of oxygen (or water vapour) is required in addition to the halogen to achieve efficient transport. For obtaining larger crystals (with size of the order of cm) from the vapour, a better control of the nucleation is required, which can be realized in different ways: (i) by using a conical or a capillary-shaped ampoule tip; (ii) by introducing a seed into the ampoule; (iii) by selective cooling of a small, defined nucleation region; (iv) by moving the ampoule relative to the temperature gradient (vapour pulling) and by adjusting the pulling speed to the material transport rate (Fig. 1.11).

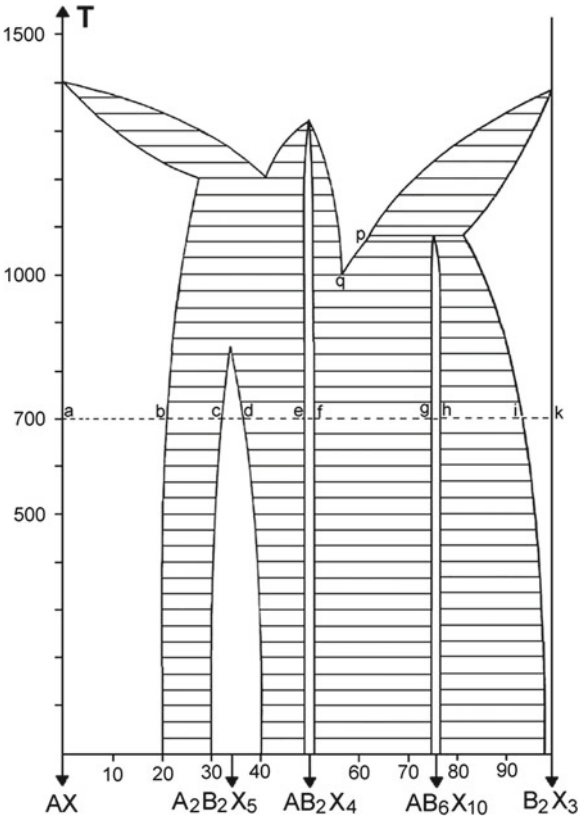

Fig. 1.9 A hypothetical, pseudobinary system with ternary compounds. Reprinted with permission from Nitsche [28]. © 1975, EDP Sciences

Another arrangement utilized for vapour growth is a system with radial gradient (Fig. 1.12), in which slightly cooled seed is placed on a pedestal in the center of a cylindrical ampoule which rotates in a radial gradient assuring the material from the periphery of the ampoule to be transported to the center [28, 34].

It was shown that vapour methods offer great possibilities to grow a large number of ternary chalcogenide crystals, and a crystal growing freely into space from a vapour potentially contains much less dislocations and other faults than a crystal being constrained by a container during growth and the cooling-down period [28].

A temperature variation method was proposed for the growth of chalcopyrite crystals by iodine vapour transport, and a two to fourfold increase in the size of crystals was obtained by means of a time-varying temperature profile procedure [35]. The principle of the method consists in a gradual raising of the source temperature, which allows, first, a reduced primary nucleation, and, secondly, the avoidance of constitutional undercooling during the first stages of the nucleus growth. The temperature profile variation with this method is schematically represented in Fig. 1.13,

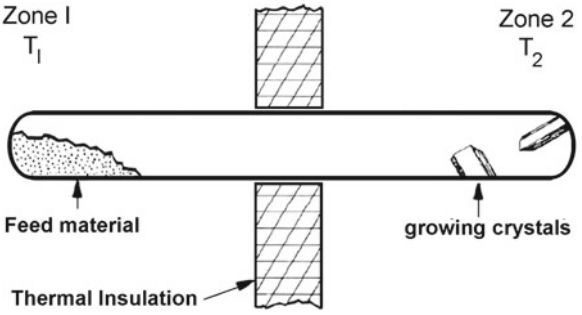

Fig. 1.10 Vapour growth in stationary ampoule. Reprinted with permission from Nitsche [28]. © 1975, EDP Sciences

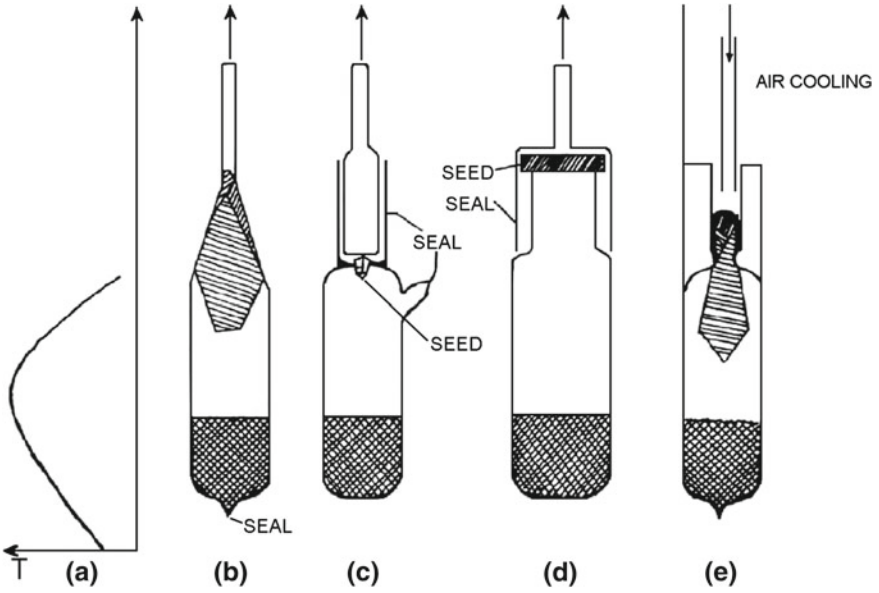

Fig. 1.11 Vapour growth by moving gradients. Reprinted with permission from Nitsche [28]. © 1975, EDP Sciences

where the source-material temperature $T_s(t)$ is a slowly raising function of time, while the deposition temperature T_d is kept constant. Initially, the ampoule is placed in a T-profile so that $T_s(t)$ is lower than T_d by about 100 °C (temperature inversion). Such temperature inversion is a very important feature of the method, because of its cleaning effect on the quartz walls of the deposition zone. After 2–3 days of temperature inversion, T_s is programmed to raise at a constant rate, calculated so as to give the final temperature profile $T_s(t_f)$ in the planned growth period $t_f - t_0$ where $T_s(t_0)$ is about 10 °C lower than T_d. Qualitatively, the growth mechanism can be described as follows. By increasing $T_s(t)$, when t reached some value $t_2 (> t_1)$, the supersaturation

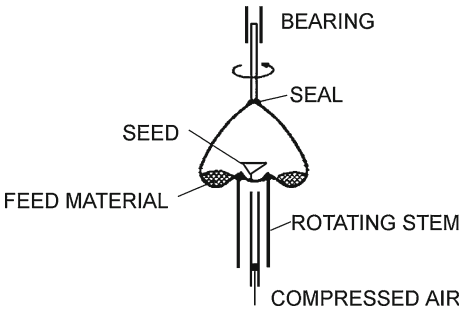

Fig. 1.12 Vapour growth in radial gradient. Reprinted with permission from Nitsche [28]. © 1975, EDP Sciences

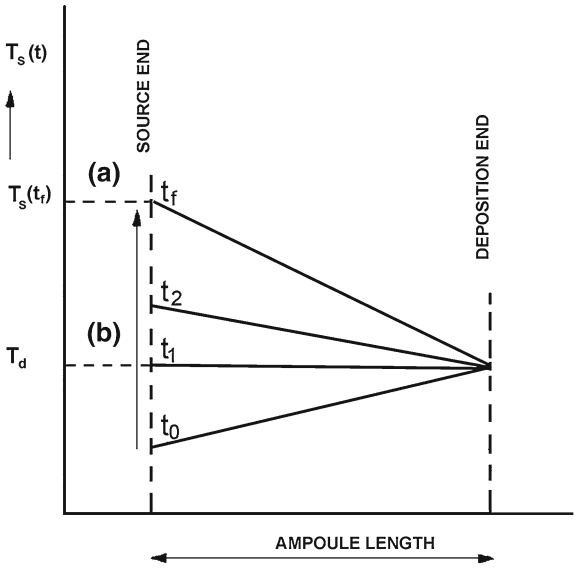

Fig. 1.13 Temperature profiles: **a** stationary temperature profile STP: $T_s(t_f)/T_d$; **b** time-varying temperature profile TVTP: $T_s(t_0) \rightarrow T_s(t_f)/T_s(t_l) = T_d$. Reprinted with permission from Paorice et al. [35]. © 1978, Elsevier

reaches a value for which primary nucleation has a high probability of occuring on some active sites of the quartz walls. Since now the growth process of these primary nuclei will result in a more probable process, their development into large single crystals is expected, at the expense of new primary nucleation.

Three different temperatures versus time profiles were for instance employed for the growth of $Zn_xCd_{1-x}In_2S_4$ pseudoternary solid solution, namely the Stationary Temperature Profile (STP), the Linear Time Varying Temperature Profile (LTVTP), and the Oscillating Temperature Profile (OTP) [36]. The STP procedure was employed to determine the best growth temperature for each nominal composi-

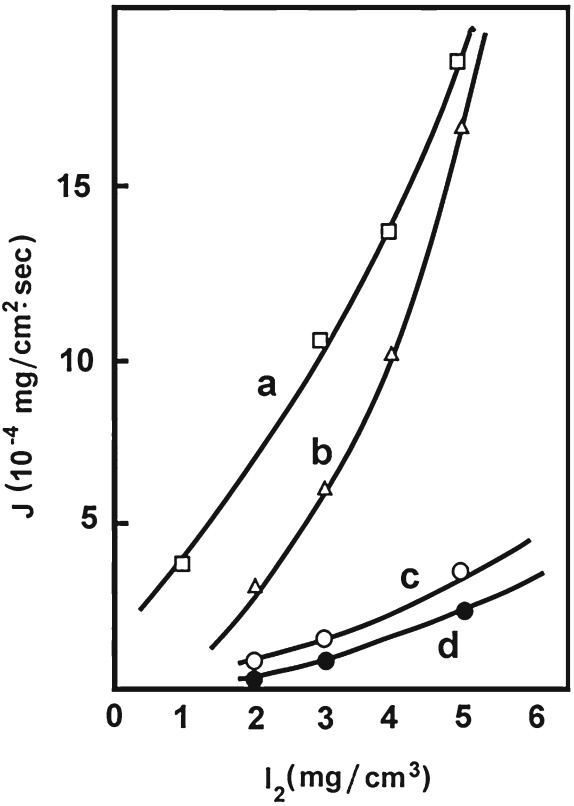

Fig. 1.14 Mass transport coefficient J for layered ($ZnIn_2S_4$-like) and cubic ($CdIn_2S_4$-like) phases as a function of iodine concentration. Stationary temperature profile: $T_s = 830\,°C$, $T_d = 780\,°C$. **a** Layered phase, 2-cm-internal-diameter ampoules; **b** spinel phase, 2-cm-internal-diameter ampoules; **c** layered phase, 1-cm-internal-diameter ampoules; **d** spinel phase, 1-cm-internal diameter ampoules. Reprinted with permission Curti et al. [36]. © 1987, Elsevier

tion. The transport kinetics observed in STP for $x = 0.6$ is reported in Fig. 1.14 as a function of iodine concentration. For this composition, phase separation has been observed. The LTVTP method, which is suitable for growth of a reduced number of larger crystals in comparison to the STP method, was employed for the crystal growth. In this method the deposition temperature T_d is kept constant, while the source temperature T_S is increased linearly with time.

LTVTP + OTP was employed in those cases in which very small amounts of one of the two phases were obtained. The LTVTP + OTP procedure is based on an initial LTVTP stage by which a few initial seed crystals are grown, followed by T_d oscillations. Large frequencies and small amplitudes of the change in T_d, once properly chosen, can control the growth of the best seeds, while reducing and even eliminating a faulty growth.

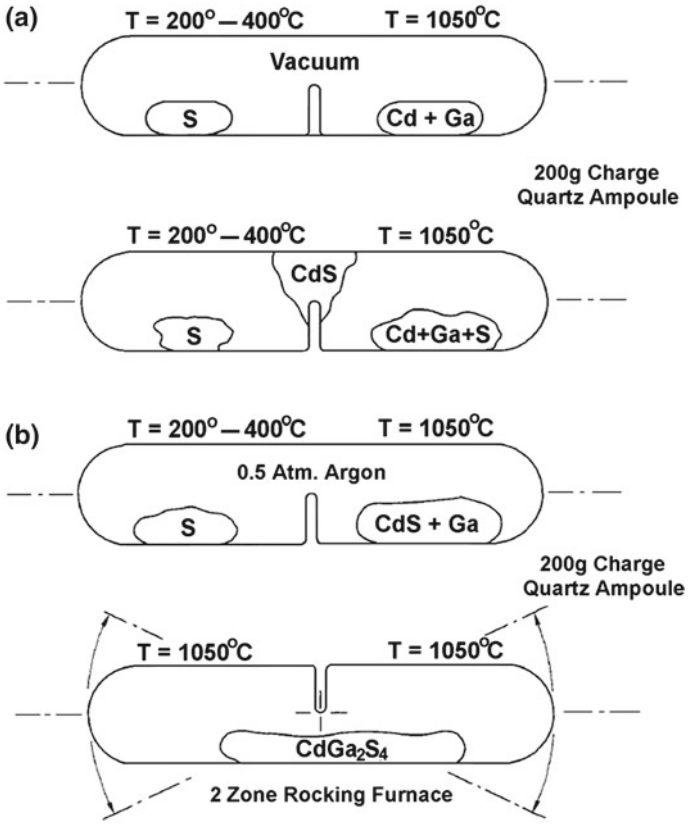

Fig. 1.15 **a** Vapor synthesis technique used for chemical reaction from the elements. **b** Vapor synthesis technique modified to prevent the formation of a CdS plug and allow complete reaction in one step. Reprinted with permission from Feigelson and Route [38]. © 1987, Elsevier

High optical quality $A^{II}B_2^{III}X_4^{VI}$ single crystals, particularly of $CdGa_2S_4$, have been also grown by the vertical Bridgman method [37, 38]. A schematic of the synthesis setup with a two-zone horizontal rocking furnace is shown in Fig. 1.15a [38]. In this method, the metallic constituents are maintained in the hot zone (~1,050 °C), and the sulfur is held between 200 and 400 °C in the cooler zone until all of the sulfur has reacted. At that point the entire ampoule is heated to a uniform 1,050 °C and rocked for several hours in order to homogenize the charge before cooling. In order to solve the problem with stopping the chemical reaction due to the formation of the volatile intermediate CdS which was deposited as a plug between the two zones during the synthesis of $CdGa_2S_4$, the fused silica ampoule was opened and the CdS plug was removed and returned to the hot zone. After several cycles, complete chemical reaction was achieved, and melt fusion and homogenization was carried out.

To avoid the formation of a CdS plug, an improved synthesis technique was later developed. The essential differences are shown in Fig. 1.15b. CdS replaced metallic cadmium in the hot zone, and a 0.5 atm backfill of argon was added before seal-off. Having the cadmium in a prereacted state prevented the vapor phase reaction of CdS in the intermediate temperature region, and the argon gas suppressed the physical vapor transport of CdS from the hot zone there.

1.3 Crystal Structure

As mentioned in the Sect. 1.1, there are mainly three structure types possible for samples with stoichiometry $A^{II}B_2^{III}X_4^{VI}$, with A = Zn, Cd, Hg; B = Al, Ga, In; and X = 0, S, Se, Te, i.e., the tetragonal defective zinc blende structure, cubic spine1 structure, and the layered rhombohedral $ZnIn_2S_4$-type structure. According to the Aufbau principle of the large majority of semiconducting structures [39, 40] the anions form a close-packed 3-dimensional array in which the cations occupy part or all of the tetrahedral and/or octahedral holes. The overall degree of filling of the sets of holes is determined by the cation valences: the total number of cation valence electrons must suffice to complete the octet of every anion.

On the basis of the Aufbau principle, Mooser and Pearton [41] investigate the question whether there exist a correlation between the chemical composition of a phase and the co-ordination configurations (tetrahedral and/or octahedral) met in its structure. They suggested that with increasing principal quantum number n of the valence shell of an atom, the directional character of the bonds formed by the atom decreases. Moreover, covalent bonds have strongly pronounced directional properties, while ionic bonds are nondirectional. As a result of this analysis they found that at low values of the average principal quantum number $\bar{n}$ and/or difference $\Delta\chi$ between the electronegativities, low coordinated (tetrahedral) structures are met, the high coordinated (octahedral) ones being found at high $\bar{n}$ and/or $\Delta\chi$ values.

Later on, Fillips [42] and Van Vechten [43] introduced two new, fully quantum-mechanical scaling co-ordinates, i.e., the average covalent energy gap E_h and the average ionic energy gap C, for extracting from available structural and physical data qualitative rules for the chemical bonding in solids. It was found that in an E_h versus C diagram, the simple AB-type of octet compounds fall into two completely separate regions, one corresponding to four-fold, and the other to sixfold co-ordination.

As mentioned in the Sect. 1.1, the $A^{II}B_2^{III}X_4^{VI}$ compounds are characterized by tetrahedral or tetrahedral and octahedral cation-to-anion co-ordination. Whenever all cation sites are tetrahedrally co-ordinated, tetragonal defective structures are formed (thiogallates). When tetrahedral and octahedral co-ordinations take place, layered structures are formed if their number is different, and cubic ones are formed in the opposite case. In both cases the lattice seems to be intrinsically disordered. Razzetti and Lottici [44] have grown 28 different compositions of sulphur compounds as shown in Fig. 1.16.

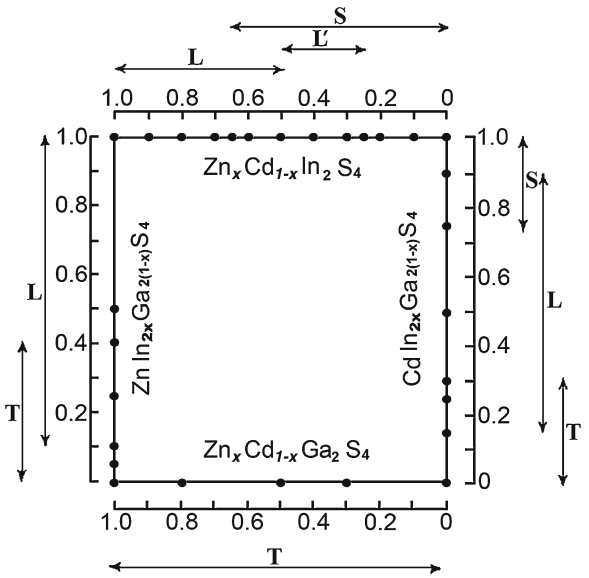

Fig. 1.16 Sulphur mixed cation quaternary compounds synthesized: the *dots* represent the starting composition of the compounds (see the text). *L*, *S* and *T* indicate the structures of the reaction products, where *L* stands for layered, *S* for spinel and *T* for tetragonal (defect chalcopyrite). The *arrows* indicate the existence region of each phase as a function of the starting composition (x). Whenever two *arrows* correspond to a particular composition, phase separation takes place, otherwise one has complete solid solution. Reprinted with permission from Razzetti and Lottici [44]. © 1983, Springer

For $Zn_xCd_{1-x}In_2S_4$ compounds it was found that (i) complete solution takes place for $x \geq 0.7$ and $x \leq 0.2$: the compounds which form in these intervals show structures similar to $ZnIn_2S_4$ and $CdIn_2S_4$, respectively; (ii) phase separation occurs in the intermediate region ($0.65 \geq x \geq 0.25$); (iii) the two different structures which form in this region ($0.65 \geq x \geq 0.5$ and $x = 0.4$, respectively) are similar to $ZnIn_2S_4$ and $Zn_3In_2S_6$.

Figure 1.17 shows a plot of the lattice parameters versus composition of the quaternary chalcogenides [45]. The spinel phase has a relatively large homogeneity range. Up to 31 % of sulfur atoms can be replaced by selenium. With increasing molar ratio of $CdIn_2Se_4$ the unit-cell dimensions of the $CdIn_2S_{4-x}Se_x$ spinel-type mixed crystals increase. The slope of the curve obeys Vegard's law. The tetragonal pseudocubic form of $CdIn_2Se_4$ (space group $P\bar{4}2m$) has a smaller homogeneity range than the spinel phase. Only up to 12 mole % of $CdIn_2S_4$ are soluble in $CdIn_2Se_4$. Between 44 and 68 mole % $CdIn_2Se_4$ the mixed crystals crystallize in the rhombo-hedral $ZnIn_2S_4$-type structure (space group R3m). The $ZnIn_2S_4$-type is an intermediate between the spinel on one hand and tetrahedral structures on the other hand. It can be formed by changing the composition in both the nonmetal sublattice and the metal sublattice.

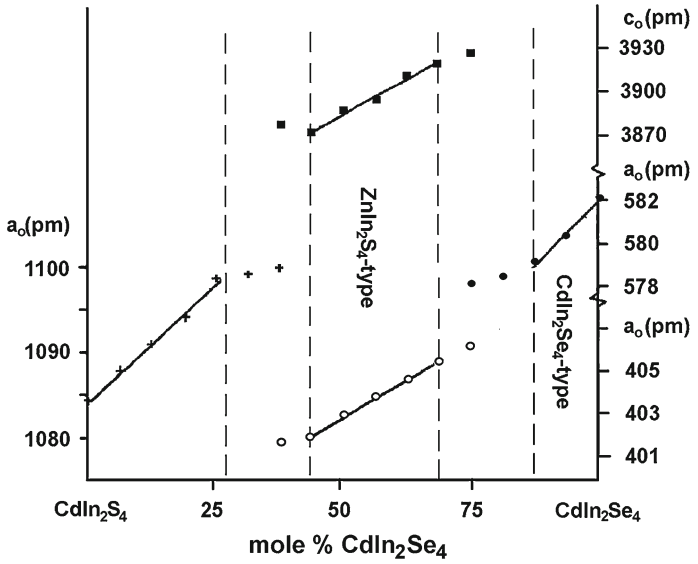

Fig. 1.17 Plot of unit-cell dimensions versus composition in the series $CdIn_2S_{4-x}Se_x$. Reprinted with permission from Haeuseler [45]. © 1979, Elsevier

Antonioli and co-workers [46] studied the nature of the near-neighbour environment in ternary and pseudoternary defect chalcopyrites of the $A^{II}B_2^{III}X_4^{VI}$ family by using the extended X-ray absorption fine structure (EXAFS) technique (Figs. 1.18 and 1.19). Bond lengths nearly constant and close to the respective distances in the end member crystals were found over all the composition range, whereas the unit cell parameter *a(x)* changes accordingly to the virtual crystal approximation (Vegard's law).

As concerns spinels, Burdett and co-workers [47] succeeded in separating the normal spinels from the inverse ones by plotting the $r_\sigma(A)$ and $r_\sigma(B)$ co-ordinates of the two cations A and B of each spinel in a diagram (see Fig. 1.20). The $r_\sigma(A)$ and $r_\sigma(B)$ coordinates have been defined conventionally in terms of s- and p-orbital radii: $r_\sigma = r_s + r_p$.

Taking into account the ternary character of the $A^{II}B_2^{III}X_4^{VI}$ compounds, Meloni and Shaukat defined an appropriate set of structural indices [48]. First, the indices for each atom in the crystal were defined as:

$$R_\sigma^A = (R_s^A + 3R_p^A)/4$$
$$R_\pi^A = (3R_s^A - R_p^A)/4$$

From these atomic values the average over cations contained in the chemical formula were formed in order to obtain a single cation parameter

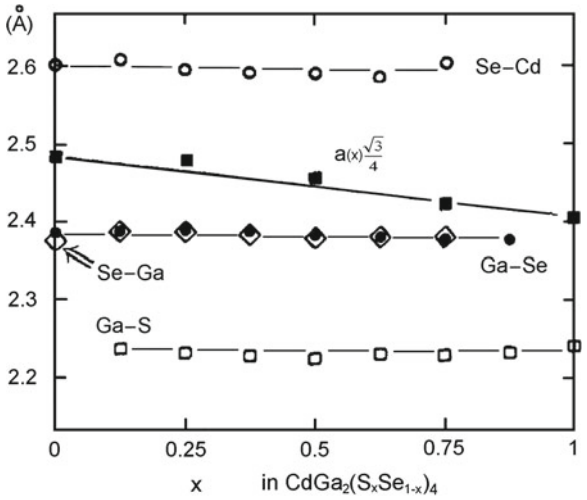

Fig. 1.18 Nearest neighbours distances as determined by EXAFS data analysis by two different methods. EXAFS data have been taken at Se and Ga K-edges. a(x) is the lattice constant in the mixed phase determined by X-ray diffraction. Reprinted with permission from Antonioli et al. [46]. © 1984, Elsevier

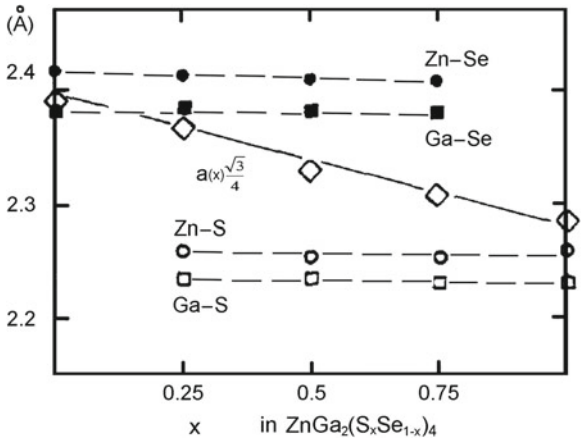

Fig. 1.19 Bond lengths in $ZnGa_2(S_xSe_{l-x})_4$ as given by the EXAFS analysis. a(x) is the lattice constant measured by X-ray diffraction. Reprinted with permission from Antonioli et al. [46]. © 1984, Elsevier

$$R_{\sigma}^{AB} = (R_{\sigma}^{A} + 2R_{\sigma}^{A})/3$$
$$R_{\pi}^{AB} = (R_{\pi}^{A} + 2R_{\pi}^{A})/3$$

Finally, the new crystal structural coordinates were constructed as:

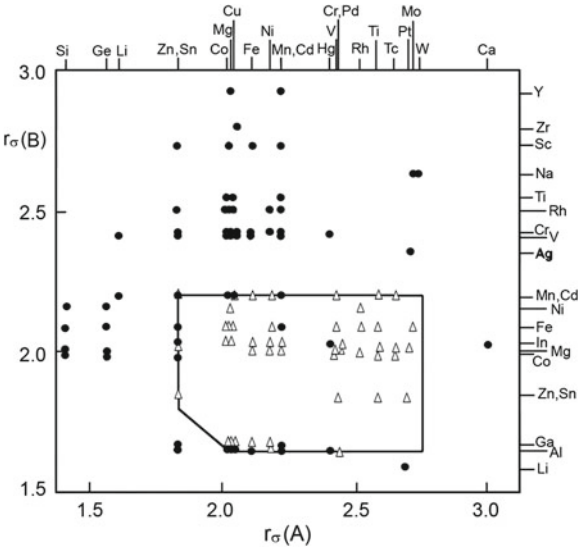

Fig. 1.20 Structural map sorting normal and inverse spinels: Δ inverse, • normal. Reprinted with permission from Burdett et al. [47]. © 1982, American Chemical Society

$$x(AB_2X_4) = R_\pi^{AB} + R_\pi^X$$
$$y(AB_2X_4) = R_\sigma^{AB} - R_\sigma^X$$

Two categories of the orbital radii were used in the analysis: the density-functional pseudopotential (DFP) orbital radii introduced by Zunger [49] and the hard-core pseudopotential orbital radii introduced by Andreoni, Baldereschi, Biemont, and Phillips (ABBP) [50].

The structural maps obtained are displayed in Figs. 1.21 and 1.22 for both normal and inverse spinels. It is evident from these figures that the introduced structural coordinate scheme can be applied successfully in separating the oxide, sulphide, selenide and telluride spinels, except for two Li-compounds, which fall a little far. It is also clear that this scheme is suitable for both sets of radii as far as it is based on the distribution of the anion component only. A further ordering of the normal spinels according to their A-cation component has been possible only with ABBP orbital radii, as shown in Fig. 1.22a.

1.4 Energy Band Structure

First-principles local-density-functional calculations for the electronic band structures of the ordered vacancy defect chalcopyrites $A^{II}B_2^{III}X_4^{VI}$ for A = Zn, Cd, Hg; B = Al, Ga, In, and X = S, Se, Te were performed by Jiang and Lambrecht [51].

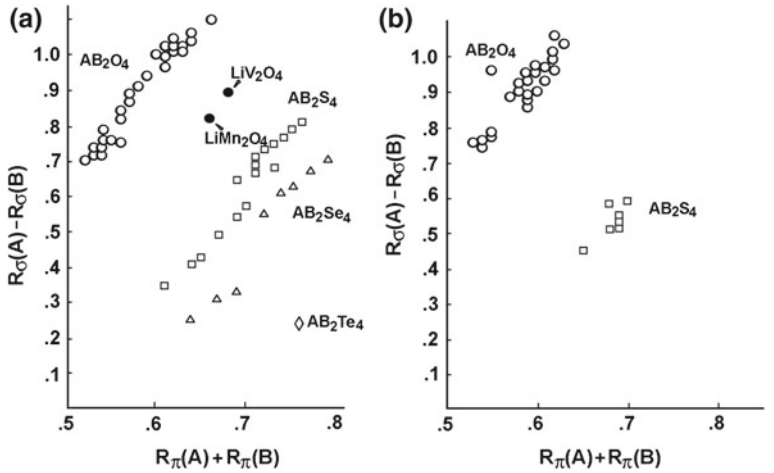

Fig. 1.21 Structural map for AB_2X_4 spinels according to Zunger in the normal (**a**) and in the inverse configuration (**b**). A stands for the A–B cation average and B for the anion. Reprinted with permission from Meloni and Shaukat [48]. © 1984, Elsevier

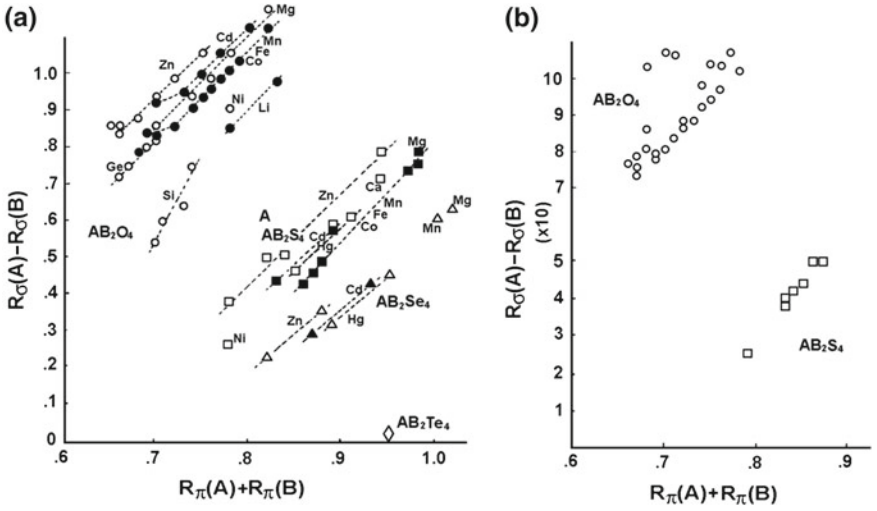

Fig. 1.22 Structural map for the AB_2X_4 spinels according to Andreoni et al. in the normal (**a**) and in the inverse configuration (**b**). Reprinted with permission from Meloni and Shaukat [48]. © 1984, Elsevier

Their relationship with the band structure of their parent chalcopyrite compounds $A^{I}B^{III}X_2^{VI}$ with A = Cu, Ag, and their grand parent $A^{II}B^{VI}$ compounds were clarified.

First Brillouin zone (BZ) of chalcopyrite structure and its relation to that of the zinc-blende (ZB) structure is shown in Fig. 1.23.

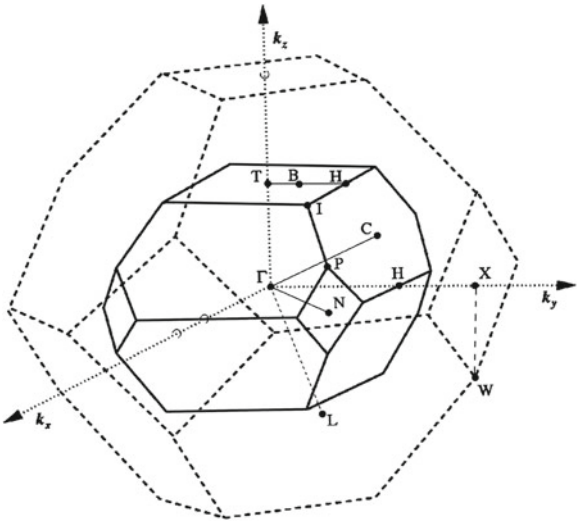

Fig. 1.23 First Brillouin zone (BZ) of chalcopyrite structure (*solid lines*) and its relation to that of the zinc-blende (ZB) structure (*dashed lines*). The points X, L, and W lie on the ZB BZ

It was found for instance that the gap decreases strongly from ZnSe to $CuGaSe_2$ and then increases again going to $ZnGa_2Se_4$. This can be explained mainly in terms of the behavior of the *d* orbitals. It was found also that all the band gaps of the $A^{II}B_2^{III}X_4^{VI}$ compounds are direct. When examinimg the chemical trends of the band gaps it was evidenced that the gap shifts are not material dependent. Nevertheless, a decrease in gap from Al to Ga to In and from S to Se to Te was observed as well as a less pronounced trend of decrease of the gaps from Zn to Cd to Hg. Along this series the gap opens across the entire BZ rather than just near the minimum gap at Γ-point. To illustrate this point, the band structures of $CdGa_2S_4$, $CdGa_2Se_4$, and $CdGa_2Te_4$ are presented in Fig. 1.24.

On the other hand, the band structures of the series $ZnAl_2Se_4$, $ZnGa_2Se_4$, $ZnIn_2Se_4$ revealed how the change of the B^{III} element affects the band structure while keeping the anion and A^{II} element fixed. In the former series an overall change of the band gap throughout the Brillouin zone was noted while in the latter, the gap is mostly affected near Γ-point. Finally, the band structures in the series $ZnGa_2Se_4$, $CdGa_2Se_4$, $HgGa_2Se_4$ suggest that the trend with group-II element is similar to that of the group-III element but less pronounced.

For all cases where experimental value are available for the defect chalcopyrites, the agreement between theory and experiment becomes rather good after a simple empirical bandgap correction with a minimal number of parameters, as shown in Fig. 1.25.

The study of optical properties of a defect-chalcopyrite-type semiconductor $CdGa_2Te_4$ by optical absorption, spectroscopic ellipsometry (SE), and electroreflectance (ER) measurements (Fig. 1.26) [52] suggest that $CdGa_2Te_4$ is a direct-gap

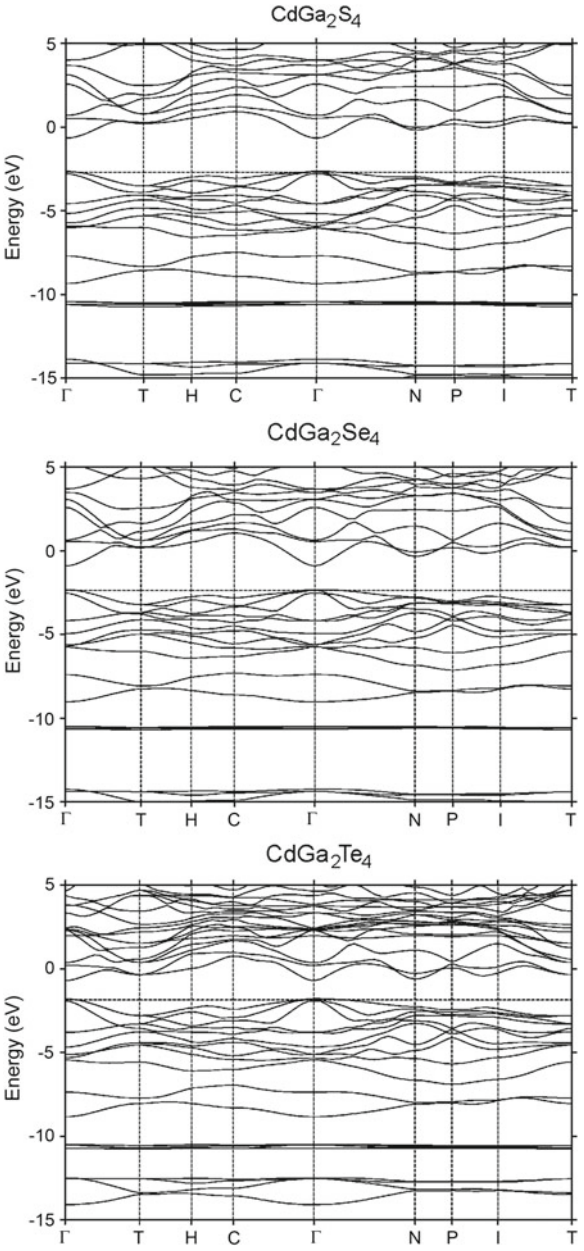

Fig. 1.24 Band structure of $CdGa_2S_4$, $CdGa_2Se_4$, and $CdGa_2Te_4$. Reprinted with permission from Jiang and Lambrecht [51]. © 2004, American Physical Society

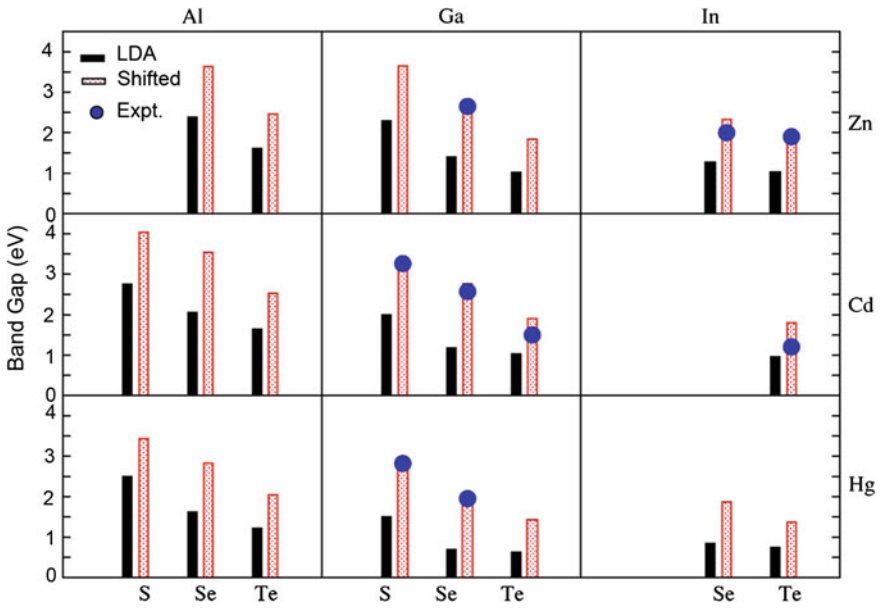

Fig. 1.25 Band gaps of defect chalcopyrites. Reprinted with permission from Jiang and Lambrecht [51]. © 2004, American Physical Society

semiconductor having the band gap of ∼1.36 eV at 300 K. The complex dielectric-function spectra measured by SE revealed distinct structures at energies of the critical points (CP's) in the Brillouin zone. By performing the band-structure calculation, these CP's were successfully assigned to specific points in the Brillouin zone.

The electronic energy-band structure of $CdGa_2Te_4$ calculated on the basis of the empirical pseudopotential method (EPM) is shown in Fig. 1.27 for a comparison with that obtained by local-density-functional calculations and presented in Fig. 1.24.

The valence band consists of two subbands separated by ∼7 eV. The top and bottom valence subbands have widths of about 4 and 1 eV, respectively. The symmetry of the top valence band Γ_{6+7} is p-like in nature. The Γ_{5+8} valence bands lie about 0.2 eV below the top valence band Γ_{6+7}, due to the crystal-field splitting. By considering the spin–orbit interaction, the Γ_{2+4} band splits into Γ_{5+8} and Γ_{6+7} bands. The spin–orbit splitting energy is ∼0.9 eV. The symmetry of the lowest conduction band Γ_{5+8} is s-like in nature. There exist upper conduction bands, Γ_{6+7} and Γ_{5+8}, at about 0.7 and 1.6 eV above the lowest conduction band Γ_{5+8}, respectively.

The E_1 and E_2 structures are originated from transitions near the Γ point. The E_3 structure may be originated from transitions at the N point. The E_4 and E_5 structures are originated mainly from transitions at the N and P points. The E_6 structure is arising principally from regions at the N point. The E_7 peak is dominated by transitions at the N, P, S, and L points. The E_8 structure is arising principally from regions at the

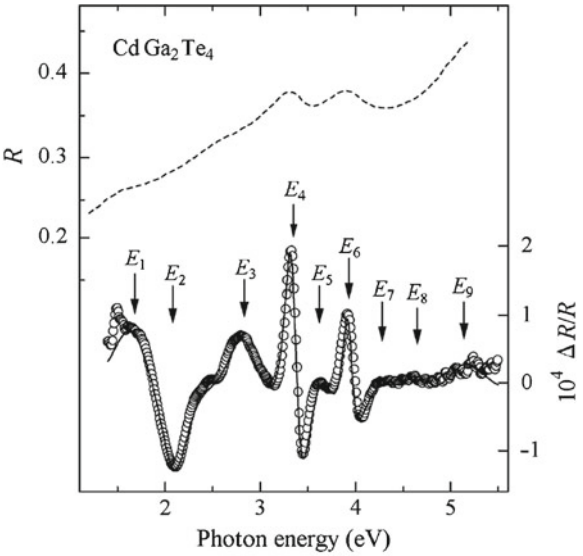

Fig. 1.26 Reflectivity R (*dashed line*) and ER spectra ΔR/R (*open circles*) for $CdGa_2Te_4$. The normal-incidence reflectivity R is calculated from experimental SE data. The *vertical arrows* indicate the positions of the CP's (E_1-E_9) determined from the standard-CP fitting. Reprinted with permission from Ozaki et al. [52]. © 2003, Elsevier

N, P, and S points. At higher energy, the E_9 structure is also arising principally from regions at the N point.

The band structure of $HgAl_2Se_4$ was also investigated within a scalar relativistic approximation using local density approximation (LDA), Perdew–Burke–Ernzerhof generalized gradient approximation (PBE–GGA) and GGA modified by Engel–Vosko (EV-GGA) [53]. The obtained results are similar in nature except the band gaps are different, which is in the order EV–GGA–PBE–GGA–LDA. The obtained bandgap from LDA formalism is 1.42 eV, with PBE-GGA it is 1.58 eV, and using EV–GGA it is 2.24 eV. The obtained energy bandgap using EV–GGA is in excellent agreement with the earlier reported experimental band gap of 2.20 eV.

In order to see the effect of spin–orbit, a comparison of the calculated EV–GGA band structure in a scalar relativistic approximation with that including spin–orbit is shown in Fig. 1.28. Except minor splitting in Se-*p* states in the valence band at the Γ-line, the effect of spin–orbit interaction is not significant.

In order to evidence the influence of the crystallographic structure upon the energy band structure, calculations by using the empirical pseudopotential method were performed in four modifications of $CdAl_2Te_4$ with space groups D^{11}_{2d}, D^{9}_{2d}, D^{1}_{2d} and S^{2}_{4} [54]. The ternary crystal pseudopotential used calculations were approximated by a superposition of atomic pseudopotentials of binary semiconductors.

The Brillouin zones for the Bravais lattices involved are shown in Fig. 1.29.

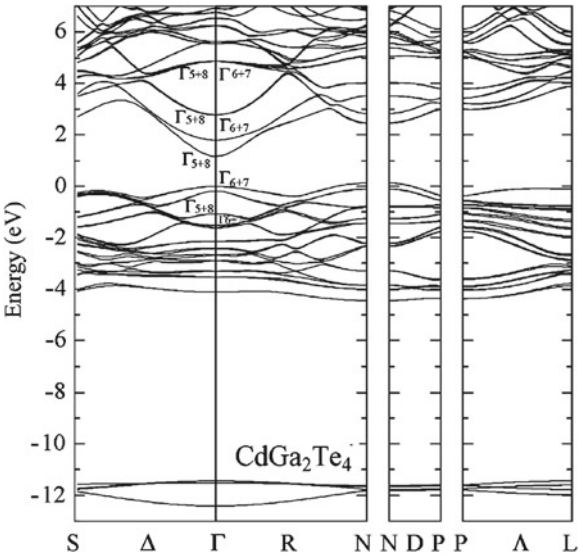

Fig. 1.27 Electronic energy-band structure of $CdGa_2Te_4$ calculated by EPM. The *numbers* denote that of the irreducible representations of double groups. Reprinted with permission from Ozaki et al. [52]. © 2003, Elsevier

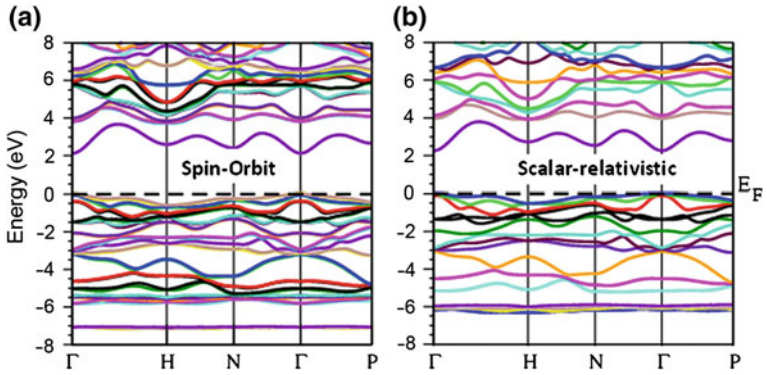

Fig. 1.28 The calculated electronic band structures along the symmetry lines using EV–GGA for $HgAl_2Se_4$ at the equilibrium lattice constant using **a** spin–orbit and **b** scalar relativistic approximation. Reprinted with permission from Singh et al. [53]. © 2011, Elsevier

The results of energy band structure calculations for four modifications of $CdAl_2Te_4$ are shown in Fig. 1.30.

In all modifications, the conduction band bottom is situated at the Γ-point, while the top of the valence band is located at the A-point (α-$CdAl_2Te_4$), N-point (β- and γ-$CdAl_2Te_4$), and Γ-point (δ-$CdAl_2Te_4$), respectively.

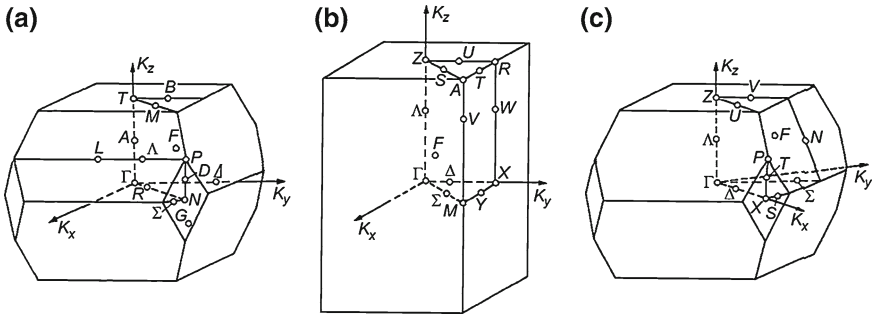

Fig. 1.29 Brillouin zones for the Bravais lattices **a** $\Gamma_q^v(a)$, **b** Γ_q, and **c** $\Gamma_q^v(b)$ with specific points, lines and planes for the special groups: **a** S_4^2, D_{2d}^1, **b** D_{2d}^{11}, and **c** D_{2d}^9. Reprinted with permission from Chizhikov et al. [54]. © 2011, John Wiley and Sons

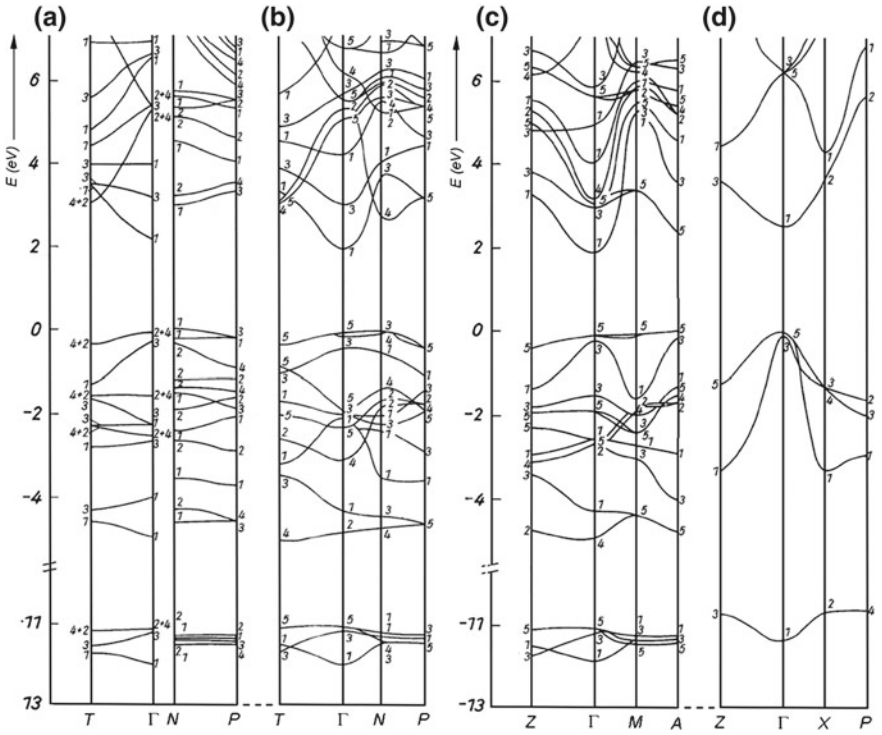

Fig. 1.30 Energy band structure of $CdAl_2Te_4$ with space groups **a** $S_4^2(\beta$-modification), **b** D_{2d}^{11} (γ), **c** D_{2d}^1 (α), **d** D_{2d}^9 (δ). Reprinted with permission from Chizhikov et al. [54]. © 2011, John Wiley and Sons

The analysis of the band structure allows one to conclude that the reconstruction of the cationic lattice of $CdAl_2Te_4$ does not lead to significant transformation of the energy band structure of α-, β- and γ-modifications. The variation of symmetry

does not lead to significant fluctuations, except for a weak diminution of the bandgap. It is evident that the electrons of the anionic lattice participating in the crystal bonds play a principal role in the formation of the band structure.

As concerns the band structure of the δ-modification, it is significantly different from that of α-, β- and γ-modifications. The statistical distribution of atoms in the cationic lattice leads to a structure of the sphalerite type.

For the band structure of the spinel type non-magnetic semiconductor $CdIn_2S_4$, quantitative calculations based on the pseudopotential method show that the absorption edge corresponds to an indirect band-to-band transition [55].

The calculations of the electronic band structures of the magnetic spinels $CdCr_2S_4$ and $CdCr_2Se_4$ using the extended Hiickel method [56] evidenced the following main features of the band structure in the paramagnetic phase (Fig. 1.31): (i) the conduction band minimum in $CdCr_2S_4$ has Λ_1 symmetry, being at a point one-fourth away from Γ to L, and the valence band maximum has Γ_{15} symmetry, corresponding to an indirect energy gap of 2.51 eV; (ii) the main features for $CdCr_2Se_4$ are not very different from the case of $CdCr_2S_4$ but the conduction band minimum has Γ_1 symmetry, corresponding to a direct gap of 1.91 eV; (iii) the dε and dγ bands are at about 0.6–0.8 eV and about 1.8–1.9 eV upwards from the top of the valence band respectively. These features are also true in the ferromagnetic phase, except for the marked downwards shift of the lowest conduction band due to the exchange splitting of the band.

The electronic band structure calculations of ferromagnetic $CdCr_2S_4$ and $CdCr_2Se_4$ performed self-consistently by using the discrete variational Xα method [57] revealed that the general features of the band structures are quite similar between sulfide and selenide (Fig. 1.32). Each structure consists of relatively narrow valence bands, fairly wide conduction bands, and very narrow *d* bands. The $3d\varepsilon$ and $3d\gamma$ bands for up spin lie in the energy region near the top of the valence bands and around the bottom of the lowest conduction band, respectively, and both *d* bands for down spin fall in the conduction bands. The fundamental energy gap at the Γ point is 2.6 eV for sulfide and 2.3 eV for selenide.

The overall features of the band structure of $HgCr_2Se_4$ are quite similar to those of $CdCr_2S_4$ and $CdCr_2Se_4$ [58]. The top of the valence bands has the Σ_4 symmetry and the bottom of the conduction bands Γ_1. The fundamental energy gap is 1.8 eV, somewhat narrower than those of the Cd compounds.

1.5 Optical and Radiative Properties

From a detailed analysis of the published data on transport properties, optical properties and photoluminescence, it was concluded that in the materials of the $A^{II}B_2^{III}X_4^{VI}$ family localized levels are present displaying common properties [59]. Practically all compounds, even if grown with different techniques (transport of iodine or direct synthesis of the elements or of the corresponding binary compounds), display an n-type conductivity. This indicates that the iodine, present in relatively high concen-

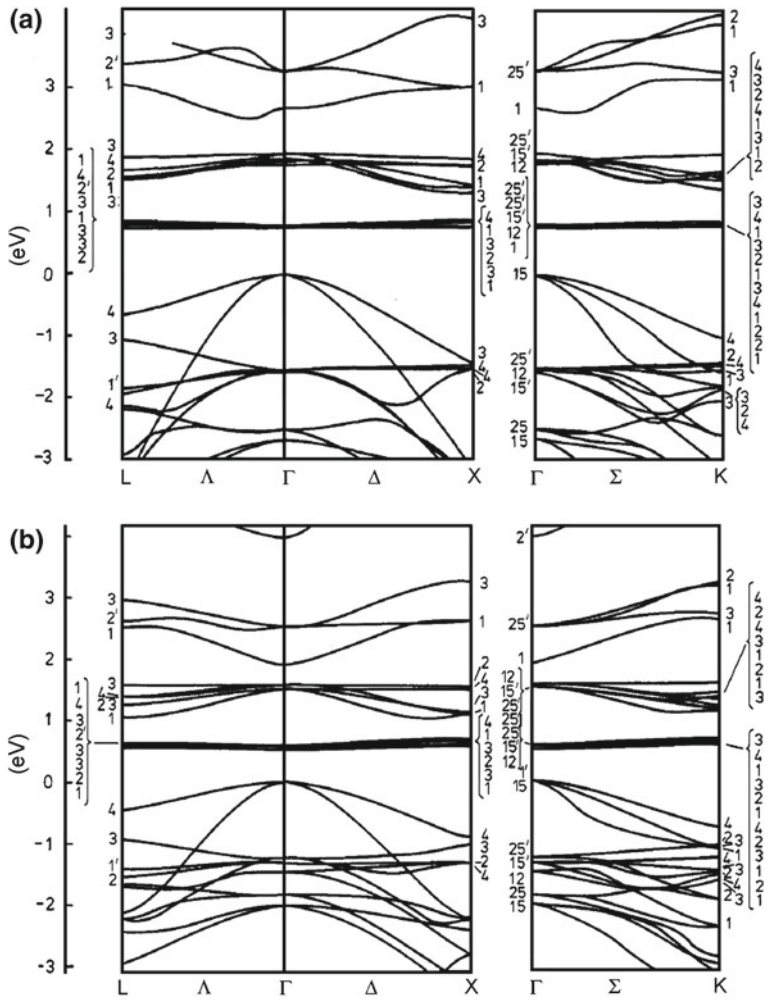

Fig. 1.31 Calculated band structure of the paramagnetic $CdCr_2S_4$ (**a**) and $CdCr_2Se_4$ (**b**) on the symmetry lines Γ–Λ–L, Γ–Δ–X and Γ–Σ–K. Reprinted with permission from Kambara et al. [56]. © 1980, IOP Publishing Ltd

trations in the transport grown single crystals, plays only a minor role in determining the extrinsic properties of the crystals grown with this technique. The intentional crystal doping with group I or group V impurities does not change the sign of the majority carriers.

By careful control of the growth conditions, high resistivity samples can be obtained. Nevertheless, also in the low conductivity samples, a high density of shallow donors is present, and these donors are distributed in energy with density described by the expression.

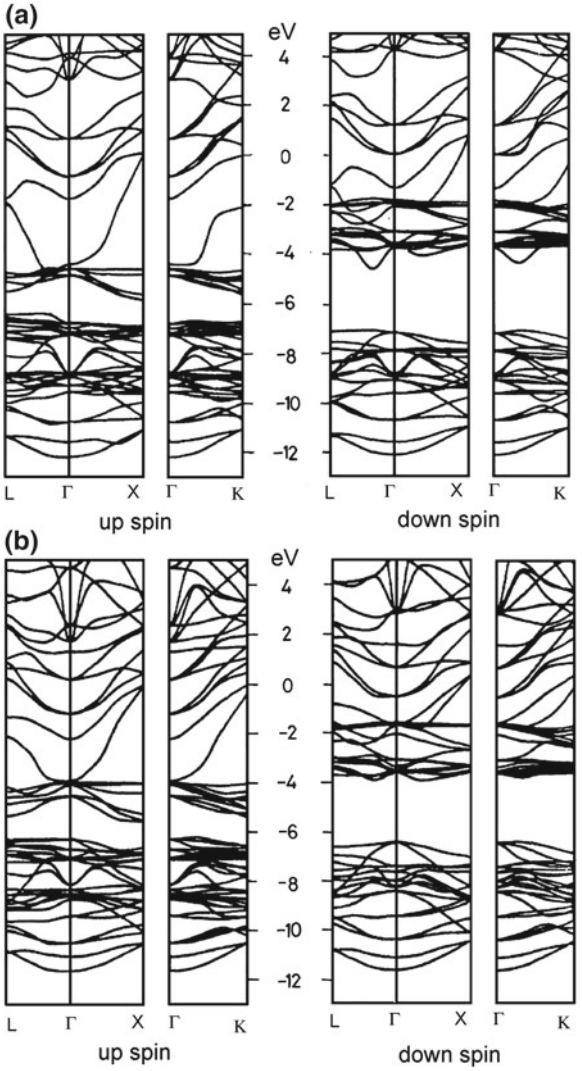

Fig. 1.32 Calculated band structure of the feromagnetic $CdCr_2S_4$ (**a**) and $CdCr_2Se_4$ (**b**). Reprinted with permission Oguchi et al. [57]. © 1980, American Physical Society

$N(E) = N_0 \exp(-\alpha E)$. Due to the high density of centers present in the crystals, the localized states broaden in energy.

It was stated that the presence of shallow donors and shallow acceptors with high and nearly equal concentrations and of deep double charged acceptors seems to be a common characteristic of the $A^{II}B_2^{III}X_4^{VI}$ semiconductors. In some cases a relatively deep donor originated by a chalcogen vacancy may be also present [59].

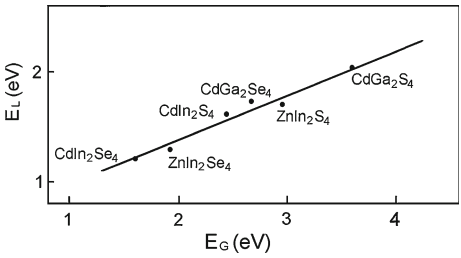

Fig. 1.33 Energy of the luminescence band maximum (E_L) for different $A^{II}B_2^{III}X_4^{VI}$ compounds as a function of the energy gap (E_G). Reprinted with permission from Guzzi and Grillii [59]. © 1984, Elsevier

The low temperature emission spectrum of the $A^{II}B_2^{III}X_4^{VI}$ compounds is generally composed of a wide (some tenths of eV) unstructured gaussian band, whose energy is of the order of one half of the energy gap.

In Fig. 1.33 the energy of the maximum of this band (E_L) is plotted as a function of the energy gap (E_G). From the linear relation between E_L and E_G indicating that the origin of this band is common in all the compounds reported in Fig. 1.33, despite the difference in the crystal structures, it was suggested that this band corresponds to a donor–acceptor pair transition. In the case of $CdIn_2S_4$, it was suggested that the donor-acceptor pairs may be originated by the In–Cd exchange in their lattice sites [60]. The best conditions for the creation of antisite defects exist in $CdIn_2X_4$ crystals as Cd and In atoms have the same value of electronegativities (1.7 eV) and practically the same ionic radii ($R_{Cd}^{2+} = 0.99 \times 10^{-8}$ cm; $R_{In}^{3+} = 0.92 \times 10^{-8}$ cm).

This attribution was supported by measurements of time-resolved emission spectra in $CdIn_2S_4$. In Fig. 1.34 the parameters of the band (energy of the maximum and halfwidth) are reported as a function of the time after the end of the excitation. The band shifts towards the red and narrows for increasing delays.

In the low temperature emission spectra of some compounds ($CdIn_2S_4$ and $CdIn_2Se_4$ for instance) a second narrower emission band centered at higher energies appears. On the basis of the emission energy and the temperature dependence of the parameters of this band, it was attributed to an electron transition from the donor level originated by the chalcogen vacancy to the valence band [59].

The energy level scheme explaining the extrinsic optical properties of $A^{II}B_2^{III}X_4^{VI}$ semiconductors is presented in Fig. 1.35. The D and A levels indicate respectively the donor level distribution and the acceptor levels present in high and nearly equal concentration. The low energy emission band, observed in all the compounds studied, was attributed to a donor–acceptor pair transition between these levels. In some cases a donor level originated by a chalcogen vacancy (indicated as V in Fig. 1.35) may be present; the V level-valence band transition originates a high energy emission band observed in some compounds.

The R level in Fig. 1.35 indicates the non-radiative recombination centre whose distance in energy from the valence band, as deduced from the infrared stimulation

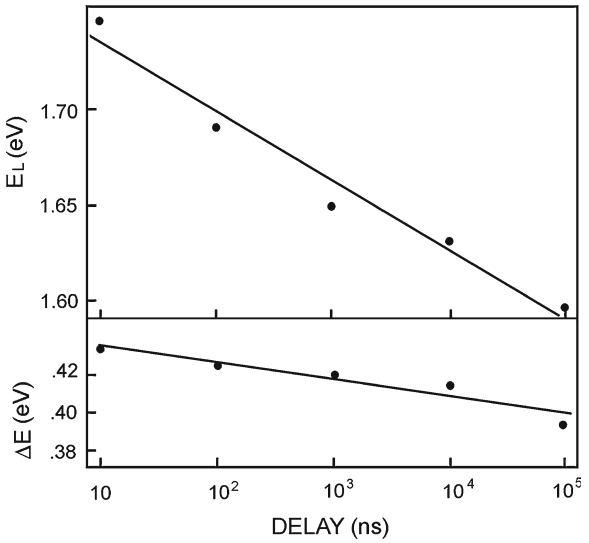

Fig. 1.34 Emission band maximum (E_L) and halfwidth (ΔE) as a function of the delay after the end of the excitation, deduced from time-resolved luminescence of $CdIn_2S_4$ at 2 K. Reprinted with permission from Guzzi and Grillii [59]. © 1984, Elsevier

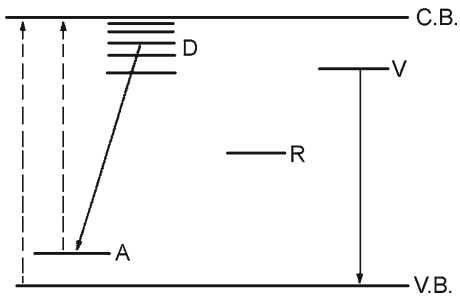

Fig. 1.35 Typical energy level scheme for localized levels in $A^{II}B_2^{III}X_4^{VI}$ semiconductors. Reprinted with permission from Guzzi and Grillii [59]. © 1984, Elsevier

and quenching of the luminescence, is of the order of 1 eV in all the compounds where it has been directly observed.

Two kinds of transitions (indicated with dotted lines in Fig. 1.35) mainly excite the photoluminescence and the photoconductivity: the interband transitions and the electron transitions from the acceptor A to the conduction band. The energy of the photoconductivity band attributed to this last process is reported as a function of the energy gap E_G in Fig. 1.36a. From these data the binding energy E_A of the acceptor A ($E_A = E_G - E_{ph}$) can be deduced. E_A calculated in this way, is reported as a function of E_G in Fig. 1.36b, together with the value of E_A deduced from the activation energy of the luminescence thermal quenching. From Fig. 1.36 it was found that the energies E_{ph} and E_A are simply related to E_G.

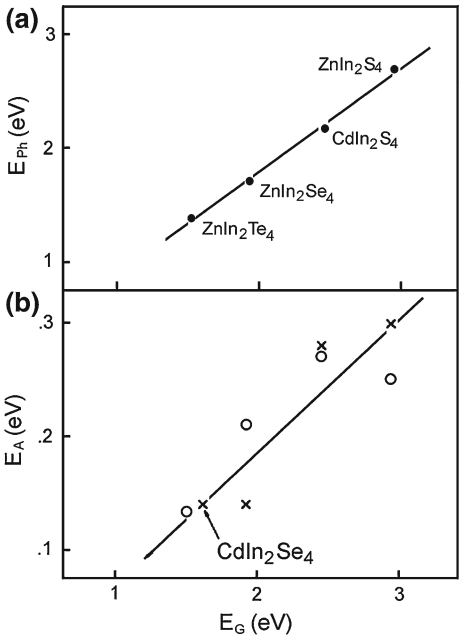

Fig. 1.36 **a** Energy of the main photoconductivity peak (E_{ph}) as a function of the energy gap (E_G) for some $A^{II}B_2^{III}X_4^{VI}$ compounds. **b** Acceptor binding energy (E_A) as a function of the energy gap (E_G). The crosses are the values deduced from the activation energy of the luminescence thermal quenching; the *open dots* are the values calculated ($E_A = E_G - E_{ph}$) from the data of (**a**). Reprinted with permission from Guzzi and Grillii [59]. © 1984, Elsevier

The parameters of two kinds of cations are not the same in the case of $CdGa_2X_4$ compounds (electronegativity of Ga equals 1.6 eV; $R_{Ga}^{3+} = 0.62 \times 10^{-8}$ cm). Consequently, one may expect $CdGa_2X_4$ crystals with stoichiometric composition to contain a small amount of localized states. The detection in $CdGa_2S_4$ and $CdGa_2Se_4$ of excitons, intrinsic conductivity up to low temperatures and band–band radiative recombination of non-equilibrlum carriers confirms the comparatively small defect degree in those semiconductors [60].

The deviation of $CdGa_2S_4$ from stoichiometry can de characterized by the formula $Cd_xGa_{2y}S_{4z}$. The ratio x/y determines the composition of crystals on the quasi-binary cut CdS–Ga_2S_3. The deviation of $CdGa_2S_4$ crystals from stoichiometry on this quasi-binary cut is described by the parameter $\delta = (x/y) - 1$. Basically Ga_{Cd} and V_{Cd} defects are formed in the case of $\delta < 0$, while Cd_{Ga} and Cd_i centers prevail when $\delta > 0$. The qualitative diagram of native defect concentration in $CdGa_2S_4$ with deviation from stoichiometry is shown in Fig. 1.37.

The luminescence spectra of $CdGa_2S_4$ crystals are well explained by the energy level scheme and electronic transitions presented in Fig. 1.38.

The deviations in stoichiometry may strongly affect the crystal properties of $A^{II}B_2^{III}X_4^{VI}$ semiconductors [60], as illustrated by the dependence of dark resistivity ρ_d and photosensitivity $Q = (\rho_d / \rho_l)$ (when light with $h\omega > E_g$ and 10^{-4} W power is absorbed) of cadmium thiogallate upon the composition of single crystals (Fig. 1.39). Similar effects have been observed in $CdIn_2S_4$ crystals.

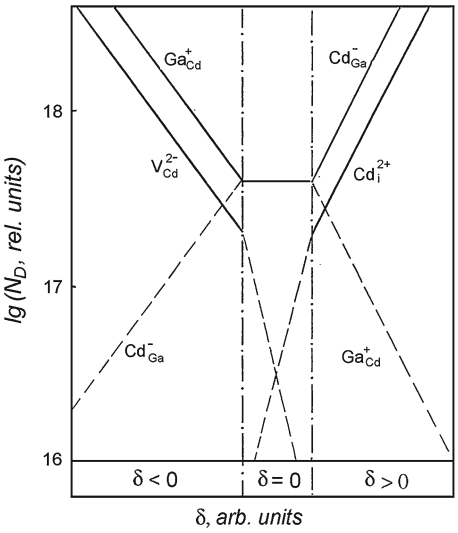

Fig. 1.37 Dependence of defect concentration in $CdGa_2S_4$ on the deviation from stoichiometry on the CdS–Ga_2S_3 quasi-binary cut

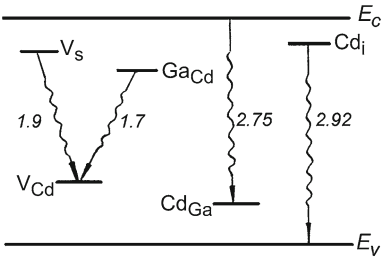

Fig. 1.38 The scheme of defect energy levels and electronic transitions responsible for luminescence bands in $CdGa_2S_4$ crystals

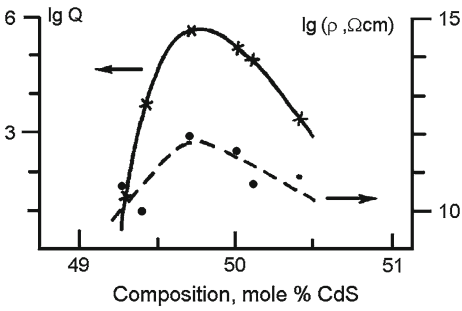

Fig. 1.39 The dependence of dark resistivity (*dashed curve*) and photosensitivity (*solid curve*) of cadmium thiogallate upon the crystal composition (at the CdS—Ga_2S_3 quasi-binary cut). T = 300 K. Reprinted with permission from Radautsan et al. [60]. © 1984, Elsevier

The self-compensation effect inherent to $A^{II}B_2^{III}X_4^{VI}$ semiconductors results in a low n-type conductivity of the crystals. As mentioned above, by means of traditional techniques (doping in the growth process, annealing) it is impossible to change the conductivity of ternary materials from n- to p-type. However, the type conductivity conversion may be successfully performed provided that ion implanta-

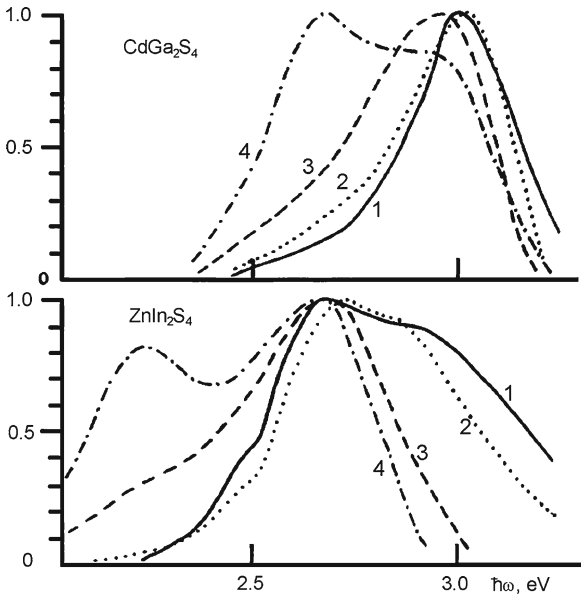

Fig. 1.40 Photoconductivity spectra of $CdGa_2S_4$ and $ZnIn_2S_4$ at T = 300 K: (*1*) initial crystals, (*2*) samples annealed in sulphur vapour at 750 °C for 0.5 h, (*3*) samples implanted by Ne^+ ions at a dose 6×10^{15} cm^{-2} and (*4*) samples implanted by Ne^+ ions at a dose 3×10^{16} cm^{-2}. Reprinted with permission from Radautsan et al. [60]. © 1984, Elsevier

tion is used [60]. It has been shown that the implantation of neon ions into $CdGa_2S_4$ and $ZnIn_2S_4$ followed by annealing of samples in sulphur vapour causes the formation of layers with hole conductivity. The ion implantation causes the appearance of photoconductivity bands in $CdGa_2S_4$ and $ZnIn_2S_4$ at 2.7 and 2.25 eV respectively (Fig. 1.40) which have been attributed to the cadmium and zinc vacancies. On the other hand, it was observed that $CdIn_2S_4$ single crystals keep the electron conductivity after ion implantation. The creation of antisite defects in the cation sublattice was suggested to be a barrier for the type conductivity conversion in this compound.

A region for the charge storage effect extending toward room temperature has been observed in $Zn_xCd_{1-x}In_2S_4$ layered crystals grown by chemical vapor deposition at the limit of existence of the quaternary layered phase [61]. Deep acceptor levels related to the ionization states of a double negatively charged center were suggested to cause these effect. A possible origin of such centers due to zinc vacancy whose density increases with the partial substitution of cadmium by zinc atoms has been assumed to prove theoretical predictions and experimental results. Similar charge storage effects and the electric field dependence of the optical quenching of photoconductivity have been reported in $ZnIn_2S_4$ crystals.

1.6 Vibrational Properties

As mentioned above, most of $A^{II}B_2^{III}X_4^{VI}$ compounds adopt tetragonal, spinel, or layered structures. Layered phases appear for compositions intermediate between spinel and tetragonal structures.

Forty-two normal vibrations are expected in the normal spinel structure at $k = 0$; they are described by following reduction into the point group's irreducible representations:

$$\Gamma = A_{1g} + E_g + T_{1g} + 3T_{2g} + 2A_{2u} + 2E_{2u} + 5T_{1u} + 2T_{2u}.$$

One of this modes (T_{1u}) is acoustic, four (T_{1u}) are IR active and five (A_{1g}, E_g, $3T_{2g}$) are Raman active. The remaining modes (T_{1g}, A_{2u}, E_{2u}, T_{2u}) are silent. It is known that A_{1g} and E_g modes correspond to vibrations of anions towards the center of tetrahedrum. The three other modes of T_{2g}-simmetry correspond to the vibrations of both anions C and A-type cations. Since in the partially inverse spinels tetrahedra are occupied by both A and B atoms, the RS spectrum presents a superposition of two sets of modes. The two modes at 360 and 367 cm^{-1} are supposed to be caused by the vibrations of InS_4 and CdS_4 tetrahedra. The vibrations of two types of tetrahedra ($A^{II}X_4$ and $B^{III}X_4$) lead to the formation of two A_{1g}modes in the RS spectrum. The relative intensity of $A_{1g}(B^{III}X_4)/A_{1g}(A^{II}X_4)$ should be related to the normality index as (1-X)/X.

Group theoretical considerations indicate that the defect chalcopyrite (DC) of $A^{II}B_2^{III}X_4^{VI}$ compounds has 15 vibrational modes with the following representation $\Gamma = 3A(R) + 6B(R; IR) + 6E(R; IR)$. The A modes, here noted A1 to A3 as a function of increasing frequency, are non-polar Raman active modes while B and the doubly degenerated E modes, here noted from 1 to 5 on increasing frequency, are polar modes that are both Raman (R) and infrared (IR) active and therefore exhibit longitudinal-transversal optic (LO–TO) splitting. Two of the 15 vibrational modes (an E mode and a B mode) are acoustic modes. In this way, we expect 13 Raman-active optical modes: $3A + 5B + 5E$, but taking into account the LO–TO splittings, it should be possible to measure a maximum of 23 Raman-active first-order optical modes in Raman experiments. Non-polar A-modes are caused by the oscillations of anion atoms, the lowest-energy A-mode (the "breathing" one) being connected to the symmetric oscillations of anions surrounding a stoichiometric vacancy. This "breathing" mode of the anions around the vacancies is characterized by a relatively weak restoring force, by large vibrational amplitudes and by a strong Raman activity. Twelve Raman-active modes are expected in the defect stannite (DS) structures; i.e., one non-polar A mode less than in the DC phase.

Razzetti et al. [15] discussed the dynamical (Raman) analysis of about 60 different ternary and pseudoternary $A^{II}B_2^{III}X_4^{VI}$ compounds or phases grouped in three different structural families: cubic-spine1 AB_2X_4 structures ($CdIn_2S_4$ like), AB_2OX_4 layered hexagonal structures ($ZnIn_2S_4$ like) and $AB_2\square X_4$ defective tetragonal structures ($CdGa_2S_4$ like).

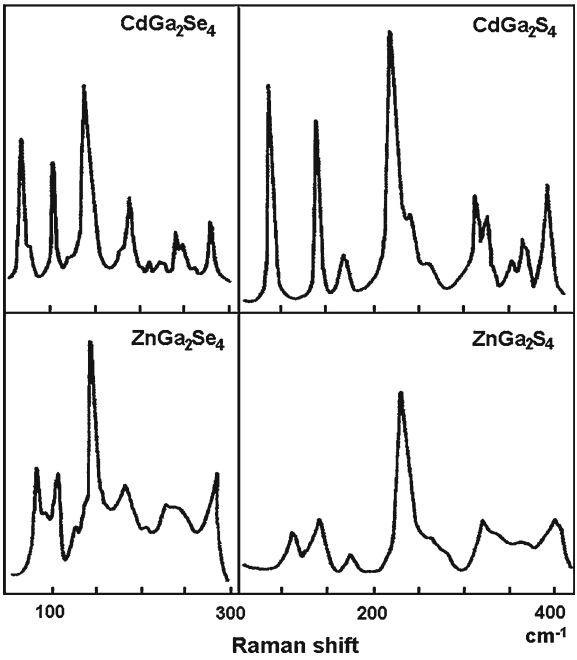

Fig. 1.41 The Raman spectra of the four tetragonal gallium ternary end members. Reprinted with permission from Razzetti et al. [15]. © 1984, Elsevier

A proportionality law between the frequencies of corresponding modes in different compounds was observed in defect chalcopyrites (Fig. 1.41). This proportionality has been explained by an independent AX_4 and BX_4 tetrahedra model, whose validity stems from some decoupling effect of the vacancies [15].

From the Raman spectra of $ZnGa_2S_4$ and $ZnCa_2Se_4$ (Fig. 1.41) a broadening of the lines was noticed: this was explained by a static cation antisite disorder. Support for this picture comes from the results obtained in the pseudoternaty system $Zn_xCd_{1-x}Ga_2S_4$ (Fig. 1.42) where the Raman peaks sharpen with decreasing x value.

As to the effects of cation interchange on the lattice dynamics, it was found that group III as well as group II cation interchange produces a generalized one-mode behaviour for the phonon peaks (Fig. 1.42) with the exception of the lowest energy polar E-symmetry mode, showing a two-mode behaviour.

Completely different results were obtained in the mixed anion compound $CdGa_2(S_xSe_{l-x})_4$: here an overall two-mode behaviour was noticed, with the exception of the lowest frequency polar mode (Fig. 1.43). A two mode behaviour is clearly shown by the strong breathing mode. As the breathing motion involves only the anions around the vacancies, this result would suggest that S and Se atoms are not distributed on the anion sublattice in a completely random way.

While only one layered compound was known to exist among the ternary end members ($ZnIn_2S_4$ and related polytypes) a variety of layered structures has been obtained in pseudoternary phases for compositions intermediate between spinel and tetragonal structures. The use of Raman scattering technique in layered phases is

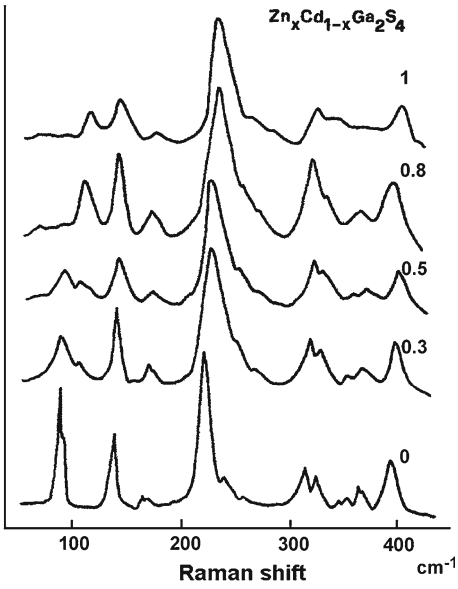

Fig. 1.42 The Raman spectral evolution with composition in the pseudoternary $Zn_xCd_{1-x}Ga_2S_4$ system. Reprinted with permission from Razzetti et al. [15]. © 1984, Elsevier

based on the typical rigid layer (RL) modes which characterize layered structures [15]. These RL modes, corresponding to out-of phase vibrations of the layers as a whole (conjugate to the acoustic modes), are observed at relatively low frequencies (10–100 cm^{-1}). The number of these modes is strictly connected to the number of layers in the primitive unit cell and their frequency mirrors mass content of the cell. It was concluded from Fig. 1.44 that the spectra of the phases L_2 and L_3 are quite similar to each other and to the spectrum of the $ZnIn_2S_4$. It was argued then that the L_2 together with L_3 has a $ZnIn_2S_4$ structure. The L_5 phase is also quite similar to $ZnIn_2S_4$. Since the phase L_1 shows a richer low frequency Raman spectrum, it was suggested that a rather high number of layers in the unit cell is inherent to this phase.

1.7 Applications

A source of interest in $A^{II}B_2^{III}X_4^{VI}$ compounds is the rather wide choice of the two cations which, in principle, should allow tailoring many physical parameters relevant for applications. The crystal structures of $A^{II}B_2^{III}X_4^{VI}$ compounds derived from the diamond type, but modified to accommodate three or more atoms of different sizes, allows additional symmetries and thus an increase in the selection of electro-optic (EO), acousto-optic (AO), and non-linear materials for device applications [62]. The exploitation of these properties has led to the development of such devices as AO and EO modulators and switches, optical filters, SAW (surface acoustic wave)

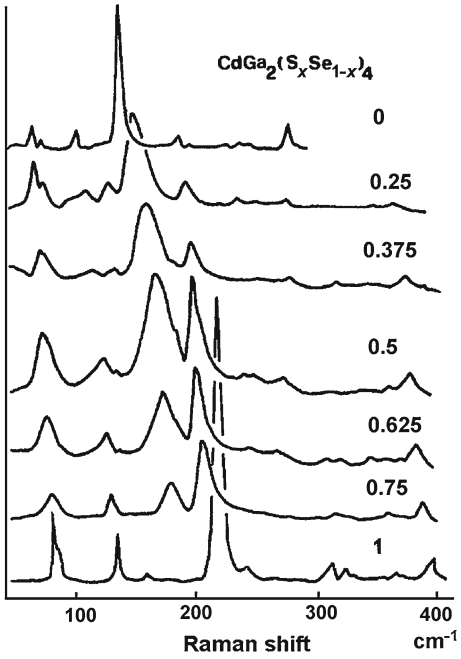

Fig. 1.43 The Raman spectral evolution with composition in the pseudoternary $CdGa_2(S_xSe_{1-x})_4$ system. Reprinted with permission from Razzetti et al. [15]. © 1984, Elsevier

devices, frequency doublers, optical parametric oscillators and photovoltaic solar cells [62]. These materials frequently have large non-linear coefficients for frequency up-conversion (second harmonic generation), frequency down-conversion and mixing (optical parametric oscillator applications) and large electro-optic coefficients. In particular, the large electro-optic coefficients make them especially suitable as electro-optic modulators, switches, and shutters as well as highly sophisticated tunable filter designs such as the Hughes Electro-Optic Tunable Filters (EOTFs) which utilize both longitudinal field (LEOTF) and transverse field (TEOTF) electro-optic modes. Particularly, the longitudinal EO coefficient ($r_{41} = r_{52}$) of $CdIn_2Te_4$ was measured to be approximately $r_{41} = 50\,pm/V$, which is larger than that of $LiNbO_3$. Combined with the average index of refraction, the figure of merit for $CdIn_2Te_4$ shows an improvement of a factor of 20 over $AgGaS_2$ which corresponds to 1/20th of the required voltage for device operation. The improved properties of $CdIn_2Te_4$ make possible its application to modulators, shutters, and filters at many IR wavelengths using state-of-the-art electronics. Figure 1.45 compares also the nonlinear optical coefficients of $CdGa_2S_4$ with other widely used materials. Another advantage of $A^{II}B_2^{III}X_4^{VI}$ compounds is their wide transparency range. For instance, the transparency range of $CdGa_2S_4$ and $HgGa_2S_4$ is approximately 0.5–13 μm. So, for all applications where high figures of merit together with wide transparency are required, defect chalcopyrites offer interesting development perspectives [11].

Levine et al. found that $HgGa_2S_4$ has a very large nonlinearity with $d_{36}(HgGa_2S_4)$ being five times larger than $d_{31}(LiNb0_3)$ [63]. Further, $HgGa_2S_4$ has an order of

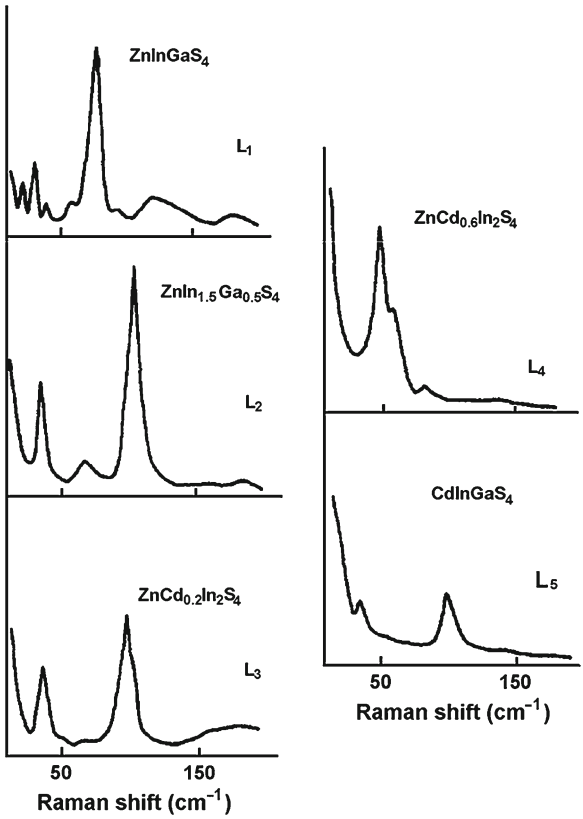

Fig. 1.44 Low frequency Raman spectra of the layered L_1-L_5 phases. Reprinted with permission from Razzetti et al. [15]. © 1984, Elsevier

magnitude larger birefringence than $CdGa_2S_4$ and thus this crystal has good device potential. The birefringence of $HgGa_2S_4$ is large enough to allow phase matching for a fundamental wavelength longer than 1.5 μm. For a nondegenerate mixing or parametric generation process even shorter pump and signal wavelengths can be used.

Ren et al. demonstrated with $HgGa_2S_4$ second harmonic generation of 30 ns TEA CO_2 laser pulses with 5 % efficiency in energy and 6.9 % in peak power [64]. It was therefore demonstrated that $HgGa_2S_4$ is suitable for frequency conversion of visible, near and middle IR lasers. As compared to other efficient middle IR crystals, it is useful even for design of OPO pumped by second harmonic of Nd:YAG, Cu-vapor, and dye lasers. Particularly, $HgGa_2S_4$ crystals are superior to widely used $ZnGeP_2$, $AgGaSe_2$, and GaSe crystals on SHG of 2 μm solid-state holmium and 3 μm erbium lasers. $HgGa_2S_4$ also outperforms $AgGaSe_2$ and GaSe in CO_2 laser SHG. It was also found [64] that the damage threshold of $HgGa_2S_4$ crystal is

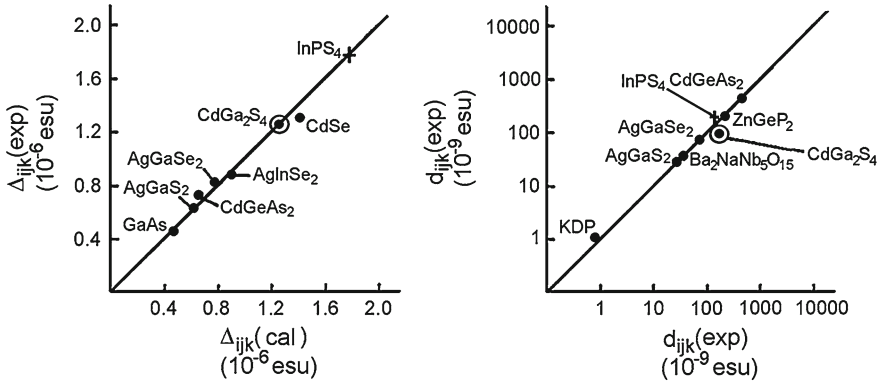

Fig. 1.45 Nonlinear optical coefficients d_{ijk} and Miller's Δ_{ijk} of $CdGa_2S_4$ (one vacancy per unit cell) and $InPS_4$ (two vacancies) compared to "normal" chalcopyrites and other "nonlinear" compounds. The graphs relate measured and calculated values from bond charge models. Reprinted with permission from Razzetti et al. [11]. © 1987, Elsevier

310 MW/cm^2 which is about 2.3 times higher than that of $CdGeAs_2$ (157 MW/cm^2), $ZnGeP_2$ (142 MW/cm^2), $AgGaSe_2$ (139 MW/cm^2), $AgGaS_2$ (149 MW/cm^2).

Promising results have been also obtained with mixed nonlinear crystals $Hg_{1-x}Cd_xGa_2S_4$ grown in accordance with diagram $HgGa_2S_4$:$CdGa_2S_4$ [65]. High efficiency of frequency doubling was obtained with mixed crystals at room temperature which is three times higher as compared to $ZnGeP_2$ and 5.5 times higher as compared to $AgGaSe_2$.

Other devices developed using $A^{II}B_2^{III}X_4^{VI}$ compounds such as photodetectors, switches, narrow band optical filters, photosensitive heterojunctions etc. are summarized in Table 1.3 [60] The photosensitivity of $A^{II}B_2^{III}X_4^{VI}$ compounds is known to depend upon the direction of light polarization as compared with the orientation of the crystal optical axis. So, ternary semiconductors may be employed in construction of polarization sensitive photodetectors.

1.8 Trends in Temperature- and Pressure-Induced Phase Transitions

It is a well-known fact that many semiconductors and their alloys undergo a solid–solid phase transition from disordered structure to an ordered one when the temperature is lowered below a critical value T_c [17, 66, 67]. This is related to the fact that different constituent atoms tend to occupy definite sites in the lattice and, as a consequence, long-range order sets in the crystal structure below T_c. This effect has already been studied extensively in tetrahedrally bonded $A^{II}B^{IV}C_2^V$ and $A^IB^{III}C_2^{VI}$ chalcopyrite compounds. As mentioned in the Sect. 1.1, a simple relationship was

Table 1.3 Parameters of some devices developed using $A^{II}B_2^{III}X_4^{VI}$ compounds

Compound	Device	Parameters
$CdGa_2S_4$	Photoresistor	Dark resistance $10^{10}-10^{11}\,\Omega$
		Sensitivity region 250–420 nm
		Relative photosensitivity 10^5
	Tunable filter	Tuning range 450–580 nm
		Bandwidth 1 nm
		Maximum transmission 48 %
	Frequency converter	Nonlinear coefficient d36 ($\lambda = 1.064$ nm)
		26.7×10^{-12} m V^{-1}
$ZnIn_2S_4$	Switch	Switching electric field 2×10^5 V/cm
		Delay time 10^{-4} s
	Photoresistor	Dark resistance 10^9–10^{10} Ω
		Sensitivity region 370–480 nm
		Relative photosensitivity 10^4
	Schottky barrier	Sensitivity region 200–420 nm
		Relaxation time 10^{-4} s
$CdIn_2S_4$	Photosensitive heterojunctions	Sensitivity region 500–1,200 nm
		Quantum efficiency ($\lambda = 633$ nm) 0.18

Reprinted with permission from Radautsan et al. [60]. © 1984, Elsevier

suggested there between the c/a ratio and the cation sublattice ordering: the order-disorder transition with increasing temperature occurs only in chalcopyrites with axial ratio c/a > 1.95. As concerns defect chalcopyrite $A^{II}B_2^{III}X_4^{VI}$ compounds, it was found that order-disorder transitions can occur with increasing temperature in materials with $\delta > 0.05$ as well [18–20].

Similar order-disorder transitions with increasing temperature occur in AB_2X_4 spinels. In particular, $MgAl_2O_4$ shows a second-order phase transition due to the mixture of Mg and Al atoms in both tetrahedral and octahedral sites prior to melting [68–70]. In some spinel compounds temperature-induced disproportionation effects were observed [71], and in some others a phase transition to a ramsdellite, phenacite, or to a rocksalt phase was observed [72–74].

Therefore, it can be concluded that temperature-induced phase transitions in AB_2X_4 materials are mainly related to order-disorder phenomena due to the unbalanced number of cations (3) and anions (4) in these compounds. In the following chapters it will be shown that similar order-disorder phenomena occur in pressure-induced phase transitions in these compounds.

1.9 Conclusions

$A^{II}B_2^{III}X_4^{VI}$ compounds represent a class of materials in a wide family of ternary compounds which hierarchy originates from binaries. These compounds can be treated as a result of pseudobinary $AX + B_2X_3$ join with a 50 % molar composition.

Among $A^{II}B_2^{III}X_4^{VI}$ compounds, according to the number of octahedral and tetrahedral cationic sites, one has spinel, layered and tetragonal structures. Similarly to most of the ternary compounds, a significant part of $A^{II}B_2^{III}X_4^{VI}$ compounds have tetrahedral structures with four-fold coordination determined by the electronic valence of the atoms. The tetrahedral complex structures are obtainable from diamond structure by Grimn–Sommerfeld splitting of an atom pair into two different atoms from other groups of the periodic system, while keeping the valence electron number per atom constant. All these compounds have the normal tetrahedral structure with different arrangements of the cations in the cationic sublattice. The Grimm–Sommerfeld rule can be extended to $A^{II}B_2^{III}X_4^{VI}$ defect tetrahedral structures by assigning to a vacancy a zero valent atom.

When analyzing the "ordered-vacancy compounds" one needs also to take into account different degrees of possible disorder which results in defect chalcopyrite, defect stannite, defect famatinite, and defective centered tetragonal structure.

Most ternary oxides can be prepared by sintering the finely powdered, binary constituents in air and crystals are usually grown by pulling from a melt or by cooling a solution of the oxides in a suitable molten-salt solvent. The synthesis of nonoxidic compounds must be carried out in vacuum or in a protective atmosphere. The growth from the vapour (either by sublimation or by chemical transport) is the most explored method for many ternary chalcogenides. For obtaining large crystals from the vapour, a control of the nucleation is required, which can be realized in different ways. A temperature variation method is an effective procedure for this purpose.

As concerns the produced crystal structure of $A^{II}B_2^{III}X_4^{VI}$ compounds, according to the number of octahedral (Ω) and tetrahedral (τ) cationic sites, one has spinel ($2\Omega + 1\,\tau$), layered ($l\Omega + 2\,\tau$) and tetragonal structures (3τ). The occupation of the tetrahedral (octahedral) positions in the lattice of the spinel is described by means of the normality index λ. Normal and inverse spinels can be derived in terms of *s*- and *p*-orbital radii.

The microscopic dielectric theory of Phillips and Van-Vechten provides a basis for understanding the structural trends of semiconductors. The four-fold or the six-fold co-ordination can be derived from the analysis of the average covalent energy gap E_h and the average ionic energy gap C diagram. The ionic effective charges are also important parameters characterizing the lattice, dynamical, electronic or optical properties of solids and are directly related to the concept of iconicity.

First-principles local-density-functional calculations for the electronic band structures of the ordered vacancy defect chalcopyrites $A^{II}B_2^{III}X_4^{VI}$ indicate that all the band gaps of these compounds are direct, while spinel structures can exhibit an absorption edge that corresponds to an indirect band-to-band transition.

From a detailed analysis of the published data on transport properties, optical properties and photoluminescence, it was concluded that in the materials of the $A^{II}B_2^{III}X_4^{VI}$ family localized levels are present displaying common properties. Practically all compounds, even if grown with different techniques, display n-type conductivity. It was stated that the presence of shallow donors and shallow acceptors with high and nearly equal concentrations and of deep double charged acceptors is

a common characteristic of the $A^{II}B_2^{III}X_4^{VI}$ semiconductors. The self-compensation effect inherent to $A^{II}B_2^{III}X_4^{VI}$ semiconductors results in a low n-type conductivity of the crystals. However, the type conductivity conversion may be successfully performed provided that ion implantation is used. The deviations in stoichiometry may strongly affect the crystal properties of $A^{II}B_2^{III}X_4^{VI}$ semiconductors.

The rather wide choice of the two cations which, in principle, should allow tailoring many physical parameters relevant for applications is a source of interest in $A^{II}B_2^{III}X_4^{VI}$ compounds. The crystal structures of $A^{II}B_2^{III}X_4^{VI}$ compounds allows an increase in the selection of electro-optic, acousto-optic, and non-linear materials for device applications as compared to other diamond type materials. The exploitation of these properties has led to the development of such devices as electro-optic and acousto-optic, modulators and switches, optical filters, SAW (surface acoustic wave) devices, frequency doublers, optical parametric oscillators and photovoltaic solar cells. Another advantage of $A^{II}B_2^{III}X_4^{VI}$ compounds is their wide transparency range. So, for all applications where high figures of merit together with wide transparency are required, defect chalcopyrites offer interesting development perspectives. Taking into account the diversity of $A^{II}B_2^{III}X_4^{VI}$ crystal structures, they are also ideal to investigate the role of structure and composition in a response to external fields such as heat, electricity, magnetism, and especially pressure.

References

1. Hahn H, Frank G, Klinger W, Meyer AK, Storger G (1953) Untersuchungen über ternäre Chalkogenide. V. Über einige ternäre Chalkogenide mit Chalkopyritstruktur. Z Anorg Allg Chem 271:153–170
2. Goodman CHL, Douglas RW (1954) New semiconducting compounds of diamond type structure. Physica 20:1107–1109
3. Bernard M (1975) Glances at ternary compounds. J de Physique. Colloque C3, 36(Suppl 9):C3–C1
4. Shay JL, Wernick JH (1975) Ternary chalcopyrite semiconductors, growth, electronic properties and applications. Pergamon Press, Oxford
5. Goryunova NA (1963) Chemistry of diamond-like semiconductors. Lenuingrad State University, Lenuingrad
6. Goryunova NA, Ryvkin SM, Fishman IM, Spenkor GI, Yarosketskii ID (1969) Second harmonic generation in ternary semiconductors. Sov Phys Semicond 2:1272
7. Berkovskii FM, Goryunova NA, Orlov VM, Ryvkin SM, Sokolova VI, Tsvetkova EV, Shpenkov GP (1969) $CdSnP_2$ laser excited with an electron beam. Sov Phys Semicond 2:1027
8. Chemla DS, Kupecek Ph, Robertson DS, Smith RC (1971) Silver thiogallate, a new material with potential for infrared devices. Opt Commun 3:29–31
9. Parthe E (1975) Crystal chemistry of tetrahedral structures. Gordon and Breach, London
10. Pamplin R (1960) Super-cell structure of semiconductors. Nature 188(4745):136–137
11. Razzetti C, Lottici PP, Antonioli G (1987) Structure and lattice Structure and lattice dynamics of nonmagnetic defective $A^{II}B_2^{III}X_4^{IV}$ compounds and alloys. Prog Crystal Growth Charact 15:43–73
12. Hahn H, Frank G, Klingler W, Storger A-D, Storger G (1955) Untersuchungen über ternäre Chalkogenide. VI. Über Ternäre Chalkogenide des Aluminiums, Galliums und Indiums mit Zink, Cadmium und Quecksilber. Z Anorg Allg Chem 279:241–270
13. Agostinelli E, Gastaldi L, Viticoli S (1985) Crystal growth and X-ray structural investigatton of two forms of $HgGa_2Te_4$. Mat Chem and Phys 12:303–312

14. Mocharnyuk GF, Babyuk TI, Derid OP, Lazarenko LS, Markus MM, Radautsan SI (1977) Order-disorder transition in $CdGa_2Se_4$-$CdIn_2Se_4$ solid solutions. Sov Phys Dokl 22:749
15. Razzetti C, Lottici PP, Zanotti L (1984) Ternary and pseudoternary AB_2X_4 compounds (A = Zn, Cd; B = Ga, In; X = S, Se). Mat Chem Phys 11:65–83
16. Bernard JE, Zunger A (1988) Ordered-vacancy-compound semiconductors: pseudocubic $CdIn_2Se_4$. Phys Rev B 37:6835–6856
17. Binsma JJM, Galing LJ, Bloem J (1981) Order-disorder behaviour and tetragonal distortion of chalcopyrite compounds. Phys Stat Sol (a) 63:595–603
18. Tiginyanu IM, Ursaki VV, Fulga VN (1989) On the order-disorder phase transition in the cation sublattice of $ZnGa_2Se_4$. Fiz Tekn Poluprov 23:1725–1727
19. Dietrich M, Unterricker M, Deicher M, Burchard A, Magerle R, Pfeiffer W, Forkel-Wirth D, Tiginyanu IM, Moldovyan NA (1996) Quadrupole interactionin defect chalcopyrite semiconductors studied by PAC. Cryst Res Technol 31:853–857
20. Dietrich M, Unterricker M, Deicher M, Burchard A, Magerle R, Pfeiffer W, Forkel-Wirth D, Tiginyanu IM, Moldovyan NA (1996) PAC investigation of ordered vacancy semiconductors II-III_2-VI_4. Hyperfine Interact (C) 1:242–246
21. Phillips JC (1973) Bonds and bands in semiconductors. Academic, New York
22. Neumann H (1983) About the average bond ionicity in $A^IB^{III}C_2^{VI}$ compounds. Cryst Res Technol 18:1391–1396
23. Kumar V (1987) Bond ionicity and susceptibility in $A^IB^{III}C_2^{VI}$ compounds. Phys Chem Sol 48:827–831
24. Ursaki VV, Burlakov II, Tiginyanu IM, Raptis YS, Anastassakis E, Anedda A (1999) Phase transitions in defect chalcopyrite compounds under hydrostatic pressure. Phys Rev B 59:257–268
25. Lottici PP, Parisini A, Razzetti C, Carra P (1984) Effective ionic charges in $CdGa_2Se_4$ and $CdGa_2S_4$. Solid State Commun 51:691–695
26. Wakamura K, Arai T (1981) Empirical relationship between effective ionic charges and optical dielectric constants in binary and ternary cubic compounds. Phys Rev B 24:7371–7379
27. Kushwaha AK, Kushwaha SS (2005) Effective charges in ternary chalcogenide spinels. Indian J Pure Appl Phys 43:664–667
28. Nitsche R (1975) Crystal chemistry, growth and properties of multi-cation chalcogenides. J de Physique. Colloque C3, 36(Suppl 9):C3–C9
29. Nitsche R (1971) Crystal growth and phase investigations in multi-component systems by vapour transport. J Cryst Growth 9:238–243
30. Bohac P, Gaumann A (1974) New fluxes for crystal growth of chalcogenides. J Cryst Growth 26:171–173
31. Yamamoto N, Miyauchi T (1972) Growth of single crystals of $CuGaS_2$ and $CuGa_{1-x}In_xS_2$ in solution. Japan J Appl Phys 11:1383–1384
32. Schafer H (1964) Chemical transport reactions. Academic Press, New York
33. Nitsche R, Bolsterli HU, Lichtensteiger M (1961) Crystal growth by chemical transport reactions-I: binary, ternary, and mixed-crystal chalcogenides. J Phys Chem Solids 21:199–205
34. Scholz H, Kluckow R (1967) In: Peiser HC (ed) Crystal growth. Pergamon Press, Oxford, p 475. Proceedings of the international conference on Crystal Growth, Boston, Mass, 20–24 June 1966
35. Paorice C, Zanotti L, Zuccalli G (1978) A temperature variation method for the growth of chalcopyrite crystals by iodine vapour transport. J Crystal Growth 43:705–710
36. Curti M, Gastaldi L, Lottici PP, Paorici C, Razzetti C, Viticoli S, Zanotti L (1987) Synthesis and characterization of the $Zn_xCd_{1-x}In_2S_4$ pseudoternary solid solution. J Solid State Chem 69:289–298
37. Badikov VV, Matveev IN, Pshenichnikov SM, Rychik OV, Trotsenko NK, Ustinov ND, Shcherbakov SI (1980) Growth and nonlinear properties of $HgGa_2S_4$. Sov J Quantum Electron 10:1300–1302

38. Feigelson RS, Route RK (1984) Crystal growth and optical properties of $CdGa_2S_4$. Prog Crystal Growth Charact 10:189–197
39. Mooser E, Pearson WB (1957) The chemical bond in semiconductors. J Electron 1:629–645
40. Mooser E (1983) Crystal chemistry and classification of multinary semiconductors. Nuovo Cimento 2D:1613–1627
41. Mooser E, Pearson WB (1959) On the crystal chemistry of normal valence compounds. Acta Crystallogr 12:1015–1022
42. Philips JC (1970) Ionicity of the chemical bond in crystals. Rev Mod Phys 42:317–356
43. Van Vechten JA (1969) Quantum dielectric theory of electronegativity in covalent systems I. electronic dielectric constant. Phys Rev 182:891–905
44. Razzetti R, Lottici PP (1983) Preparation and Raman spectroscopy of $Zn_xCd_{1-x}In_2S_4$ mixed cation layered compounds. Nuovo Cimento 2D:2044–2049
45. Haeuseler H (1979) X-ray investigations in the system $CdIn_2S_4-CdIn_2Se_4$. J Solid St Chem 29:121–123
46. Antonioli G, Lottici PP, Parisini A, Razzettit C (1984) EXAFS study of mixed crystals of the $A^{II}B_2^{III}X_4^{VI}$ family. Prog Crystal Growth Charact 10:9–18
47. Burdett JK, Price GD, Price SL (1982) Role of the crystal-field theory in determining the structure of spinels. J Am Chem Soc 104:92–95
48. Meloni F, Shaukat A (1984) Classification of the AB_2C_4 spinels: a pseudopotential orbital radii approach. Prog Crystal Growth Charact 10:37–43
49. Zunger A (1980) Structural stability of 495 binary compounds. Phys Rev Lett 44:582–586
50. Andreoni W, Baldereschi A, Biemont E, Phillips JC (1979) Hard-core pseudopotentials and structural maps of solids. Phys Rev B 20:4814–4823
51. Jiang X, Lambrecht WRL (2004) Electronic band structure of ordered vacancy defect chalcopyrite compounds with formula II-III_2-VI_4. Phys Rev B 69:035201
52. Ozaki S, Muto K, Adachi S (2003) Optical properties and electronic band structure of $CdGa_2Te_4$. J Phys Chem Sol 64:1935–1939
53. Singh P, Verma UP, Jensen P (2011) Electronic and optical properties of defect chalcopyrite $HgAl_2Se_4$. J Phys Chem Sol 72:1414–1418
54. Chizhikov VI, Panyutin VL, Ponedelnikov BE, Rozencon AE (1981) Structure de bande lectronique de $CdAl_2Te_4$ dans les modifications avec les groupes spatiaux D_{2d}^{11}, D_{2d}^{9}, D_{2d}^{1} et S_4^2. Phys Stat Sol B 106:91–98
55. Baldereschi A, Meloni F, Aymerich F, Mula G (1977) Electronic band structure of cubic spinel $CdIn_2S_4$. Inst Phys Conf Ser 35:193–200
56. Kambara T, Oguchi T, Gondaira KI (1980) Electronic band structures of semiconducting ferromagnetic spinels $CdCr_2S_4$ and $CdCr_2Se_4$. J Phys C Solid St Phys 13:1493–1512
57. Oguchi T, Kambara T, Gondaira KI (1980) Self-consistent electronic structures of magnetic semiconductors by a discrete variational Xα calculation. I. Ferromagnetic spinels, $CdCr_2S_4$ and $CdCr_2Se_4$. Phys Rev B 22:872–879
58. Oguchi T, Kambara T, Gondaira KI (1981) Self-consistent electronic structures of magnetic semiconductors by a discrete variational Xα calculation. II. $HgCr_2Se_4$. Phys Rev B 24:3441–3444
59. Guzzi M, Grillii E (1984) Localized levels and luminescence of AB_2X_4 semiconducting compounds. Mater Chem Phys 11:295–304
60. Radautsan SI, Georgobiani AN, Tiginyanu IM (1984) II-III_2-VI_4 compounds: proterties and trends for applications. Prog Crystal Growth Charact 10:403–412
61. Tarricone L, Zanotti L (1984) Photoconductivity and photomemory in $Zn_xCd_{1-x}In_2S_4$ layered crystals. Mater Chem Phys 11:161–176
62. Gentile AL (1984) Devices using ternary or multinary compounds. Prog Crystal Growth Charact 10:241–256
63. Levine BF, Bethea CG, Kasper HM, Thiel FA (1976) Nonlinear optical susceptibility of $HgGa_2S_4$. IEEE J Quant Electron QE-12:367–368
64. Ren D, Huang J, Qu Y, Hu X, Zhang L, Andreev Yu, Geico P, Badikov V, Lanskii G, Tikhomirov A (2003) Optical properties and CO_2 laser SHG with $HgGa_2S_4$. Chinese Optics Lett 1:613–615

65. Ren D, Huang J, Hu X, Qu Y, Andreev YM, Geico PP, Badikov VV (2004) Efficient CO_2 frequency doubling with $Hg_{1-x}Cd_xGa_2S_4$. Proc SPIE 5397:205–211
66. Zunger A (1987) Order-disorder transformation in ternary tetrahedral semiconductors. Appl Phys Lett 50:164–166
67. Rincon C (1992) Order-disorder phase transition in ternary chalcopyrite compounds and pseudobinary alloys. Phys Rev B 45:12716–12719
68. Yamanaka T, Takeuchi Y, (1983) Order-disorder transition in $MgAl_2O_4$ spinel at high temperatures up to 1700°C. Z Kristallographie Cryst Mater 165:65–78
69. Cynn H, Sharma SK, Cooney TF, Nicol M (1992) High-temperature Raman investigation of order-disorder behavior in the $MgAl_2O_4$ spinel. Phys Rev 45:500–502
70. De Ligny D, Neuville DR, Flank A-M, Lagarde P (2009) Structure of spinel at high temperature using in-situ XANES study at the Al and Mg K-edge. J Phys Conf Ser 190:012178
71. Navrotski A, Kasper RB (1976) Spinel disproportionation at high pressure: calorimetric determination of enthalpy of formation of Mg_2SnO_4 and Co_2SnO_4 and some implications for silicates. Earth Planet Sci Lett 31:247–254
72. Petrov K, Tsolovski I (1980) On the high temperature spinel-ramsdellite transformation of lithium titanate ($Li_{1+x}Ti_{2-x}O_4$). Phys Stat Sol A 58(1):K85–K88
73. Tang XC, Huang BY, He YH (2006) Phase transition of lithiated-spinel $Li_2Mn_2O_4$ at high temperature. Trans Nonferrous Metals Soc China 16:438–445
74. Sekine T, Mitsuhashi T (2001) High-temperature metastability of cubic spinel Si_3N_4. Appl Phys Lett 79:2719

Part I
Spinel-Structured AB_2X_4 Chalcogenide Compounds

Chapter 2
AB_2O_4 Compounds at High Pressures

Daniel Errandonea

Abstract In this chapter, we present an overview of the effects of pressure on the crystalline structure and physical properties of oxygen-based spinels and other related oxides. Recent X-ray diffraction and Raman spectroscopy studies are summarized. A brief description of pressure-driven transitions and post-spinel structures is also provided. We also compare the response to high-pressure of several spinel oxides. We conclude with an examination of elastic and magnetic properties.

Keywords Spinel · Post-spinel · Phase transition · Crystal structure · Lattice vibrations · Elastic properties

2.1 Introduction

Many compounds of the AB_2X_4 family, in particular oxides (X = O), crystallize at ambient conditions in the spinel structure. Spinel is the magnesium aluminum oxide member of this large group of materials. It has the formula $MgAl_2O_4$ and gives its name to the family of compounds that share the same structural arrangement. Consequently, here we will name as spinel to any material of general formulation AB_2X_4 which crystallizes in the cubic (isometric) crystal system with space group $Fd\bar{3}m$ (No. 227). In this structure, shown in Fig. 2.1, the X anions are located at (u, u, u), Wyckoff position 32e, with $u \approx 0.25$. They are arranged in a cubic close-packed lattice. In addition, the cations A and B occupy in the lattice respectively tetrahedral (1/8, 1/8, 1/8) sites, Wyckoff position 8a, and octahedral (1/2, 1/2, 1/2) sites, Wyckoff position 16d. Therefore, the single positional parameter u plus the unit-cell parameter a are sufficient to determine the spinel structure.

D. Errandonea (✉)
Universitat de Valencia, Valencia, Spain
e-mail: daniel.errandonea@uv.es

F. J. Manjón et al. (eds.), *Pressure-Induced Phase Transitions in AB_2X_4 Chalcogenide Compounds*, Springer Series in Materials Science 189,
DOI: 10.1007/978-3-642-40367-5_2,

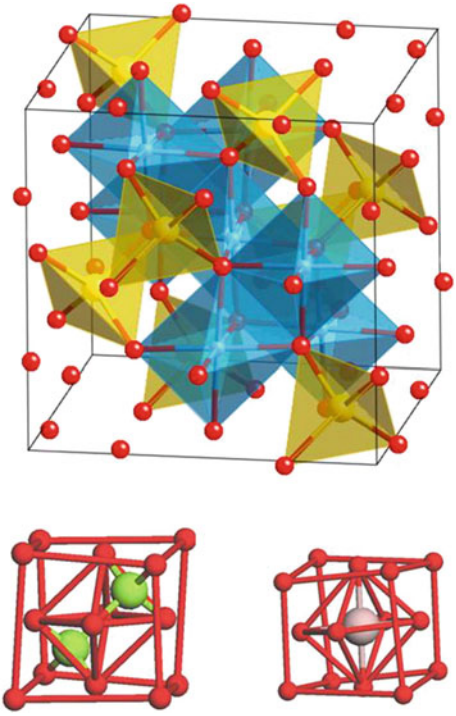

Fig. 2.1 Schematic view of the spinel structure with octahedral (*blue*) and tetrahedral units (*yellow*). Oxygen atoms are represented in red. In the lower part the tetrahedral (*left*) and octahedral (*right*) coordination of cations is represented. Drawings made using crystal maker

In spinels, A and B can be divalent, trivalent, or tetravalent cations, including magnesium, zinc, iron, manganese, aluminum, chromium, gallium, titanium, and silicon among other elements of the Periodic Table. Although the anion is normally oxygen (oxospinels), it can be also a chalcogen element, like S (thiospinels) or Se (selenospinels). Spinels can either be synthesized in the laboratory or in some cases occur as minerals. Some of the principal members of the oxide spinel family are: spinel ($MgAl_2O_4$), gahnite ($ZnAl_2O_4$), hercynite ($FeAl_2O_4$), cuprospinel ($CuFe_2O_4$), magnetite (Fe_3O_4), ulvöspinel ($TiFe_2O_4$), chromite ($FeCr_2O_4$), magnesiochromite ($MgCr_2O_4$), galaxite ($MnAl_2O_4$), magnesioferrite ($MgFe_2O_4$), franklinite ($ZnFe_2O_4$), trevorite ($NiFe_2O_4$), and the high-pressure silicate ringwoodite [$(Mg, Fe)_2SiO_4$]. Spinels are usually ordered (A and B in tetrahedral and octahedral sites, respectively) and they are referred as "normal" spinels, but mutual substitution of A and B cations has been reported in many materials. The extreme cases of cation substitution lead to "inverse" spinels such as $CoFe_2O_4$, where the Co cation occupies one half of the octahedral sites and the Fe cation occupies all the tetrahedral sites. In general, most spinels have some degree of inversion. A particular case is $NiAl_2O_4$. In this oxide a complete randomization of both cations in octahedral and tetrahedral sites is observed.

After Finger et al. [1] studied the structure of spinel and magnetite under compression up to 4 GPa, many high-pressure studies have been performed in spinels.

The main interest to study these materials comes from geophysics, but also from technological applications and fundamental physics. In particular, spinel oxides have been extensively studied under pressure because they are constituents of many igneous and metamorphic rocks. Also because of the fact that the 660 km seismic discontinuity in the Earth's mantle has long been identified with the decomposition of ringwoodite into (Mg, Fe)SiO_3 perovskite and (Mg, Fe)O magnesiowüstite [2].

In this chapter we will review different high-pressure studies on spinel-structured oxides. We will mainly focus on X-ray diffraction and Raman studies since the pressure behavior of oxospinels has been mostly studied with these two techniques. We will describe the effects of pressure in the spinel structure discussing facts like bulk and polyhedral compressibility, cation size, and cation substitution. We will also comment on pressure-induced phase transitions and on the different post-spinel structures. In particular, zinc gallate ($ZnGa_2O_4$) will be used as a test model. A comprehensive review on high-pressure effects on spinel oxides was published more than a decade ago by Smyth [3], but recently a lot of progress has been done in the understanding of the behavior of spinels at high pressures. Therefore, we think it is timely to include a section devoted them here.

2.2 Isothermal Compression of the Spinel Phase: X-ray Diffraction Studies

The effect of pressure on the lattice parameter, hence the volume, for different spinels has been determined at room temperature by means of powder X-ray diffraction measurements employing diamond-anvil cells. These experiments show that in most spinel oxides, the diffraction patterns can be indexed with the cubic spinel structure up to around 30 GPa. At higher pressures, phase transitions to different post-spinel structures take place. In contrast with oxide spinels, in sulfide and selenide spinels the pressure range of stability is smaller, being transition pressures smaller than 15 GPa, as will be discussed in the next chapter. A summary of transition pressures in spinel oxides is given in Table 2.1 [4–17]. From the refinements of X-ray diffraction patterns collected under compression, the evolution of the unit-cell parameters and atomic positions can be obtained as a function of pressure.

Figure 2.2 shows the pressure dependence of the volume for the spinel phase of $ZnGa_2O_4$, $MgCr_2O_4$, $MgAl_2O_4$, and the natural chromium spinel $(NaMgFeTi)_{0.9661}(CrAl)_{2.0241}O_4$. As can be seen in the figure, $ZnGa_2O_4$ is the less compressible material of all of them. A fit to the $ZnGa_2O_4$ data with a third-order Birch–Murnaghan equation of state (EOS) [19] gives: $V_0 = 580.1(9)$ Å^3, $B_0 = 233(8)$ GPa, and $B_0' = 8.3(4)$, where V_0, B_0, and B_0' are the zero-pressure volume, bulk modulus, and its pressure derivative, respectively. According to this result, $ZnGa_2O_4$ is the most incompressible among the studied oxide spinels up to now. The bulk modulus of different oxide spinels is summarized in Table 2.2 [4, 8–10, 14, 15, 20–30]. As can be observed in Table 2.2, sulfide and selenide spinels are much more compressible than oxide spinels.

Table 2.1 Transition pressures (P_t) and high-pressure phases of different spinels (space groups are indicated for HP phases when known)

Compound	P_t (GPa)	HP phase	Reference	Compound	P_t (GPa)	HP phase	Reference
$ZnGa_2O_4$	31.2	$I4_1/amd$	[4]	$ZnCr_2O_4$	17–35	unknown	[11]
	55	*Pnma*					
$(Mg, Fe)_2SiO_4$	24	$(Mg,Fe)SiO_3$+ (Mg,Fe)O	[5]	Fe_3O_4	24	*Pbcm*	[12]
$MgAl_2O_4$	25	*Pnma*	[6]	$ZnCr_2S_4$	10	amorphization	[13]
	40	*Cmcm*					
$MgFe_2O_4$	27.7	unknown	[7]	$ZnTi_2O_4$	24–32	*Cmcm*	[18]
$NiMn_2O_4$	12	$I4_1/amd$	[8]	$MgIn_2S_4$	9.8	$Fd\bar{3}m$	[14]
$ZnFe_2O_4$	25	unknown	[9]	$CdIn_2S_4$	9.3	$Fd\bar{3}m$	[14]
$CoFe_2O_4$	27	unknown	[9]	$MnIn_2S_4$	6.8	$Fd\bar{3}m$	[14]
$MgFe_2O_4$	30	unknown	[9]	$FeCr_2S_4$	9	I_2/m	[15]
$MgCr_2O_4$	20	$I4_1/amd$	[10]	$CuIr_2S_4$	4	unknown	[16]
				$CuIr_2Se_4$	2.6	unknown	[17]

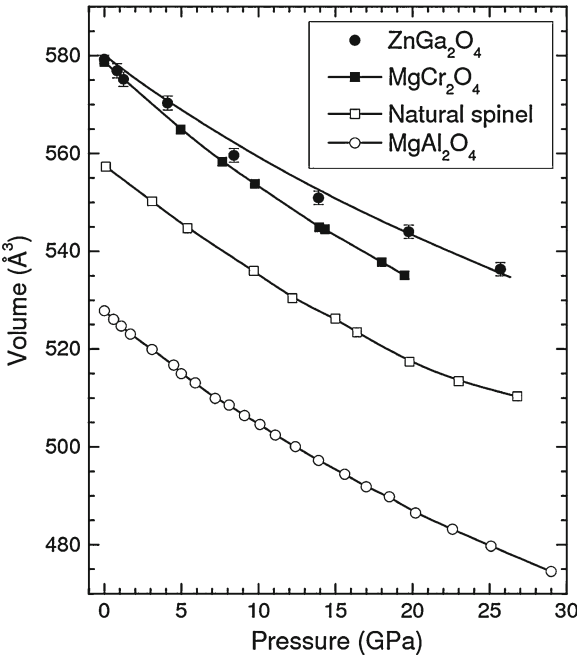

Fig. 2.2 Pressure dependence of the unit-cell volume of different spinel oxides. Data taken from [4, 10, 24, 27]

Table 2.2 Comparison of experimentally-determined bulk moduli of different oxide spinels

Compound	B_0 (GPa)	B_0'	Reference	Compound	B_0 (GPa)	B_0'	Reference
$ZnGa_2O_4$	233	8.3	[4]	$MgAl_2O_4$	194–212	4–5.6	[27, 28]
$ZnAl_2O_4$	201–211	4.8–7.6	[9, 20]	$MgFe_2O_4$	179–181	3.3–6.3	[9, 21]
$ZnCr_2O_4$	183	7.9	[21]	$MgCr_2O_4$	189	7.2	[10]
$ZnFe_2O_4$	166–185	3.1–9.3	[22]	Mg_2SiO_4	184	4	[28]
$ZnMn_2O_4$	183	4	[23]	$CoFe_2O_4$	179	3.7	[9]
$ZnMn_2O_4$	162	4	[18]	$NiMn_2O_4$	206	4	[8]
Natural chromiumspinel	209	7	[24]	Ni_2SiO_4	220	4	[27]
Fe_2SiO_4	188	5.5	[25]	$CuMn_2O_4$	198	4	[29]
Fe_3O_4	183–192	4–5.6	[26]	$CdIn_2S_4$	79.8	3.1	[14]
$FeCr_2S_4$	85.4	4	[14]	$MgIn_2S_4$	76	2.8	[14]
$CdCr_2Se_4$	101	5.2	[30]	$MnIn_2S_4$	78	3.2	[15]
$CdGa_2Se_4$	48	4.8	[30]				

$ZnGa_2O_4$ is apparently the less compressible compound among them. The pressure derivative of the bulk modulus is also included for completeness. Sulphur and selenium spinels (to be discussed in next chapter) are included here to facilitate comparison

An interesting fact to note here, it is that apparently, cation inversion could cause a change of the compressibility of spinels. Evidence of such pressure-induced cation inversion has been found in other oxide spinels upon compression; e.g. $NiAl_2O_4$ [31]. In particular, compressibilities for normal (fully ordered) versus inverse (with disordered octahedral cations) variants were shown to differ by as much as 17 % [28].

From the data collected for $ZnGa_2O_4$ it was also deduced a negative pressure coefficient of the parameter u under compression. This tendency indicates that zinc gallate tries to reach the ideal structure ($u = 0.25$) when pressurized. The pressure dependence of u is shown in the inset on Fig. 2.3. A similar behavior was observed in other cubic spinels like $ZnAl_2O_4$ [20]. Ab initio calculations predict a similar behavior for $ZnAl_2O_4$ and $ZnIn_2O_4$ [32]. The oxygen u parameter in spinels reflects

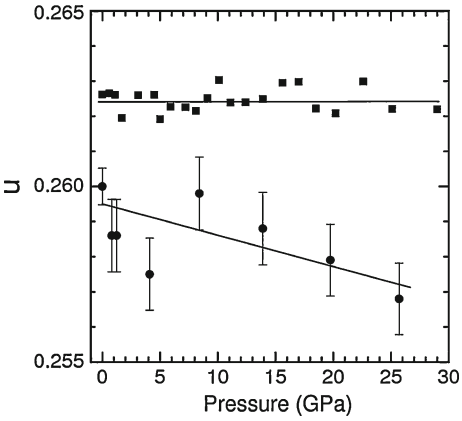

Fig. 2.3 Pressure dependence of the oxygen parameter u for $ZnGa_2O_4$ [4] (*circles*) and Fe_2SiO_4 [33] (*squares*)

the relative size of A and B cations in their respective tetrahedral and octahedral sites. Thus, their behavior under compression is determined by the relative compressibility of these two polyhedral units. Difference in octahedral and polyhedral compression may lead to different behaviors of u with pressure. In particular, it can be seen in Fig. 2.3 that in Fe_2SiO_4 [33] u remains nearly constant up to 30 GPa. In order to illustrate better the influence of pressure on u, it is instructive the comparison made by Finger et al. [26] of the high-pressure behavior of this parameter in $MgAl_2O_4$, Fe_3O_4, and Ni_2SiO_4. The u parameter of $MgAl_2O_4$ decreases with pressure, this indicating that MgO_4 tetrahedra compress more than the AlO_6 octahedra. On the other hand, the u parameter is not affected by pressure in Fe_3O_4 since Fe–O are equally compressible in both tetrahedral and octahedral units, and therefore the spinel structure simply scales with pressure. Finally, u increases upon compression in Ni_2SiO_4 due to the incompressibility of the SiO_4 tetrahedron in comparison to NiO_6 octahedron.

In the particular case of $ZnGa_2O_4$, the decrease of u with pressure is a consequence of the larger polyhedral compressibility of the ZnO_4 tetrahedra than that of the GaO_6 octahedra. To understand better the relation between polyhedral compressibility and the pressure evolution of u, we should remember that the Zn–O and Ga–O bond distances are given by: $R_{Zn\text{–}O} = \sqrt{3}(u - 0.125)a$ and $R_{Ga\text{–}O} = \sqrt{\left(3u^2 - 2u + 0.375\right)}\, a$. This means that at $u = 0.2625$ $R_{Zn\text{–}O} = R_{Ga\text{–}O}$ and at $u = 0.25$ the oxygen atoms form a perfect face-centered cubic (fcc) sublattice, being the following relations obtained: $\partial R_{Zn\text{–}O}/\partial u = \sqrt{3a}$ and $\partial R_{Ga\text{–}O}/\partial u = -a$. Thus when u increases, the tetrahedral bond distances increase while the octahedral bond lengths decrease, and the tetrahedral bond length change faster than the octahedral one. Therefore, upon compression we have two competing effects. On one side, both bond distances tend to decrease because of the reduction of the unit-cell parameter. On the other hand, the reduction of u contributes to the decrease of the Zn–O distance but partially compensate the decrease of the Ga–O distance (because $\partial R_{Ga\text{–}O}/\partial u = -a$). Thus, Zn–O bonds are expected to be more compressible than Ga–O bonds. This result is in excellent agreement with experimental results summarized in Fig. 2.4. In addition to $ZnGa_2O_4$, other nice examples to understand the differential bond compressibility of spinels are $MgAl_2O_4$ [34], $ZnAl_2O_4$ [25], and Fe_2SiO_4 [33]. The differences in polyhedral compressibilities of different compounds are in good agreement with the predictions of Recio et al. [35]. In particular, these authors show that the bulk compressibility in spinel–type compounds can always be expressed in terms of cation–oxygen polyhedral compressibilities and the pressure effect of the internal oxygen position in the unit cell. This behavior contrast with that of other binary oxide compounds, like zircon or scheelite, where the bulk modulus is mainly controlled by the larger cation polyhedra [36].

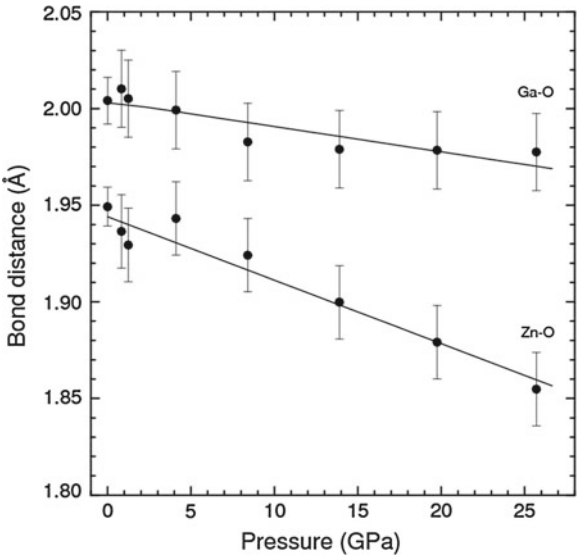

Fig. 2.4 Bond distances versus pressure obtained from X-ray experiments performed in $ZnGa_2O_4$ [4]

2.3 High Pressure Phases of Oxospinels

Due to the possible relation of the 660 km seismic discontinuity in the mantle the Earth with pressure-induced changes in $(Mg, Fe)_2SiO_4$, many studies have been carried out examining post-spinel structures. Particular attention has been given to experiments of the transformation of $(Mg, Fe)_2SiO_4$ from ringwoodite to (Mg, Fe)O-magnesiowustite and $(Mg, Fe)SiO_3$-perovskite. In contrast with this silicate, many AB_2O_4 spinels have been found to transform to post-spinel structures without decomposition. In particular, the postspinel mineral $MgAl_2O_4$ exists under severe pressure conditions in the subducted oceanic lithosphere in the Earth's deep interior. The orthorhombic structures of $CaMn_2O_4$ (space group *Pbcm*), $CaFe_2O_4$ (space group *Pnma*), and $CaTi_2O_4$ (space group *Cmcm*) have been reported as post-spinel phases [6]. Because these structures are very similar, several ambiguities and inconsistencies appear in high-pressure studies. The structures of CaB_2O_4 (where B = Mn, Fe, Ti) are very similar; distorted BO_6 octahedra sharing edges and corners create a framework, with the Ca^{2+} ions occupying one-dimensional six-sided channels coordinated by eight O atoms. $CaMn_2O_4$ occurs as the mineral marokite, with highly distorted MnO_6 octahedra, which is due to the strong first-order Jahn–Teller effect of Mn^{3+}. Differences between the spinel structure and these three types of structures can be seen in Fig. 2.5. Basically, the atomic arrangements are denser in the high-pressure phases. In fact, cations change their coordination from tetrahedral and octahedral to octahedral and dodechahedral, respectively, during the transformation from the spinel to these high-pressure phases. Consequently, a more compact three

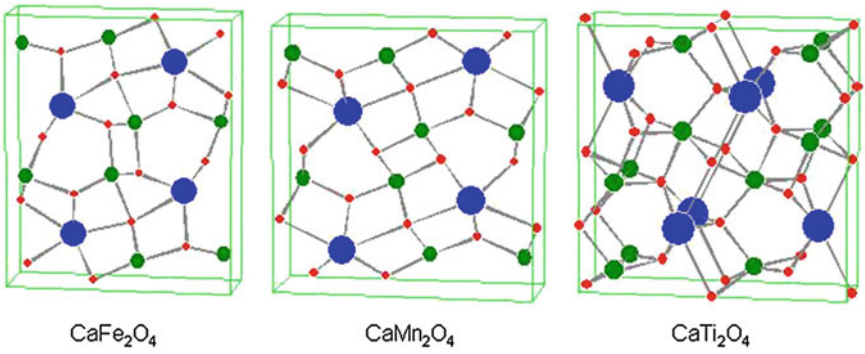

Fig. 2.5 Schematic view of the orthorhombic post-spinel structures. *Blue spheres*: B cations, green *spheres*: A cations, and *red spheres*: O atoms

dimensional network is formed and consequently the phase transition occurs together with a small volume collapse [18]. The high-pressure phase has also a bulk modulus approximately 25 % larger than the spinel phase [18].

An interesting fact of the transformation to CaB_2O_4-type structures is that it is not only induced by high-pressure experiments. This process has been also discovered to occur naturally, as it was discovered in the Suizhou meteorite [37]. In the laboratory, the transition has been reproduced over a large number of oxides; e.g. $MgAl_2O_4$, $ZnCr_2O_4$, $CoFe_2O_4$, $CdCr_2O_4$, etc. [38]. A possible mechanism for this post-spinel transformation has been recently proposed [38]. According to it, the transition involves not only simple cation displacements, but also full octahedral movements, which implies a reconstructive transformation. This is likely the reason why phase coexistence is observed in a wide pressure range in many cases [18]. One exception to this rule is natural chromite in which a distortive transition to a $CaAl_2O_4$-type orthorhombic structure occurs.

An interesting fact to highlight is the existence of an intermediate phase between the cubic spinel and the orthorhombic post-spinel structures in some compounds. This phase is usually a distortion of the cubic structure. A particular compound following this behavior is $ZnGa_2O_4$. Figure 2.6 shows a series of X-ray powder diffraction patterns collected in $ZnGa_2O_4$ at different pressures and RT. The diffraction patterns can be assigned to the cubic spinel structure up to 31.2 GPa where changes in the diffraction patterns are found. Peaks become much broader and many of them split, as indicated by arrows in Fig. 2.6. This is indicative of the occurrence of a phase transition. Changes become more notorious at higher pressure as can be seen in the spectra recorded at 34.8–48.7 GPa. The changes of the diffraction patterns cannot be explained by any of the known high-pressure post-spinel phases ($CaFe_2O_4$-, $CaMn_2O_4$-, and $CaTi_2O_4$-type). A possible explanation to the experimental results is given by the consideration of the tetragonal spinel structure, the structure of $ZnMn_2O_4$ and $MgMn_2O_4$ [23, 39]. This phase belongs to space group $I4_1/amd$, a translationgleiche subgroup of $Fd\bar{3}m$. It is formed by a tetragonal

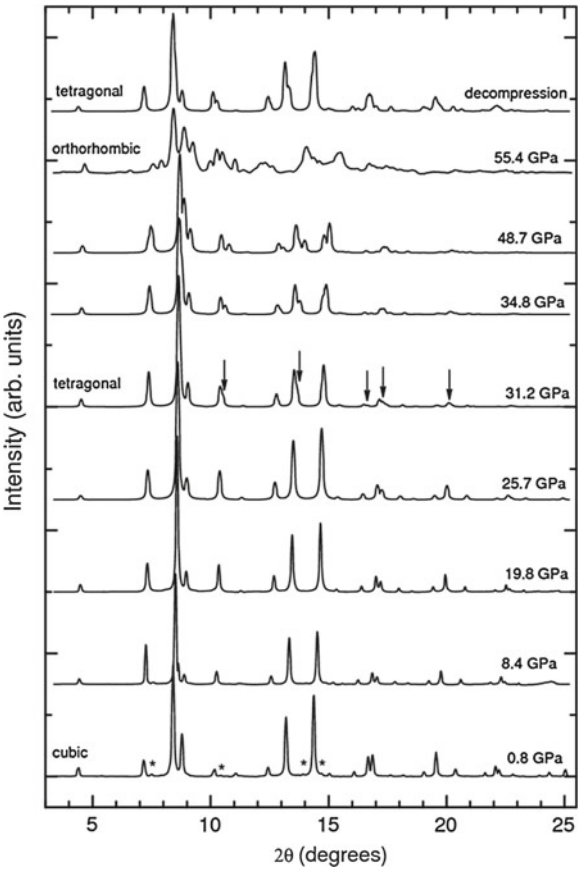

Fig. 2.6 Selection of XRD patterns collected from $ZnGa_2O_4$ at different pressures. Pressures are indicated and characteristic patters of each phase labeled. The stars indicate impurity peaks assigned to Ga_2O_3. The vertical arrows depict the changes associated to the onset of the cubic-tetragonal transition

distortion of the cubic spinel (if in the tetragonal structure $c/a = \sqrt{2}$ is satisfied, it is reduced to the cubic spinel structure). The cubic-tetragonal transition does not involve any detectable change in the volume. However, upon compression the tetrahedral distortion of the $I4_1/amd$ structure gradually increases. These facts, and the group-subgroup relationship existent between the cubic and tetragonal phases, point towards the occurrence of a second-order pressure-induced transition in $ZnGa_2O_4$. It is important to note, that the cubic-tetragonal transition has been documented also in $NiMn_2O_4$ at 12 GPa [8]. Regarding cation coordination, tetragonal $ZnGa_2O_4$ also consists of ZnO_4 tetrahedra and GaO_6 octahedra, but in contrast with cubic $ZnGa_2O_4$, the octahedral are distorted showing four long distances and two short distances.

In $ZnGa_2O_4$ at 55.4 GPa a second transition is detected (see Fig. 2.6). At this pressure, there are important changes observed in the diffraction patterns. The number of diffraction peaks increases considerably in the diffraction patterns, probably as a consequence of a symmetry reduction. In particular, the patterns resemble those of the orthorhombic post-spinel structures of $MgAl_2O_4$ and homologous compounds. In this particular case, the post-spinel phase has a $CaMn_2O_4$-type structure (marokite) [40]. The transition to the orthorhombic post-spinel structure involves an estimated volume collapse of around 7 %, similar to that observed in other spinels.

Before concluding this section, we would like to mention that high-pressure studies have been also performed on the post-spinel structures. Since these structures are denser than spinel and have a more efficient packing, they are less compressible than spinel. In addition, powder diffraction studies indicated that $CaMn_2O_4$, $CaFe_2O_4$, and $CaTi_2O_4$ have further high-pressure polymorphs [41]. $CaMn_2O_4$ transforms to the $CaTi_2O_4$ structure at 30 GPa. Also a new phase was observed at pressures above 50 GPa during compression of $CaFe_2O_4$ [41]. Rietveld refinements demonstrated that the HP structure, with space group *Pnam*, is produced via a martensitic transformation by displacing one of every three layers perpendicular to the *c* axis. $CaTi_2O_4$ has also a HP polymorphs with space group *Bbmm* [41]. Very noticeably is the fact that the transition in $CaFe_2O_4$ is associated to a Fe^{3+} spin transition. Single-crystal diffraction measurements have shown that the 50 GPa transition of this compound is isosymmetric, but marked by a 8.4 % volume collapse [42]. X-ray emission spectroscopic data suggest that the transition is related to the Fe^{3+} high-spin/low-spin transition. The bulk modulus is remarkably different for the high-spin (159 GPa) and low-spin (235 GPa) structures.

2.4 Lattice Vibrations in Spinels

At ambient conditions, the vibrational properties of spinel oxides have been mostly studied with Raman (R) and infrared (IR) spectroscopy but a few studies using inelastic neutron scattering are available [43]. However, high-pressure studies of the lattice dynamics have been mostly performed using Raman spectroscopy. Therefore, in this section we will concentrate on discussing Raman results.

The normal vibrations of a crystal can be determined if one knows its crystalline structure (the primitive unit cell) and applies group theory. To calculate lattice vibrations the full cubic unit cell of spinel is redundant. It contains 56 atoms, but the smallest Bravais cell; i.e., the primitive cell, has only 14 atoms. As a result, one should expect 42 vibrational modes. Group theory analysis predicts the following irreducible representations for the modes at the Γ point of the Brillouin zone [44]:

$$\Gamma = A_{1g}(R) + E_g(R) + T_{1g} + 3T_{2g}(R) + 2A_{2u} + 2E_u + 4T_{1u}(IR) + T_{1u} + 2T_{2u}$$

where Raman- and infrared-active modes are indicated, and the rest of the modes are acoustic or silent modes. Note that T modes are also noted as F modes in the

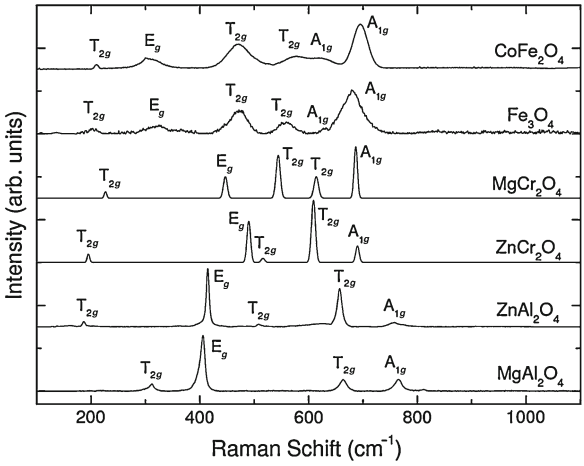

Fig. 2.7 Selection of ambient conditions Raman spectra of different ABO_4 spinels

literature and that E and T modes are double and triple degenerate, respectively. In normal non-defective spinels selection rules indicate that only five modes should be Raman active and four modes infrared active. Non-stoichiometry, the presence of vacancies, interstitial cations, and defects in general, may result in activation of phonon modes not predicted by group theory.

Figure 2.7 shows a selection of Raman spectra collected from different compounds at ambient conditions. There it can be seen that in $MgAl_2O_4$ usually only four of the five allowed modes are observed. A typical feature of all the spectra is that the A_{1g} mode is the one with highest frequency. In general, the mode frequencies follow the sequence $T_{2g} < E_g < T_{2g} < T_{2g} < A_{1g}$. In addition the lowest frequency T_{2g} mode is one of the weakest modes. In the figure, it can be also seen that the Raman spectra of different aluminates resemble very much to each other. The same can be said for chromites and ferrites. These similarities are related to the fact that some Raman vibrations can be associated to internal vibrations of the BO_6 octahedra and AO_4 tetrahedra. It is noticeably in the cases of Fe_3O_4 and $CoFe_2O_4$ the splitting of the high-frequency A_{1g} mode. This fact is caused by a partial cation redistribution [45], being the relative intensity ratio between both A_{1g} peaks decreasing with lowering of inversion in the spinel structure.

$MgAl_2O_4$ has been one of the most studied spinels. Table 2.3 summarizes the theoretical and experimental Raman modes [43, 46–49]. The calculated frequencies agree with the experimental values within 5 %. Most experiments found only four Raman modes. Only one experiment [46] reported a fifth mode which is very weak. As the differences in frequency of this mode with the "missing" T_{2g} mode is larger than 15 % there are doubts about its assignation. In particular, it has been stated that its occurrence could be probably related to cation disorder [43]. Cation disorder is also the cause of the A_{1g} mode splitting reported in [46] and [49]. Calculations also agree

Table 2.3 Frequencies of the Raman modes of $MgAl_2O_4$ at ambient conditions. All frequencies are given in cm^{-1}

Mode	Theory	Experiments			
		Reference [46]	Reference [47]	Reference [48]	Reference [49]
T_{2g}	319	311	311	312	311
E_g	426	410	408	407	409
T_{2g}		492			
T_{2g}	570				
T_{2g}	682	671	669	666	670
A_{1g}		727			727
A_{1g}	776	772	770	767	770

well with experiments regarding IR modes [43]. For these modes, the mode assignment is more complicated than in Raman because the induced macroscopic electric field lifts the threefold degeneracy of IR-active T_{1u} modes. Consequently, they split into twofold degenerate TO modes and a single LO mode. The TO (LO) modes measured in experiments are 304 (312), 476 (610), 578 (575), and 676(868) cm^{-1}.

Before discussing pressure effects on Raman modes we will dedicate a few paragraphs to relate atomic motions with Raman modes. The A_{1g} mode corresponds to a symmetric breathing mode of the AO_4 tetrahedron [50] where only the oxygen atoms move. Regarding the highest-frequency T_{2g} mode the literature disagrees. Some authors assign it to an anti-symmetric breathing mode of the AO_4 tetrahedron and others to an asymmetric bending motion of the oxygens bonded to the A cation [50]. The assignment is clear for the remaining modes [50]. The lowest-frequency T_{2g} mode is a complete translation of the BO_6 octahedron against the A cation. The E_g mode is a symmetric bending motion of the oxygens within the AO_4 units and

Table 2.4 Experimental Raman frequencies (in cm^{-1}) for different modes of several ABO_4 spinels

Spinel	T_{2g}	E_g	T_{2g}	T_{2g}	A_{1g}	Reference
$MgAl_2O_4$	311	409		670	727, 770	[49]
$MgCr_2O_4$	227	447	544	614	687	[51]
$MgMn_2O_4$	313	313	375	507	666	[52]
$MgFe_2O_4$	217	333	486	554	646, 715	[7]
$ZnAl_2O_4$	197	417	509	658	758	[53]
$ZnCr_2O_4$	180	430, 457	511	605	687	[54]
$ZnMn_2O_4$	300	320	381	475	678	[52]
$ZnFe_2O_4$	221	246	355	451	647	[51]
$FeAl_2O_4$	184		593	701	753	[55]
$FeCr_2O_4$					686	[56]
Fe_3O_4	193	306		538	668	[57]
$MnCr_2O_4$		457	511	600	671, 685	[58]
$MnFe_2O_4$	189	339	446	559	647	[59]
Mn_3O_4	300	320	382	475	678	[52]

the remaining T_{2g} mode is a translation along one direction of the lattice, with the cations and oxygen atoms moving in opposite directions. Summarized in Table 2.4 there are the Raman modes for different compounds to illustrate the influence of cation replacement in them. Clearly the A_{1g} mode is strongly affected by B cation substitution and the lowest-frequency T_{2g} mode by A cation substitution.

2.5 High-Pressure Raman Scattering Studies

As commented, experimental high-pressure studies of lattice dynamics in oxospinels have been done by using Raman scattering measurements. Table 2.5 summarizes Raman modes and pressure coefficients of different zinc oxospinels. There, it can be seen that among the modes of the spinel phase the two low-wave number modes exhibit pressure coefficients smaller than the other modes. In particular, it is noticeably that the low-frequency T_{2g} mode, associated to translations of the octahedral BO_6 units, has the smallest pressure coefficient of all modes. Another systematic behavior to stress is that the A_{1g} high-frequency mode of the ZnO_4 tetrahedral groups tends to have a larger pressure coefficient than the bending modes associated to these groups. The first feature is related to the fact that Zn–O bonds are shorter than the B–O bonds in all spinel oxides. This means that the Zn–O distance is less compressible than the B–O distance; therefore, the low-frequency T_{2g} mode, which triggers the Zn–O distance, is almost unaffected by compression. The second one suggests than in spinels bond stretching has a larger force constant than bond-bending. A similar systematic behavior than in ZnB_2O_4 spinels has been found for MgB_2O_4 spinels [7, 51]. This picture is supported by lattice-dynamics calculations [53, 60]. Similar high-pressure evolutions are also obtained for IR-active modes. In both $ZnAl_2O_4$ and $ZnGa_2O_4$, the highest frequency IR mode has $d\omega/dP > 4\,cm^{-1}/GPa$ and the lowest frequency IR modes have $d\omega/dP < x\,cm^{-1}/GPa$. An interesting fact to remark before discussing the Raman modes of high-pressure phases is the not existence of soft modes within the pressure range of stability of the cubic spinel phase in any of the studied compounds. Thisindicate that the observed pressure-induced transitions

Table 2.5 Experimental Raman-mode frequencies at ambient conditions (ω) and their pressure dependences ($d\omega/dP$) for $ZnBO_4$ spinels

Mode	$ZnFe_2O_4$		$ZnCr_2O_4$		$ZnAl_2O_4$		$ZnGa_2O_4$	
	ω (cm^{-1})	$d\omega/dP$ (cm^{-1}/GPa)	ω (cm^{-1})	$d\omega/dP$ (cm^{-1}/GPa)	ω (cm^{-1})	$d\omega/dP$ (cm^{-1}/GPa)	ω (cm^{-1})	$d\omega/dP$ (cm^{-1}/GPa)
T_{2g}	221	1.31	180	2.05	196			
E_g	246	0.77	430	2.67	417	2.2		
T_{2g}	355	4.01	511	4.07	488		465	3.5
T_{2g}	451	3.95	605	4.11	658	3.8	608	3.7
A_{1g}	647	2.76	692	4.61	758		710	4.4

Data taken from references [11, 51, 53]

are not caused by mechanical instabilities of the spinel phase and occur because high-pressure phases become thermodynamically more stable than the spinel phase upon compression. A final fact to highlight on high-pressure measurements on the low-pressure cubic spinel phase is that the intensities of the Raman bands gradually decrease as pressure approach the phase-transition pressure. In most compounds, the majority of the Raman modes completely disappear before the transition is completed (there is a phase coexistence within a large pressure range). Usually, only the peak resulting from the A_{1g} mode can be observed continuously up to the completion of the transition. Note that most high-pressure Raman studies were performing using less hydrostatic pressure media than He or Ne. Therefore, the influence of non-hydrostatic stresses in the results cannot be neglected. Future studies carried out under quasi-hydrostatic conditions will probably clarify this issue.

2.6 Raman of Post-Spinel Phases

According to group-theory analysis, the tetragonal spinel structure observed in $ZnGa_2O_4$ and other spinels has the following set of Raman-active modes:

$$\Gamma = 2A_{1g} + 3B_{1g} + B_{2g} + 4E_g$$

With the correlation between the modes of the point groups of the cubic and tetragonal structure (remember that the tetragonal group is a subgroup of the cubic), the five modes of the cubic spinel transform into ten modes. In particular, the Raman inactive T_{1g} mode of the cubic spinel transforms into $A_{2g} + E_g$ modes. On the other hand, the Raman-inactive A_{2g} mode of cubic spinel is also inactive in the tetragonal structure. Raman experiments have been carried out in tetragonal $CoFe_2O_4$ [61] and only six modes have been observed. These modes clearly correspond to the splitting of the cubic modes and their pressure evolution is similar. In special, the high-frequency modes have pressure coefficients an order of magnitude larger than the lowest frequency mode, resembling the pressure behaviour of the Raman modes in cubic spinel. Unfortunately, high-pressure Raman studies performed in $ZnGa_2O_4$ did not reached the cubic-tetragonal transition pressure [53]. Extension of these studies could give a quite elegant confirmation of the transition. Raman modes are expected to gradually split as observed in similar (second order) transitions where the low- and high-pressure phases are related by group-subgroup relationships [62].

According to group-theory analysis, the three different orthorhombic post-spinel structures are associated with the following three sets of Raman-active modes:

$$(CaFe_2O_4\text{-type}) : \Gamma = 7A_{1g} + 5B_{1g} + 7B_{2g} + 5B_{3g}$$

$$(CaMn_2O_4\text{-type}) : \Gamma = 6A_{1g} + 7B_{1g} + 6B_{2g} + 5B_{3g}$$

$$(CaTi_2O_4\text{-type}) : \Gamma = 6A_{1g} + 4B_{1g} + 2B_{2g} + 6B_{3g}$$

The A_{1g} and E_g modes of the cubic structure transform to the A_{1g} modes of the orthorhombic structures and the T_{2g} modes of cubic spinel transform to the $B_{1g} + B_{2g} + B_{3g}$ modes. The orthorhombic structures have 18 or 24 Raman active modes. However, considerably much less modes have been observed in the experiments from these phases [53]. The reasons for it are not clear yet. One remarkable fact is that in the high-pressure phases the pressure coefficients of the observed mode frequencies are at most around $3\,cm^{-1}$/GPa, while in the spinel phase coefficients around $5\,cm^{-1}$/GPa are observed for the high-frequency modes. This behaviour is related to the compressibility decrease of the post-spinel phases (see 2.5). Calculations also predict a similar behaviour [53]. In particular, in post-spinel phases of $ZnAl_2O_4$ and $ZnGa_2O_4$ all Raman-active modes are located between 100 and $980\,cm^{-1}$ and pressure coefficients are smaller than $3.4\,cm^{-1}$/GPa [53]. Again, as in the low-pressure phase, Raman-active soft modes have not been observed in any of the post-spinel structures.

2.7 Elastic Constants

The elastic constants of magnesium aluminate spinel have been measured by an ultrasonic technique. The results are $C_{11} = 279$ GPa, $C_{44} = 153$ GPa, and $C_{12} = 153$ GPa [63]. In the case of Mg_2SiO_4 the obtained constants are $C_{11} = 327$ GPa, $C_{44} = 112$ GPa, and $C_{12} = 126$ GPa [64]. The set of elastic constants calculated fulfil the stability criteria for a cubic crystal: $(C_{11} - C_{12}) > 0$, $C_{11} > 0$, $C_{44} > 0$, and $(C_{11} + 2C_{12}) > 0$, pointing to their mechanical stability. Similar results have been obtained from Brillouin scattering and theoretical calculations [64]. These constants allow the calculation of the shear (G) and bulk modulus (B), as well as of the isotropic velocities for shear (v_S) and pressure (v_P) waves [64, 65]. In the case of Mg_2SiO_4 their values are B = 185 GPa, G = 119 GPa, $v_S = 5.77$ km/s, and $v_P = 9.79$ km/s. The Young modulus, E = 293 GPa, and the Poisson ratio, $\nu = 0.23$, of Mg_2SiO_4 can be also obtained. In particular, it is observed that the elastic constant anisotropy, the Zener ratio $A = 2C_{44}/(C_{11} - C_{12})$, is weak (A = 1.04). Additionally, the Zener ratio increases with increasing pressure, reaching 1.06 at pressures close to that of the Earth's transition zone, and subsequently increasing up to 1.09 at 30 GPa. Figure 2.8 shows the typical calculated behaviour for the elastic constants upon compression.

Elastic constants can be used to estimate the hardness and ductility of materials. In the case of spinels, it is usually found that B/G is smaller than 1.75 which indicates that spinel oxides are brittle materials. This conclusion is consistent with the fact that spinel has a brittleness similar to that of sapphire. Regarding the hardness of spinel, it is known to be 8 in the Mohs scale. Employing the correlation between the shear modulus and the Vickers hardness reported by Teter [66], since most oxospinels have a similar shear modulus, it is possible to conclude that most oxospinels should a similar hardness than $MgAlO_4$.

The pressure dependence of the sound velocities, single-crystal elastic constants, and shear and adiabatic bulk moduli of a natural gahnite ($ZnAl_2O_4$) spinel have

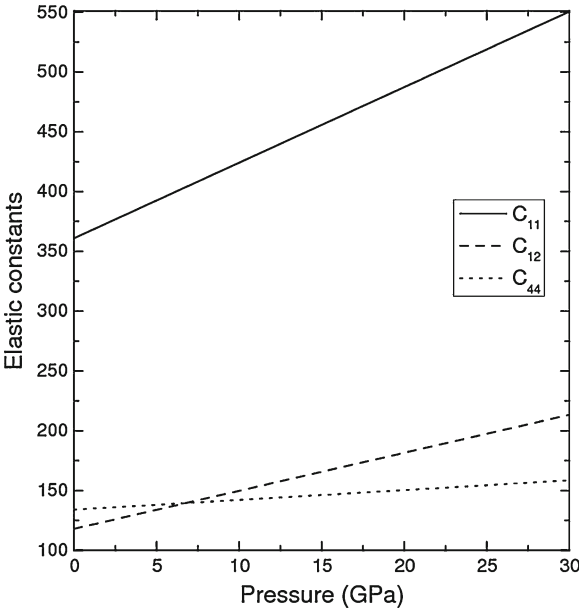

Fig. 2.8 Pressure evolution of the elastic constants of Mg_2SiO4

been determined to 9 GPa by gigahertz ultrasonic interferometry in a DAC [67]. The elastic constants of gahnite are $C_{11} = 290$ GPa, $C_{12} = 169$ GPa, and $C_{44} = 146$ GPa. The elastic constants C_{11} and C_{12} have similar pressure derivatives of 4.48 and 5.0, while the pressure derivative of C_{44} is 1.47. In contrast to $ZnAl_2O_4$ and the previous described spinels, magnetite exhibits C_{44} mode softening under pressure.

The elastic constants of $CoAl_2O_4$, a normal spinel, and $CoFe_2O_4$, an inverse spinel, have been determined by an ultrasonic method [68]. The measured values are: $C_{11} = 290.5$ GPa, $C_{12} = 170.3$ GPa, and $C_{44} = 138.6$ GPa for $CoAl_2O_4$, and $C_{11} = 257.1$GPa, $C_{12} = 150.0$ GPa, and $C_{44} = 85.3$ GPa for $CoFe_2O_4$. By comparing these constants with the above summarized data and previously published data of other spinel crystals, it can be concluded that the cation valence and cation distribution have little influence on the elastic properties of the spinel materials.

To conclude this section, we would like to mention that recently accurate measurement of elastic constants have been performed in natural chromian spinels (found in mantle xenoliths from Sveyagin, Russia) by high-frequency resonant ultrasound spectroscopy [69]. The elastic constants of this mineral are $C_{11} = 263.3$ GPa, $C_{12} = 138.0$ GPa, and $C_{44} = 123.71$ GPa, respectively. Comparison with elastic constants of $FeAl_2O_4$ and $FeCr_2O_4$ confirms that compositional difference have little influence in the elastic constants.

2.8 Miscellanous

Along this chapter we have described the structural, mechanical, and vibrational properties of spinel oxides and their evolution with pressure. There are many other physical properties that have been extensively studied, but they will not be discussed here. Here we will only briefly mention some interesting recent results that we consider should be highlighted. In this respect, we will describe a few important results on magnetism, which has been extensively studied in magnetic spinels like Fe_3O_4 and $CoFe_2O_4$. A nice review on the magnetic properties of spinel oxide solutions has been published by Harrison and Putnis [70]. In contrast to magnetism, optical and dielectric properties have been also studied, but little has been done under pressure yet. Consequently, these studies have been not included in this chapter for the sake of briefness. For the same reason, we will not make any comment on spinel nanomaterials and thin films.

Regarding the magnetic properties, probably the most studied compounds are spinel ferrites. They are broadly used in transformer or electromagnetic cores because they have a low coercivity. An interesting fact observed in spinel ferrites is that cation migration is related to changes in the magnetic ordering [71]. Regarding the effects of pressure in magnetization, the magnetic moment is continuously reduced by compression. More interesting is the fact that in Fe_3O_4 and $CoFe_2O_4$, pressure induces a quenching of magnetism, being the non-magnetic configuration recovered after pressure release [72]. Another interesting phenomenon observed in spinels is highly frustrated magnetism induced by compression [73]. In particular, the structure of spinels makes them unique as a testing ground for the physics of frustration. An interesting topic related to magnetic frustration is the formation of the spin-liquid states. To conclude, we will mention that magnetostriction is another interesting phenomenon observed in spinel ferrites which deserves to be studied under pressure.

2.9 Summary

In this chapter we have reviewed the effects of pressure in the structural, mechanical, and lattice-dynamics properties of spinel oxides. The behaviour of different compounds having the spinel structure is summarized and the occurrence of phase transitions described. Particular emphasis on the behaviour of archetypical compounds has been given and the behaviour of post-spinel structures discussed. Furthermore, the elastic constants are discussed. The interest on the high-pressure behaviour of oxospinels is constantly on the rise and therefore soon new results will be added soon to those here summarized. The recent structural studies on Co_3O_4 which shows that the cubic spinel structure persist up to 42 GPa in spite of the charge transfer induced at lower pressures [74] and the non-monotonic behavior recently observed for the charge gap in ZnV_2O_4 [75] are only two examples of the permanent progress

done on the study of physical properties of spinels under compression. We hope the results here reviewed will help to trigger new studies to further elucidate the effects of pressure on the properties of spinel and post-spinel compounds [62].

References

1. Finger LW, Hazen RM, Hofmeister AM (1986) High-pressure crystal-chemistry of spinel ($MgAl_2O_4$) and Magnetite (Fe_3O_4) - Comparisons with silicate spinels. Phys Chem Minerals 13:215–220
2. Shim SH, Duffy TS, Shen G (2001) The post-spinel transformation in Mg_2SiO_4 and its relation to the 660-km seismic discontinuity. Nature 411:571–574
3. Hazen RM, Downs T (eds) (2000) Reviews in mineralogy, vol 41. Mineralogical Society of America, Washington D.C. ISBN 0-939950-53-7
4. Errandonea D, Kumar RS, Manjón FJ, Ursaki VV, Rusu EV (2009) Post-spinel transformations and equation of state in $ZnGa_2O_4$: Determination at high pressure by in situ X-ray diffraction. Phys Rev B 79(6):024103
5. Shim SH, Duffy TS, Shen G (2001) Stability and structure of $MgSiO_3$ perovskite to 2300-kilometer depth in Earth's mantle. Science 293:2437–2440
6. Ono S, Kikegawa T, Ohishi Y (2006) The stability and compressibility of $MgAl_2O_4$ high-pressure polymorphs. Phys Chem Miner 33:200–206
7. Wang Z, Lazor P, Saxena SK, O'Neill HS (2002) High-pressure Raman spectroscopy of ferrite $MgFe_2O_4$. Mater Res Bull 37:1589–1602
8. Asbrink S, Waskowska A, Olsen JS, Gerwand L (1998) High-pressure phase of the cubic spinel $NiMn_2O_4$. Phys Rev B 57:4972–4974
9. Greenberg E, Rozenberg GK, Xu W, Arielly R, Pasternak MP, Melchior A, Garbarino G, Dubrovinsky LS (2009) On the compressibility of ferrite spinels: a high-pressure X-ray diffraction study of MFe_2O_4 (M = Mg, Co., Zn). High Press Res 29:764–779
10. Yong W, Botis S, Shieh SR, Shi W, Withers AC (2012) Pressure-induced phase transition study of magnesiochromite ($MgCr_2O_4$) by Raman spectroscopy and X-ray diffraction. Phys Earth & Planet Int 196–197:75–82
11. Wang Z, Lazor P, Saxena SK, Artioli G (2002) High-pressure Raman spectroscopic study of spinel ($ZnCr_2O_4$). J Solid Sate Chem 165:165–170
12. Fei YW, Frost DJ, Mao HK, Prewitt CT, Hausermann D (1999) In situ structure determination of the high-pressure phase of Fe_3O_4. Am Miner 84:203–206
13. Wittlinger J, Werner S, Schulz H (1997) On the amorphisation of $ZnCr_2S_4$ spinel under high pressure: X-ray diffraction studies. Phys Chem Miner 24:597–600
14. Santamaria-Perez D, Amboage E, Manjón FJ, Errandonea D, Muñoz A, Rodriguez-Hernandez P, Mujica A, Radescu S, Ursaki VV, Tiginyanu IM (2012) Crystal chemistry of $CdIn_2S_4$, $MgIn_2S_4$, and $MnIn_2S_4$ Thiospinels under High Pressure. J Phys Chem C 116:14078–14087
15. Amiel Y, Rozenberg GK, Nissim N, Milner A, Pasternak MP, Hanfland M, Taylor RD (2011) Intricate relationship between pressure-induced electronic and structural transformations in $FeCr_2S_4$. Phys Rev B 84(9):224114
16. Tang J, Matsumoto T, Furubashi T, Kosaka T, Nagata S, Kato Y (1998) Metal-insulator transition of $CuIr_2(S, Se)_4$ under high pressure. J Magn Magn Mat 177–181:1363–1364
17. Furubayashi T, Kosaka T, Tang J, Matsumoto T, Kato Y, Nagata S (1997) Pressure induced metal-insulator transition of selenospinel $CuIr_2Se_4$. J Phys Soc Japan 66:1563–1564
18. Wang A, Saxena SK, Zha CS (2002) In situ X-ray diffraction and Raman spectroscopy of pressure-induced phase transformation in spinel Zn_2TiO_4. Phys Rev B 66(6):024103 (6)
19. Birch F (1978) Finite strain isotherm and velocities for single-crystal and polycrystalline NaCl at high-pressures and 300° K. J Geophys Res 83:1257–1268

20. Levy D, Pavese A, Sani A, Pischedda V (2001) Structure and compressibility of synthetic $ZnAl_2O_4$ (gahnite) under high-pressure conditions, from synchrotron X-ray powder diffraction. Phys Chem Miner 28:612–618
21. Levy D, Diella V, Pavese A, Dipiaggi M, Sani A (2005) P-V equation of state, thermal expansion, and P-T stability of synthetic zincochromite ($ZnCr_2O_4$ spinel). Am Mineral 90:1157–1162
22. Levy D, Pavese A, Hanfland M (2000) Phase transition of synthetic zinc ferrite spinel ($ZnFe_2O_4$) at high pressure, from synchrotron X-ray powder diffraction. Phys Chem Miner 27:638–644
23. Asbrink S, Waskowska A, Gerward L, Olsen JS, Talik E (1999) High-pressure phase transition and properties of spinel $ZnMn_2O_4$. Phys Rev B 60:12651–12656
24. Fan D, Zhow W, Liu C, Liu Y, Jing X, Wan F, Liu J, Li X, Xie H (2008) Thermal equation of state of natural chromium spinel up to 26.8 GPa and 628 K. J Mater Sci 43:5546–5550
25. Nestola F, Boffa Ballaran T, Dal Negro A (2010) New accurate compression data for gamma-Fe_2SiO_4. Phys Earth Planet Interiors 183:421–425
26. Hofmeister AM, Wopenka B, Locock AJ (2004) Spectroscopy and structure of hibonite, grossite, and $CaAl_2O_4$: Implications for astronomical environments. Geochim Cosmochim Acta 68:4485–4503
27. Wittlinger J, Werner S, Schulz H (1998) Pressure-induced order-disorder phase transition of spinel single crystals. Acta Cryst B 54:714–721
28. Hazen RM, Yang H (1999) Effects of cation substitution and order-disorder on P-V-T equations of state of cubic spinels. Am Mineral 84:1956–1960
29. Waskowska A, Gerward L, Olsen JS, Talik E (2001) $CuMn_2O_4$: properties and the high-pressure induced Jahn-Teller phase transition. J. Phys.: Condens. Matter 13:2549–2562
30. Waskowska A, Gerward L, Olsen JS, Feliz M, Llusar R, Gracia L, Marques M, Recio JM (2004) High-pressure behaviour of selenium-based spinels and related structures - an experimental and theoretical study. J. Phys.: Condens. Matter 16:53–63
31. Halevy I, Dragoi D, Üstündag E, Yue AF, Arredondo EH, Hu J, Somayazulu M (2002) The effect of pressure on the structure of $NiAl_2O_4$. J Phys Condens Matter 14:10511–10516
32. Bouhemadou A, Khenata R (2006) Pseudo-potential calculations of structural and elastic properties of spinel oxides ZnX_2O_4 (X = Al, Ga, In) under pressure effect. Phys Lett A 360:339–343
33. Nestola F, Balic-Zunic T, Koch. Müller M, Secco L, Princivalle F, Parisi F, Dal Negro A, (2011) High-pressure crystal structure investigation of synthetic Fe_2SiO_4 spinel. Miner Mag 75:2649–2655
34. Nestola F, Ballaran TB, Balic-Zunic T, Princivalle F, Secco L (2007) Comparative compressibility and structural behavior of spinel $MgAl_2O_4$ at high pressures: The independency on the degree of cation order. Am Miner 92:1838–1843
35. Recio JM, Franco R, Martin Pendas A, Blanco MA, Pueyro L, Pandey R (2001) Theoretical explanation of the uniform compressibility behavior observed in oxide spinels. Phys Rev B 63(7):184101
36. Errandonea D, Manjón FJ (2008) Pressure effects on the structural and electronic properties of ABX_4 scintillating crystals. Prog Mat Sci 53:711–773
37. Chen M, Shu J, Xie X, Mao HK (2003) Natural $CaTi_2O_4$-structured $FeCr_2O_4$ polymorph in the Suizhou meteorite and its significance in mantle mineralogy. Geochim Cosmochim Acta 67:3937–3942
38. Arevalo-Lopez AM, Dos Santos-Garcia AJ, Castillo-Martinez E, Duran A, Alario-Franco MA (2010) Spinel to $CaFe_2O_4$ Transformation: Mechanism and Properties of beta-$CdCr_2O_4$. Inorg. Chem. 49:2827–2833
39. Malavasi L, Tealdi C, Flor G, Amboage M (2005) High-pressure stability of the tetragonal spinel $MgMn_2O_4$: role of inversion. Phys Rev B 71(9):174102
40. Giesber H, Pennington WT, Kolis JW (2001) Redetermination of $CaMn_2O_4$. Acta Cryst C 57:329–330
41. Yamanaka T, Uchida A, Nakamoto Y (2008) Structural transition of post-spinel phases $CaMn_2O_4$, $CaFe_2O_4$, and $CaTi_2O_4$ under high pressures up to 80 GPa. Am Mineral 93:1874–1881

42. Merlini M, Hanfland M, Gemmi M, Huotari S, Simonelli L, Strobel P (2010) Fe^{3+} spin transition in $CaFe_2O_4$ at high pressure. Am Mineral 95:200–203
43. De Wijs GA, Fang CM, Kresse G, de With G (2002) First-principles calculation of the phonon spectrum of $MgAl_2O_4$ spinel. Phys Rev B 65(5):094305
44. White WB, de Angelis BA (1967) Interpretation of the vibrational spectra of spinels. Spectrochim Acta A 23:985–995
45. Chandramohan P, Srinivasan MP, Velmurugan S, Narasimhan SV (2011) Cation distribution and particle size effect on Raman spectrum of $CoFe_2O_4$. J Solid State Chem 184:89–96
46. O'Horo MP, Frisillo AL, White WB (1973) Lattice-vibrations of $MgAlO_4$ spinel. J Phys Chem Solids 34:23–28
47. Malezieux JM, Piriou B (1988) Relationship between chemical composition and vibrational behaviour in synthetic and natural spinels investigated by Raman microspectroscopy. Bull Miner 111:649–669
48. Chopelas A, Hofmeister AM (1991) Vibrational spectroscopy of aluminate spinels at 1 atm and of $MgAlO_4$ to over 200 kbar. Phys Chem Miner 18:279–293
49. Cynn H, Sharma SJ, Cooney TF, Nicol M (1992) High-temperature Raman investigation of order-disorder behaviour in the $MgAlO_4$ spinel. Phys Rev B 45:500–502
50. Verble JL (1974) Temperature-dependent light-scattering of verwey transition and electronic disorder in magnetite. Phys Rev B 9:5236–5248
51. Wang Z, O'Neil HSC, Lazor P, Saxena SK (2002) High-pressure Raman spectroscopic study of spinel $MgCr_2O_4$. J Phys Chem Solids 63:2057–2061
52. Malavasi L, Galinetto P, Mozzati MC, Azzoni CB, Flor G (2002) Raman spectroscopy of AMn_2O_4 (A = Mn, Mg and Zn) spinels. Phys Chem Chem Phys 4:3876–3880
53. Lopez-Moreno S, Rodriguez-Hernandez P, Muñoz A, Romero AH, Manjon FJ, Errandonea D, Rusu E, Ursaki VV (2011) Lattice dynamics of $ZnAl_2O_4$ and $ZnGa_2O_4$ under high pressure. Ann Phys 523:157–167
54. Kant C, Deisenhofer J, Rudol T, Mayr F, Schrettle F, Loidl A, Cnezdilov V, Wulferding D, Lemmens P, Tsurkan V (2009) Optical phonons, spin correlations, and spin-phonon coupling in the frustrated pyrochlore magnets $CdCr_2O_4$ and $ZnCr_2O_4$. Phys Rev B 80(10):214417
55. Ospitali F, Sabetta T, Tullini F, Nannetti MC, Di Lonardo G (2005) The role of Raman microspectroscopy in the study of black gloss coatings on Roman pottery. J Raman Spectrosc 36:18–23
56. McCarty KF, Boehme DR (1989) A Raman-study of the systems $Fe_{3-x}Cr_xO_4$ and $Fe_{2-x}Cr_xO_3$. J Solid State Chem 79:19–27
57. Shebanova ON, Lazor P (2003) Raman spectroscopic study of magnetite ($FeFe_2O_4$): a new assignment for the vibrational spectrum. J Solid State Chem 31:424–430
58. Taken from the RRUFF database, file R070719
59. Gupta HC, Sinha MM, Balram B, Tripathi BB (1993) A study of the interatomic interaction in oxide spienl $MnCrO_4$. Physica B 192:343–344
60. Thibaudeau P, Gervais F (2002) Ab initio investigation of phonon modes in the $MgAl_2O_4$ spinel. J Phys Condens Matter 14:3543–3552
61. Wang Z, Downs RT, Pischedda V, Shetty R, Saxena SK, Zha CS, Zhao YS, Schiefer D, Waskowska A (2003) High-pressure X-ray diffraction and Raman spectroscopic studies of the tetragonal spinel $CoFe_2O_4$. Phys Rev B 68(6):094101
62. Errandonea D, Martinez-Garcia D, Segura A, Haines J, Machado-Charry E, Canadell E, Chervin JC, Chevy A (2008) High-pressure electronic structure and phase transitions in monoclinic InSe: X-ray diffraction, Raman spectroscopy, and density functional theory. Phys Rev B 77(9):045208
63. Lewis MF (1966) Elastic constants of magnesium aluminate spinel. J Acoust Soc Am 40:728–729
64. Kiefer B, Stixrude L, Wentzcovitch R (1997) Calculated elastic constants and anisotropy of Mg_2SiO_4 spinel at high pressure. Geophys Res Lett 24:2841–2844
65. Errandonea D, Ferrer-Roca C, Martinez-Garcia D, Segura A, Gomis O, Muñoz A, Rodriguez-Hernandez P, Lopez-Solano J, Alconchel S, Sapiña F (2010) High-pressure X-ray diffraction

and ab initio study of Ni_2Mo_3N, Pd_2Mo_3N, Pt_2Mo_3N, Co_3Mo_3N, and Fe_3Mo_3 N: Two families of ultra-incompressible bimetallic interstitial nitrides. Phys Rev B 82(8):174105
66. Teter DM (1998) Computational alchemy: The search for new superhard materials. MRS Bull 23:22–27
67. Reichmann HJ, Jacobsen SD (2007) Sound velocities and elastic constants of $ZnAl_2O_4$ spinel and implications for spinel-elasticity systematics. Am Miner 91:1049–1054
68. Li Z, Fischer ES, Liu JZ, Nevitt MV (1991) Single-crystal elastic constants of Co–Al and Co–Fe spinels. J Mat Sci 10:2621–2624
69. Harada Y, Yoneda A, Yamamoto J, Yamazaki D, Yoshino T, Okuchi T, Watanabe T (2011) Report of the Japan Geoscience Union Meeting
70. Harrison RJ, Putnis A (1999) Determination of the mechanism of cation ordering in magnesioferrite ($MgFe_2O_4$) from the time- and temperature-dependence of magnetic susceptibility. Phys Chem Miner 26:322–332
71. Yu T, Shen ZX, Shi Y, Ding J (2002) Cation migration and magnetic ordering in spinel $CoFe_2O_4$ powder: micro-Raman scattering study. J Phys Condens Matter 14:L613–L618
72. Subías G, Cuartero V, Garcia J, Blasco J, Mathon O, Pascarelli S (2009) Pressure-induced magnetic transition in Fe_3O_4 and $CoFe_2O_4$ spinels. J Phys Conf Series 190(4):012089 (4)
73. Takagi H, Niitaka S (2011) Introduction to frustrated magnetism, Springer series in solid state sciences, Part 3, vol 164. Springer-Verlag Berlin Heidelberg, pp 155–175. ISBN: 978-3-642-10588-3
74. Bai L, Pravica M, Zhao Y, Park C, Meng Y, Sinogeikin S, Shen G (2012) Charge transfer in spinel Co_3O_4 at high pressures. J Phys Condens Matter 24(7):435401
75. Kuntshcer C, Rabia K, Forthaus MK, Abd-Elmeguid MM, Ravadulla F, Kato Y, Batista CD (2012) Nonmonotonic evolution of the charge gap in ZnV_2O_4 under pressure. Phys Rev B 86(5):020405

Chapter 3
AB_2S_4 and AB_2Se_4 Compounds at High Pressures

David Santamaria-Perez and Javier Ruiz-Fuertes

Abstract Thiospinels and selenospinels are compounds with general formula $A^{II}B_2^{III}X_4^{VI}$, where A and B are cations and X is sulfur and selenium, respectively. Within the huge compositional range of these families, there exist materials with different interesting physical properties, such as nonlinear optics, high concentration defects in semiconductors or metal-insulator transitions. In this chapter, we gather together previously reported studies addressing the effect of high pressure on the crystal and electronic structures of these compounds. Special emphasis has been placed on the crystal chemistry of indium thiospinels under pressure and the evolution of their structural, electronic, and optical properties. The observed pressure-induced phase transition to a post-spinel structure in AIn_2S_4 compounds is discussed in detail. These results could be particularly relevant for Geophysics since thiospinels can be considered as structural analogs of $MgAl_2O_4$, a common constituent of the Earth's upper mantle.

Keywords Spinels · Thiospinels · Selenospinels · X-ray diffraction · Raman spectroscopy · Optical absorption

3.1 Introduction

Many compounds of the type AB_2X_4, in which A, B and X are divalent metal, trivalent metal and S or Se atoms, respectively, by and large adopt the cubic spinel structure at ambient conditions. This structure is described within the cubic *Fd*-3*m*

D. Santamaria-Perez (✉)
Universidad Complutense de Madrid, Madrid, Spain
e-mail: dsantamaria@quim.ucm.es

J. Ruiz-Fuertes
Harvard University, Cambridge, USA
e-mail: jarviz@physics.harvard.edu

F. J. Manjón et al. (eds.), *Pressure-Induced Phase Transitions in AB_2X_4 Chalcogenide Compounds*, Springer Series in Materials Science 189,
DOI: 10.1007/978-3-642-40367-5_3,

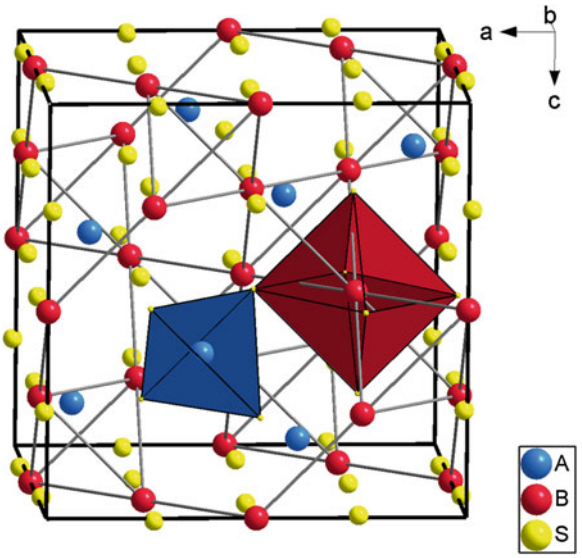

Fig. 3.1 View of the atomic arrangement in normal thiospinels ($x = 1$). The structure consists of an approximately *fcc* packing of S atoms (*yellow spheres*), with the A divalent (*blue*) and B trivalent (*red*) metal atoms occupying tetrahedral and octahedral sites, respectively. Note that the metallic subarray (AB_2) adopts the same topology that the Laves phase $MgCu_2$

space group with a lattice parameter between 10 and 11 Å and eight formula units per cell ($Z = 8$). It consists of an approximately cubic closed packed arrangement of the sulphur/selenium atoms with the A and B metal atoms occupying 1 tetrahedral site (*T*) and 2 octahedral sites (O) per formula unit (see Fig. 3.1). In real spinels, the ordering of the metal atoms in these interstitial sites range from the 'normal' distribution of cations, where the A cation occupies the tetrahedral site and the two B cations occupy the octahedral sites, to the 'inverse' cation distribution with one of the B cations occupying the tetrahedral site and the remaining A and B cations occupying the octahedral sites. Consequently, the spinel structure would be better described with the formula $A_xB_{1-x}(A_{1-x}B_{1+x})X_4$ in terms of the normality index (x) : $x = 1$ would be considered as a normal spinel and $x = 0$ as a complete inverted spinel. It is also important to highlight that the cubic spinel structure has only two structural variables: the unit-cell parameter a and the anion internal positional parameter u (a value of $u = 0.25$ would define an ideal close-packed *fcc* structure of S or Se atoms if the origin of the cell is on an inversion center). A more detailed description of this structure type can be found in the previous chapter devoted to the oxide spinels.

Representatives of the sulfide spinel (or thiospinel) family show a wide range of chemical compositions. To our knowledge, at least 48 different ternary sulphides belong to the spinel family, which come from the combination of the following A^{II} and B^{III} metal atoms: A = Cd, Co, Cr, Cu, Fe, Hg, Mg, Mn, Ni, Rh, Zn, and B = Al,

Co, Cr, Dy, Er, Fe, Ho, In, Ir, Lu, Ni, Rh, Sc, Ti, Tm, V, Y, Yb, Zr. Some of these metal atoms also combine to give almost a score of selenium-based spinels.

Thiospinels form an interesting group of materials for optoelectronic applications given their nonlinear optical properties [1]. Their partial degree of cation inversion makes them defect semiconductors with high concentration of antisite defects [2]. The unusual physical properties of thiospinels have also attracted current interest because they present a new type of metal-insulator transition [3, 4]. Furthermore, indium thiospinels have been recently proposed as ideal materials for photovoltaic cells operating with an intermediate band [5]. As regards selenospinels, it is interesting to note that the ACr_2Se_4 subgroup combines both, ferromagnetic and semiconducting properties [6].

On the other hand, the large variety of compositions make spinel compounds an excellent testing ground for investigating the influence of the external thermodynamic variables, pressure and temperature, on their physical properties. Thus, for instance, the concentration of antisite defects can be tuned by means of pressure application, making thiospinels useful materials for defect engineering applications [7]. A pressure-induced superconductor-insulator transition was also recently found [8]. What is more, the study of sulphur- and selenium-based spinels, particularly their pressure-induced phase transitions, could contribute to shed some light over post-spinel structures in order to understand the systematics of pressure-induced phase transitions in AB_2X_4 compounds. Besides, it would contribute to the understanding of the behavior of oxide spinels at much higher pressures since it is a well-known trend that heavier elements (S or Se atoms), going down in the same column of the Periodic Table, crystallize at low pressure in high-pressure structures of their parent lighter elements (O atoms). The obtained results would be particularly relevant for Geophysics, since $MgAl_2O_4$ is a common constituent of the shallow upper mantle [9].

Very few experiments under pressure have dealt with thiospinels or selenospinels. This chapter will present our recent results and the data available in the literature, showing the behaviour of these materials under extreme pressure conditions. Section 3.2 is devoted to review the current state of knowledge of this particular research field. Particular emphasis is placed on the indium thiospinel subgroup AIn_2S_4 (A = Cd, Mg, Mn), which is treated separately. Sections 3.3, 3.4, and 3.5 present the most recent results of angle-dispersive X-ray diffraction, Raman, and optical absorption measurements of the AIn_2S_4 (A = Cd, Mg, Mn) family under high pressure at room temperature. The effects of pressure on the phase stabilities and transformation pathways of spinel-type semiconductors, as well as on their vibrational and electronic properties are discussed. Finally, we will present in Sect. 3.6 a general overview which hopefully will contribute to achieve a better understanding of the behaviour of thiospinels and selenospinels under compression.

3.2 High-Pressure Studies in Sulfide and Selenide Spinels

3.2.1 High-Pressure Studies on Thiospinels

The structural and electronic properties at room pressure of compounds of the thiospinel family have been studied for many years. Particular interest has been paid to the effect of the chemical modification in interesting properties such as ferromagnetism [10] and ferrimagnetism [11, 12], charge ordering [3], colossal magnetoresistance [13] or superconductivity [14, 15]. However, high-pressure studies of these properties are rather scarce.

To our knowledge, Albers and Rooymans were the firsts who observed a high-pressure polymorph of a substance, having a thiospinel lattice at atmospheric pressure [16]. They reported the preparation of a hexagonal defect NiAs-type structure in $FeCr_2S_4$ after quenching from 2–4 GPa pressure and 600–1000 °C temperature (see Fig. 3.2). Since the NiAs structure has octahedral coordination for both metal atoms and is denser than the spinel structure, other chromium thiospinel compounds were expected to undergo a phase transition to the NiAs structure at high pressures. This fact was later confirmed by Bouchard and coworkers who found that $MnCr_2S_4$ and $CoCr_2S_4$ transform at 6.5 GPa pressure into defect NiAs-related materials when heated at 1000 °C and then quenched [17, 18]. These compounds could be indexed on the basis of a monoclinic *I*2/*m* distortion of the defect NiAs unit cell.

More recently, several authors have studied the high-pressure behavior of thiospinels in the low (ambient) temperature region. In this context, Wittlinger et al. evidenced an amorphisation of $ZnCr_2S_4$ spinel above 8 GPa [19], while Vaqueiro et al. observed a phase transition in $CoCr_2S_4$ above 6.8 GPa to an unidentified cubic structure exhibiting a considerable disorder [20]. These authors also reported *in situ* high-pressure high-temperature neutron diffraction measurements on $CoCr_2S_4$ that showed the transformation to the defect NiAs-type phase. However, quenching of the

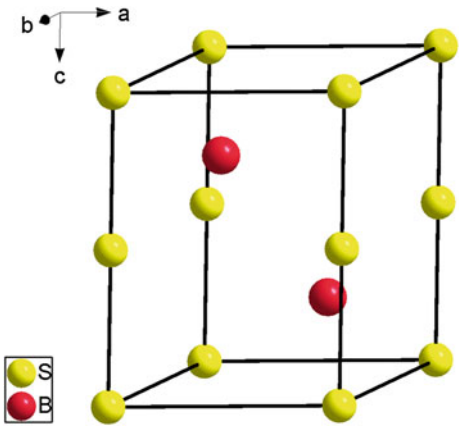

Fig. 3.2 Defect NiAs-type structure obtained in $FeCr_2S_4$ after quenching from high pressures (2–4 GPa) and high temperatures (600–1000 °C). In this structural type, the S atoms adopt an *hcp* configuration and all cations (named B, *red spheres*) are octahedrally coordinated. 1/4 of the B positions would correspond to a vacant site

hexagonal HP-HT phase resulted in a transition to a monoclinic Cr_3S_4-type phase (in good agreement with Bouchard's data), due to the ordering of the metal vacancies in every second layer [20]. Similarly to Vaqueiro et al., Nakamoto et al. [21] and Garg et al. [22] observed a phase transition in $CuCrZrS_4$ and $CuIr_2S_4$ at room temperature above 15 and 12 GPa, respectively, to unidentified structures.

Hence, an open question still to be solved is the identification of the post-spinel high-pressure structures in thiospinels, especially at room temperature. There are many possibilities for post-spinel phases since as pressure increases the anion is more compressible than the cation [23] so S can be squeezed to the size of O and consequently post-spinel structures found in oxide spinels, which include the tetragonal spinel (a tetragonal distortion of the cubic spinel), the $LiFeO_2$, $NaFeO_2$, $LiTiO_2$, $CaFe_2O_4$, $CaTi_2O_4$, or $CaMn_2O_4$ structures (see Chap. 2 on oxospinels), could be also possible [24–27]. In connection with this, Ursaki and coworkers observed significant changes in the phonon spectrum of the thiospinel $ZnAl_2S_4$ at the critical pressure of 23 GPa, which were attributed to a reversible phase transition to a denser HP phase, having a similar structure to that of calcium ferrite [28].

It is noteworthy the recently found pressure-induced superconductor-insulator transition in the thiospinel $CuRh_2S_4$ [8]. Resistivity measurements show that, initially, the superconducting transition temperature T_C increases with pressure up to 4 GPa ($T_C = 6.4$ K). With further compression, superconductivity disappears drastically at approximately 5 GPa, becoming an insulator [8].

Phase transitions in indium thiospinels at room temperature were also evidenced between 7 and 12 GPa, but the nature of the high-pressure phase was not well determined and either the presence of a disordered rocksalt structure or a defect $LiTiO_2$-type structure were proposed [29–31]. In this regard, a very recent high-pressure structural study on AIn_2S_4 thiospinels (A = Cd, Mg, Mn) has confirmed that compression induces a phase transition to a defect $LiTiO_2$-type structure which can also be described in the same cubic *Fd*-3*m* space group that the spinel [32]. The systematic study of the structural, electronic, and optical properties of indium thiospinels deserves special attention and will be treated in detail in Sects. 3.3, 3.4 and 3.5, respectively.

3.2.2 High-Pressure Studies on Selenospinels

Only two studies about pressure-induced phase transitions in selenium-based spinels are reported to our knowledge. Banus and Lavine observed that the selenospinel $CdCr_2Se_4$ transformed under high-pressure and temperature to a new monoclinic symmetry related to the defect NiAs-type structure [33]. This is consistent with the spinel-to-monoclinic transformations found for the thiospinels (Co, Mn)Cr_2S_4 [17]. This structural change was accompanied by a change from semiconducting to metallic behavior. The structural changes in cubic spinels $CdCr_{2-x}Ga_xSe_4$ ($x = 0.06$ and 0.12) were also studied by means of single-crystal X-ray diffraction at low temperatures [34]. It was found that at high pressure the cubic spinel transforms to a tetragonal spinel at about 10 GPa.

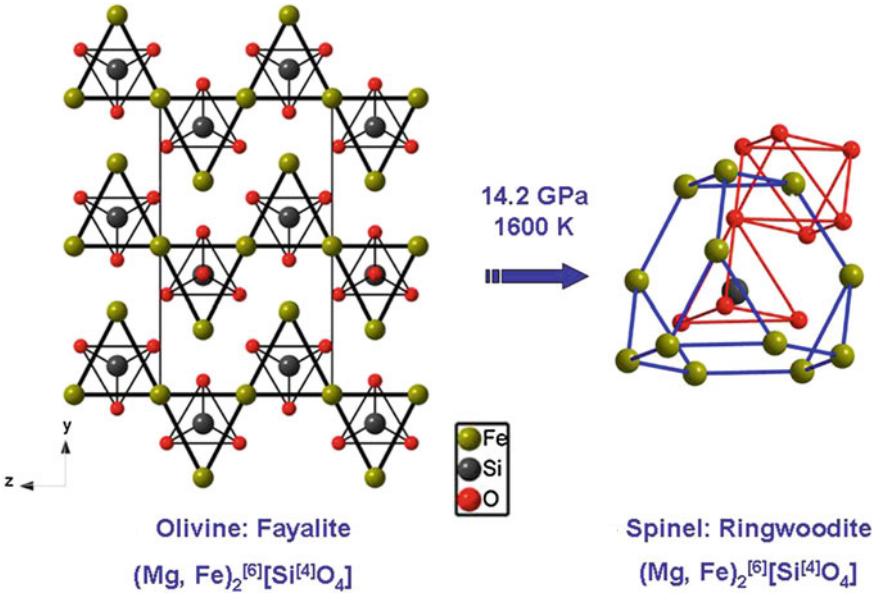

Fig. 3.3 Olivine-spinel phase transition in $(Mg,Fe)_2SiO_4$ occurring in the Earth's mantle at high-temperature high-pressure conditions. A similar transition was observed in the selenium compound Mn_2SiSe_2 at high-pressure and room temperature

Many oxides with the olivine structure were known to transform to the spinel structure at high pressure. In particular, in the boundary between the upper and the intermediate Earth mantle the olivine-type $(Mg, Fe)_2SiO_4$ fayalite mineral converts into the spinel-structured $(Mg, Fe)_2SiO_4$ ringwoodite (see Fig. 3.3). However, it was not demonstrated for sulfide or selenide compounds until a work of Grzechnik et al., who reported the pressure-induced olivine-spinel phase transition on Mn_2SiSe_4 at 2–4 GPa at room temperature [35].

Another interesting point comes up when analyzing the compressibility of the different chalcogenide spinels. Finger et al. found empirically that the bulk moduli of normal oxide spinels at zero pressure are around 200 GPa [36]. This result was confirmed by many experiments [37–39]. This observation has been justified theoretically on the basis of the substructure of oxygen anions which form a nearly close-packed *fcc* structure [40, 41]. These works suggested that the compressibility of spinels is mainly governed by the anion sublattice. Furthermore, it has been recently stated that the bulk modulus of selenide spinels is 90–100 GPa, thus evidencing that the compressibility of selenide spinels is governed by the selenium substructure [34, 42–44]. From these empirical observations, it could be inferred that, on the basis of the larger size of S with respect to O and the smaller size of S with respect to Se, sulfide spinels have similar compressibilities with bulk moduli around 125 GPa. However, such hypothesis has not been confirmed experimentally as we will see in Sect. 3.3.

3.3 High-Pressure Structural Study of Indium Thiospinels

Previously, we have mentioned that the crystal chemistry of the indium thiospinels under pressure and the evolution of their structural, electronic, and optical properties merit special attention. The reason is that they have been the best studied chalcogenide spinels for several A^{II} cations and with different experimental techniques. Consequently, the information obtained from them could be of guide for high-pressure studies of other less well-studied spinels. In particular, this section will deal particularly with the dependence of the structural lattice on the nature of the metal divalent *A* atom at high pressures.

3.3.1 Low-Pressure Spinel Phase

AIn_2S_4 (A = Cd, Mg, Mn) compounds adopt a cubic spinel structure at ambient conditions [45, 46]. In a recent study, high-pressure powder XRD measurements of $CdIn_2S_4$, $MgIn_2S_4$ and $MnIn_2S_4$ were carried out up to 19, 20 and 41 GPa, respectively, using MoK_α ($\lambda = 0.7107$ Å) and synchrotron ($\lambda = 0.40896$ Å) radiation and two different quasi-hydrostatic pressure media: a mixture 4:1 methanol–ethanol and nitrogen [32]. At high-pressure, the X-ray diffraction patterns can be indexed using the initial cubic spinel structure up to 9.5, 8.3 and 6.8 GPa for $CdIn_2S_4$, $MgIn_2S_4$ and $MnIn_2S_4$, respectively, in good agreement with results from other characterization techniques [29–31] as we will see in the following sections. By way of illustration, the XRD patterns of $MnIn_2S_4$ at different pressures are plotted in Fig. 3.4. At the above-mentioned critical pressures, a structural phase transition occurs as we will discuss below. The Rietveld refinements of the synchrotron data allowed us to obtain the evolution of the lattice parameters and atomic coordinates of the three thiospinels and the normality index (x) of those of Mg and Mn.

Thus, from the refined lattice constants, volumes of the cubic unit-cell can be derived (see Fig. 3.5). The pressure-volume dependence was described analytically by a third-order Birch–Murnaghan equation of state (EOS) [47, 48].

$$P = \frac{3}{2}B_0\left(\left(\frac{V}{V_0}\right)^{-\frac{7}{3}} - \left(\frac{V}{V_0}\right)^{-\frac{5}{3}}\right)\left[1 + \frac{3}{4}\left(B'_0 - 4\right)\left(\left(\frac{V}{V_0}\right)^{-\frac{2}{3}} - 1\right)\right]$$

obtaining the zero-pressure volumes (V_0), the bulk moduli (B_0) and their pressure derivatives (B'_0). These characteristic parameters are collected in Table. 3.1.

The values of the bulk modulus of this family of compounds are confined within a very narrow range ($B_0 \sim 78$ GPa and $B'_0 \sim 3$). Essentially, the explanation of these similar high compressibilities is based on the fact that S atoms that form the *fcc* net occupy most of the crystal volume. Additionally, 16. In atoms per unit cell are located either in T or O sites. Therefore, the overall compressibility would be mainly determined by the In_2S_4 sublattice. Total-energy calculations present an overall good

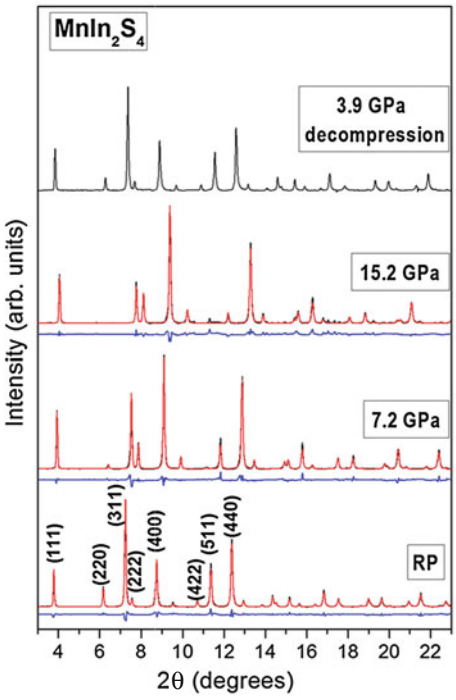

Fig. 3.4 XRD patterns of $MnIn_2S_4$ at four different pressures, three upstroke and one downstroke. Bragg peak intensities clearly change in the pressure-induced spinel—defect $LiTiO_2$-type phase transition. Structural transformations are reversible. The observed, calculated and difference XRD profiles are represented as *black*, *red* and *blue solid lines*, respectively

agreement with experimentally observed lattice parameters. Computational details and theoretical results will be given in Chap. 4 of this book.

Curiously, the experimental results indicate that thiospinels have a slightly higher compressibility than selenospinels, although it is important to remark that indium thiospinels have significantly smaller B'_0 values. As already commented, one would expect bulk moduli for thiospinels in between those of oxospinels (~200 GPa) and selenospinels (~90 GPa). This phenomenon seems to be intimately related to the fact that the compressibility of spinels is mainly governed by the tetrahedral compressibility (see Fig. 3.6) which in turn is related to the T–X bond distances (X = S, Se). Thus, the experimentally observed unit-cell volumes of the three thiospinels considered here are similar or even larger than those of selenospinels. The experimental value of V_0 for $CdCr_2Se_4$ is, for instance, 1240 $Å^3$ [43], whereas $V_0 = 1274$ $Å^3$ in $CdIn_2S_4$. This means that the tetrahedral volumes and the T–X distances are comparable. Nevertheless, in some cases, the bulk moduli of thiospinels contradict the empirical B_0–V inverse law. For the sake of example: The selenospinel $CdCr_2Se_4$ ($V_0 = 1240$ $Å^3$) has a bulk modulus of 101 GPa ($B'_0 = 5.2$) [43], which is slightly larger than that of the thiospinel $ZnCr_2S_4$ ($V_0 = 992.1$ $Å^3$, $B_0 = 97$ GPa and B'_0 fixed to 4) [49]. In conclusion, more experimental and theoretical work is needed to understand the compressibility behavior of both sulfide and selenide spinels.

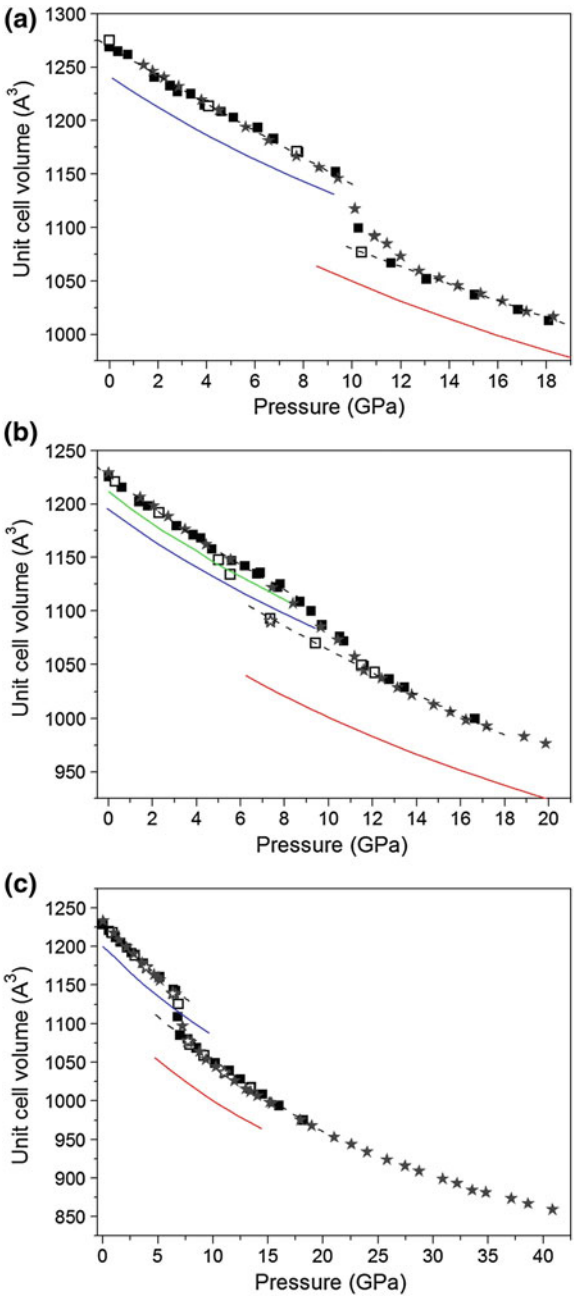

Fig. 3.5 Unit-cell volumes of **a** $CdIn_2S_4$, **b** $MgIn_2S_4$ and **c** $MnIn_2S_4$ as a function of pressure. Results from experiments using an in-home Xcalibur diffractometer ($\lambda = 0.7107$ Å) and synchrotron radiation ($\lambda = 0.409$ Å) are represented by *squares* and *stars*, respectively. *Empty* symbols correspond to decompression data points. Calculated curves for both, the normal spinel and the defect-$LiTiO_2$-type phases are depicted as *blue* and *red lines*. Calculated data for $MgIn_2S_4$ using the space group *Imma* to describe an inverse spinel structure are depicted as a *green line*

Table 3.1 Unit cell volumes at zero pressure (V_0), bulk moduli (B_0) and first derivatives with pressure (B'_0) of both, the low-pressure (LP) spinel- and the high-pressure (HP) defect-$LiTiO_2$-type postspinel phases of the AIn_2S_4 compounds. Experimental and LDA theoretical results are included

	EOS	V_0(Å^3)	B_0(GPa)	B'_0
$CdIn_2S_4$	LP-experimental	1274(2)	78(4)	3.1(8)
	LP-theoretical ($x = 0$)	1241.45(2)	79.8(2)	4.65(6)
	HP-experimental	1206(6)	74(4)	4, fixed
	HP-theoretical	1174.6(8)	71.6(4)	4, fixed
$MgIn_2S_4$	LP-experimental	1227(1)	76(3)	2.8(7)
	LP-theoretical ($x = 1$)	1194.8(1)	78.7(2)	4.16(4)
	HP-experimental	1222(6)	55(2)	4, fixed
	HP-theoretical	1124.8(6)	68.8(4)	4, fixed
$MnIn_2S_4$	LP-experimental	1230(1)	78(4)	3.2(1)
	LP-theoretical ($x = 0$)	1200.7(5)	80(2)	3.9(3)
	HP-experimental	1187(2)	62(1)	4, fixed
	HP-theoretical	1121.0(4)	70.1(3)	4, fixed

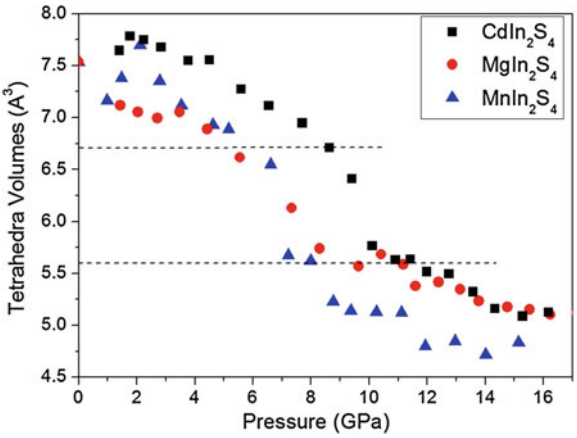

Fig. 3.6 Evolution of the tetrahedral volumes in $CdIn_2S_4$ (*black squares*), $MgIn_2S_4$ (*red circles*) and $MnIn_2S_4$ (*blue triangles*). The onset of the structural phase transition coincides with the abrupt decrease in the tetrahedral volumes. Interestingly, the transition always occurs when the tetrahedral volumes reach a value of *ca*. 6.7 Å^3

Another interesting aspect of the compression of indium thiospinels is that the internal positional parameter u moves towards a more symmetric distribution of anions in the structure ($u = 0.25$). This fact has been observed for many other representatives of the spinel group and entails the disappearance of compression along the (111) three fold axis of the cubic cell, the octahedra and tetrahedra becoming nearly symmetric [49].

It is also noteworthy that the inversion parameters of indium thiospinels estimated from the Rietveld refinements do not change much up to the proximity of the transition pressure, where the normality index increases slightly. Our pressure dependence of the normality index ($x_{Mg} = 0.27$ and $x_{Mn} = 0.75$ at ambient pressure) is in good agreement with the results obtained from Raman scattering data (see Sect. 3.3.2) and suggest that the distribution of cations in these spinels could be slightly modified by applying pressure, in a similar way as changing the synthesis temperature [50].

3.3.2 Phase Transition and the High-Pressure Post-Spinel Phase

Above 9.5, 8.3 and 6.8 GPa, $CdIn_2S_4$, $MgIn_2S_4$ and $MnIn_2S_4$ spinels transform into a post-spinel phase, with a volume collapse of 5.7, 3.0 and 4.5 %, respectively [32]. The completion of the phase transition is almost instantaneous in the case of the Mn compound whereas for Cd and Mg spinels the transition takes place gradually. These results seem to point out that the size of the metal atoms occupying the *T* positions in spinel is correlated with the transition pressure and the range of the coexistence of phases; i.e. a larger atomic radius (Mn < Mg < Cd ~ In) would imply larger pressures for the phase transition's onset and larger ranges of coexistence of phases. This is also directly related with the fact that the phase transition always occurs when the tetrahedral volumes reach a value of circa 6.7 $Å^3$ (see Fig. 3.6). Smaller volumes seem to be not suitable to accommodate the different cations, independently of their size and nature.

The high-pressure phase adopts a defect $LiTiO_2$-type structure in the three compounds studied. This structure can be described in the same cubic space group, *Fd-3m*, as the initial spinel structure, with the phase transition consisting of a progressive displacement of the atoms placed in tetrahedral sites of the sulphur lattice to octahedral sites (occupation factor of 0.5). This high-pressure phase is illustrated in Fig. 3.7. The S atoms and the cations previously located in O sites remain immovable. Then, this migration entails an approx. 2 Å displacement of the T atoms along the diagonal of the cube, these atoms increasing their coordination number from 4 to 6. This high-pressure structure was successfully modelled in theoretical calculations using an orthorhombic *Imma* subgroup of the cubic *Fd-3m* structure (see Chap. 4 of this book) and presented a good agreement with experimental results.

The phase transition is therefore caused by transposition of cations from tetrahedral sites to octahedral ones unoccupied in the parent spinel. The high-pressure structure may be derived from the rock-salt motif. It consists of a cubic close-packed S^{2-} *fcc* arrangement interpenetrated by a similar arrangement that consists of octahedral sites occupied by A and In atoms and 1/4 occupied by vacancies. The observed decrease in the unit cell volume at the transition could be explained by the fact that octahedra can be better packed. It is noteworthy to mention that a similar transition was induced by ion-beam irradiation in $MgAl_2O_4$ [51].

The pressure dependence of the unit-cell volumes of the high-pressure defect $LiTiO_2$-type phases of the AIn_2S_4 compounds were also fitted to a third-order Birch–Murnaghan equation of state. Curiously, the bulk compressibilities of the

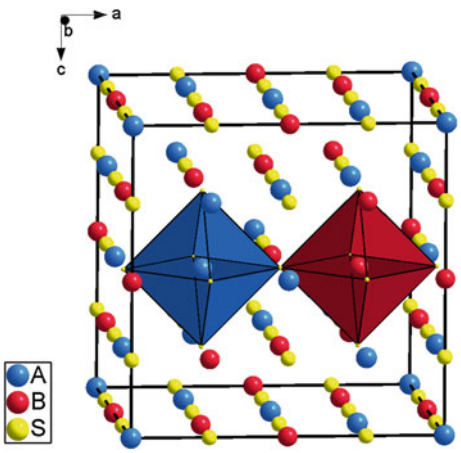

Fig. 3.7 $LiTiO_2$-type structure adopted by the high-pressure phase in AIn_2S_4 compounds (A = Cd, Mg, Mn). The S atoms form a quasi-ideal *fcc* lattice and the metal atoms occupy octahedral sites. Note that, in our case, it is a defective structure and the octahedral positions here depicted as *blue spheres* would only be half occupied

high-pressure phases, obtained from the equations of state, are slightly larger than those of the low-pressure spinel structures for the three studied compounds. This fact is likely due to the presence of stoichiometric vacancies in the unit-cell of the high-pressure phase. In fact, a similar effect occurs for other compounds. The bulk modulus of compounds with defect chalcopyrite and defect stannite structures, which are zincblende-derived compounds with stoichiometric vacancies in the unit cell, is smaller than those of their parent zincblende structures with no vacancies in the structure [52, 53].

Finally, it is necessary to note that the pressure-induced phase transition in thiospinels is fully reversible and the cubic spinel-type phase is recovered at ambient pressure on downstroke. Moreover, after releasing pressure, the S atoms return to the initial positions ($u \sim 0.256$) and the anion packing slightly distorts.

3.4 High-Pressure Vibrational Study of Indium Thiospinels

Despite high-pressure Raman and infrared (IR) measurements are relatively easy techniques to study matter under extreme temperature and pressure conditions, and the importance of the vibrational properties of sulfide and selenide spinels, the number of works concerning this subject is very scarce. Only one high-pressure Raman spectroscopy study of indium thiospinels [31] and one high-pressure IR spectroscopy study of $CuIr_2Se_4$ [54] can be found in the literature, and the latter only concerns its metal-insulator phase transition, not getting involved in the vibrational properties.

Raman spectroscopy is well known to be a very sensitive technique to detect the occurrence of structural phase transitions. In addition, the careful study of the intensity of some specific Raman modes under compression can provide valuable information about the spinels normality index which can be compared with the structural information described in Sect. 3.3. Here we are presenting Raman spectroscopy

results of Mg, Mn and Cd indium thiospinels under high pressure. These measurements were performed in a Syassen–Holzapfel DAC using a mixture 4:1 methanol–ethanol as pressure media. Pressure was measured, as in XRD experiments, by means of the ruby luminescence scale from a ruby chip placed together with the sample in the pressure chamber. Raman spectra were obtained in backscattering geometry exciting with a Kr^+-ion laser ($\lambda = 647.1$ nm) and collecting light using a Jobin-Ybon T64000 triple spectrometer with a liquid-nitrogen-cooled CCD.

3.4.1 Low-Pressure Spinel Phase

In the introduction of this chapter it has been stated that $A^{II}B_2^{III}X_4^{VI}$ spinels belong to the *Fd*-3*m* (O_h^7) space group with $Z = 8$. This means that the cubic unit cell of the spinel structure contains 56 atoms. Nonetheless, only the two octants of the cell that lie along the main body diagonal are different and, consequently, to determine the number of vibrations we can take the smallest Bravais lattice (primitive unit cell) that contains 14 atoms. In this way, one expects a total number of $14 \times 3 = 42$ vibrational modes. According to group theoretical calculations for an O_h point group with the atomic species at the symmetry sites T_d, D_{3d} and C_{3v} we would have at the center of the Brillouin zone the following irreducible representations for the vibrational modes:

$$\Gamma = A_{1g}(R) + E_g(R) + T_{1g} + 3T_{2g}(R) + 2A_{2u} + 2E_u + 4T_{1u}(IR) + T_{1u} + 2T_{2u}$$

of those modes only five ones ($A_{1g} + E_g + 3T_{2g}$) are Raman active, whereas four of the T_{1u} are IR-active and one T_{1u} is an acoustic mode, the rest being silent modes. Interestingly, all Raman modes in spinels can be uniquely assigned by means of polarized Raman spectroscopy because their respective Raman tensors have at least one unique component [55]. Following the modes assignation made by means of polarized measurement in $MnIn_2S_4$ at ambient conditions by Lutz et al. in Figs. 3.8a, 3.9a and 3.10a we present a collection of Raman spectra of $MgIn_2S_4$, $MnIn_2S_4$, and $CdIn_2S_4$, respectively, at different pressures after [31].

In the Raman spectra of these three spinels it can be seen that, in addition to the symmetry allowed modes, some other bands appear. For spinels with nearly normal structure ($x = 1$) like chromium sulphides the maximum number of Raman peaks observed is five, in good agreement with the symmetry requirements; however, the failure of the translation symmetry present in inverse spinels like the indium sulphide ones results in band broadening and the observation of new bands. In particular, in all three compounds, we observe an additional band in the region 230–260 cm^{-1} that corresponds to an all symmetric clustering mode A_{1g} [55, 56] which is due to a high density of states in a phonon branch out of the Brillouin zone center. Moreover, the random distribution of the divalent metals and indium in the octahedral sites has as a consequence the induction of polarizability changes in the system by vibrations that in principle should only cause changes in the dipolar moment. This turns out into the detection of the IR-active T_{1u} modes in the Raman spectra of indium thiospinels

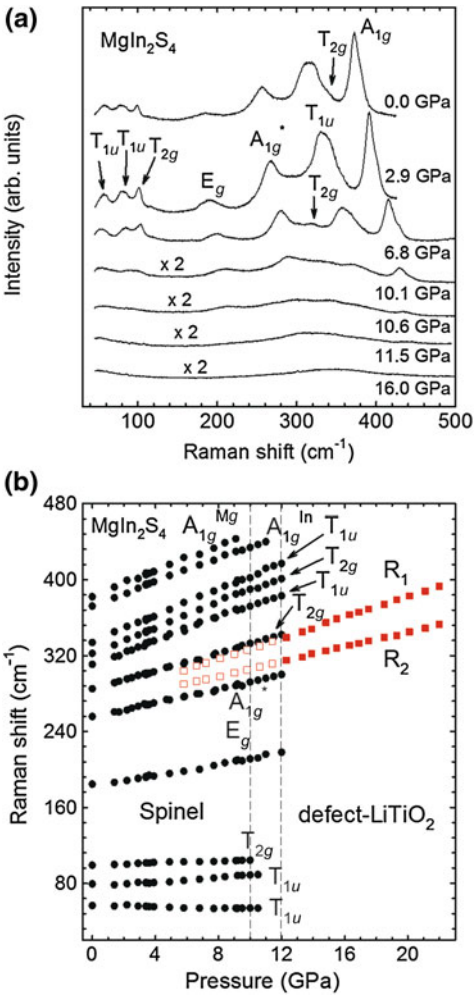

Fig. 3.8 **a** Raman spectra of $MgIn_2S_4$ at various pressures. **b** Raman frequencies as a function of pressure in $MgIn_2S_4$: *black circles* (*spinel phase)* and *red squares* (defect-$LiTiO_2$ phase). *Full symbols* represent data taken on upstroke and *empty symbols* those obtained on downstroke. The *vertical dashed line* indicates the pressure at which the phase transition between the spinel and the $LiTiO_2$ structures occurs

at frequencies that are in reasonable agreement with IR reflectivity measurements [57–59].

Another interesting feature that happens to the Raman-active all-symmetric breathing A_{1g} mode in these compounds is its splitting dependence on the metal ion involved. This mode corresponds to the vibrations of the divalent metallic anion A^{II} towards the center of the tetrahedron in a normal spinel. However, in partially inverse spinels, like indium thiospinels, tetrahedral positions are occupied by both A^{II} and In atoms and so two different bands are observed for the A_{1g} mode. The energy of this mode basically depends on the bonding distance and covalency which for Mg– and Cd–S in the $[A^{II}S_4]$ tetrahedra turns out to be very similar to the In–S ones as opposite to Mn-S distances which happen to be larger. This result gives rise

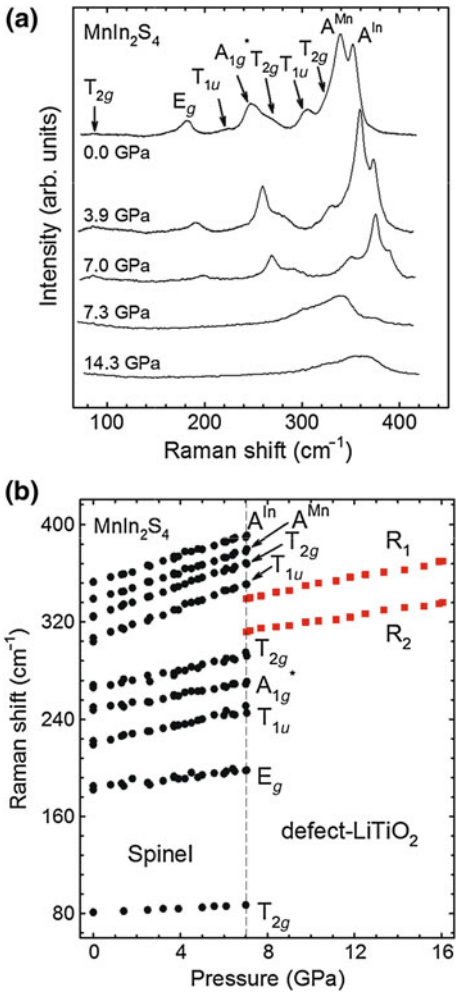

Fig. 3.9 **a** Raman spectra of $MnIn_2S_4$ at various pressures. **b** Raman frequencies as a function of pressure in $MnIn_2S_4$: *black circles* (*spinel phase*) and *red squares* (defect-$LiTiO_2$ phase). The *vertical dashed line* indicates the pressure at which the phase transition between the spinel and the $LiTiO_2$ structures occurs

to a larger splitting of the A_{1g} all-symmetric breathing mode in $MnIn_2S_4$ than in the other two indium sulphide spinels. Finally, in the case of $CdIn_2S_4$ two additional bands appear in the Raman spectra that are attributed to second-order Raman modes and local vibrational modes of the sulphur vacancies (V_S), respectively [60].

As pressure is increased all the low-pressure modes in the three thiospinels can be easily followed up to a sudden intensity decrease at 10, 9.3 and 7.2 Pa that points out the onset of the respective phase transitions for $MgIn_2S_4$, $CdIn_2S_4$ and $MnIn_2S_4$, respectively, to a structure in which only two broad Raman bands can be observed. These transition pressures agree reasonably well with those obtained from XRD experiments. Interestingly, whereas this phase transition is abrupt in both $MgIn_2S_4$ and $MnIn_2S_4$ it is gradual for $CdIn_2S_4$ which is otherwise the indium thiospinel with

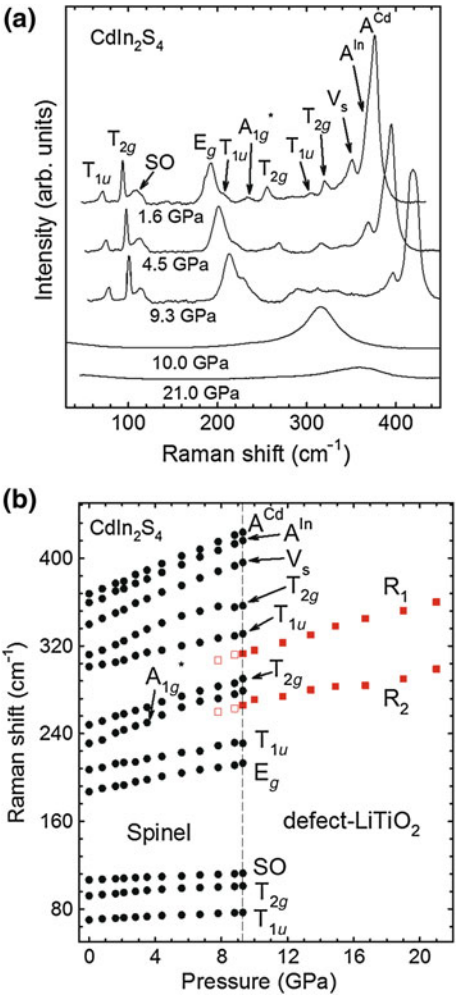

Fig. 3.10 **a** Raman spectra of $CdIn_2S_4$ at various pressures. **b** Raman frequencies as a function of pressure in $CdIn_2S_4$: *black circles* (*spinel phase*) and *red squares* (defect-$LiTiO_2$ phase). Full symbols represent data taken on upstroke and empty symbols those obtained on downstroke. The *vertical dashed line* indicates the pressure at which the phase transition between the spinel and the $LiTiO_2$ structures occurs

higher inversion, as we will discuss below. The Raman shifts as a function of pressure for all the modes are represented in Figs. 3.8, 3.9, and 3.10 for $MgIn_2S_4$, $MnIn_2S_4$, and $CdIn_2S_4$, respectively. All the modes for the three compounds increase linearly with pressure and their pressure coefficients can be found in Table. 3.2 together with the zero-pressure phonon frequencies (ω_0) and their Grüneisen parameters $\gamma = (B_0/\omega_0) \cdot (\mathrm{d}\omega/\mathrm{d}P)$, using the bulk moduli B_0 obtained in Sect. 3.3.1 and shown in Table. 3.1.

Before starting the description of the vibrational properties of the post-spinel phase in indium sulphides we will go in greater depth into the information that can be obtained about the normality index dependence with pressure from the spinel phase [31]. We have seen that the all-symmetric breathing A_{1g} mode in these compounds

Table 3.2 Raman modes frequencies at ambient pressure (cm^{-1}), pressure derivatives (cm^{-1} GPa^{-1}) and Grüneisen parameter for the three thiospinels

Mode	$MnIn_2S_4$			$CdIn_2S_4$			$MgIn_2S_4$		
	ω_0	$d\omega/dP$	γ	ω_0	$d\omega/dP$	γ	ω_0	$d\omega/dP$	γ
F_{2g}	81	0.9	0.89	93	1.0	0.84	99	0.5	0.38
F_{2g}	266	3.8	1.11	249	4.4	1.38	285	4.7	1.25
F_{2g}	325	6.2	1.49	315	5.0	1.24	322	6.7	1.58
E_g	183	2.2	0.94	188	2.7	1.12	184	2.7	1.12
A_{1g}(In)	353	5.5	1.22	360	6.1	1.32	373	6.1	1.24
A_{1g}(B)	338	5.8	1.34	367	6.1	1.30	381	6.1	1.22
A_{1g}*	247	3.2	1.01	232	5.2	1.75	256	3.6	1.07
F_{1u}				70	0.7	0.78	57	−0.3	−0.40
F_{1u}							77	1.1	1.09
F_{1u}	221	4.0	1.41	207	2.6	0.98	311	6.1	1.49
F_{1u}	306	6.5	1.66	301	3.3	0.86	335	6.8	1.54

Values are given in cm^{-1} but for the Grüneisen parameter which does not have units. Mode Grüneisen parameters γ have been calculated using the bulk modulii obtained in previous section by means of powder X-ray diffraction

split due to the partial spinel inversion. Therefore, the relative Raman intensity ratio $A_{1g}(A^{II}S_4)/A_{1g}(InS_4)$ should be equal to $x/(1-x)$ and thus studying the evolution of the intensity ratio with pressure we could obtain the pressure dependence of the spinel normality index x (see Fig. 3.11). For this purpose, the A_{1g} band that varies less from one compound to other has been assigned to the InS_4 vibration. In the three compounds both A_{1g} bands are separated in 8 cm^{-1} at least which allow the bands to be solved and followed with increasing pressure. At ambient pressure the normality indices that we have obtained are 0.16, 0.80, and 0.55 for $MgIn_2S_4$, $CdIn_2S_4$ and $MnIn_2S_4$, respectively. These values compare well with the normality indices obtained though the Rietveld refinement performed to the XRD ambient pressure diffractograms presented in Sect. 3.3.1. As pressure increases, the inversion slightly increases for $MgIn_2S_4$ and remains almost constant for $CdIn_2S_4$ up to the pressure at which the phase transition starts approaching. At that point, in both compounds the inversion suffers a steep decrease and the phase transition takes place. For $MnIn_2S_4$, the behaviour is radically opposite and pressure induces a reduction of the inversion so that this compound becomes a normal spinel at 7 GPa, just before the occurrence of the phase transition.

3.4.2 High-Pressure Phase

According to powder XRD results presented in Sect. 3.3.2, the high-pressure phase of Mg, Cd, and Mn indium thiospinels is a defect-$LiTiO_2$-type structure with the same space group than the low-pressure phase. In this structure both A^{II} and B^{III} cations occupy octahedral positions with atomic coordinates 16c and 16d and the S anions

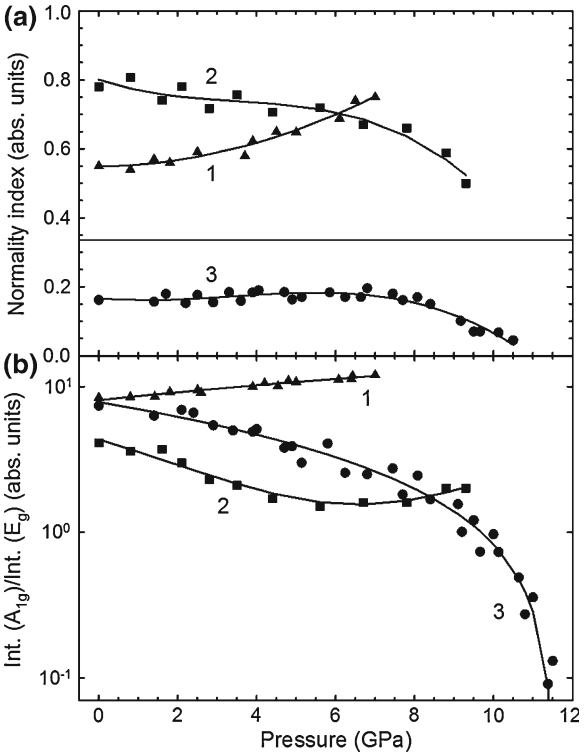

Fig. 3.11 Pressure dependences of the normality index x (**a**) and of the integral intensity of the A_{1g} mode normalized to the intensity of E_g mode (**b**) for $MnIn_2S_4$ (*curve* 1, *triangles*), $CdIn_2S_4$ (*curve* 2, *squares*), and $MgIn_2S_4$ (*curve* 3, *circles*). The *curves are the tendency lines*

remain in the 32e atomic coordinate. Therefore, after group theoretical calculations, this phase presents the following vibration modes at zone center:

$$\Gamma = A_{1g}(R) + E_g(R) + T_{1g} + 2T_{2g}(R) + 3A_{2u} + 3E_u + 5T_{1u}(IR) + T_{1u} + 3T_{2u}$$

Of these modes, four ($A_{1g} + E_g + 2T_{2g}$) are Raman-active (R) and five T_{1u} modes are IR-active (IR), one T_{1u} mode corresponds to acoustic modes, and the rest (T_{1g}, A_{2u}, E_u, and T_{2u}) are silent modes. In this context, it is interesting to remark that in previous assignments of the Raman modes for the high-pressure phase of indium thiospinels [31] it was assumed that the structure was of the rocksalt type which does not present any Raman active mode.

The observed steep intensity decrease of the Raman signal after the phase transition in the three compounds was interpreted as an extinction of the Raman signal, in agreement with a transition to a *Fm*-3*m*—NaCl phase. However, the two broad bands observed after the phase transition, were followed in pressure but not unequivocally understood. Now, under the light of the high-pressure phase structural solution we

can confirm that those two broad bands are in fact due to four Raman active modes present in the defect-$LiTiO_2$-type structure with space group *Fd*-3*m*. The broadening of the bands can be understood on the basis that the defect-$LiTiO_2$-type structure happens to be disordered in two ways: (i) the 16c Wyckoff sites are 50 % occupied by vacancies and another 50 % occupied by A^{II} and In cations, and (ii) the 16d sites are occupied both by In and A^{II} cations. Therefore, the disorder at cation sites could turn on the Raman activation of modes for each cation and the activation of IR-active modes associated to these two atomic positions. Nonetheless the problem might be solved performing a polarized Raman spectroscopy experiment; however, it is well known that these experiments are not reliable in DAC because the multiple scattering that takes place with both sample and diamonds tends to depolarize the light. Therefore, all the information that can be extracted from both broad bands is that already presented by Ursaki et al. [31]; i.e. their linear energy increase with pressure that correlates well with a reduction of interatomic distances as observed by means of powder XRD experiments presented in Sect. 3.3.2.

3.5 Experimental High-Pressure Optical Absorption Study of Indium Thiospinels

From the optical point of view, sulfide spinels are interesting materials for optoelectronic applications due to their non-linear optical susceptibility and birefringence [1]. Besides, spinels in general have attracted great attention as transparent semiconductors in solar cells [61]. Therefore, a deep understanding of the optical properties of these indium thiospinels is of great importance, and the high-pressure study of their optical absorption coefficient under pressure could provide inestimable information of their optical properties as the electronic density is varied. In this context, the measurement of the direct band gap under pressure by means of optical absorption is a straightforward method to obtain information about the electronic band structure of these compounds. A work from Nakanishi and Irie [62] from the early 1980s studying the band gap with pressure of $CdIn_2S_4$ up to 4 GPa and a later one [30] studying the band gap of $MgIn_2S_4$, $CdIn_2S_4$, and $MnIn_2S_4$ up to 20 GPa, constitute all the bibliography about this topic in thiospinels. In this section we are presenting the pressure dependence of the band gap of the three indium thiospinels $MgIn_2S_4$, $CdIn_2S_4$, and $MnIn_2S_4$ [46]. Optical absorption spectra were measured from employing the sample-in sample-out technique described elsewhere [63].

3.5.1 Low-Pressure Spinel Phase

Figures 3.12, 3.13, and 3.14 show the optical absorption spectra at selected pressures for $MgIn_2S_4$, $CdIn_2S_4$, and $MnIn_2S_4$, respectively. Taking into account the thickness

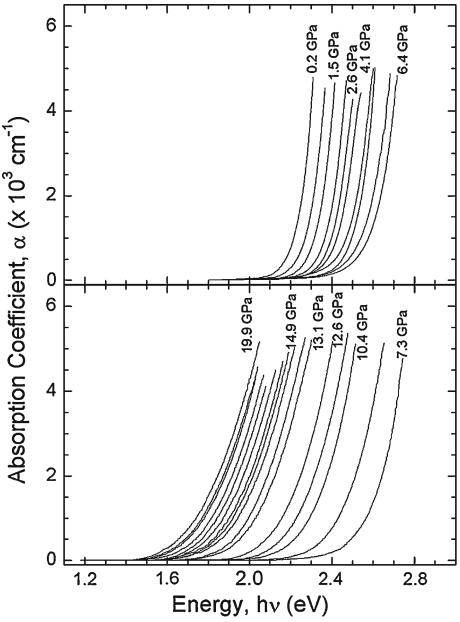

Fig. 3.12 Optical absorption spectra of $MgIn_2S_4$ at different pressures of up to 15 GPa.

of our samples, the steep shape of the spectra and the maximum measured value of the absorption coefficient α, the spectra correspond to the low-energy tail of direct band gap absorption edges. However, they exhibit an exponential dependence on the photon energy, being their behaviour governed by Urbach's law [64]. This type of behaviour is typical of the low-energy tails of direct absorption edges with excitonic effects. Interestingly, for values lower than $50\,cm^{-1}$, the dependence is no longer exponential but follows a potential law. Within the three compounds, this tail is specially pronounced in the case of $CdIn_2S_4$; a fact that has led some authors to propose an indirect band gap for this compound of 2.2 eV [65] in clear disagreement with the steep increase in the dependence of α with photon energy that can be observed in Fig. 3.13. Note that if Urbach's law is not taken into account to obtain the band gap from the absorption edge of $CdIn_2S_4$ one could consider that the low-energy tail of the absorption edge should be fitted to get the band gap. This procedure would result in an underestimation of the band gap value that would allow explaining why [30] gives a value for the band gap of $CdIn_2S_4$ of 2.35 eV, 0.15 eV larger than in [65]. In this context, it is curious that references that do not make use of Urbach's law to model the absorption edge for $MgIn_2S_4$ and $MnIn_2S_4$ [66–68] provide the same band gap values at ambient conditions (2.28 and 1.95 eV, respectively) than [30] which uses Urbach's law. This can be explained because for these two compounds the low-energy tail of the band edge is quite less pronounced, meaning that the excitonic effects are smaller than in $CdIn_2S_4$.

In Figs. 3.12 and 3.13 we can observe that the absorption spectra of the low-pressure spinel phase of $MgIn_2S_4$ and $CdIn_2S_4$ move toward higher energies under

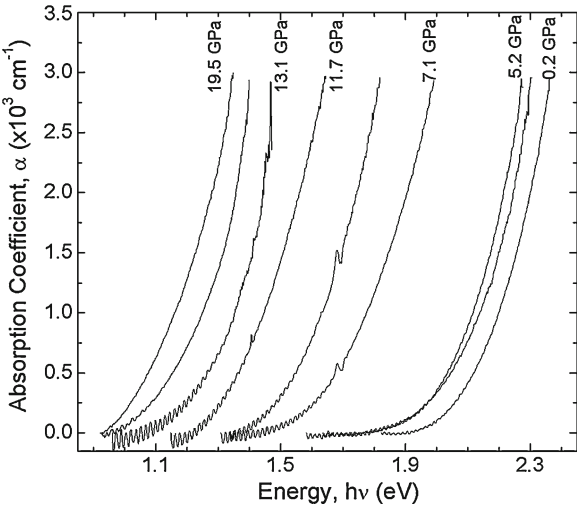

Fig. 3.13 Optical absorption spectra of $MnIn_2S_4$ at different pressures of up to 15 GPa.

pressure up to 8.5 and 10 GPa, respectively. Above these pressures a sudden redshift jump of the absorption edge is observed. The case of $MnIn_2S_4$ is slightly different as can be seen in Fig. 3.14, with its absorption edge showing a small movement toward higher energies up to 3 GPa continued by a small movement toward smaller energies up to 7.2 GPa when the sudden redshift jump takes place in this spinel. This steep shift in the absorption edge, observed for the three thiospinels indicates the occurrence of a pressure-induced band gap collapse related to a phase transition.

It has been seen before that the absorption edges of these direct band-gap compounds have an exponential dependence that is explained by Urbach's rule $\alpha = A_0 e^{-(E_g - h\nu)/E_U}$ [64], where E_U is known as Urbarch's energy and is related to the steepness parameter of the absorption tail, and $A_0 = k\sqrt{E_U}$ for a direct band gap, with k being a characteristic parameter of each material. Carrying out this analysis to the spectra in Figs. 3.12, 3.13, and 3.14 as explained in [30], and assuming k constant with pressure, the results for the band gap E_g and Urbach's energy E_U with pressure are presented in Fig. 3.15 for $MgIn_2S_4$, $MnIn_2S_4$, and $CdIn_2S_4$ spinels. For $MgIn_2S_4$ and $CdIn_2S_4$, E_g linearly increases up to 8.5 and 10 GPa respectively, with a pressure coefficient of $dE_g/dP = 70$ meV/GPa in good agreement with Nakanishi and Irie [62] results up to 4 GPa in $CdIn_2S_4$ as can be observed in Fig. 3.15c as well. Differently, the band gap E_g of $MnIn_2S_4$ spinel shows a nonlinear variation with pressure up to 7.2 GPa with a maximum at 3 GPa and a pressure coefficient of 20 meV/GPa at ambient pressure. Following the results presented by Kawazoe and Ueda [69], the energy of the direct gap in AB_2X_4 spinels is mainly due to the B–X hybridization rather than the A–X hybridization. Moreover, these authors evidenced that metal cations with no d or f orbitals, or with filled d and f orbitals would form an extended conduction band, which is the case of $MgIn_2S_4$ and $CdIn_2S_4$. Therefore, it

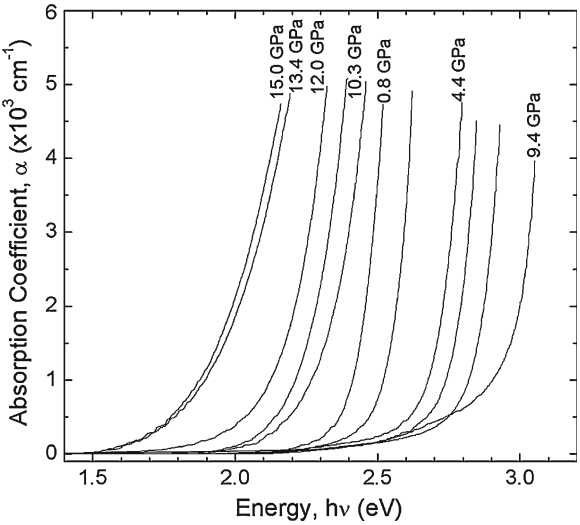

Fig. 3.14 Optical absorption spectra of $CdIn_2S_4$ at different pressures of up to 15 GPa.

is expected for these two spinels to have similar electronic band structures basically due to In–S hybridization and so present similar band gaps and pressure coefficients as has been experimentally determined. On the contrary, in the case of $MnIn_2S_4$, Mn 3*d* orbitals play an important role in the uppermost valence band and lower part of the conduction band that results on a lowering of the band gap and a smaller pressure coefficient with respect to the other two spinels. Concerning the different type of pressure dependence of the band gap, both $MgIn_2S_4$ and $CdIn_2S_4$ follow the standard behaviour of direct-band gap semiconductors, i.e. since under pressure In distances reduce, the bonding-antibonding splitting of the In 5*s* states increases, shifting up in energy the antibonding orbitals that basically constitute the lower part of the conduction band. This is translated into a linear band gap increase under pressure. On the other hand, the non-linear pressure dependence of the direct band gap of $MnIn_2S_4$, showing a small increase at low pressures and a decrease above 2 GPa, is somewhat unusual. We may speculate that a possible band crossing might be the cause of the non-linear behaviour of the direct band gap as happens with adamantine ordered-vacancy compounds (OVCs) [70] and discussed in Chap. 6 in this book. However, high-pressure band-structure calculations are needed for $MnIn_2S_4$to completely understand its nonlinear behaviour since contrary to OVCs $MnIn_2S_4$ does not contain stoichiometric vacancies inducing a band crossover in the conduction band.

As commented above, the three compounds experience a band gap energy drop of 0.3 eV in $MgIn_2S_4$ at 8.5 GPa, of 0.65 eV in $CdIn_2S_4$ at 10 GPa, and of 0.3 eV in $MnIn_2S_4$ at 7.2 GPa. Additionally, a second abrupt change in their band gaps is found at 12, 12, and 9 GPa for $MnIn_2S_4$,$MnIn_2S_4$, and $MnIn_2S_4$ respectively. Under the light of the structural and vibrational information shown in Sects. 3.3 and 3.4, the first abrupt band-gap energy drop observed in the three compounds correlates

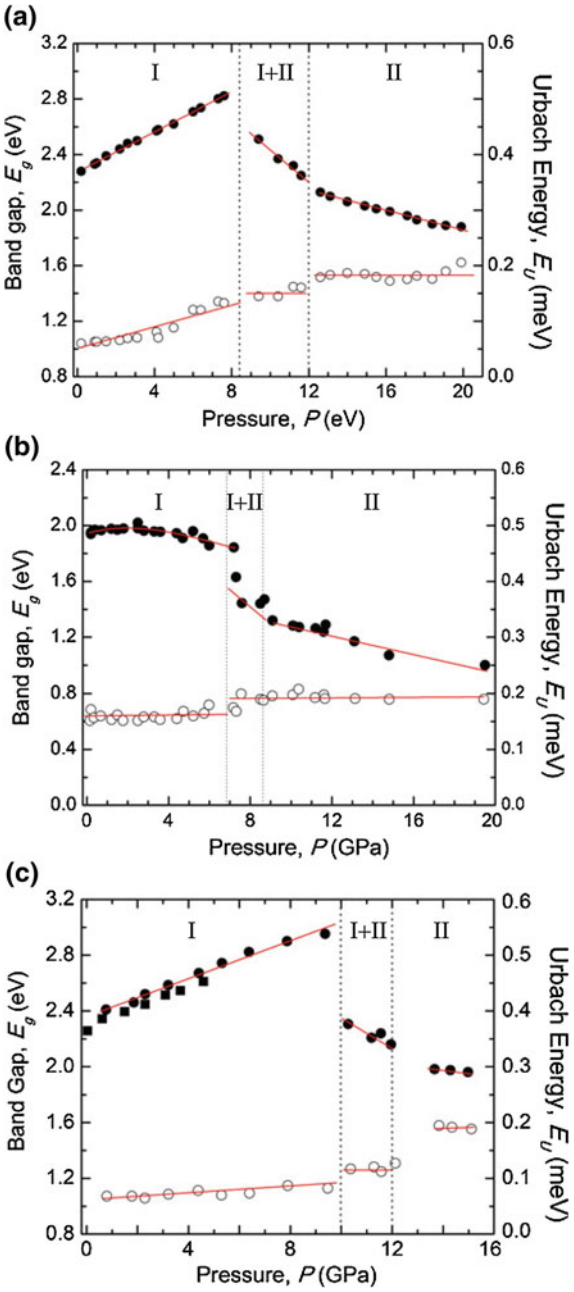

Fig. 3.15 **a** Pressure dependence of the band-gap energy (*solid circles*) and Urbach's energy (*empty circles*) in $MgIn_2S_4$. The *solid vertical lines* indicate the onset and completion of the phase transition. I (II) indicates the pressure range of stability of the low-(high) pressure phase and I + II is the region of phase coexistence. **b** Same but for $MnIn_2S_4$. **c** Same but for $CdIn_2S_4$. *Solid squares* belong to [32]

well with the onset of the structural phase transition from the spinel structure to a $LiTiO_2$-type structure since it has been shown in Sect. 3.3 that both, the low- and the high-pressure phases coexist during a certain pressure range in $CdIn_2S_4$ and $MnIn_2S_4$. Therefore, the second band-gap energy drop corresponds to the completion of the phase transition. The coexistence is not so explicit in the case of the Raman experiments, which is in the line of being a much more local technique.

3.5.2 High-Pressure Phase

Concerning the dependence of E_g after the onset of the phase transition it can be noted in Fig. 3.15 that the band-gap energy has large negative coefficients in the three compounds from $dE_g/dP = -80$ to -110 meV/GPa up to the completion of the phase transition. Once the phase transition is complete E_g keeps redshifting but with a smaller pressure coefficients from $dE_g/dP = -20$ to -30 meV/GPa. After pressure release, the low pressure phase is recovered in $MgIn_2S_4$ and $MnIn_2S_4$ without almost hysteresis in good agreement with XRD and Raman spectroscopic experiments. However in the case of $CdIn_2S_4$ the phase transition was found to be irreversible in opposition to XRD or Raman spectroscopic results, suggesting that the creation of defects in the sample during the phase transition in this compound might be translated into a band due to defects that would mask the band gap.

Finally, another parameter obtained through the Urbach's law analysis of the spectra is Urbach's energy E_U. As explained at the beginning of this section, this parameter relates to the shape of the absorption edge or, in other words, it measures how steep the absorption edge is. Therefore, it is indirectly related to the disorder and appearance of defects in spinels. Whereas for $MgIn_2S_4$ and $CdIn_2S_4$ at ambient pressure, E_U takes the same value of 50 meV, in $MnIn_2S_4$ it is more than three times larger (160 meV) suggesting a higher concentration of defects than in the other two spinels. In Fig. 3.15 we can observe for $MgIn_2S_4$ and $CdIn_2S_4$ spinels, that E_U linearly increases in the low-pressure spinel phase indicating an increase of defects as pressure is increased. When the phase transition takes place E_U abruptly increases for both compounds and remains constant up to the end of the phase transition when it increases again up to 200 meV and remains constant with pressure. This means that while samples remain in the spinel-type phase, the defect concentration increases with pressure, reaching constant values once the samples have transited. Regarding $MnIn_2S_4$, E_U remains constant with pressure in the low-pressure phase and slightly increases to 200 meV after the phase transition to remain again constant with pressure.

3.6 Conclusions

The empirical results presented in this chapter furnish convincing evidence that most of sulphur- and selenium-based spinels undergo a phase transition under compression to defect-like structures. Thus, experiments at high pressures and

temperatures confirm the existence of the spinel-defect–NiAs–type transition in this class of compounds, whereas recent experiments in indium thiospinels at high-pressure and ambient temperature suggest that these materials transform into a defect–$LiTiO_2$-type structure. This latter structure may be derived from the rock-salt motif, which is the cubic analog of the hexagonal NiAs arrangement. Both polymorphs are usually very close energetically and a temperature increase may be enough to convert the defective $LiTiO_2$-type structure into the defective NiAs-type.

It is not yet clear what role the atomic interactions play in determining the high pressure structure. What are the ultimate reasons that guide the transformation of thiospinels into the defect $LiTiO_2$ postspinel phase under compression? No precise answer can be given to this question. Nevertheless, this continuous structural transformation has been tracked using several characterization techniques (X-ray diffraction, Raman scattering, and optical absorption spectroscopy) and their analysis provides some insight into the high-pressure behaviour of the indium thiospinel family. The phase transition is caused by transposition of cations from tetrahedral sites to octahedral ones, this fact entailing a sudden collapse of the tetrahedral volumes existing in the quasi-*fcc* S lattice. Since the variation of the octahedral cavities is more continuous, a contraction of the unit cell takes place at the transition. This volume change, as well as the transition pressure, the hysteresis and the range of coexistence of phases, depends on the nature of the A atom in AIn_2S_4. An interesting feature is that bulk compressibilities of the post-spinel phases are similar or slightly larger than those of the low-pressure spinel structures, which could be due to the observed incorporation of stoichiometric octahedral vacancies to the unit cell.

From the foregoing, it is obvious that the phase diagram of thio- and seleno-spinels possess many features that are unique and worthy of further investigation. A more detailed understanding of this phase diagram invites new experiments and calculations.

Acknowledgments Financial support from the Spanish Consolider Ingenio 2010 Program (Project No. CDS2007-00045) is acknowledged. The work was also supported by Spanish MICCIN and MINECO under Projects No. CTQ2009-14596-C02-01 and CTQ2012-38599-C02-02, as well as from Comunidad de Madrid and European Social Fund: S2009/PPQ-1551 4161893 (QUIMAPRES). J R-F is indebted to the Spanish MCYT for granting an FPI fellowship (BES-2008-002043).

References

1. Georgobiani AN, Radautsan SI, Tiginyanu IM (1985) Wide-gap $A(II)B(III)_2C(VI)_4$ semiconductors—optical and photoelectric properties, and potential applications. Soviet Phys Semicond Ussr 19:121–132
2. Ball JA, Pirzada M, Grimes RW, Zacate MO, Price DW, Uberuaga BP (2005) Predicting lattice parameter as a function of cation disorder in $MgAl_2O_4$ spinel. J Phys Condens Matter 17: 7621–7631
3. Radaelli PG, Horibe Y, Gutmann MJ, Ishibashi H, Chen CH, Ibberson RM, Koyama Y, Hor YS, Kiryukhin V, Cheong SW (2002) Formation of isomorphic $Ir3^+$ and $Ir4^+$ octamers and

spin dimerization in the spinel $CuIr_2S_4$. Nature 416:155–158
4. Tang J, Matsumoto T, Furubayashi T, Kosaka T, Nagata S, Kato Y (1998) Metal–insulator transition of $CuIr_2(S, Se)_4$ under high pressure. J Magn Magn Mater 177:1363–1364
5. Palacios P, Aguilera I, Sanchez K, Conesa JC, Wahnon P (2008) Transition-metal-substituted indium thiospinels as novel intermediate-band materials: prediction and understanding of their electronic properties. Phys Rev Lett 101:046403
6. Okonska-Kozlowska I, Malicka E, Waskowska A, Heimann J, Mydlarz T (2001) Distribution of metal ions and magnetic properties in spinel system $CdCr_{2-x}Ga_xSe_4$. J Solid State Chem 158:34–39
7. Radautsan SI, Tiginyanu IM (1993) Defect engineering in II-III_2-VI_4 and related compounds. Jpn J Appl Phys 32 Part 1:5–9
8. Ito M, Hori J, Kurisaki H, Okada H, Kuroki AJP, Ogita N, Udagawa M, Fujii H, Nakamura F, Fujita T, Suzuki T (2003) Pressure-induced superconductor-insulator transition in the spinel compound $CuRh_2S_4$. Phys Rev Lett 91(4):077001
9. Irifune T, Fujino K, Ohtani E (1991) A new high-pressure form of $MgAl_2O_4$. Nature 349: 409–411
10. Menyuk N, Dwight K, Arnott RJ, Wold A (1966) Ferromagnetism in $CdCr_2Se_4$ and $CdCr_2S_4$. J Appl Phys 37:1387–1388
11. Gibart P, Dormann JL, Pellerin Y (1969) Magnetic properties of $FeCr_2S_4$ and $CoCr_2S_4$. Phys Stat Solidi 36:187–194
12. Menyuk N, Dwight K, Wold A (1965) Magnetic properties of $MnCr_2S_4$. J Appl Phys 36: 1088–1090
13. Ramirez AP, Cava RJ, Krajewski J (1997) Colossal magnetoresistance in Cr-based chalcogenide spinels. Nature 386:156–159
14. Hagino T, Seki Y, Wada N, Tsuji S, Shirane T, Kumagai KI, Nagata S (1995) Superconductivity in spinel-type compounds $CuRh_2S_4$ and $CuRh_2Se_4$. Phys Rev B 51:12673–12684
15. Vanmaaren NH, Schaeffe GM, Lotgering FK (1967) Superconductivity in sulpho- and selenospinels. Phys Lett A 25:238–239
16. Albers W, Rooymans CJM (1965) High-pressure polymorphism of spinel compounds. Solid State Commun 3:417–419
17. Bouchard RJ (1967) Spinel to defect NiAs structure transformation. Mater Res Bull 2:459–464
18. Bouchard RJ, Russo PA, Wold A (1965) Preparation and electrical properties of some thiospinels. Inorg Chem 4:685–688
19. Wittlinger J, Werner S, Schulz H (1997) On the amorphisation of $ZnCr_2S_4$ spinel under high pressure: X-ray diffraction studies. Phys Chem Mineral 24:597–600
20. Vaqueiro P, Powell AV, Hull S, Keen DA (2001) Pressure-induced phase transitions in chromium thiospinels. Phys Rev B 63(6):064106
21. Nakamoto Y, Matsuoka T, Kagayama T, Shimizu K, Tang J, Kobayashi N, Nagata S, Kikegawa T (2005) The phase transition of $CuCrZrS_4$ at high pressure. Phys B Condens Matter 359: 1213–1215
22. Garga AB, Vijayakumar V, Godwal BK, Choudhury A, Hochheimer HD (2007) Reentrant high-conduction state in $CuIr_2S_4$ under pressure. Solid State Commun 142:369–372
23. Errandonea D, Manjon FJ (2008) Pressure effects on the structural and electronic properties of ABX_4 scintillating crystals. Prog Mater Sci 53:711–773
24. Errandonea D, Kumar RS, Manjon FJ, Ursaki VV, Rusu EV (2009) Post-spinel transformations and equation of state in $ZnGa_2O_4$: Determination at high pressure by in situ X-ray diffraction. Phys Rev B 79(6):024103
25. Levy D, Pavese A, Hanfland M (2000) Phase transition of synthetic zinc ferrite spinel ($ZnFe_2O_4$) at high pressure, from synchrotron X-ray powder diffraction. Phys Chem Mineral 27:638–644
26. Ono S, Kikegawa T, Ohishi Y (2006) The stability and compressibility of $MgAl_2O_4$ high-pressure polymorphs. Phys Chem Mineral 33:200–206
27. Yamaura K, Huang Q, Zhang L, Takada K, Baba Y, Nagai T, Matsui Y, Kosuda K, Takayama-Muromachi E (2007) Magnetic properties of the calcium ferrite-type $Li_{0.92}Mn_2O_4$. J Magn Magn Mater 310:1578–1580

28. Ursaki VV, Burlakov II, Tiginyanu IM, Raptis YS, Anastassakis E, Aksenov I, Sato K (1998) Pressure induced phase transitions in spinel and wurtzite phases of $ZnAl_2S_4$ compound. Jpn J Appl Phys 37:135–140
29. Manjon FJ, Segura A, Amboage M, Pellicer-Porres J, Sanchez-Royo JF, Itie JP, Flank AM, Lagarde P, Polian A, Ursaki VV, Tiginyanu IM (2007) Structural and optical high-pressure study of spinel-type $MnIn_2S_4$. Phys Stat Solidi B 244:229–233
30. Ruiz-Fuertes J, Errandonea D, Manjon FJ, Martinez-Garcia D, Segura A, Ursaki VV, Tiginyanu IM (2008) High-pressure effects on the optical-absorption edge of $CdIn_2S_4$, $MgIn_2S_4$, and $MnIn_2S_4$ thiospinels. J Appl Phys 103(5):063710
31. Ursaki VV, Manjon FJ, Tiginyanu IM, Tezlevan VE (2002) Raman scattering study of pressure-induced phase transitions in MIn_2S_4 spinels. J Phys Condens Matter 14:6801–6813
32. Santamaria-Perez D, Amboage M, Manjon FJ, Errandonea D, Rodriguez-Hernandez P, Muñoz A, Mujica A, Radescu S, Ursaki VV, Tiginyanu IM (2012) Crystal chemistry of $CdIn_2S_4$, $MgIn_2S_4$ and $MnIn_2S_4$ thiospinels under high pressure. J Phys Chem C 116:14078–14087
33. Banus MD, Lavine MC (1969) Polymorphism in selenospinels—a high pressure phase of $CdCr_2Se_4$. J Solid State Chem 1:109–116
34. Waskowska A, Gerward L, Olsen JS, Malicka E (2002) Temperature- and pressure-induced lattice distortion in $CdCr_{2-x}Ga_xSe_4$ (x = 0, 0.06, and 0.12). J Phys Condens Matter 14: 12423–12431
35. Grzechnik A, McMillan PF, Ouvrard G (1997) Olivine-spinel phase transformations in Mn_2SiSe_4 at high pressure. Nucl Instrum Methods Phys Res B 133:24–27
36. Finger LW, Hazen RM, Hofmeister AM (1986) High-pressure crystal chemistry of spinel $MgAl_2O_4$ and magnetite Fe_3O_4—comparisons with silicate spinels. Phys Chem Mineral 13:215–220
37. Asbrink S, Waskowska A, Gerward L, Olsen JS, Talik E (1999) High-pressure phase transition and properties of spinel $ZnMn_2O_4$. Phys Rev B 60:12651–12656
38. Asbrink S, Waskowska A, Olsen JS, Gerward L (1998) High-pressure phase of the cubic spinel $NiMn_2O_4$. Phys Rev B 57:4972–4974
39. Waskowska A, Gerward L, Olsen JS, Steenstrup S, Talik E (2001) $CuMn_2O_4$: properties and the high-pressure induced Jahn-Teller phase transition. J Phys Condens Matter 13:2549–2562
40. Pendas AM, Costales A, Blanco MA, Recio JM, Luaña V (2000) Local compressibilities in crystals. Phys Rev B 62:13970–13978
41. Recio JM, Franco R, Pendas AM, Blanco MA, Pueyo L (2001) Theoretical explanation of the uniform compressibility behavior observed in oxide spinels. Phys Rev B 63(7):184101
42. Gerward L, Jiang JZ, Olsen JS, Recio JM, Waskowska A (2005) X-ray diffraction at high pressure and high or low temperature using synchrotron radiation—selected applications in studies of spinel structures. J Alloys Compd 401:11–17
43. Waskowska A, Gerward L, Olsen JS, Feliz M, Llusar R, Gracia L, Marques M, Recio JM (2004) High-pressure behaviour of selenium-based spinels and related structures—an experimental and theoretical study. J Phys Condens Matter 16:53–63
44. Waskowska A, Gerward L, Olsen JS, Marques M, Contreras-Garcia J, Recio JM (2009) The bulk modulus of cubic spinel selenides: an experimental and theoretical study. High Press Res 29:72–75
45. Hahn H, Klingler W (1950) Uber die Kristallstruktur einiger ternarer Sulfide, die sich von Indium(III)-Sulfid ableiten. Z Anorg Chem 263:177–190
46. Nitsche R (1971) Crystal growth and phase investigations in multi-component systems by vapour transport. J Cryst Growth 9:238–243
47. Birch F (1947) Finite elastic strain of cubic crystals. Phys Rev 71:809–824
48. Murnaghan FD (1944) The compressibility of media under extreme pressures. Proc Natl Acad Sci USA 30:244–247
49. Wittlinger J, Werner S, Schulz H (1998) Pressure-induced order-disorder phase transition of spinel single crystals. Acta Cryst B 54:714–721
50. Seminovski Y, Palacios P, Wahnon P, Grau-Crespo R (2012) Band gap control via tuning of inversion degree in $CdIn_2S_4$ spinel. Appl Phys Lett 100(3):102112

51. Ishimaru M, Afanasyev-Charkin IV, Sickafus KE (2000) Ion-beam-induced spinel-to-rocksalt structural phase transformation in $MgAl_2O_4$. Appl Phys Lett 76:2556–2558
52. Madelung O (1992) Semiconductors: other than group IV elements and III-V compounds. Springer-Verlag, Berlin
53. Errandonea D, Kumar RS, Manjon FJ, Ursaki VV, Tiginyanu IM (2008) High-pressure X-ray diffraction study on the structure and phase transitions of the defect-stannite $ZnGa_2Se_4$ and defect-chalcopyrite $CdGa_2S_4$. J Appl Phys 104(9):063524
54. Chen L, Matsunami M, Nanba T, Matsumoto T, Nagata S, Ikemoto Y, Moriwaki T, Hirono T, Kimura H (2005) Far-infrared spectroscopy of electronic states of $CuIr_2Se_4$ at high pressure. J Phys Soc Jpn 74:1099–1102
55. Lutz HD, Becker W, Muller B, Jung M (1989) Raman single-crystal studies of spinel-type MCr_2S_4 (M = Mn, Fe, Co., Zn, Cd), MIn_2S_4 (M = Mn, Fe, Co., Ni), $MnCr_{2-2x}In_{2x}S_4$ and $Co_{1-x}Cd_xCr_2S_4$. J Raman Spectrosc 20:99–103
56. Fu ZW, Dow JD (1987) Clustering modes in the vibrational spectra of $Hg_{1-x}Cd_xTe$ alloys. Phys Rev B 36:7625–7626
57. Lutz HD, Waschenbach G, Kliche G, Haeuseler H (1983) Lattice vibration spectra. XXXIII. Far-red reflection spectra, TO and LO phonon frequencies, optical and dielectric constants, and effective charges of the spinel-type compounds MCr_2S_4 (M = Mn, Fe, Co., Zn, Cd, Hg), MCr_2Se_4 (M = Zn, Cd, Hg) and MIn_2S_4 (M = Mn, Fe, Co., Ni, Cd, Hg). J Solid State Chem 48:196–208
58. Syrbu NN, Kretsu R, Gezlevan VE (1997) IR vibration modes of $MgIn_2S_4$ and $CdIn_2S_4$ crystals. Opt Spectrosc 82:247–252
59. Wakaki M, Shintani O, Ogawa T, Arai T (1982) Crystal structure and lattice absorption of partially inverse spinel compound $MgIn_2S_4$. Jpn J Appl Phys 21:958–959
60. Gubanov VA, Kulikova OV, Kulyuk LL, Radautsan SI, Ratseev SA, Salivon GI, Tezlevan VE, Tsytsanu VI (1988) Raman scattering in $CdIn_2S_4$ and phonon modes in some $A^{II}B_2^{III}C_4^{VI}$ spinel semiconductors. Sov Phys Solid State 30:457–461
61. Gracia L, Beltran A, Andres J, Franco R, Recio JM (2002) Quantum-mechanical simulation of $MgAl_2O_4$ under high pressure. Phys Rev B 66(7):224114
62. Nakanishi H, Irie T (1984) Pressure effect on the absorption edges of $CdIn_2S_4$ and related compounds. Phys Stat Solidi B 126:145–148
63. Segura A, Sans JA, Errandonea D, Martinez-Garcia D, Fages V (2006) High conductivity of Ga-doped rock-salt ZnO under pressure: Hint on deep-ultraviolet-transparent conducting oxides. Appl Phys Lett 88(3):011910
64. Urbach F (1953) The long-wavelength edge of photographic sensitivity and of the electronic absorption of solids. Phys Rev 92:1324–1324
65. Meloni F, Mula G (1970) Pseudo-potential calculation of band structure of $CdIn_2S_4$. Phys Rev B 2:392–396
66. Betancourt L, Sagredo V, Rincon C, Delgado GE (2006) Optical absorption and dependence of the band gap energy on the temperature of monocrystals in the $Cd_{1-x}Mn_xIn_2S_4$ system. Rev Mex Fis 52:164–166
67. Marinelli M, Baroni S, Meloni F (1988) Structural and electronic properties of spinel semiconductors–Ab initio pseudopotential study of $MgIn_2S_4$. Phys Rev B 38:8258–8263
68. Niftiev NN (1994) Optical absorption in $MnIn_2S_4$ single-crystals. Solid State Commun 92: 781–783
69. Kawazoe H, Ueda K (1999) Transparent conducting oxides based on the spinel structure. J Am Ceram Soc 82:3330–3336
70. Manjon FJ, Gomis O, Rodriguez-Hernandez P, Perez-Gonzalez E, Munoz A, Errandonea D, Ruiz-Fuertes J, Segura A, Fuentes-Cabrera M, Tiginyanu IM, Ursaki VV (2010) Nonlinear pressure dependence of the direct band gap in adamantine ordered-vacancy compounds. Phys Rev B 81(7):195201

Chapter 4
Theoretical Ab Initio Calculations in Spinels at High Pressures

P. Rodríguez-Hernández and A. Muñoz

Abstract Advances in the accuracy and efficiency of ab initio calculations have allowed detailed studies of properties of material under pressure. In this chapter we present an overview of the theoretical work done from first principles on the structural, elastic, electronic, and vibrational properties of spinels under pressure as well as pressure-induced post-spinel phases. Theoretical results are compared with experimental data when available. As there is a lack in the study of vibrational properties of thiospinels under pressure, we also report an analysis of the vibration modes for the cubic spinel $CdIn_2S_4$.

Keywords Ab initio · Spinel · Post-spinel · High pressure · Elasticity · Lattice dynamics · Phase transitions

4.1 Introduction

The spinel structure is named after the mineral spinel ($MgAl_2O_4$) which is a major constituent of the shallow upper mantle and plays an important role in Geophysics [1]. Since this oxide spinel (also named oxospinel) became also a technological important compound, there has been a great interest in the study of the oxospinel family [2]. However, the thiospinel family (with sulfur instead of oxygen) also forms an interesting group of materials due to their unusual properties [3–5] making thiospinels potential materials for engineering applications [6, 7].

P. Rodríguez-Hernández (✉) · A. Muñoz
Departamento de Física Fundamental II and Instituto de Materiales y Nanotecnología, Universidad de La Laguna, 38207 La Laguna, Tenerife, Spain
e-mail: plrguez@ull.edu.es

A. Muñoz
e-mail: amunoz@ull.edu.es

F. J. Manjón et al. (eds.), *Pressure-Induced Phase Transitions in AB_2X_4 Chalcogenide Compounds*, Springer Series in Materials Science 189,
DOI: 10.1007/978-3-642-40367-5_4,

Since the earlier studies of Ringwood and Reid on spinel under pressure [8] there has been an increasing interest in the experimental study of oxospinels at high pressures. However, a limited number of high pressure studies have been performed on thiospinels and very few studies have been performed in selenospinels. In addition to knowing the pressure effects on the properties of thiospinels, high-pressure studies have shown that pressure-induced phase transitions in thiospinels occur at a much lower pressure than in oxospinels [3–5]. Hence, the study of thiospinels may help to understand the behavior of oxoespinels under pressure and clarify the nature of the postspinel structure.

From a theoretical approach most of the studies on spinels have been made with empirical or semi empirical models [9, 10]. However, progress in first principles techniques in the last 20 years have made possible to compute with great accuracy an important number of structural and electronic properties of solids. This allows explain and predict material characteristics even in complex systems like spinels.

This chapter presents an overview of the results obtained from first-principles methods, on the evolution of the many properties of the spinels under pressure, mainly the structural, elastic, vibrational, and electronic properties. Most of the investigations on spinels under pressure are based on the application of the Density Functional Theory (DFT) [11] with different types of functionals for the description of the exchange-correlation energy, usually the Local Density Approximation (LDA) [12] or the Generalized Gradient Approximation (GGA) [13]. The application of DFT-based total energy calculations to the study of semiconductor properties under high pressure has been reviewed in [14] showing that the phase stability and electronic and dynamical properties of compounds under pressure are well described by DFT.

4.2 Crystal Structure. Calculations of the Spinel Phase

The spinel family is a group of compounds with chemical formula AB_2X_4 that crystallize in the space group *Fd*-3 m, No. 227, with Z = 8, where A and B are cations and X are anions. When X = O, S, or Se the compounds are named oxospinels, thiospinels or selenospinels. A and B cations occupy tetrahedral and octahedral sites, respectively, while the anion sublattice forms a quasi ideal close-packed *fcc* structure, see Fig. 4.1. In the cubic spinel structure the description of the atomic position depends on the choice of the origin. Two conventional options are possible for the unit cell origin namely: at −43 m on an A cation site or at −3 m on an octahedral vacancy (an inversion center) [15]. Upon selecting the origin at −3 m, A atoms occupy 8*a* (1/8, 1/8, 1/8), B atoms 16*d* (1/2, 1/2, 1/2) and X atoms 32*e* (*u, u, u*) Wyckoff positions. This structure is characterized by two parameters: the lattice constant *a* and the anion positional parameter *u*. This description stands for the direct spinel structure, the "normal" spinels (e.g., $MgAl_2O_4$). However in nature there is a partial disorder of the cations, some A and B cations can interchange theirs position in the in unit cell. To describe this situation a degree of inversion (or cation inversion parameter) *x* is defined. So a spinel is represented by the general

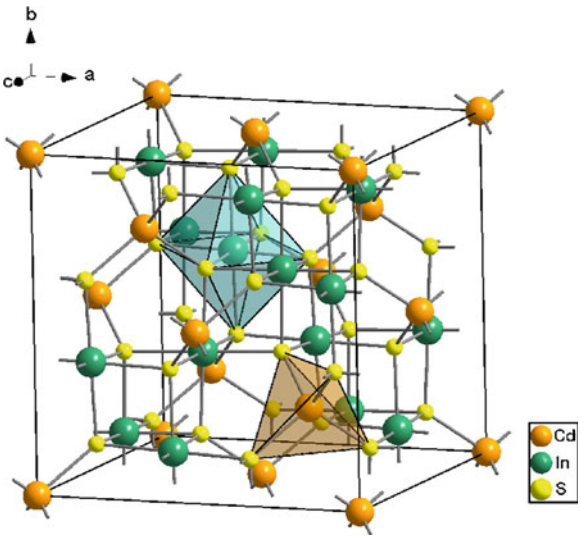

Fig. 4.1 Schematic view of the spinel structure of $CdIn_2S_4$ with octahedral (*green*) and tetrahedral polyhedra (*orange*). *Orange spheres* represent Cd atoms, *green spheres* represent In atoms, and *yellow spheres* represent S atoms

formula $(A_{1-x}B_x)[A_xB_{2-x}]X_4$. Here, cations in the parentheses occupy the tetrahedral sites and cations in the square brackets occupy the octahedral sites. For the case $x = 0$, all A atoms are in tetrahedral position and all B atoms are in octahedral positions, thus resulting the direct (or normal) $(A)[B_2]X_4$ spinel structure. For the case $x = 1$, all A atoms occupy octahedral sites and half of the B atoms occupy tetrahedral sites and the other half occupy octahedral sites, thus resulting the "inverse" $(B)[AB]X_4$ spinel structure, which is partially disordered. Values of x between 0 and 1 describe partially inverse spinel structures with a total cation disorder (mixture of cations in both tetrahedral and octahedral cation sites).

To perform calculations of a crystalline compound it is necessary to know the atomic positions of cations and anions into the unit cell (56 atoms in the spinel case). Experimentally, the ground state of many spinels has not been clarified because on one hand the degree of inversion depends on the synthesis conditions and because on the other hand the cation positions are many times not well determined from diffraction techniques [5, 16]. The atomic positions of some inverse spinels are often described as partially occupied (occupation factor $\neq 1$). To describe an inverse spinel or spinels with some degree of inversion very large supercells would be needed which is very expensive from a computational point of view. From first principles studies the cationic disorder has been studied with cluster expansion and canonical Monte Carlo simulation [17, 18]. The inverse spinels were also modeled with the special quasi-random structure (SQS) [19–21], which is based on the fact that the physical properties of an alloy are uniquely determined by its atomic structure and that the structure can be quantified by atomic correlation functions for atomic clusters.

An alternative approach to model disordered spinels is the virtual crystal approximation (VCA) [22]. On this method for each of the disordered sites one chemical pseudopotential is constructed mixing the atoms that participate in the solid solution in the appropriate amounts [23, 24].

For simplicity, in many practical cases some disordered spinels are simulated as direct or inverse structures, according to which is the closest structure to the experiment. Nevertheless, some degree of disorder can be simulated with an affordable computational cost. The primitive cell of direct spinel contains two formula units, which allows to consider inversion degrees of $x = 0$, 0.5, and 1, as for each value of x, there is only one symmetrically different configuration of cations [16]. In particular, it is possible to simulate an inverse spinel (x = 1) because this structure can be simulated with the orthorhombic space group (SG) *Imma*, No. 74, Z = 4. In this case, the lattice parameters of the orthorhombic structure are: $a' = a/\sqrt{2}$, $b' = a/\sqrt{2}$, and $c' =$ a, where a is the lattice parameter of the direct (cubic) spinel structure (SG *Fd*-3 m No. 227, Z = 8) [5, 25, 26].

Table 4.1 shows the calculated lattice and structural parameters a and u and the bulk modulus of some spinels at equilibrium compared with experimental data at ambient conditions. The data present an overall good agreement with the experimental results with a slight underestimation of the unit cell volumes, which is characteristic of the LDA approximation.

In the last decades there has been an increasing interest in understanding the pressure behavior of $MgAl_2O_4$. Besides its technological interest, the prediction of physical properties may provide valuable information in the study of others materials with a similar structure. The prototypical $MgAl_2O_4$ spinel has a direct spinel structure so it is characterized by a *fcc* structure of oxygens with Mg atoms occupying the tetrahedral sites and Al atoms occupying the octahedral sites.

As pressure increases, the calculated unit cell lattice parameter a and the internal parameter u of spinel decrease, this is a general result for direct spinels [2, 29, 31]. The pressure dependence of the internal parameter u is quadratic with a moderate negative slope, $\partial u/\partial \mathrm{P} = -4.38 \cdot 10^{-5}\,\mathrm{GPa}^{-1}$ [2], $\partial u/\partial \mathrm{P} = -4.72 \cdot 10^{-5}\,\mathrm{GPa}^{-1}$ for $MgAl_2O_4$ [29]. The reaction of the spinel phase to the applied pressure can be explained in terms of the different pressure response of the elementary polyhedra [2, 31]. It is to be noted that the occupied tetrahedra are regular regardless the value of u; however, the occupied octahedra are distorted (they are regular only at $u = 0.25$). In general, direct spinels respond to pressure trying to reach the ideal structure with non-distorted octahedral polyhedra. The ideal spinel is characterized by $u = 0.25$, and therefore since u is larger than this value in direct spinels u decreases with increasing pressure. Regarding the cation-anion bond lengths at the tetrahedral and octahedral interstices, d_{A-O} and d_{B-O}, respectively, the distances of oxygens to trivalent cations are less compressible than those to divalent ones, as expected since d_{B-O} is shorter than d_{A-O} [31]. These are the general trends for the direct oxide spinels listed in Table 4.1.

The disorder parameter, x, of $MgGa_2O_4$ is close to the inverse limit, and so it is interesting to study this spinel in both structures. Structural properties for $MgGa_2O_4$ calculated in the direct as well as in the indirect spinel structure by Recio et al.

Table 4.1 Zero pressure lattice constant a_0 (in Å), internal parameter u, bulk modulus B_0 (in GPa), and its pressure derivative B_0' for some spinels. Calculated values are compared with experimental available data

Compound	Theory					Experiment				
	a_0	u	B_0	B_0'	Ref.	a_0	u	B_0	B_0'	Ref.
$MgAl_2O_4$	7.782	–	206.43	–	[27]	8.08	0.386	191	6.7	[32]
	8.161	–	186	4(fix.)	[28]					
	8.0747[a]	0.2644	208	3.20	[29]					
	8.0072[b]	0.2644	198	3.38	[29]					
	8.027	0.263	202.18	4.14	[30]					
$MgGa_2O_4$	8.460[a]	0.2616	163	3.75	[29]	8.280	0.3790	–	–	[33]
	8.3122[b]	0.2616	188	3.67	[29]					
	8.283	0.2563	–	–	[21]					
	8.021	0.2683	204.56	3.80	[31]					
(inverse)[c]	7.969	0.2559	215.30	3.65	[31]					
$MgIn_2O_4$	9.1022[a]	0.2561	132	3.9	[29]	8.810	0.3820	–	–	[33]
	8.9447[b]	0.2558	146	4.16	[29]					
	8.846	0.2598	–	–	[21]					
$ZnAl_2O_4$	8.321	0.2651	236.77	5.129	[34]	8.086	0.2654	201.7	7.72	[37]
	8.020	0.2638	219.65	4.02	[25]					
$ZnGa_2O_4$	8.603	0.2614	227.23	6.837	[34]	8.341	0.2599	233	8.3	[37]
	8.4412	–	163.46	4.40	[36]					
	8.289	0.2608	218.93	4.35	[35]					
$ZnIn_2O_4$	9.092	0.2555	148.70	5.388	[34]					
$CdAl_2O_4$	8.3844	0.2697	187	4.133	[38]	8.355				[38]
$SnMg_2O_4$	8.709[a]	0.2557	151.48	4.881	[39]	8.600	0.3750	–	–	[33]
	8.557[b]	0.2569	182.92	4.893	[39]					
	8.642	0.2585	–	–	[21]					
$SnZn_2O_4$	8.785[a]	0.2555	150.95	4.700	[39]	8.657	0.3900	–	–	[33]
	8.569[b]	0.2574	191.78	4.948	[39]					
	8.658	0.2583	–	–	[21]					
$SnCd_2O_4$	8.6310[a]	0.2502	124.19	4.551	[39]	9.143	0.3920	–	–	[33]
	9.112[b]	0.2491	161.87	4.998	[39]					
	9.164	0.2623	–	–	[21]					
$MgIn_2S_4$	10.611	–	78.7	4.16	[5]	10.707	–	76	2.8	[5]
	10.917	0.2565	66.53	4.95	[40]					
$MgIn_2S_4$ (direct)[c]	10.666	–	75.4	4.3	[5]					
$MgMn_2S_4$	10.629	–	80	3.9	[5]	10.714	–	78	3.2	[5]
$ZnAl_2S_4$	10.039	–	78.91	3.97	[36]					
$CdIn_2S_4$	10.748	–	79.8	4.65	[5]	10.841	–	78	3.1	[5]
	11.107	0.2616	66.90	5.17	[40]					
$CdCr_2Se_4$	10.375	0.2664	92.0	4.59	[25]	10.743	–	101.2	5.2	[25]
$CuCr_2Se_4$	10.308[a]	0.258	69.1	–	[41]	10.357	–	96	–	[41]
	9.982[b]	0.257	112.4	–	[41]					
$ZnCr_2Se_4$	10.334	–	78.448	3.962	[42]	10.443	–	98	–	[41]
	10.572	0.261	79.0	–	[41]					
	10.265	0.260	119.7	–	[41]					

[a] GGA, [b] LDA, [c] Hypothetical structure

[31] are given in Table 4.1. The effect of the hydrostatic pressure on the internal parameter u in inverse spinels is different with respect to that found in direct ones. In inverse spinels $\partial u/\partial P > 0$ due to the different occupancies of the tetrahedral and octahedral interstices [31]. The unit cell of inverse spinels has eight tetrahedral interstices occupied by B cations and 16 octahedral interstices equally shared by A and B cations. Since tetrahedra are regular in the spinel structure at any value of u, it is the constraint to keep regular octahedra what forces u to increase with pressure in inverse spinels [31]. In the case of $MgGa_2O_4$, the cation–anion distances are $d_{Ga-O} = 1.946$, 1.807 Å (at octahedral and tetrahedral sites respectively) and $d_{Mg-O} = 1.946$ Å. As expected, the shortest d_{Ga-O} distance (1.807 Å) shows the lowest compressibility.

Some studies on the behavior of structural properties under pressure have been performed in other oxide spinels like SnB_2O_4 (B = Mg, Zn, and Cd) [26, 39, 43]. The calculated lattice constant and internal parameter agree at zero pressure with experimental results. As expected the bulk modulus B_0 decrease in the following sequence $SnMg_2O_4 > SnZn_2O_4 > SnCd_2O_4$ [39]. Authors of [26] and [43] found $SnZn_2O_4$ stable in the inverse spinel structure.

Finger et al. [44] observed that normal spinel oxides (AB_2O_4) behave in a similar way under hydrostatic pressure. The bulk moduli of these compounds are about 200 GPa for all of them. This result was confirmed by many experiments [5], and was justified by Pendás et al. and Recio et al. [31, 45] on the basis of polyhedral analysis. The explanation is based on the fact that the oxygen anions form a nearly close-packed *fcc* structure, accounting for most of the crystal volume, on the other hand the cations A and B are low-compression chemical species. Therefore, the overall bulk compressibility is determined mainly by the oxygen sublattice. These works suggest that the compressibility of spinels is governed by the anion sublattice.

Waskowska et al. [25, 41] have studied the normal selenide spinels $CdCr_2Se_4$, $CuCr_2Se_4$, and $ZnCr_2Se_4$. The ferromagnetic character of these compounds was simulated by means of spin-polarized calculations. Although the calculations for $CdCr_2Se_4$ were based on the local density approximation (LDA) and that of $CuCr_2Se_4$, and $ZnCr_2Se_4$ were performed on the generalized gradient approximation (GGA), the authors found a similar bulk modulus for this family of compounds. Thus confirming that the compressibility of selenide spinels is governed by the selenium (anion) sublattice. The bulk modulus of selenium spinels is lower than the bulk modulus of oxide spinels, mainly due to the greater size and greater polarizable character of the Se anion compared to the O anion [25].

Bulk modulus calculations were recently reported by Santamaría-Pérez et al. for sulfur spinels AIn_2S_4 (A = Cd, Mg and Mn) [5]. The calculated bulk modulus of this family of compounds is very similar $B_0 = 79.8$, 78.7, and 80 GPa for $CdIn_2S_4$, $MgIn_2S_4$, $MnIn_2S_4$, respectively, in very good agreement with experimental results (see Table 4.1). The fact that the values of bulk moduli are so similar can also be explained on the light of [31]: the sulfur atoms form the anion sublattice that determines the compressibility of AIn_2S_4 compounds.

Sulfide and selenide spinels have a bulk modulus significantly lower than that of oxide spinels and thus have much greater compressibility. Since the bulk modulus

of normal oxide spinels is about 200 GPa and the bulk moduli for of selenide spinels is approximately 90 GPa one would expect the values for the sulfur spinels in between, due to the size of S in between the size of O and Se, and if we consider that long bonds are more compressible than short bonds. For instance, the In–S distances in indium thiospinels (2.60–2.64 Å) [5], are smaller than In–Se distance (2.73 Å). However the available data do not confirm this hypothesis [5]. Nevertheless, comparing the bulk moduli B_0 and unit cell volume at equilibrium V_0 of selenium ($CdCr_2Se_4$, $CuCr_2Se_4$ and $ZnCr_2Se_4$) and sulfur ($CdIn_2S_4$, $MgIn_2S_4$, $MnIn_2S_4$) spinels the empirical B_0–V inverse law seems to work quite well. In conclusion, more theoretical and experimental work needs to be done to understand the anomaly of the bulk modulus of thiospinels.

Lattice and internal parameters of sulfide and selenide spinels decrease with increasing pressure. For the direct selenide spinel $ZnCr_2Se_4$ the lattice constant depends on pressure as $a = 10.3325(0.9986 - 0.00327\,P + 2.63128 \times 10^{-5}P^2)$ and the Cr–Se distance as $d_{Cr–Se} = 2.49029(0.99825 - 0.00296\,P + 2.40018 \times 10^{-5}P^2)$, where P is pressure in GPa, and a and $d_{Cr–Se}$ are expressed in Å [42]. As for sulfur spinels AIn_2S_4 (A = Cd, Mg and Mn) theoretical calculations show that the internal parameter u decreases slightly with a non-linear pressure dependence from its initial value towards $u = 0.25$ in agreement with experiments [5, 46]. On the basis of the polyhedral analysis, Recio et al. [31] explained the increase of u with the pressure for inverse oxide spinels. The same behavior could be expected for the inverse $MgIn_2S_4$ however calculus and experiments show a decrease of u with pressure.

Although in the range of low pressure the inverse spinel structure is thermodynamically more stable than the normal spinel structure for $MgIn_2S_4$ from the experimental point of view, in [5] calculations were done to compare both structures. The bulk modulus of the inverse spinel is around 4.4 % larger than that of the normal spinel. A similar result is found in [31], the bulk modulus of the inverse $MgGa_2O_4$ is about 5.3 % larger than that of the normal spinel, and in [25] for the $CdGa_2Se_4$ analyzed in the hypothetical direct and inverse spinel structures. Hence it could be argued that there also exits a dependence of the compressibility of the spinels on the degree of inversion.

4.3 Elastic Properties

Cubic crystals, as Fd-3m spinels, have only three independent elastic constants C_{11}, C_{12}, and C_{44}. Under hydrostatic pressure a cubic crystal is mechanically stable when the generalized Born stability criteria [47] are simultaneously satisfied:

$$C_{11} + 2C_{12} + P > 0, C_{44} - P > 0, C_{11} - C_{12} - 2P > 0 \tag{4.1}$$

Magnesium aluminum spinel ($MgAl_2O_4$) exhibits several desirable properties, and plays an important role in geophysics and therefore has been the subject of

many experimental and theoretical studies. Since the pioneering work of Catti et al. [48] the elastic constants at ambient conditions in a number of spinels have been calculated by several authors (see Table 4.2). Furthermore, Bouhemadou et al. [29] and Caracas et al. [49] have reported the evolution with pressure of the elastic constants. Bouhemadou et al. performed the first principles calculations using DFT whereas Caracas et al. used the Density Functional Perturbation Theory (DFPT) [53, 54]. As can be seen in Table 4.2 the results obtained with both formalisms are very similar. The C_{11} and C_{12} elastic constants increase linearly with pressure, being the variation of C_{44} very weak.

The elastic constants enable to obtain the bulk modulus, $B_0 = (C_{11} + C_{12})/3$, which is the inverse of the compressibility and it is related to the resistance of the material to hydrostatic pressure. Caracas et al. [49] obtained from the above equation a bulk modulus of $B_0 = 205$ GPa for $MgAl_2O_4$ in excellent agreement with the bulk modulus $B_0 = 202$ GPa obtained from fitting the theoretical data to a $3rd$ order Birch–Murnaghan equation of state. These authors found that the anisotropy ratio, $A = 2C_{44}/kl$, is 1.72 at ambient pressure. This value indicates a large anisotropy of the elastic properties. The anisotropy ratio increases almost linearly up to 20 GPa, then it slightly deviates upward. It should be noted that $MgAl_2O_4$ decomposes in a mixture of oxides at about 15 GPa (see Table 4.8). The isotropic compressional (V_p) and shear (V_s) wave velocities calculated for homogeneous polycrystalline aggregates change with pressure as: $V_p = 9.824 + 0.021P$ (km/s) and $V_s = 5.518 - 0.014$ P (km/s). These results are in agreement with the experimental observations [55].

The elastic constants and their pressure derivatives for a number of oxospinels are listed in Table 4.2. The results are obtained with various calculations employing LDA or GGA approximation for the exchange and correlation energy and pseudopotential and all-electron implementations. The theoretical values are compared with experiments when available. The overall trends are that the elastic constants vary linearly with pressure and the elastic constants C_{11} and C_{12} increase and are more sensitive to pressure than are the C_{44}. The small variation of the C_{44} with pressure is a characteristic of the oxide spinels (see Table 4.2) due to the coupling between atomic displacements and shear strains [49]. The low values of C_{44} reflect a weak resistance to shear deformation. Pressure coefficients of C_{44} are even negative for some spinels as $MgIn_2O_4$, $CdAl_2O_4$, $CdGa_2O_4$, and $CdIn_2O_4$. This behavior could indicate a possible mechanical instability that would result in a phase transition under pressure.

There are few theoretical data on the evolution of the properties of the thiospinels under pressure. The elastic constants were calculated for $CdIn_2S_4$ and $MgIn_2S_4$ [40, 46]. The elastic constants for $MgIn_2S_4$ are very similar to those of $CdIn_2S_4$ as shown in Table 4.2. For both compounds C_{11} is higher than C_{44} so in these materials the resistance to the shear deformation is weaker than the resistance to compression [40, 46]. The first pressure derivatives of the elastic constants: $\partial C_{11}/\partial P$, $\partial C_{12}/\partial P$ and $\partial C_{44}/\partial P$ are listed in Table 4.2. For both compounds, C_{11} and C_{12} elastic constants increase linearly with increasing pressure while C_{44} is much less sensitive to pressure and indeed decrease with increasing pressure. This behavior

Table 4.2 Calculated elastic constants C_{ij} (in GPa), linear pressure coefficient $\partial C_{ij}/\partial P$, bulk modulus $B_0 = (C_{11} + 2C_{12})/3$ (in GPa), and its pressure derivative $\partial B_0/\partial P$. Calculated values are compared with available data

	C_{11}	C_{12}	C_{44}	$\partial C_{11}/\partial P$	$\partial C_{12}/\partial P$	$\partial C_{44}/\partial P$	B_0	$\partial B_0/\partial P$	Ref.
$MgAl_2O_4$	324	163.77	184.05	–	–	–	206.4	–	[27]
	293.32	157.09	150.26	–	–	–	202.5	–	[30]
	292	162	161	3.55	4.05	0.6	205	4.27	[49]
	262	140	154	3.107	3.19	0.162	180	3.37	[29][a]
	276	154	153	2.59	3.79	0.29	196	3.16	[29][b]
	378	140	124	–	–	–	220	–	[50]
Exp.	281.31	155.44	154.59	–	–	–	197.4	–	[51]
$MgGa_2O_4$	233	129	112	3.083	3.894	0.014	163	3.597	[29][a]
	262	145	118	2.45	4.31	0.005	186	3.7	[29][b]
$MgIn_2O_4$	182	96	68	2.266	4.097	−0.228	125	3.794	[29][a]
	213	114	71	2.39	4.56	−0.305	147	3.82	[29][b]
$ZnAl_2O_4$	450.08	136.83	158.36	8.8372	2.8924	2.9248	241.25	4.874	[34]
	436	171	139	–	–	–	260	–	[50]
Exp.							201.7	7.62	[37]
$ZnGa_2O_4$	390.41	142.77	113.77	9.1480	3.1440	3.0464	225.25	5.1453	[34]
Exp.							233	8.3	[37]
$ZnIn_2O_4$	331.95	107.66	112.93	8.8664	3.2322	2.5896	182.43	5.1204	[34]
$SnMg_2O_4$	289.04	135.24	75.40	7.5459	4.4635	1.5744	186.51	5.4910	[39]
	180	107	90	2.88	4.65	0.43	133.58	4.06	[52][a]
	228	132	102	2.43	4.84	0.33	163.98	4.12	[52][b]
$SnZn_2O_4$	250.75	161.36	42.74	6.8886	3.8240	1.5424	191.16	4.8456	[39]
$SnCd_2O_4$	227.10	128.69	48.55	7.2600	3.7842	1.7261	161.50	4.9428	[39]
$CdAl_2O_4$	292	134	78	6.6156	2.8912	1.8611	187	4.133	[38]
	231	149	115	3.306	3.700	−0.231	180	2.1054	[29]
$CdGa_2O_4$	203	130	91	2.840	4.643	−0.414	154	4.028	[29]
$CdIn_2O_4$	159	102	57	2.982	4.988	−0.463	121	4.188	[29]
$MgIn_2S_4$	95	64	38	2.88	4.88	−0.02	74.3	4.2	[46]
	102.34	48.62	26.11	7.55	3.67	1.92	66.53	4.95	[40]
Exp.							78		[5]
$CdIn_2S_4$	96	69	38	3.30	5.02	−0.05	78.0	4.44	[46]
	102.46	49.13	21.46	6.42	4.54	1.48	66.90	5.17	[40]
Exp.							78		[5]

[a] GGA, [b] LDA

of C_{44} indicates that a phase transition can take place under pressure in $CdIn_2S_4$ and $MgIn_2S_4$ at rather small pressures what is in good agreement with experimental findings [3]. In fact, as expected, the elastic constants of thiospinels are smaller than those of oxospinels but behave similarly under pressure. The two thiospinels $CdIn_2S_4$ and $MgIn_2S_4$ satisfy the generalized Born stability criteria (4.1) up to 8 GPa indicating that they should be in the cubic spinel structure up to a pressure of about 8 GPa. This is in agreement with experimental results that report transition pressures of 8 and 12 GPa [3–5].

4.4 Electronic Structure

The evolution of the electronic band structure under pressure of several spinel oxides and thiospinels has been analyzed performing first-principles calculations within the framework of the DFT. Of course, it is well known that DFT systematically underestimates the band gap, but the pressure evolution and the symmetry of the band gap are usually well described [56].

The prototypical spinel $MgAl_2O_4$ is a direct band gap semiconductor at ambient conditions. The direct band gap ($\Gamma-\Gamma$) at ambient pressure varies from 5.5 to 7.90 eV depending on the computational method used [2, 57–59]. The total and atomic site projected density of states (DOS) indicates the nature of the electronic band structure. For $MgAl_2O_4$ and $ZnAl_2O_4$, the upper valence band is composed from O 2*p* states. A significant contribution of Zn 3*d* states occurs in $ZnAl_2O_4$, indicating a strong hybridization of O and Zn states. On the other hand, the conduction band is composed of *s* and *p* states of Mg (Zn) and Al atoms in $MgAl_2O_4$ ($ZnAl_2O_4$) [50].

Gracia et al. [2] have studied the effect of pressure on the direct band gap of $MgAl_2O_4$ up to 65 GPa. They found a direct band gap ($\Gamma-\Gamma$) of 7.90 eV in good agreement with the experimental value (7.8 eV) [60]. The gap increases with pressure at a rate of 47 meV/GPa, while the valence bandwidth increases 0.025 eV/GPa. Khenata et al. [50] found a lower value of 5.5 eV and a quadratic variation of the gap with pressure $E_g\ (P) = E_g\ (0) + b\ P + c\ P^2$, where E_g (P) is the band gap energy at the pressure P and b and c are the first and second order pressure coefficients, respectively. The values of E*g*(0), b and c for several spinels are summarized in Table 4.3.

The behavior of the band gap in spinel oxides $ZnAl_2O_4$, $ZnGa_2O_4$, and $ZnIn_2O_4$ under pressure was investigated by Zerarga et al. [34]. The Engel–Vosko scheme (GGA–EV) was applied for the electronic properties. The GGA–EV is a functional form of the GGA. This approach yields a better band splitting, on the other hand, in this method the equilibrium volume and the bulk modulus are in poor agreement with experiments [34]. At ambient pressure $ZnAl_2O_4$ and $ZnIn_2O_4$ have direct band gaps ($\Gamma-\Gamma$) of 4.44 and 1.82 eV, respectively, while $ZnGa_2O_4$ has an indirect band gap, K–Γ, of 2.69 eV. These results compare well with other theoretical findings [35, 63]. Experimental values reported for the gap are 3.8–3.9 eV in the case of $ZnAl_2O_4$ and 4.1–4.3 eV for $ZnGa_2O_4$ [61]. The upper valence bands of the $ZnAl_2O_4$ are composed mostly of hybridized O-2*p* and Zn-3*d* state with a very small contribution from Al-*s,p,d* states. In the cases of $ZnGa_2O_4$ and $ZnIn_2O_4$ a new structure appears in the density of states, originated from the contribution of Ga-3*d* and In-4*d* electrons to the valence bands, respectively. The bottom of the conduction band of all the tree compounds is composed predominantly by Zn-*s* states. The *p–d* hybridization at Γ repels upwards the valence band maximum without affecting the conduction band minimum, so the lowering of the band gap from the $ZnAl_2O_4$ to the $ZnIn_2O_4$ [34]. When pressure increases the energy gaps of $ZnAl_2O_4$, $ZnGa_2O_4$, and $ZnIn_2O_4$ spinels increase and fit well to a quadratic function (see Table 4.3). Brik also found an indirect gap for $ZnGa_2O_4$ but at L–Γ [36]. The band gap of 4.15 eV agrees with the experimental value and increases with at a linear rate of 0.028 eV/GPa, which is lower than other reported values [34].

Table 4.3 Calculated band gap $E_g(0)$ at zero pressure (in eV) and first and second pressure derivatives, b and c, respectively, of the band gap for some spinels. The band gap can be fitted as $E_g(P) = E_g(0) + bP + cP^2$, b is in 10^{-2} eV $(GPa)^{-1}$, c is in 10^{-4} eV $(GPa)^{-2}$

Compound	Type	E_g (0)	b	c	Ref.
$MgAl_2O_4$	Γ−Γ	7.90	4.7	0	[2]
	Γ−Γ	5.55	4.34	−3.56	[50]
Exp.	Γ−Γ	7.8	–	–	[58]
$ZnAl_2O_4$	Γ−Γ	4.24	–	–	[35]
		4.443	1.97	1.01	[34]
Exp.	–	3.90	–	–	[61]
$ZnGa_2O_4$	K–Γ	2.78	–	–	[35]
		2.686	3.14	−2.39	[34]
	L–Γ	4.145	2.8	0	[36]
$ZnIn_2O_4$	Γ−Γ	1.817	−0.45	20.30	[34]
Cd Al_2O_4	Γ−Γ	3.669	2.929	−2.250	[38]
$SnMg_2O_4$	Γ−Γ	2.47, 1.85	3.239, 40.05	−292, −42.9	[52]
		2.823	4.54	−4.22	[39]
$SnZn_2O_4$	Γ−Γ	1.155	1.90	−1.17	[39]
$SnCd_2O_4$	Γ−Γ	0.735	2.97	−1.82	[39]
$MgIn_2S_4$	Γ−Γ	2.24	1.5	0	[40]
Exp.	direct	2.28	2	–	[4]
$CdIn_2S_4$	K−Γ	1.92	5.3	0	[40]
Exp	direct	2.35	7	0	[4]
$ZnAl_2S_4$	(L−Γ)−Γ	3.407	−0.8	0	[36]

The band gap can be fitted as $E_g(P) = E_g(0) + bP + cP^2$, b is in 10^{-2} eV $(GPa)^{-1}$, c is in 10^{-4} eV $(GPa)^{-2}$

Theory predicts that the oxide spinel $CdAl_2O_4$ has a direct band gap of 3.67 eV at Γ [38]. The top of the valence band is similar to that of $ZnAl_2O_4$, with hybridization of Cd-4*d* and O-2*p* states while the lower conduction bands result from Cd-3*s* states. With pressure increase the band gap increases and can also be fitted to a quadratic function (see Table 4.3).

The effects of pressure on the energy band gaps of $SnMg_2O_4$, $SnZn_2O_4$, and $SnCd_2O_4$ have also been investigated. As expected, the upper valence bands are composed mostly of O-2*p* states in $SnMg_2O_4$, while in $SnZn_2O_4$, and $SnCd_2O_4$ the Zn-3*d* and Cd-4*d* states, respectively, hybridize strongly with the oxygen *p* states. As for the bottom of the conduction band, it is predominantly composed of Sn-*p* state in the tree compounds. The band gaps (2.823, 1.155, and 0.735 eV at ambient pressure for $SnMg_2O_4$, $SnZn_2O_4$, and $SnCd_2O_4$, respectively) are direct at Γ and increase quadratically with pressure [39]. Gracia et al. found a direct gap of 3.46 eV at ambient pressure for $SnZn_2O_4$ [26] in good agreement with experimental data (3.6–3.7 eV) [64] and a composition of the conduction band somewhat different since the Zn 4*s*, p_x, and p_y dominate over the Sn 5*s* contribution.

Similar calculations for thiospinels are scarce. In the case of $ZnAl_2S_4$ the gap reported is 3.41 eV, indirect at Γ [36] which agrees with the experimental result of 3.42 eV [65]. The upper valence band and the bottom of the conduction band are different from the corresponding Zn-oxide spinel $ZnAl_2O_4$. The lower part of the conduction band is formed by Al 3*s* and 3*p* states hybridized with the S 3*p* states. The upper part of the valence band is a mixture of the S 3*p* states and Al 3*s* and 3*p* states while the main contribution of Zn 3*d* states is localized in the lower part. The band gap of $ZnAl_2S_4$decreases linearly with pressure at a rate of −0.008 eV/GPa [36]. Usually, direct band gaps increase with pressure but the same is not true for indirect band gaps. Nevertheless examples of decreased band gaps with applied pressure have been reported for a number of compounds including spinels [3, 21, 27]. The reason for such behavior can be either the high covalency of the chemical bond or significant redistribution of the electron density in the space between the atoms. The $ZnAl_2S_4$ is a more covalent compound than $ZnAl_2O_4$, with a quite considerable contribution of the sulfur ions into the conduction bands [36].

The structure of the electronic bands and the density of state of thiospinels $CdIn_2S_4$ and $MgIn_2S_4$ have been analyzed theoretically by several authors [7, 16, 40, 66, 67]. Lucero et al. [67] performed calculations in the DFT scheme employing different exchange–correlation functionals. The resulting band structures for the direct $CdIn_2S_4$ and totally inverse $MgIn_2S_4$ (the structure experimentally observed) exhibit all of them a flat non-dispersed character in the valence band; however, the conduction band exhibits a high degree of structure, as also observed for oxospinels [35]. The conduction bands for both thiospinels have a similar curvature at the bottom of the conduction band, with a clear separation between the In 5*s* and the S 3*p* orbitals, being the latter slightly higher in energy.

The calculated band gap of direct spinel $CdIn_2S_4$ is indirect with a value between 1.7 and 2.33 eV as reported by different authors [40, 66, 67]. Reported experimental band gaps are on the order of 2.1–2.7 eV [4, 67]. Although there is agreement, from the theoretical point of view, about the indirect nature of the gap and that the conduction band minimum occurs at the Γ point, there is still some controversy about the valence band maximum: at the K point [40] or along the X–W direction [66]. From the total and partial density of states [40, 66] it is clear that the topmost of the valence band consists mainly of S 3*p* states and the structure at the lower part of the upper valence bands originates from a mixture of In *s* and S *p* states. The lowest conduction band is formed mainly by In 5*s* and Cd 5*s* states hybridized with S *p* states. This indicates that the value of the band gap is determined by the In–Cd interaction, because the dispersion of the bottom conduction band depends on this interaction [66]. Although the experimental and calculated values for the gap agree, some experiments found a direct gap in $CdIn_2S_4$ [4] so there is also some controversy as to whether this gap is direct or indirect [66]. The calculated difference between the direct and the indirect gap is very small, this is maybe the responsible for the disagreements about the nature of the transition [66, 67]. In this respect, the effect of pressure on the band gap energy for $CdIn_2S_4$ was theoretically investigated [43].

The direct gap (Γ–Γ) and the indirect gap (K−Γ) increase with pressure coefficients of 53 and 34 meV/GPa, respectively, while the experimental pressure coefficient for the direct gap is 70 meV/GPa [4].

Seminovki et al. [16] and Lucero et al. [67] also studied the value of the band gap as a function of the degree of inversion of the spinel for $CdIn_2S_4$. Lucero et al. performed electronic structure calculations within the DFT scheme and compared the calculated band gap obtained with four different functionals for the exchange-correlation energy, for the normal and full inverse configurations of $CdIn_2S_4$. For the normal direct spinel structure the four functionals predict an indirect gap of 2.33 eV. The direct gap is approximately 10 meV higher than the indirect gap. The experimentally unobserved full inverse spinel also has an indirect band gap, whose predicted value is 1.2 eV, being the direct gap only 1 meV higher. Consequently, the gap narrows with increasing of cation inversion as a consequence of order–disorder phenomena [67, 68]. Seminovski et al. [16] presented theoretical results suggesting that the degree of inversion could be modified by changing the synthesis temperature [69] and that even a moderate change in the degree of inversion leads to significant change in the band gap of the material. The effect of inversion on the band gap is quite drastic, a decrease of almost 1 eV is found in both (direct an inverse) gaps of $CdIn_2S_4$ when the degree of inversion change from 0 to 0.5 [16].

The band gap for the inverse spinel $MgIn_2S_4$ is found to be direct at Γ [40] in agreement with the experimental finding [4] although the predicted theoretical value varies from 0.9 [66] and 2.24 eV [40]. The top valence band has mainly S 3*p* character as for the $CdIn_2S_4$, but the bottom of the conduction band is formed mostly by In *s* states and the Mg 3*s* contribute to both the valence and conduction bands, while they contribute not at all in the bands of relevance to the gap in the normal (direct) ordering [40, 67]. The direct band gap increases linearly with pressure with a coefficient of 15 meV/GPa [40] which compares nicely with the experimental value (20 meV/GPa) [4].

As for the $CdIn_2S_4$, Lucero et al. [67] also calculated the band gap for the normal, full inverse, and an intermediate configuration of $MgIn_2S_4$. For the fully inverse structure, the four functionals predict an indirect band gap of 1.98 eV close to the experimental one (2.1–2.3 eV) [4], in contrast with the findings of [40, 66]. For the unobserved direct spinel $MgIn_2S_4$ the band gap is found to be direct with a predicted value of 2.83 eV. For the partial inverse structure ($x = 0.84$) the band gap also is found to be indirect with prediction of 2.04 eV.

In summary, an overall trend of oxospinels and thiospinels is that all the gaps decrease as the cation ordering becomes more inverted [59]. It must been taken into account when comparing experimental and theoretical results, that all the spinels have some degree of inversion which is not taken into account when simulating full direct or full inverse structures.

4.5 Vibrational Analysis

The primitive unit cell of cubic spinel contains two formula units, i.e., 14 atoms. Therefore, there are 42 normal modes, of which three are acoustic modes and 39 are optical modes. According to group theory, the irreducible representations of phonon modes at the Brillouin zone center, Γ, are:

$$\Gamma = A_{1g}(R) + E_g(R) + T_{1g} + 3T_{2g}(R) + 2A_u + 2E_u + 5T_{1u}(IR) + 2T_{2u} \quad (4.2)$$

where (R) stands for Raman active and (IR) stands for infrared active, so five modes are Raman active modes, five are infrared active modes and the remaining optical modes are silent.

The study of spinel is complicated as the degree of inversion depends on the growth conditions [67] and it is well known the fact that spectra of different samples of $MgAl_2O_4$ are qualitatively different [70]. From Raman spectroscopy only four of the five allowed modes have been reported for natural spinel, the occurrence of another mode has been attributed to cationic disorder [71]. The proper assignment of the vibrational modes in $MgAl_2O_4$ is a longstanding problem. In particular, in the Raman spectra of natural spinel, above 600 cm^{-1}, there are only two peaks at $\sim$ 670 and 770 cm^{-1} but, an additional well defined peak is observed at 727 cm^{-1} in synthetic spinels [72]. This peak was related to the structural disorder by Cynn et al. [72] and attributed to the tetrahedral breathing mode of AlO_4.

Ab initio infrared and Raman phonon modes in the normal cubic spinel $MgAl_2O_4$ were calculated at the first Brillouin zone center at ambient pressure [71, 73, 74]. Table 4.4 shows the general agreement of the computed phonon frequencies with the experimental ones for natural spinel $MgAl_2O_4$ [76]. Calculations of de Wijs et al. [71] confirmed the assignment of the mode observed at 727 cm^{-1} by Cynn et al. [72]. The Raman spectra of $MgAl_2O_4$ have been computed for the perfect and the partially inverse spinel crystal by Lazzery and Tibaudeau [70]. The spectrum calculated for the perfect direct spinel agrees well with the measured spectrum of natural spinel. They found five Raman active modes, however the T_{2g} mode at $\sim$ 557 cm^{-1} is very weak and so is not visible experimentally and there is not a Raman active mode in correspondence with the 727 cm^{-1} peak observed in synthetic spinels. On the other hand, in the calculated Raman spectrum for a partially inverse structure (x = 0.3) a well-defined peak at $\sim$727 cm^{-1}, similar to the one observed in synthetic spinel, is clearly visible. Studies on the character of the peak conclude, contrary to previous assignment, that this mode is due to a phonon that is silent in the perfect crystal and become Raman active in the partially inverted structure because of the coupling with the tetrahedral breathing mode of Mg [70].

The variation with pressure of the optical modes in $MgAl_2O_4$ has been analyzed by Caracas et al. [49]. The low-frequency modes show a weak dependence with pressure, while the frequencies of the other modes increase under compression. The infrared modes show an increasingly large LO–TO splitting at high frequencies. On the other hand, there are not experimental data about the behavior of $ZnSn_2O_4$

Table 4.4 Vibrational modes (in cm^{-1}) of $MgAl_2O_4$ spinel at ambient conditions in the Γ point

Mode Symmetry	Theory			Exp.
	ω_0 [73]	ω_0 [71]	ω_0 [75]	ω_0 [76]
T_{2u}	191	265		
T_{1u}(IR) (TO)	307	311	325	304
(TO)	309	319	327	312
T_{2g}(R)	309	319		312
T_{1g}	315	360		
E_u	392	412		
E_g(R)	680	426		407
T_{2u}	495	483		
T_{1u}(IR) (TO)	478	512	476	476
(TO)	612	580	583	610
T_{2g}(R)	553	570		
T_{1u}(IR) (TO)	564	588	595	575
(TO)	565	638	631	578
E_u	602	608		
A_{2u}	669	668		
T_{2g}(R)	661	682		666
T_{1u}(IR) (TO)	666	698	684	676
(TO)	854	866	851	868
A_{2u}	742	763		
A_{1g}(R)	760	776		767

under compression. However, the vibrational modes of the inverse spinel $ZnSn_2O_4$ are predicted to show pressure coefficients in the range of 0.7 to 5.4 cm^{-1}/GPa [26].

Vibrational properties of $ZnAl_2O_4$ and $ZnGa_2O_4$ spinels under hydrostatic pressure have been reported by López et al. [35, 77]. Calculations were performed in the framework of the density functional theory DFT. The mode frequencies at ambient conditions agree well with other theoretical calculations [77, 78] and experimental results [76, 77, 79]. The total density of states exhibits a expectrum that extends up to ∼800 cm^{-1}without gap. The partial density of states (PDOS) of $ZnAl_2O_4$ shows the contribution of each ion to the spectrum. The low-frequency region is mainly due to Zn ions, while the Al and O ions are involved in the remaining vibrational modes over a wide range with a major contribution of O ions. Near the end of the spectrum the O contributions are the predominantly ones [77, 78]. In the case of $ZnGa_2O_4$ the low-energy region is dominated by the motion of Zn and Ga ion, and in the high frequencies the major contribution comes from O ions, like in $ZnAl_2O_4$. This difference occurs because Ga has a greater mass than Al [77]. The $ZnAl_2O_4$ spinel is isostructural with $MgAl_2O_4$, and the ionic radius and local bonding environment of Zn and Mg are similar on both compounds. Fang et al. explained that the difference in their phonon spectra is due to the difference of mass between Zn and Mg [78].

These authors showed that the T_{2g} and T_{1u} modes that contain a great contribution from Zn or Mg vibrations are the more influenced by the effect of the mass, while the others modes have smaller changes.

Tables 4.5 and 4.6 summarize the calculated and experimental modes of $ZnAl_2O_4$ and $ZnGa_2O_4$ and their pressure coefficients. A good agreement is found between calculated and measured values. The lowest Raman modes (the low T_{2g} and the E_g) have a significantly smaller pressure coefficient than the others modes while the high frequency A_{1g} mode has the largest pressure coefficient. The small pressure coefficient of the low-frequency T_{2g} mode is related to the fact that the Zn–O bonds are shorter, and less compressible than the B–O bonds in all spinels, as the T_{2g} mode switch the Zn–O distance, this mode is almost unaffected when the pressure increases. The largest pressure coefficient of the A_{1g} mode suggests that the band stretching has a larger force constant than the bond bending. A similar behavior has been found in $MgAl_2O_4$ [49] and experimentally in $ZnFe_2O_4$ and $ZnCr_2O_4$ [80, 81]. This suggests a systematic behavior of these vibrational modes in spinels. Moreover, the lowest T_{1u} infrared mode is almost not affect by compression and the highest mode has a much larger pressure coefficient than the other modes. Calculations suggest a non-linear behavior under pressure in the second IR T_{1u} mode of $ZnAl_2O_4$ and the first IR T_{1u} mode of $ZnGa_2O_4$ [77].

Finally, there have been very few ab initio studies of vibrational properties on thiospinels. The phonons at ambient pressure have been calculated for some thiospinels, Marinelli et al. [10] calculated only one zone center phonon Γ for the direct, inverse and partially inverse spinel $MgIn_2S_4$. The Raman and infrared modes were studied for the ferromagnetic $CdCr_2S_4$ by Fennie et al. [82]. The Raman and infrared modes of $CdIn_2S_4$ have been calculated by Seminovski et al. [16].

We report here for the first time the calculated pressure dependence of phonons for the direct $CdIn_2S_4$ spinel. The ab initio calculations were performed within the DFT scheme using the exchange correlation energy described by the LDA approximation. Figure 4.2 shows the calculated total and partial densities of states (PDOS).

The total DOS extends up to about 375 cm^{-1}. The low frequency region is due mainly to In ions motion with a peak at ~75 cm^{-1} due to Cd ions. From ~90 to

Table 4.5 Calculated and experimental Raman modes (in cm^{-1}) of $ZnAl_2O_4$ and $ZnGa_2O_4$ and their pressure derivatives (in cm^{-1}/GPa)

Raman mode symmetry	$ZnAl_2O_4$				$ZnGa_2O_4$			
	Theory		Experiment		Theory		Experiment	
	ω_0 [35]	$d\omega/dP$ [77]	ω_0 [77]	$d\omega/dP$ [77]	ω_0 [35]	$d\omega/dP$ [77]	ω_0 [77]	$d\omega/dP$ [77]
T_{2g}	194	0.6			186	0.7		
E_g	427	2.0	418	2.2	395	1.8		
T_{2g}	513	3.0			488	3.4	465	3.5
T_{2g}	655	3.4	659	3.8	618	3.4	608	3.7
A_{1g}	775	3.8			717	4.0	710	4.4

Table 4.6 Calculated and experimental IR-active modes (in cm^{-1}) of $ZnAl_2O_4$ and $ZnGa_2O_4$ and their pressure derivatives (in cm^{-1}/GPa). Frequencies of the split TO and LO modes are noted as TO (LO)

Infrared mode symmetry	$ZnAl_2O_4$				$ZnGa_2O_4$		
	Theory			Exp.	Theory		Exp.
	ω_0 [35]	ω_0 [78]	$d\omega/dP$ [77]	ω_0 [64]	ω_0 [35]	$d\omega/dP$ [77]	ω_0 [79]
T_{1u}	222	226 (240)	0.34	220 (231)	175	0.00	175
T_{1u}	496	507 (528)	2.72	440 (533)	342	1.63	328
T_{1u}	548	562 (648)	2.74	543 (608)	429	2.52	420
T_{1u}	666	675 (832)	4.01	641 (838)	580	4.30	70

Frequencies of the split TO and LO modes are noted as TO (LO)

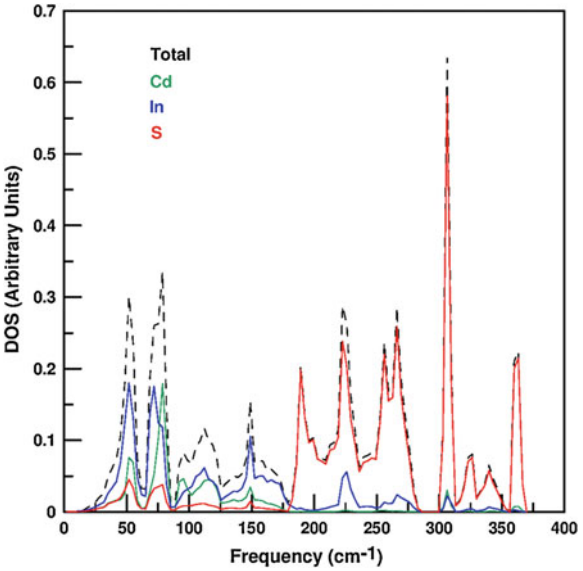

Fig. 4.2 Total and partial density of states of $CdIn_2S_4$

$\sim$175 cm^{-1} the contribution comes from In ions with a minor contribution of Cd ions, the rest of the spectrum is dominated by S motions, in particular there is a sharp peak at $\sim$300 cm^{-1}. A small gap is found between 250 and 300 cm^{-1}. The frequencies at ambient conditions and the pressure coefficient are in good agreement with experiments [3] (see Table 4.7). It should be noted the weak dependence of the low T_{2g} mode with pressure and that the A_{1g} mode has the highest pressure coefficient, as in the case of oxide spinels. Symmetry allows for four T_{1u} infrared modes, each of them is split into a twofold degenerate TO level and a single LO mode. Under pressure the infrared modes behave similarly to those of oxoespinels. The first T_{1u} infrared mode is almost unaffected by compression. As for the silent modes, it should be noted that the first T_{2u} located at 47.40 cm^{-1} has a negative

Table 4.7 Vibrational modes (in cm^{-1}) of $CdIn_2S_4$ thiospinel and their pressure derivatives (in cm^{-1}/GPa). Frequencies of the split TO and LO modes are noted as TO (LO)

	Theory		Experiment [3]	
	ω_0	dω/dP	ω_0	dω/dP
Raman modes				
T_{2g}	93.17	0.81	93	1.0
E_g	193.67	2.42	188	2.7
T_{2g}	246.05	3.99	249	4.4
T_{2g}	308.33	6.10	315	5.0
A_{1g}	364.5	6.09	A1g (In) 360	A1g (In) 6.1
			A1g (Cd) 367	A1g (Cd) 6.1
Infrared modes				
T_{1u}	68.85 (69.02)	−0.72 (−0.72)	70	0.7
T_{1u}	173.49 (174.09)	2.55 (2.55)	207	2.6
T_{1u}	221.09 (232.30)	3.92 (4.08)	301	3.3
T_{1u}	310.16 (336.75)	7.21 (6.74)		
T_{1u}	173.49 (174.09)	2.55 (2.55)	207	2.6
Silent modes				
T_{2u}	47.40	−1.72		
E_u	77.93	0.25		
T_{1g}	181.17	2.62		
A_{2u}	187.97	1.74		
T_{2u}	232.44	3.87		
E_u	277.54	4.09		
A_{2u}	362.89	6.40		

Frequencies of the split TO and LO modes are noted as TO (LO)

pressure coefficient. This may indicate structural instability at high pressures and a possible phase transition. It should be noted the almost inexistent LO–TO splitting in the two low frequency T_{1u} modes.

4.6 Pressure-Induced Phase Transitions in Spinels

The behavior of $MgAl_2O_4$ spinel under hydrostatic pressure has been the subject of several experimental and theoretical studies as a constituent of the shallow upper mantle of the Earth. Ringwood and Reid [8] already suggested in 1969 the decomposition of some spinels into oxide mixtures or the transformation to denser single phases.

There is a general agreement between experimental and theoretical studies about the range of stability of the spinel phase (see Table 4.8). This phase, stable at ambient conditions, decomposes into its simple oxides periclase and corundum (MgO $+\alpha$-Al_2O_3) at a pressure of 12–14 GPa [2, 28, 49, 83]. With increasing pressure the oxides recombine and a second phase changes occurs. Ono et al. [28] performed first

Table 4.8 Transition pressure (in GPa), high-pressure phase, bulk modulus B_0 (in GPa), and its pressure derivative B_0', for different spinels

	Pt (GPa)	High Pressure Phase	B_0 (GPa)	B_0'	Ref.
$MgAl_2O_4$	15	$MgO + Al_2O_3$			[5]
	13.7	$MgO + Al_2O_3$			[28]
	15	$MgO + Al_2O_3$			[49]
	12.1	$MgO + Al_2O_3$			[83]
	35	*Pnma* ($CaFe_2O_4$-type)			[2]
	45	*Pnma* ($CaFe_2O_4$-type)	197.9	4.01	[28]
	62	*Pnma* ($CaFe_2O_4$-type)			[2]
	68	*Cmcm* ($CaTi_2O_4$-type)	202.05	4.03	[28]
	45	*Cmcm* ($CaTi_2O_4$-type)	221	4.26	[49]
(Exp.)	12.3 (273 K)	$MgO + Al_2O_3$			[84]
	26 (1273 K)	*Pnma* ($CaFe_2O_4$-type)	213	4 (fixed)	[85]
	26.6 (1873 K)	*Pnma* ($CaFe_2O_4$-type)			[86]
	40 (1000 K)	*Cmcm* ($CaTi_2O_4$-type)	219	4 (fixed)	[87]
$MgIn_2O_4$	66	–	–	–	[29]
$ZnAl_2O_4$	38.5	*Pnma* ($CaFe_2O_4$-type)	–	–	[35]
	36[a]	I_{41}/amd			[35]
$ZnGa_2O_4$	33.44	*Pbcm* ($CaMn_2O_4$-type)	–	–	[35]
	42.5	*Cmcm* ($CaTi_2O_4$-type)			[77]
	32[a]	I_{41}/amd			[35]
(Exp.)	31.2	I_{41}/amd	257	7.5	[37]
	55.4	*Pbcm* ($CaMn_2O_4$-type)			[37]
$SnZn_2O_4$	39	*Cmcm* ($CaTi_2O_4$-type)	178.5	4.2	[26]
	54	*Pnma* ($CaFe_2O_4$-type)	161.4	4	[26]
$CdIn_2S_4$	11.5	*Imma*	71.6	4, fixed	[5]
(Exp.)	9.5	Fd-3m ($LiTiO_2$-type)	74	4, fixed	[5]
$MgIn_2S_4$	7.8	*Imma*	68.8	4, fixed	[5]
(Exp.)	8.3	Fd-3m ($LiTiO_2$-type)	55	4, fixed	[5]
$MnIn_2S_4$	6.9	*Imma*	70.1	4, fixed	[5]
(Exp.)	6.8	Fd-3m ($LiTiO_2$-type)	62	4, fixed	[5]

a Non hydrostatic conditions

principle simulations to investigate the stability of $MgAl_2O_4$ polymorphs at high pressure up to 150 GPa. To investigate de stability of each phase, the enthalpy difference was calculated. The enthalpy ($H = E + PV$, where E is the internal energy, P is the pressure and V is the volume), is the same as the Gibbs energy when the temperature is cero. The calculated transition sequence:

$$MgAl_2O_4(\text{spinel}) \rightarrow MgO + \alpha\text{-}Al_2O_3 \rightarrow \text{Calciumferrite-type} \rightarrow \text{Calciumtitanate-type}$$

is in good agreement with experimental observations [84]. At the transition pressure from spinel to simple oxides the reduction in volume is large while the reduction in volume from Calcium ferrite-type to Calcium titanate-type is very small. The predicted pressure transition from spinel to $MgO + \alpha\text{-}Al_2O_3$ is 13.7 GPa, consistent

with previous results. The theoretical phase transition pressures from the oxide mixture to the Calcium ferrite-type and from this one to the Calcium titanate-type are 45 and 68 GPa, respectively. These results are in agreement with those of [2]. However they are greater than the experimental data (26 and 40 GPa). It should be considered that the calculations were performed at 0 K while the experimental data were collected at high temperature. The recently calculated phase boundary between Calcium ferrite-type, $MgAl_2O_4$ and α-Al_2O_3 [86] has a negative slope of -0.006 GPa/K and passes through 26.6 GPa at 1,873 K and 29.8 GPa at 1,300 K. Nevertheless the discrepancy in the transition from Calcium ferrite-type to Calcium titanate-type cannot be explained only by a temperature effect. Another reason may be that the enthalpy difference between the two phases is very small over a wide pressure range because Calcium ferrite-type and Calcium titanate-type structures are quite similar, and the change in volume at the transition is small. As the two phases are so similar in enthalpy small uncertainties in the calculation of enthalpies can lead to greater uncertainty in the transition pressure [28].

The stability of the inverse spinel $SnZn_2O_4$ against compression has been recently analyzed [26]. The calculations predict the transformation of the mixture of 2ZnO and SnO_2 to the inverse spinel structure $SnZn_2O_4$ at 12 GPa. Experimental results show that the oxide mixture is stable at non-pressure induced circumstances [26, 88]. The inverse spinel structure transforms to the calcium titanate-type structure at 39 GPa and to the calcium ferrite-type at 54 GPa. Both forms are denser than the cubic spinel. They are considered the densest known structures with AB_2O_4 stoichiometry. These structures have a nearly isotropic pressure response. Gracia et al. showed the effect of the pressure on the band gap for the $SnZn_2O_4$ high pressure polymorphs and the pressure dependences of the Raman modes [26].

The behavior under pressure of $MgAl_2O_4$ and $ZnGa_2O_4$ spinels are very different, unlike $MgAl_2O_4$, $ZnGa_2O_4$ does not decompose under pressure. The mixture of oxides was not observed experimentally and theoretical calculations have found that this possibility is not energetically competitive [35]. The transition sequence under pressure for $ZnGa_2O_4$ has been investigated experimentally by Errandonea et al. [37] up to 56 GPa. The $ZnGa_2O_4$spinel undergoes a second-order phase transition to a tetragonal-spinel with $I4_1/amd$ symmetry and $c/a = 1.398$ above 31 GPa and a second structural phase transition to the orthorhombic *Pbcm* $CaMn_2O_4$-type structure at 55 GPa.

First principles studies were performed by López et al. on $ZnGa_2O_4$ spinel [35], where the *c/a* value reported in experiments [37] was imposed in the calculations. The results show that under non-hydrostatic conditions the tetragonal spinel structure is competitive in energy with the cubic spinel structure. However, the tetragonal spinel structure reduces to the cubic spinel structure under hydrostatic conditions [35, 89]. Therefore, $ZnGa_2O_4$ has a first order phase transition under hydrostatic pressure to the $CaMn_2O_4$-type structure at 33.4 GPa in accordance with experimental findings [37]. Although the $CaTi_2O_4$-type structure is also competitive in energy, the $CaMn_2O_4$-type structure provides the best match with the observed diffraction data [37]. The volume collapse at the transition 7.76 %, in good agreement with results from [37]. The theoretical transition pressure is lower than the experimental

one, but it is known that the transition pressure calculated by the equal enthalpy construction is usually a lower estimate of the experimental transition pressure [14]. The calculated pressure transition is the thermodynamical transition pressure, the difference between the experimental and theoretical transition pressures can be due to the possible existence of kinetic barriers that are not included in the calculations. Upon increasing compression, a second order phase transition with no change in volume and no changes in coordination in Zn and Ga cations is predicted at 42.5 GPa from the $CaMn_2O_4$-type structure (*Pbcm*) to the $CaTi_2O_4$-type (*Cmcm*) [77]. The transition from the *Pbcm* to *Cmcm* phase in AB_2O_4 compounds has been observed previously in $CaMn_2O_4$ [90]. Ab initio calculated frequencies, Grüneisen parameters, and pressure coefficients of the phonon modes of $ZnGa_2O_4$ in the *Pbcm* and *Cmcm* phases are given in [77].

High pressure X-ray diffraction studies have shown that $ZnAl_2O_4$ does not undergo any phase transition till 43 GPa [91]. López et al. have performed first principles calculations to study the stability of the spinel structure of $ZnAl_2O_4$ [35]. In this case, results show that a first-order phase transition should occurs at 38.5 GPa from a cubic spinel to a $CaFe_2O_4$-type structure (*Pnma*). Like in $ZnGa_2O_4$, the experimental transition pressure would be higher, probably due to the kinetic barriers, and this transition was not observed by Levy et al. [91]. The different behavior of these two Zn-spinels can be understood because of the replacement of the cation B (Al or Ga), it is well know the role of *d* electrons in many semiconductor compounds under pressure [14]. As in the case of $ZnGa_2O_4$, a tetragonal spinel structure is competitive with a cubic spinel structure under non-hydrostatic conditions in $ZnAl_2O_4$ [35].

Pressure-induced phase transitions were recently studied both theoretically and experimentally by Santamaría-Pérez et al. in three indium thiospinels ($CdIn_2S_4$, $MgIn_2S_4$, and $MnIn_2S_4$) [5]. From the experimental point of view the high pressure phase adopts a defect $LiTiO_2$-type structure in the three compounds. This structure can be described in the same space group as the initial spinel structure, Fd-3m. The calculations were carried out within the DFT. In the case of $MnIn_2S_4$ the study was performed in the framework of LDA + U, U = 5.25 eV [92] since Mn is a transition metal, indeed a strongly correlated system, which is not well described by standard DFT. On the other hand, $CdIn_2S_4$ and $MnIn_2S_4$ were studied as direct spinel (x = 0) while $MgIn_2S_4$ was treated both as a direct spinel and as a fully inverse spinel (x = 1). The theoretically calculated high-pressure phase is an orthorhombic *Imma*, No.74, with Z = 4. Both structure the experimental cubic Fd-3m, defect $LiTiO_2$-type structure, and the theoretical orthorhombic *Imma* are related [5]. The *Imma* high-pressure phase deviate slightly (<1.5 %) from the ratio $a = b = c/\sqrt{2}$, corresponding to the experimentally observed high-pressure cubic phase. The enthalpy of each structure was calculated in order to determine the transition pressure. Figure 4.3 shows the enthalpy difference (taking the spinel structure as a reference) as a function of pressure. It is clear that the *Imma* structure becomes the stable phase at high pressures, being the volume collapse of 6.5, 7.0, and 7.5 % for $CdIn_2S_4$, $MgIn_2S_4$, and $MnIn_2S_4$, respectively. The transition pressures obtained from the enthalpy are 11.5, 7.8, and 6.9 GPa for $CdIn_2S_4$, $MgIn_2S_4$, and $MnIn_2S_4$, respectively, in good agreement with the experimental ones (9.5, 8.3, and 6.8 GPa) [3–5].

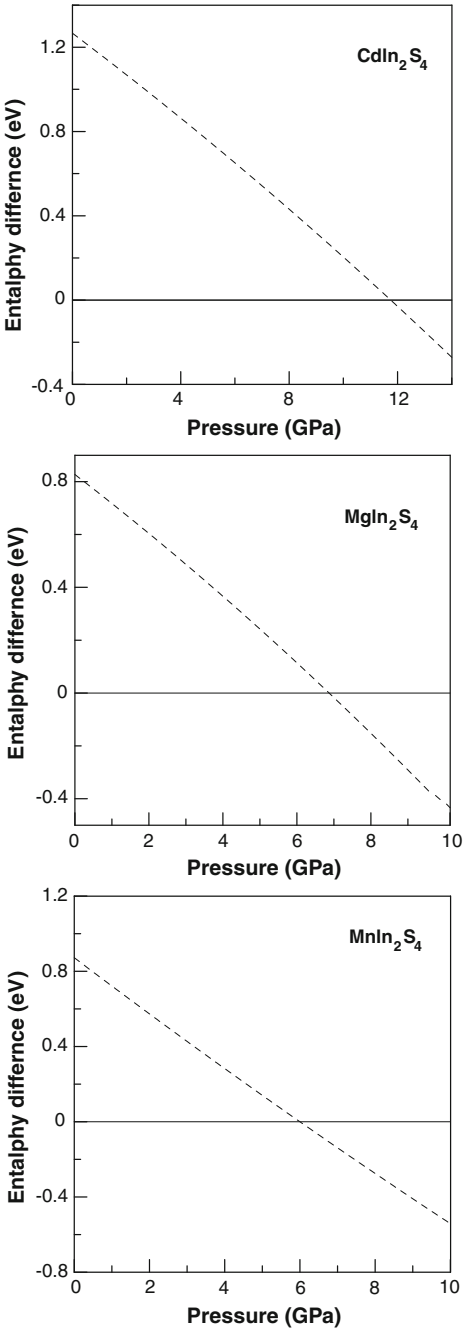

Fig. 4.3 Enthalpy variation versus pressure for the spinel structure and the Imma structure (spinel structure is taken as a reference) for $CdIn_2S_4$, $MgIn_2S_4$, and $MnIn_2S_4$

The bulk modulus for the high pressure defect $LiTiO_2$ phase in indium thiospinels is smaller than that of the low pressure spinel phase (see Table 4.3). This result suggests that the high pressure $LiTiO_2$-type structure is more compressible than the spinel structure for the three compounds.

In the case of AIn_2S_4 (A = Cd, Mg, Mn) spinels, the volume of the tetrahedra collapse at the pressure transition due to the change of the *u* parameter, while the volumes of the octahedra vary in a more continuous way with pressure. The phase transition always occurs when the tetrahedral volumes reach a value of circa 6.7 $Å^3$. Smaller volumes seem to be not suitable to accommodate the different cations, independently of their size and nature. It seems that the size of the metal atoms occupying the tetrahedral positions in spinel is correlated with the transition pressure, i.e.: a larger atomic radius (Mn < Mg < Cd ∼ In) would imply larger pressures for the onset of the phase transition [5].

As already mentioned, it should be emphasized that the pressure-induced phase transition in the thiospinels occurs at much lower pressure than in oxospinels. So the study of thiospinels may contribute to the understanding of the behavior of oxospinels at high pressures.

4.7 Conclusions

In this chapter we have made an overview of the structural, elastic, electronic, vibrational, and optical properties of spinels under pressure as well as the possible pressure-induced postspinel phases from a theoretical point of view. First principle calculations are a powerful complement to experimental techniques. Theoretical calculations provide detailed structural information at the atomic level. However, high pressure studies on spinels are scarce due to computational difficulties related to the inversion of cations at their respective sites. Most of the studies have been performed on direct oxide spinels, while there are very few works devoted to inverse spinels as well as on sulfur and selenide spinels. There are almost no studies of the vibrational properties under pressure, and works on optical and elastic properties are scarce. Theoretical studies can help to elucidate some controversies on the structural properties and on the unknown high-pressure phases of most spinels. We hope this overview will encourage further studies that cover the lack of data on spinels under pressure.

References

1. Irifune T, Fujino K, Ohtani E (1991) A new high-pressure form of $MgAl_2O_4$. Nature 349: 409–411
2. Gracia L, Beltrán A, Andrés J, Franco R, Recio JM (2002) Quantum-mechanical simulation of $MgAl_2O_4$ under high pressure. Phys Rev B 66(7):224114
3. Ursaki VV, Manjon FJ, Tiginyanu IM, Tezlevan VE (2002) Raman scattering study of pressure-induced phase transitions in MIn_2S_4 spinels. J Phys Condens Matter 14:6801–6813

4. Ruiz-Fuertes J, Errandonea D, Manjón FJ, Martínez-García D, Segura A, Ursaki VV, Tiginyanu IM (2008) High-pressure effects on the optical absorption edge of $CdIn_2S_4$, $MgIn_2S_4$, and $MnIn_2S_4$ thiospinels. J Appl Phys 103: 063710 (5)
5. Santamaría-Pérez D, Amboage M, Manjón FJ, Errandonea D, Muñoz A, Rodríguez-Hernández P, Mújica A, Radescu S, Ursaki VV, Tiginyanu IM (2012) Crystal Chemistry of $CdIn_2S_4$, $MgIn_2S_4$, and $MnIn_2S_4$ Thiospinels under High Pressure. J Phys Chem C 116:14078–14087
6. Radautsan SI, Tiginyanu IM (1993) Defect engineering in II-III_2-VI_4 and Related Compounds. Jpn J Appl Phys 32(1):5–9
7. Palacios P, Aguilera I, Sánchez K, Cones JC, and Wahnón P (2008) Transition-metal-substituted indium thiospinels as novel intermediate-band materials: prediction and understanding of their electronic properties. Phys Rev Lett 101: 046403 (4)
8. Ringwood AE, Reid AF (1969) High pressure transformations of spinels (I). Earth Planet Sci Lett 5:245–250
9. Meloni F, Mula G (1970) Pseudopotential Calculation of the band structure of $CdIn_2S_4$. Phys Rev B 2:392–396
10. Marinelli M, Baroni S, Meloni F (1988) Structural and electronic properties of spinel semiconductors: An ab initio pseudopotential study of $MgIn_2S_4$. Phys Rev B 38:8258–8263
11. Hohenberg P, Kohn W (1964) Inhomogenous electron gas. Phys Rev 136:B864–B871
12. Kohn W, Sham LJ (1965) Self-consistent equations including exchange and correlation effects. Phys Rev 140:A1133–A1138
13. Perdew JP, Ruzsinszky A, Csonka GI, Vydrov OA, Scuseria GE, Constantin LA, Zhou X, Burke K (2008) Restoring the density-gradient expansion for exchange in solids and surfaces. Phys Rev Lett 100(4):136406
14. Mujica A, Rubio A, Muñoz A, Needs RJ (2003) High-pressure phase of group-IV, III-V, and II-VI compounds. Rev Mod Phys 75:863–912
15. Sickafus KE, Wills JM, Grimes NW (2004) Structure of Spinel. J Am Ceram Soc 82:3279–3292
16. Seminovski Y, Palacios P, Wahnón P, Grau-Crespo R (2012) Band gap control via tuning of inversion degree in $CdIn_2S_4$spinel. Appl Phys Lett 100(3):102112
17. Seko A, Yuge K, Oba F, Kuwabara A, Tanaka I, Yamamoto T (2006) First-principles study of cation disordering in $MgAl_2O_4$ spinel with cluster expansion and Monte Carlo simulation. Phys Rev B 73(6):094114
18. Sanchez J, Ducastelle F, Grayias D (1984) Generalized cluster description of multicomponent systems. Physica A 128:334–350
19. Wei SH, Ferreira LG, Bernard JE, Zunger A (1990) Electronic properties of random alloys: special quasirandom structures. Phys Rev B 42:9622–9649
20. Zunger A, Wei SH, Ferreira LG, Bernard JE (1990) Special quasirandom structures. Phys Rev Lett 65:353–356
21. Wei SH, Zhang SB (2001) First-principles study of cation distribution in eighteen closed-shell $A^{II}\,B_2^{III}O_4$ and $A^{IV}\,B_2^{II}O_4$ spinel oxides. Phys Rev B 63(8):045112
22. Bellaiche L, Vanderbilt D (2000) Virtual crystal approximation revised: application to dielectric and piezoelectric properties of perovskites. Phys Rev B 61:7877–7882
23. Giantomasi M, Boeri L, Bachelet GB (2005) Electrons and phonons in the ternary alloy $CaAl_{2-x}Si_x$ as a function of composition. Phys Rev B 72(9):224512
24. Keinan E, Schechter I, Cohen ML (2007) Quantum alchemy, ch. 14. In: Chemistry for the 21st century, Wiley, VCH
25. Waskowska A, Gerard L, Gracia L, Marqués M, Recio JM (2004) High-pressure behaviour of selenium-based spinels and related structures-an experimental and theoretical study. J Phys Condens Matter 16:53–63
26. Gracia L, Beltrán A, Andrés J (2011) A theoretical study on the pressure-induced phase transitions in the inverse spinel structure Zn_2SnO_4. J Phys Chem 115:7740–7746
27. Zhang L, Ji GF, Zhao F, Meng CM, Wei DQ (2011) The first-principle studies of the crystal phase transitions: Fd3m-$MgAl_2O_4$ →F4-3m-$MgAl_2O_4$. Physica B 406:335–338
28. Ono S, Brodholt JP, Price GD (2008) First-principles simulation of high-pressure polymorphs in $MgAl_2O_4$. Phys Chem Minerals 35:381–386

29. Bouhemadou A, Khenata R, Zerarga F (2007) Ab initio study of the structural and elastic properties of spinels MgX_2O_4 (X = Al, Ga, In) under pressure. Eur Phys J B 56:1–5
30. Wdowik UD, Parlinski K, Siegel A (2006) Elastic properties and high-pressure behavior of $MgAl_2O_4$ from ab initio calculations. J Phys Chem Solids 67:1477–1483
31. Recio JM, Franco R, Martín Pendás A, Blanco MA, Pueyo L (2001) Theoretical explanation of the uniform compressibility behavior observed in oxide spinels. Phys Rev B 63(7):184101
32. Levy D, Pavese A, Hanfland M (2003) Synthetic $MgAl_2O_4$ (spinel) at high-pressure conditions (0.0001–30 GPa): a synchrotron X-ray powder diffraction study. Am Mineral 88:93–98
33. Hill RJ, Craig JR, Gibbs GV (1979) Systematics of the spinel structure type. Phys Chem Minerals 4:317–339
34. Zerarga F, Bouhemadou A, Khenata R, Bin-Omran S (2011) Structural, electronic and optical properties of spinel oxides $ZnAl_2O_4$, $ZnGa_2O_4$, and $ZnIn_2O_4$. Solid State Sci 13:1638–1648
35. López S, Romero AH, Rodriguez-Hernandez P, Muñoz A (2009) First-principles study of the high-pressure phase transition in $ZnAl_2O_4$ and $ZnGa_2O_4$: From cubic spinel to orthorhombic post-spinel structure. Phys Rev B 79(7):214103
36. Brik MG (2010) First-principles calculations of electronic, optical and elastic properties of $ZnAl_2S_4$ and $ZnGa_2O_4$. J Phys Chem Solids 71:1435–1442
37. Errandonea D, Kumar RS, Manjón FJ, Ursaki VV, Rusu EV (2009) Post-spinel transformations and equation of state in $ZnGa_2O_4$: Determination at high pressure by in situ X-ray diffraction. Phys Rev B 79(6):024103
38. Bouhemadou A, Zerarga F, Almuhayya A, Bin-Omran S (2011) FP-LAPW study of the fundamental properties of the cubic spinel $CdAl_2O_4$. Mat Res Bull 46:2252–2260
39. Allali D, Bouhemadou A, Bin-Omran S (2011) Theoretical prediction of the structural, electronic and optical properties of SnB_2O_4 (B = Mg, Zn, Cd). Comp Mat Sci 51:194–205
40. Semari F, Khenata R, Rabah M, Bouhemadou A, Reshak AH, Rached D (2010) Full potential study of the elastic, electronic, and optical properties of spinels $MgIn_2S_4$ and $CdIn_2S_4$ under pressure effect. J Solid State Chem 183:2818–2825
41. Waskowska A, Gerard L, Marqués M, Contreras-García J, Recio JM (2009) The bulk modulus of cubic spinel selenides: an experimental and theoretical study. High Press Res 29:72–75
42. Avram NM, Brik MG, Sildos L (2011) Electronic and optical properties of $ZnCr_2Se_4$ as explored by first principles and crystal field calculations. Phys Stat Sol C 8:2585–2588
43. Segev D, Wei SH (2005) Structure-derived electronic and optical properties of transparent conducting oxides. Phys Rev B 71(11):125129
44. Finger LW, Hazen RM, Hofmeister AM (1986) High-pressure crystal chemistry of spinel ($MgAl_2O_4$) and magnetite (Fe_3O_4): comparisons with silicate spinels. Phys Chem Minerals 13:215–220
45. Martín Pendas A, Costales A, Blanco MA, Recio JM, Luaña V (2000) Local compressibilities in Crystals. Phys Rev B 62:13970–13978
46. Bouhemadou A, Haddadi K, Khenata R, Rached D, Bin-Omran S (2012) Structural, elastic and thermodynamic properties under pressure and temperature effects of $MgIn_2S_4$ and $CdIn_2S_4$. Physica B 407:2295–2300
47. Wang J, Yio S, Phillpot SR (1993) Crystal instabilities at finite strain. Phys Rev Lett 71:4182–4185
48. Catti M, Freyria Fava F (1999) High-pressure decomposition of MCr_2O_4 spinels (M = Mg, Mn, Zn) by ab initio methods. Phys Chem Minerals 26:389–395
49. Caracas R, Banigan EJ (2009) Elasticity and Raman and infrared spectra of $MgAl_2O_4$ spinel from density functional perturbation theory. Phys Earth Planet Inter 174:113–121
50. Khenata R, Sahnoun M, Baltache H, Rérat M, Reshak AH, Al-Douri Y, Bouhafs B (2005) Full-potential calculations of structural, elastic and electronic properties of $MgAl_2O_4$ and $ZnAl_2O_4$ compounds. Phys Lett A 344:271–279
51. Suzuki I, Ohno I, Anderson OL (2000) Harmonic and anharmonic properties of spinel $MgAl_2O_4$. Am Miner 85:304–311
52. Reffas M, Bouhemadou A, Khenata R, Ouahrani T, Bin-Omran S (2010) Ab initio study of structural, elastic, electronic and optical properties of spinel $SnMg_2O_4$. Physica B 405:4079–4085

53. Gonze X, Allan DC, Teter PM (1992) Dielectric tensor, effective charges and phonon in a-quartz by vibrational density-functional perturbation theory. Phys Rev Lett 68:3603–3606
54. Baroni S, de Gironcoli P, Giannozzi P (2001) Phonons and related crystal properties from density-functional perturbation theory. Rev Mod Phys 73:515–562
55. Yoneda A (1990) Pressure Derivatives of Elastic Constants of Single Crystal MgO and $MgAl_2O_4$. J Phys Earth 38:19–55
56. Fahy S, Kang KJ, Louie SG, Cohen ML (1987) Pressure coefficients of band gaps of diamond. Phys Rev B 35:5856–5859
57. Hosseini SM (2008) Structural, electronic and optical properties of spinel $MgAl_2O_4$ oxide. Phys Stat Sol B 245:2800–2807
58. Amin B, Khenata R, Bouhemadou A, Ahmad I, Maqbool M (2012) Opto-electronic response of spinels $MgAl_2O_4$ and $MgGa_2O_4$ through modified Becke-Johnson exchange potential. Physica B 407:2588–2592
59. Mo SD, Ching WY (1996) Electronic structure of normal, inverse, and partially inverse spinels in the $MgAl_2O_4$ system. Phys Rev B 54:16555–16561
60. Bortz ML, French RH, Jones DJ, Kasowski RV, Ohuchi FS (1990) Temperature-dependence of the electronic-structure of oxides-MgO, $MgAl_2O_4$ and Al_2O_3. Phys Scripta 41:537–541
61. Sampath SK, Cordaro JF (1998) Optical properties of zinc aluminate, zinc gallate, and zinc aluminogallate spinels. J Am Ceram Soc 81:649–654
62. Gracia L, Beltrán A, Andrés Franco R, Recio JM (2002) Quantum-mechanical simulation of $MgAl_2O_4$ under high pressure. Phys Rev B 66(7):224114
63. Pisani L, Maitra T, Valentí R (2006) Effects of Fe substitution on the electronic, transport, and magnetic properties of $ZnGa_2O_4$: A systematic ab initio study. Phys Rev B 73(11):205204
64. Alpuche-Aviles MA, Wu YY (2009) Photoelectrochemical study of the band structure of Zn_2SnO_4 prepared by the hydrothermal method. J Am Chem Soc 131:3216–3224
65. Güner S, Yildiz F, Rameev B, Aktas B (2005) Electron paramagnetic resonance study of $ZnAl_2S_4$ spinel. J Phys Condens Matter 17:3943–3952
66. Aguilera I, Palacios P, Sanchez K, Whanón P (2010) Theoretical optoelectronic analysis of $MgIn_2S_4$ and $CdIn_2S_4$ thiospinels: effect of transition-metal substitution in intermediate-band formation. Phys Rev B 81(9):075206
67. Lucero MJ, Aguilera I, Diaconu CV, Palacios P, Wahnón P, Scuseria GE (2011) Screened hybrid and self-consistent GW calculations of cadmium/magnesium indium sulfide materials. Phys Rev B 83(12):205128
68. Brewer LN, Kammler DR, Mason TO, Dravid VP (2001) Combined electron diffraction/microanalysis investigation of crystallography and cation distribution in the transparent conductive oxide $Cd_{1+x}In_{2-2x}Sn_xO_4$. J Appl Phys 89:951–954
69. Kulikova OV, Kulyuk LL, Radaustan SI, RatseeV SA, Strumban EE, Tezlevan VE, Tsitanu VI (1988) Influence of defect generation processes in $CdIn_2S_4$ single-crystals on the photoluminescence and Raman-scattering spectra. Phys Stat Sol A 107:373–377
70. Lazzeri M, Thibaudeau P (2006) Ab initio Raman spectrum of the normal and disordered $MgAl_2O_4$ spinel. Phys Rev B 74(4):140301
71. de Wijs GA, Fang CM, Kresse G, de With G (2002) First-principles calculation of the phonon spectrum of $MgAl_2O_4$ spinel. Phys Rev B 65(5):094305
72. Cynn H, Sharma SK, Cooney TF, Nicol M (1992) High-temperature Raman investigation of order-disorder behavior in the $MgAl_2O_4$ spinel. Phys Rev B 45:500–502
73. Thibaudeau P, Gervais F (2002) Ab initio investigation of phonon modes in the $MgAl_2O_4$ spinel. J Phys Condens Matter 14:3542–3552
74. Slotznick SP, Shim SH (2008) In situ Raman spectroscopy measurements of $MgAl_2O_4$ spinel up to 1400 ^oC. Am Miner 93:470–476
75. Zeng Q, Zhang L, Zhang X, Chen Q, Feng Z, Cai Y, Cheng L, Wheng Z (2011) Phys Lett A 375:3521–3524
76. Chopelas A, Hofmeister AM (1991) Vibrational spectroscopy of aluminate spinels at 1 atm and of $MgAl_2O_4$ to over 200 kbar. Phys Chem Minerals 18:279–293

77. López-Moreno S, Rodríguez-Hernández P, Muñoz A, Romero AH, Manjón FJ, Errandonea D, Rusu E, Ursaki VV (2010) Lattice dynamics of $ZnAl_2O_4$ and $ZnGa_2O_4$ under high pressure. Ann Phys 523:157–167
78. Fang CM, Loong CK, de Wijs GA, de With G (2002) Phonon spectrum of $ZnAl_2O_4$ spinel from inelastic neutron scattering and first-principles calculations. Phys Rev B 66(7):144301
79. Van Gorkom GGP, Haanstra JH (1973) Infrared and Raman spectra of the spinel $ZnGa_2O_4$. J Raman Spectrosc 1:513–519
80. Wang Z, Schiferl D, Zhao Y, O'Neill HStC, (2003) High pressure Raman spectroscopy of spinel-type ferrite $ZnFe_2O_4$. J Phys Chem Sol 64:2517–2523
81. Wang ZR, Lazor P, Saxena SK, Artioli G (2002) High-pressure Raman spectroscopic study of spinel ($ZnCr_2O_4$). J Solid State Chem 165:165–170
82. Fennie CJ, Rabe KM (2005) Polar phonons and intrinsic dielectric response of the ferromagnetic insulating spinel $CdCr_2S_4$ from first principles. Phys Rev B 72(5):214123
83. Dutta R, Mandal N (2012) Effects of Fe^{2+} and Zn^{2+} substitution on the structure and high pressure stability of $MgAl_2O_4$ spinel from DFT calculations. J Phys Chem Solids 73:1099–1105
84. Akaogi M, Hamada Y, Suzuki T, Kobayashi M, Okada M (1999) High pressure transitions in the system $MgAl_2O_4$-$CaAl_2O_4$: a new hexagonal aluminous phase with implication for the lower mantle. Phys Earth Planet Int 115:67–77
85. Irifune T, Naka H, Sanehira T, Inoue T, Funakoshi K (2002) In situ X-ray observation of phase transitions in $MgAl_2O_4$ spinel to 40 GPa using multianvil apparatus with sintered diamond anvils. Phys Chem Minerals 29:645–654
86. Kojitani H, Takayuki I, Akaogi M (2012) Thermodynamic investigation on phase equilibrium boundary between calcium ferrite-type $MgAl_2O_4$ and MgO + α-Al_2O_3. Phys Earth Planet Int 212–213:100–105
87. Ono S, Kikegawa T, Ohishi Y (2006) The stability and compressibility of $MgAl_2O_4$ high-pressure polymorphs. Phys Chem Minerals 33:200–206
88. Nakayama M, Nogami M, Yoshida M, Katsumata T, Inaguma Y (2010) First-principles studies on novel polar oxide $ZnSnO_3$: pressure-induced phase transition and electric properties. Adv Mater 22:2579–2582
89. López-Moreno S, Romero AH, Rodríguez-Hernández P, Muñoz A (2009) Ab initio study of the high-pressure phases and dynamical properties of $ZnAl_2O_4$ and $ZnGa_2O_4$. High Press Res 27:573–577
90. Wang ZW, Saxena SK, Neumeier JJ (2003) Raman scattering study on pressure-induced phase transformation of marokite ($CaMn_2O_4$). J Solid State Chem 170:382–389
91. Levy D, Pavese A, Sani A, Pishedda V (2001) Structure and compressibility of synthetic $ZnAl_2O_4$ (gahnite) under high-pressure conditions, from synchrotron X-ray powder diffraction. Phys Chem Minerals 28:612–618
92. Floris A, de Gironcoli S, Gross EKU, Cococcioni M (2011) Vibrational properties of MnO and NiO from DFT + U-based density functional perturbation theory. Phys Rev 84(4):161102

Part II
Ordered-Vacancy AB_2X_4 Chalcogenide Compounds

Chapter 5
AB_2S_4 Ordered-Vacancy Compounds at High Pressures

Francisco Javier Manjón and Rosario Isabel Vilaplana

Abstract In this chapter, an overview of the effects of pressure on the crystalline structure and physical properties of sulphur-based ordered-vacancy compounds of the $A^{II}B_2^{III}X_4^{VI}$ family is presented. Recent X-ray diffraction and Raman spectroscopy studies are presented with a main focus on the discussion of pressure-induced phase transitions and their inherent cation and cation-vacancy disordering processes.

Keywords Defect chalcopyrite · Thiogallate · Defect stannite · Defect famatinite · Pseudocubic · High pressure · X-ray diffraction · Lattice dynamics · Phase transitions

5.1 Introduction

Adamantine ordered-vacancy compounds (OVCs) constitute a class of compounds, derived from the diamond or zincblende structure (space group (S.G.) F-43 m, No. 216, $Z = 4$) of binary AX semiconductors, that have an unbalanced number of anions and cations (they have one anion more); thus, a cation site is occupied by a vacancy in an ordered and stoichiometric fashion. In OVCs, cations are tetrahedrally coordinated while anions are surrounded by three cations and a vacancy. The family of OVCs includes binary B_2X_3 compounds, like sesquisulfides and sesquiselenides, and ternary AB_2X_4 compounds. In particular, many $A^{II}B_2^{III}S_4$ compounds with A^{II} and B^{III} being divalent and trivalent metals, respectively, usually crystallize at ambient

F. J. Manjón (✉)
Instituto de Diseño para la Fabricación y Producción Automatizada, MALTA Consolider Team, Universitat Politècnica de Valencia, 46022 València, Spain
e-mail: fjmanjon@fis.upv.es

R. I. Vilaplana
Centro de Tecnologías Físicas: Acústica, Materiales y Astrofísica, MALTA Consolider Team, Universitat Politècnica de València, 46022 València, Spain
e-mail: rovilap@fis.upv.es

F. J. Manjón et al. (eds.), *Pressure-Induced Phase Transitions in AB_2X_4 Chalcogenide Compounds*, Springer Series in Materials Science 189,
DOI: 10.1007/978-3-642-40367-5_5,

conditions in tetragonal structures. The only known exceptions among sulphides is that of compounds with B = In, which curiously crystallize in the spinel structure and whose behaviour under pressure has been already reviewed in the chapter devoted to thiospinels and selenospinels.

Adamantine OVCs constitute a class of semiconductors that exhibit extraordinary and unusual properties. Since they have a different number of anions and cations, unlike in the zincblende structure, A and B cations are unequivalent cations located in different Wyckoff sites. The doubling of the cubic zincblende unit cell along the *c* axis in these compounds leads them to crystallize in a tetragonal space group which provides them with special properties not present in cubic zincblende-type compounds. In particular, adamantine OVCs have important applications in optoelectronics, solar cells, and non-linear optics that have attracted considerable attention in the last 30 years, as evidenced in several reviews [1–4].

From the theoretical point of view, OVCs are also important materials in Solid State Physics because they allow us to understand the role played by vacancies in the physical and chemical properties of solids. Note that they constitute a bridge between defect materials (with vacancies as point defects) and perfect materials. Additionally, ternary OVCs of the AB_2X_4 family are of interest to study the order-disorder phase transitions occurring in tetrahedral semiconductors, like ABX_2 chalcopyrites [5–8], since many ternary OVCs undergo order-disorder transitions on increasing temperature [8–13].

The family of ternary OVCs include AB_2X_4 compounds mainly with X = S, Se, and Te, which typically crystallize at ambient conditions in one of three tetragonal structures: (i) the ordered defect chalcopyrite (DC) structure (S.G. I-4, No. 82, Z = 2) shown in Fig. 5.1a; (ii) the ordered defect stannite (DS) structure (S.G. I-42 m, No. 121, Z = 2) also known as defect famatinite (Fig. 5.1b); and (iii) the ordered pseudocubic (PC) structure (S.G. P-42 m, No. 111, Z = 1) shown in Fig. 5.1c. In this respect, AB_2S_4 (A = Cd, Hg; B = Al, Ga) compounds crystallize in the DC phase [14–16] with the exception of $HgAl_2S_4$ that crystallizes in a disordered variant of the DS structure in which vacancies and Ga atoms get mixed in the same cation plane perpendicular to the *c* axis as shown in Fig. 5.1d. On the other hand, $ZnGa_2S_4$ is suggested to crystallize in two possible disordered variants of the DS phase: (i) one in which Zn and Ga atoms get mixed in the same cation plane perpendicular to the *c* axis (Fig. 5.1e) [17]; and (ii) one in which Zn and Ga atoms are mixed along the whole structure (Fig. 5.1f) [18]. There is no knowledge of any sulfur-based OVC crystallizing in the PC phase. However, there are reports of some sulfur-based OVCs, like $CoGa_2S_4$ [19], crystallizing at ambient conditions in the disordered zincblende (DZ) phase, where A and B cations and vacancies are randomly distributed at the only Wyckoff site (*4a*) for cations in the DZ structure (Fig. 5.1g).

The usual way to describe the atomic positions in the DC structure, like that found in $CdGa_2S_4$, followed till now in the Inorganic Chemistry Structural Database (ICSD) assumes that in $CdGa_2Se_4$ Cd atoms occupy *2a* Wyckoff sites, Ga atoms occupy *2b* and *2c* Wyckoff sites, vacancies occupy *2d* sites, and S atoms occupy *8g* sites (see Table 5.1). However, sometimes it is convenient for the comparison with the DS structure to put Ga atoms at *2a* and *2c* Wyckoff sites, and vacancies and Cd

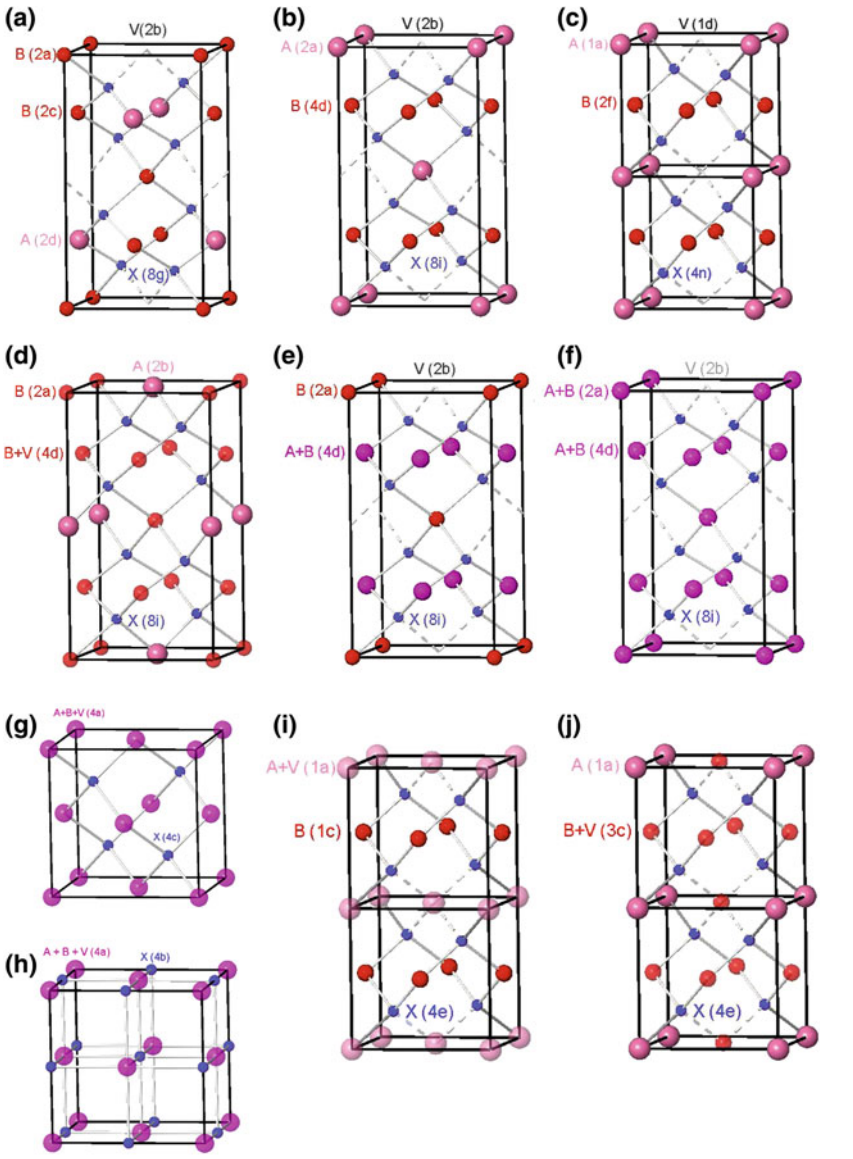

Fig. 5.1 Scheme of atoms in OVCs of the AB_2X_4 family in the: **a** ordered defect chalcopyrite (DC) structure (model 1); **b** ordered defect stannite (DS) (model 1) structure; **c** ordered pseudocubic (PC) structure (model 1); **d** disordered DS (model 7) structure; **e** disordered DS (model 6) structure; **f** disordered DS (model 2) structure; **g** disordered zincblende (DZ) structure; **h** disordered rocksalt (DR) structure; **i** disordered CuAu-like (DCA) structure (model 1); and **j** disordered Cu_3Au-like (DC3A) structure (model 1). Small (*blue*) atoms are X anions, medium-size (*red*) atoms are B cations, and large (*light pink*) atoms are A cations. Mixed A and B atoms are shown in *pink* color. Mixed vacancies with A, B, or A + B cations are shown in semitransparent *light pink*, *red*, or *pink* colors. For the sake of clarity Wyckoff sites in the different structures are given in parenthesis

Table 5.1 Atomic positions and site occupation fraction (SOF) refined for $CdGa_2S_4$ at ambient pressure

Atom	Site	x	y	z	SOF
Cd	2a	0	0	0	1
Ga	2b	0	0	1/2	1
Ga	2c	0	1/2	1/4	1
Vacancy	2d	0	1/2	3/4	0
S	8g	0.271(8)	0.261(8)	0.140(4)	1

Defect-chalcopyrite structure, space group: $I\bar{4}$, Z = 2. After [28]

atoms at *2b* and *2d* Wyckoff sites, respectively, in the DC structure. The DC structure is the same but there is a different unit cell shifted and rotated with respect to the *c* axis of the tetragonal structure.

Temperature-induced order-disorder phase transitions have been studied in several adamantine ordered-vacancy compounds [8–13]. In particular, many $A^{II}B_2^{III}X_4^{VI}$ compounds undergo a phase transition to the disordered zincblende (DZ) structure on increasing temperature. Bernard and Zunger suggested that temperature-induced order-disorder transitions should undergo via intermediate phases of partial disorder between the low-temperature fully ordered phases and the high-temperature fully disordered phases following two stages of disorder [3]. On the other hand, several $A^{II}B_2^{III}X_4^{VI}$ compounds undergo a phase transition to the disordered rocksalt (DR) structure (Fig. 5.1h) on increasing pressure so several works have suggested that pressure-induced order-disorder phase transitions in OVCs should also occur via intermediate phases of partial cation/vacancy disorder [20–22].

A partial or total exchange of cations and/or vacancies may result in different forms of disordered structures that lead from the totally ordered DC, DS, and PC structures (see Fig. 5.1a–c) to the totally disordered zincblende (DZ) structure (Fig. 5.1g). This has been discussed in several works [8, 18, 23–26]. Table 5.2 shows the cation distribution in the different possible intermediate phases between the fully ordered structures and the fully disordered DZ structure. A full explanation of the different phases which can occur through different paths of disorder can be found in [26]. We only want to note here that one of the possible structures in which a DC structure can be converted upon cation and/or vacancy disorder is the DS structure (models 2–9). As already commented, X-ray diffraction (XRD) measurements suggest that $ZnGa_2S_4$ adopts either model 2 or model 6 of the DS structure [17, 18]. In model 6 of the DS structure, Ga atoms at *2a* sites and vacancies at *2b* sites remain ordered while Ga and Zn atoms at *2c* and *2d* sites mix together resulting in a fractional occupation (1/2Zn + 1/2Ga) of the *4d* Wyckoff sites of the DS phase (see Fig. 5.1e). In model 2 of the DS structure, Zn atoms at *2d* sites of the DC phase and Ga atoms at *2a* and *2c* sites of the DC phase get mixed completely resulting in a fractional occupation (1/3Zn + 2/3Ga) of the *2a* and *4d* Wyckoff sites of the DS phase while vacancies remain ordered in the *2b* sites (see Table 5.3 and Fig. 5.1f). Finally, we must note that between the DS and the DZ phases other

Table 5.2 Distribution of cations and vacancies in the Wyckoff sites of different structures that can be originated upon disorder of OVC's (after [26])

Wyckoff site		Model 1	Wyckoff site		Model 1	Wyckoff site		Model 1	
1a (0,0,0)	Cation plane 1	$2A^{II}$	2a (0,0,0)	cation plane 1	$2A^{II}$	2a (0,0,0)	Cation plane 1	$2B^{III}$	Ordered
1d (1/2,1/2,0)		2V	2b (0,0,1/2)		2V	2b (0,0,1/2)		2V	
2f (1/2,0,1/2)	Cation plane 2	$4B^{III}$	4d (0,1/2,1/4)	cation plane 2	$4B^{III}$	2c (0,1/2,1/4)	Cation plane 2	$2B^{III}$	
						2d (0,1/2,3/4)		$2A^{II}$	

P-42m space group (PC structure)			I-4 space group (DC structure)			
Wyckoff site		Model 2	Wyckoff site		Model 2	Model 3
1a (0,0,0)	Cation plane 1	$2/3(A^{II}+2B^{III})$	2a (0,0,0)	Cation plane 1	$A^{II}+B^{III}$	$2B^{III}$
1d (1/2,1/2,0)		2V	2b (0,0,1/2)		2V	$V+B^{III}$
2f (1/2,0,1/2)	Cation plane 2	$4/3(A^{II}+2B^{III})$	2c (0,1/2,1/4)	Cation plane 2	$2B^{III}$	$V+B^{III}$
			2d (0,1/2,3/4)		$A^{II}+B^{III}$	$2A^{II}$

P-43m space group (DC3A structure)					I-42d space group (DIC structure)			
Wyckoff site		Model 1	Model 2	Model 3	Wyckoff site		Model 1	Model 2
1a (0,0,0)	In both cat. planes	$2A^{II}$	$2/3(A^{II}+2B^{III})$	$2/3(V+2B^{III})$	4a (0,0,0)	In both cation planes	$4B^{III}$	$2(A^{II}+B^{III})$
3c (0,1/2,1/2)		$2V+4B^{III}$	$2V+4/3(A^{II}+2B^{III})$	$2A^{II}+4/3(V+2B^{III})$	4b (0,0,1/2)		$2(V+A^{II})$	$2(V+B^{III})$

I-42m space group (DS structure)									
Wyckoff site		Model 2	Model 3	Model 4	Model 5	Model 6	Model 7	Model 8	Model 9
2a (0,0,0)	Cation plane 1	$2/3(A^{II}+2B^{III})$	$2A^{II}$	$2B^{III}$	$2B^{III}$	$2B^{III}$	$2B^{III}$	$2B^{III}$	$A^{II}+B^{III}$
2b (0,0,1/2)		2V	$2/3(V+2B^{III})$	$A^{II}+B^{III}$	$V+B^{III}$	2V	$2A^{II}$	$V+A^{II}$	$V+B^{III}$
4d (0,1/2,1/4)	Cation plane 2	$4/3(A^{II}+2B^{III})$	$4/3(V+2B^{III})$	$2V+A^{II}+B^{III}$	$2A^{II}+V+B^{III}$	$2(A^{II}+B^{III})$	$2(V+B^{III})$	$V+A^{II}+2B^{III}$	$V+A^{II}+2B^{III}$

P-4m2 space group (DCA structure)							
Wyckoff site		Model 1	Model 2	Model 3	Model 4	Model 5	Model 6
1a (0,0,0)	Cation plane 1	$2(V+A^{II})$	$2V+2/3(A^{II}+2B^{III})$	$2A^{II}+2/3(V+2B^{III})$	$A^{II}+3B^{III}$	$V+3B^{III}$	$2(V+B^{III})$
1c (1/2,1/2,1/2)	Cation plane 2	$4B^{III}$	$4/3(A^{II}+2B^{III})$	$4/3(V+2B^{III})$	$2V+A^{II}+B^{III}$	$2A^{II}+V+B^{III}$	$2(A^{II}+B^{III})$

Wyckoff site	F-43m space group (DZ structure)	
4a (0,0,0)	$2A^{II}+2V+4B^{III}$	Totally disordered

Table 5.3 Atomic positions and site occupation fraction (SOF) refined for $ZnGa_2S_4$ at ambient pressure

Atom	Site	x	y	Z	SOF
Ga	2*a*	0	0	0	0.66
Zn	2*a*	0	0	0	0.33
Ga	4*d*	0	1/2	1/4	0.66
Zn	4*d*	0	1/2	1/4	0.33
Vacancy	2*b*	0	0	1/2	0
Se	8*i*	0.2576(1)	0.2576(1)	0.1190(1)	1

Defect-stannite structure (model 2), space group: $I\bar{4}2m$, Z = 2. After [18]

intermediate structures with disordered CuAu-like (DCA) layered structure [see Fig. 5.1i] or disordered Cu_3Au-like (DC3A) structure [see Fig. 5.1j] can be found.

Very few high-pressure experiments have studied sulfur-based OVCs [20–22, 27–29]. In this chapter we are going to review the few studies performed in sulfur-based OVCs of the ternary AB_2X_4 family at high pressures and in particular we will comment on the pressure-induced order–disorder processes that take place in these semiconductors. The next chapter will be devoted to selenium-based OVCs and there will be no chapter for those with Te since to our knowledge there is no experimental study under pressure in OVCs with Te. Section 5.2 is devoted to review high-pressure X-ray diffraction studies in sulphide-based OVCs. Section 5.3 is devoted to a discussion regarding pressure-induced phase transitions in ternary OVCs. Section 5.4 deals with high-pressure Raman scattering measurements in sulphide-based OVCs. Finally, Sect. 5.5 will summarize the main conclusions of this work.

5.2 Isothermal Compression of AB_2S_4 OVCs: X-ray Diffraction Studies

The effect of pressure on the lattice parameters and the volume has been studied in three sulfur-based ternary OVCs: DC-$CdGa_2S_4$ [28], DC-$CdAl_2S_4$ [29, 30], and DS-$HgAl_2S_4$ [31]. Table 5.1 shows the atomic positions refined for DC-$CdGa_2S_4$ at room pressure [28]. Powder X-ray diffraction measurements in these compounds show that the diffraction patterns can be indexed with the DC (or DS) structure till 17, 9, and 21 GPa for DC-$CdGa_2S_4$, DC-$CdAl_2S_4$, and DS-$HgAl_2S_4$, respectively. However, recent XRD measurements in DC-$CdAl_2S_4$ [30] suggest that the DC phase can be observed till 13.5 GPa. At higher pressures, phase transitions to different structures may take place.

Figure 5.2 shows XRD patterns of DC-$CdGa_2S_4$ at selected pressures till 22 GPa. From the refinements of X-ray diffraction patterns collected under compression, the evolution of the unit-cell parameters and atomic positions can be obtained as a function of pressure. Figure 5.3a shows the pressure dependence of the volume and the lattice parameters for DC-$CdGa_2S_4$. A fit to the DC-$CdGa_2S_4$ volume data with

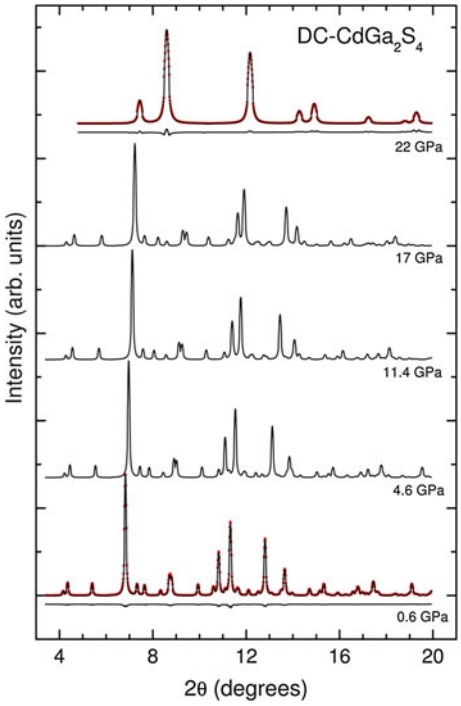

Fig. 5.2 X-ray diffraction patterns of $CdGa_2S_4$ at selected pressures. The background was substracted. At 0.6 and 22 GPa the collected pattern (*dots*) is shown together with the refined patterns (*solid line*) and the residuals of the refinement

a third-order Birch–Murnaghan equation of state (EOS) [28] gives: $V_0 = 311.38(4)$ Å^3, $B_0 = 64(2)$ GPa, and $B_0' = 4.1(3)$, where V_0, B_0, and B_0' are the zero-pressure volume, bulk modulus, and its pressure derivative, respectively. A similar analysis of $CdAl_2S_4$ data fitted with a third-order Birch–Murnaghan EOS, where the B_0' is fixed to 4, yields $V_0 = 319.03$ Å^3 and $B_0 = 44.6$ GPa [29]. More recent data suggest a slightly larger bulk modulus around 47 GPa [30]. On the other hand, data of DS-$HgAl_2S_4$ fitted to a third-order Birch-Murnaghan EOS, yields $V_0 = 311$ Å^3, $B_0 = 33$ GPa, and $B_0' = 8$ [31], while DC-$HgGa_2S_4$ fitted to a third-order Birch–Murnaghan EOS, yields $V_0 = 310.5$ Å^3, $B_0 = 45$ GPa, and $B_0' = 5.5$ [32]. These results suggest that AB_2S_4 OVCs with Hg are more compressible than those with Cd. This result is expected because it is usually found that structures holding cations of larger ionic radius exhibit smaller bulk moduli; however, the larger ionic radius of Hg with respect to Cd does not result in a larger unit cell volume of DS-$HgAl_2S_4$ than that of DC-$CdAl_2S_4$. On the other hand, the above results suggest that AB_2S_4 OVCs with Al are more compressible than those with Ga in contrast to the above stated rule since Ga has a larger ionic radius than Al.

More structural information can be obtained from the pressure dependence of the lattice parameters. Figure 5.3b shows the pressure dependence of the lattice parameters of DC-$CdGa_2S_4$. It can be observed that a and c lattice parameters decrease as a function of pressure from $a = 5.536(3)$ Å and $c = 10.160(6)$ Å at ambient

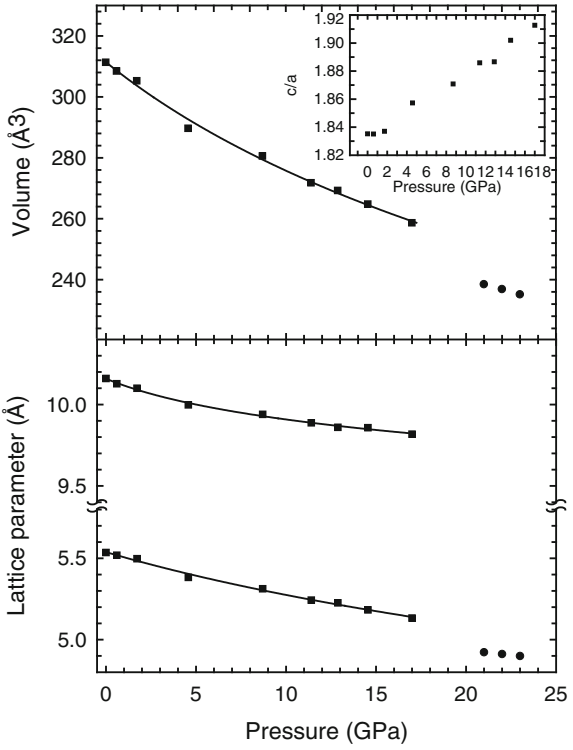

Fig. 5.3 Pressure evolution of the volume (**a**) and lattice parameters (**b**) of the low-pressure phase of $CdGa_2S_4$. *Solid squares*: low-pressure phase. *Solid circles*: high-pressure phase. The *solid lines* represent the reported EOS for both the volume and axial parameters. Inset shows the pressure dependence of the *c/a* ratio of the low-pressure phase on increasing pressure

pressure to $a = 5.064(4)$ Å and $c = 10.156(5)$ Å at 17 GPa. These lattice parameters have compresibilities for a and c axes at zero pressure of $\kappa_a = 5.9 \cdot 10^{-3}\,\mathrm{GPa}^{-1}$ and $\kappa_c = 4.5 \cdot 10^{-3}\,\mathrm{GPa}^{-1}$. Unfortunately, the variation of the lattice parameters of DC-$CdAl_2S_4$ have not been reported by Meenakshi et al. The lattice parameters of DS-$ZnGa_2S_4$ are reported to be $a = 5.274$ Å and $c = 10.407$ Å at ambient pressure [17] but the effect of pressure on them is not known.

Finally, we want to analyze the evolution of the *c/a* ratio with pressure in sulfur-based OVCs since the tetragonal distortion, $\delta = 2 - c/a$, could give information of the behavior of the sample with pressure. The inset of Fig. 5.3a shows the pressure dependence of the *c/a* ratio versus pressure for $CdGa_2S_4$ [28]. The *c/a* ratio increases from 1.84 at ambient pressure to 1.91 at 17 GPa. On the other hand, the *c/a* ratio in $CdAl_2S_4$ increases from 1.82 at ambient pressure to 1.88 at 15 GPa [30]. Similarly, the *c/a* ratio in DS-$HgAl_2S_4$ increases from 1.85 at ambient pressure to 1.96 at 20.5 GPa. The *c/a* ratios at ambient pressure of DC-$CdGa_2S_4$, DC-$CdAl_2S_4$ and DS-$HgAl_2S_4$, which are below 1.85, contrast with the value for DS-$ZnGa_2S_4$

which is around 1.97 [18]. It is noteworthy that AGa_2X_4 compounds (A = Mn, Zn, Cd, Hg; X = S, Se) with tetragonal DC structure have *c/a* values at ambient pressure below 1.90 [8, 19, 29, 33, 34]; however, $ZnGa_2S_4$ and $ZnGa_2Se_4$ with tetragonal DS structure (models 2 and 6) have *c/a* ratios above 1.97 at ambient pressure [18, 28, 35]. Furthermore, a *c/a* ratio at ambient pressure very close to 2, or equivalently a very small tetragonal distortion of the DC phase, has been considered up to now as a measure of complete cation disorder [8, 19]. In fact, the value of 2 would occur for complete cation disorder leading to the cubic DZ phase which is more symmetrical than the tetragonal structures. Therefore, our results show that DC-$CdGa_2S_4$ and DS-$HgAl_2S_4$become more symmetric structures with increasing pressure. The increase of the symmetry in DC and DS structures with increasing pressure is consistent with an increase of the cation disorder with increasing pressure but it remains to be unknown if the increase of disorder leads to any of the proposed intermediate phases of disorder (still not observed by XRD measurements) of Table 5.2.

5.3 Pressure-Induced Phase Transitions in Adamantine OVCs

As already commented, ternary OVCs of the AB_2X_4 family with tetragonal structure derive from the diamond or zincblende structure (typical of binary AX compounds). These tetragonal structures are related to those chalcopyrite-type (CP) ternary ABX_2 compounds which also derive from the zincblende-type structure. Therefore, it is worthy to understand the pressure-induced phase transitions of ternary AB_2X_4 OVCs on the basis of the pressure-induced phase transitions in zincblende and chalcopyrite structures.

It is known that tetrahedrally-coordinated elemental semiconductors like Si and Ge undergo a phase transition towards the metallic octahedrally-coordinated β-Sn structure. Similarly, binary zincblende compounds undergo pressure-induced phase transitions towards a octahedrally-coordinated phases, like the Imm2 structure (the binary analog of the β-Sn phase), orthorhombic Cmcm, or rocksalt structures [36, 37]. Therefore, a similar situation is expected to occur in ternary chalcopyrites and in ternary defect chalcopyrite and defect stannite compounds. In particular, in ternary ABX_2 chalcopyrites a phase transition towards the disordered rocksalt structure and later to the Cmcm structure have been recently found or predicted [38, 39].

In the two high-pressure XRD studies published for AB_2S_4 compounds ($CdGa_2S_4$ and $CdAl_2S_4$), a pressure-induced phase transition from the totally ordered DC phase towards the totally disordered rocksalt (DR) structure (S.G. Fm-3m, No. 225, Z = 1) has been found [28, 29]. The high-pressure DR phase [see Fig. 5.1g] has been observed above 17 GPa in $CdGa_2S_4$and between 9 and 15 GPa in $CdAl_2S_4$. The DR phase has been also observed in a number of high-pressure studies of AB_2Se_4 compounds which will be commented in the Chap. 6. However, recent Raman experiments in $CdAl_2S_4$ suggest that the high-pressure phase could not correspond to the DR structure. This result will be commented in Sect. 5.4.

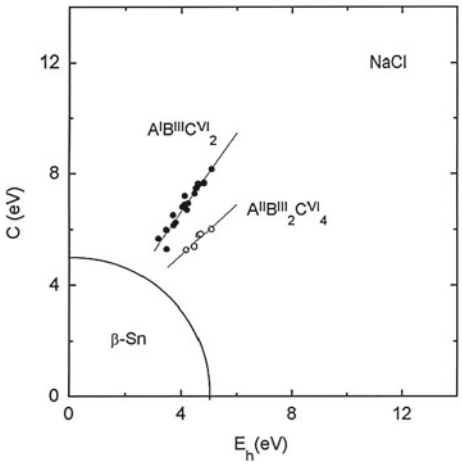

Fig. 5.4 Phase diagram for $A^IB^{III}X^V_{22}$ and $A^{II}B^{III}_2X^{VI}_4$ compounds at ambient pressure. Reprinted with permission from [21], V. V. Ursaki et al., *Phys. Rev. B* 59, 257 (1999). © 1999, American Physical Society

In order to understand the pressure-induced phase transition from the fourfold-coordinated structures to sixfold-coordinated rocksalt-type structure, several trends have been noted in adamantine compounds. The microscopic dielectric theory of Phillips and Van-Vechten provides a basis for understanding the structural trends of semiconductors. With the dielectric theory it became possible to establish a criterion based on an ionicity scale which divided the fourfold and sixfold structures. Figure 5.4 shows a phase diagram containing most of the $A^IB^{III}X^{VI}_2$ compounds with chalcopyrite structure and some of $A^{II}B^{III}_2X^{VI}_4$ with DC one at ambient pressure. The homopolar energy gap E_h and the ionic energy gap C are plotted along the horizontal and vertical axes, respectively. A circle centred at the origin is drawn to separate the two high pressure phases according to the theory of Phillips and Van-Vechten. One can see that all compounds involved fall outside this circle, indicating that a phase transition to the rocksalt-type structure is expected under pressure for both $A^IB^{III}X^{VI}_2$ and $A^{II}B^{III}_2X^{VI}_4$ [21]. This prediction seems to be correct since the high-pressure rocksalt-structure phase has been confirmed by X-ray analysis for most of the $A^IB^{III}X^{VI}_2$ compounds and $A^{II}B^{III}_2X^{VI}_4$ OVCs.

Chelikowsky and Burdett proposed an approach for examining the relationship between spectroscopic crystal ionicity and spatial structure [40]. To determine the phase stability of a given structure, they consider the free energy for prototypical III–V, II–VI, and I–VII materials by varying the relative cation to anion potential strengths. The results of calculations of the phase diagram are presented in Fig. 5.5. It was noted that the fields in Fig. 5.5 are compatible with the known structural behaviour of binary AX compounds. For example, the more covalent species are predicted to transform to the β-Sn structure under pressure and the more ionic II–VI species transform to rocksalt or Cmcm phases. Moreover, it is possible to predict generic trends with this diagram. It predicts that a zincblende to β-Sn to rocksalt transformation cannot occur, while a zincblende (Zb) to rocksalt to β-Sn transition can occur. One should note that the diagram in Fig. 5.5 is restricted in its applicability

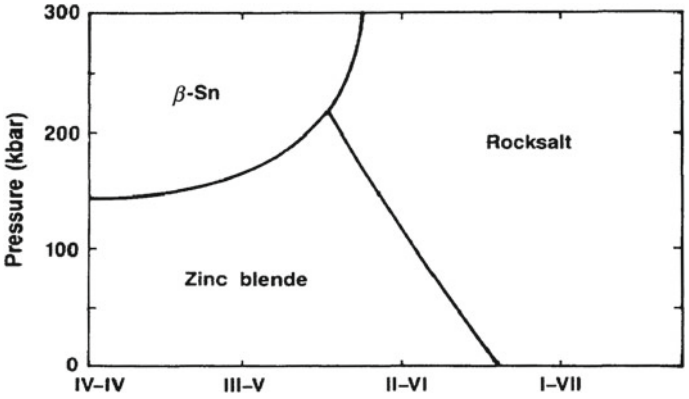

Fig. 5.5 Phase diagram for prototypical crystal-structure types. The diagram is categorized by material and by pressure. Orbital or size effects are not included. The reference structure is GaAs. Reprinted with permission from [41] © 1987, American Physical Society

to zincblende semiconductors which preserve the bond length of the reference crystal, in this case GaAs.

Chelikowsky used a combination of pseudopotential total-energy method with an empirical ionicity scale to predict phase transitions as a function of pressure for all diamond and zincblende semiconductors of the form $A^N X^{8-N}$, where A and X are simple metals or metalloids and N is the number of valence electrons for species A [41]. Two parameters enter in his discussion, the crystal ionicity from dielectric theory and the equilibrium crystal volume. Figure 5.6 displays an overview with various semiconductors categorized by ionicity and by bond length, and the corresponding predictions as to whether the preferred high-pressure phase is β-Sn or rocksalt. While most of the pressure-induced phase transitions to the rocksalt phase were confirmed, most of the transitions to the β-Sn phase were not observed, except for GaSb and InSb, and phase transitions to the Cmcm phase and other orthorhombic phases, intermediate between both β-Sn and rocksalt phases, were observed instead. The reasons for the absence of the β-Sn related phases in many zincblende-type materials were discussed by Ozolins and Zunger [42].

In Fig. 5.7, a comparison of experimental and calculated transition pressures for compounds crystallizing in the zincblende and diamond structures is presented. Since $A^{I}B^{III}X_2^{VI}$ CP compounds and $A^{II}B_2^{III}X_4^{VI}$ DC and DS compounds are derivatives from the zincblende structure and undergo a phase transition to the rocksalt structure under pressure, it was discussed whether the above theory applies to CP and DC compounds [21]. For this purpose, the ionicities and bond lengths for $A^{I}B^{III}X_2^{VI}$ and $A^{II}B_2^{III}X_4^{VI}$ compounds along with experimental values of phase transition pressures to the rocksalt structure are presented in Table 5.4.

Figure 5.8 illustrates the transition pressure for the transformation from a fourfold-coordinated structure to a sixfold-coordinated one, as a function of ionicity, for $A^{II}X^{VI}$, $A^{I}B^{III}X_2^{VI}$ and $A^{II}B_2^{III}X_4^{VI}$ compounds. The dashed lines in the figure are the result of calculations according to the model of Chelikowsy [41] and the frozen-

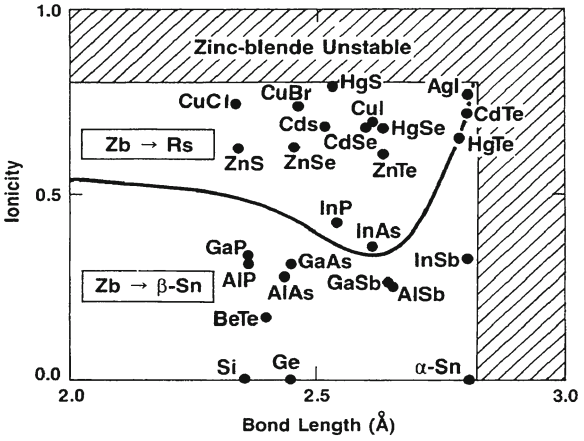

Fig. 5.6 High-pressure domains for diamond and zincblende semiconductors. The zinc-blende to white tin transition (Zb-β-Sn) and zincblende to rocksalt (Zb-Rs) regimes are indicated in an "ionicity-bond length" space. Above the critical ionicity of 0.79, zincblende structures are not stable at normal pressure. Also, for bond lengths greater than about 2.8 Å no zincblende structures exist. The theory is not applicable to compounds with bond length less than ~2.3 Å. Reprinted with permission from [41] © 1987, American Physical Society

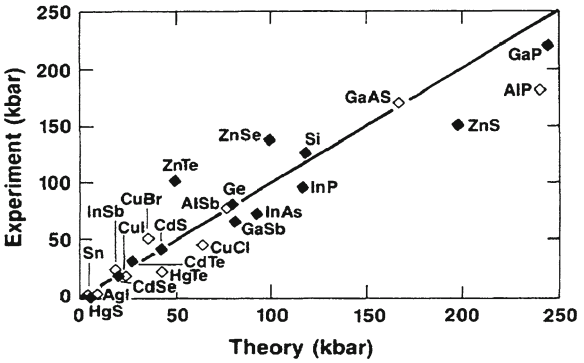

Fig. 5.7 A comparison between the predicted and measured transition pressures. The theoretical results correspond to transitions from the zincblende, or diamond, structure to the high-pressure structures of rocksalt and white tin. The solid points correspond to experimentally determined structures which are either rocksalt or white tin. The open points correspond to structures other than those examined theoretically. Reprinted with permission from [41], J.R. Chelikowsky, *Phys. Rev. B* 35, 1174 (1987). © 1987, American Physical Society

potential model of Christensen [43]. The solid lines are the linear least squares fits of the experimental data for $A^{I}B^{III}X_2^{VI}$ and $A^{II}B_2^{III}X_4^{VI}$ compounds. One can observe that Chelikowsky's theoretical results fit very well the experimental data for the $A^{II}X^{VI}$ materials with high ionicity. The opposite is true for the theoretical results of Christensen et al. Specifically, it was found that MgS and MgSe fall on

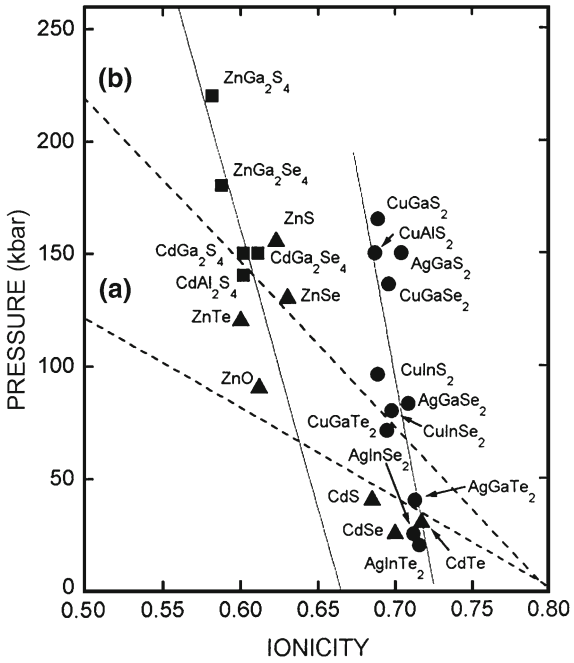

Fig. 5.8 Critical pressure for transformation from the fourfold-coordinated structure to the sixfold-coordinated one, as a function of ionicity for $A^{II}B^{VI}$, $A^{I}B^{III}X_2^{VI}$ and $A^{II}B_2^{III}X_4^{VI}$ compounds. The dashed lines are the results of calculation following **a** the Chelikowsky and **b** the Christensen model. Solid lines are the linear least-squares fits of the experimental data. Reprinted with permission from [21], V. V. Ursaki et al., *Phys. Rev. B* 59, 257 (1999). © 1999, American Physical Society

the transition boundary of zincblende and rocksalt structures, the predicted critical ionicity being consistent with the Phillips value [Chelikowsky has found $f_i^c = 0.80$, in close agreement with the Phillips value $f_i^c = 0.795$]. For the materials with low ionicity the agreement with experiment is only qualitative. Nevertheless, the theoretical approach predicts a difference between the Zn and Cd salts. Namely, the Zn salts should possess a higher transition pressure from zincblende to rocksalt structure than the Cd salts. This general trend was confirmed by experiments. Note that this trend was found to be valid for our $A^{II}B_2^{III}X_4^{VI}$ compounds as well. As concerns $A^{I}B^{III}X_2^{VI}$ CP and $A^{II}B_2^{III}X_4^{VI}$ DC and DS compounds, it was observed that the experimental data are very well approximated by linear fits (which, however, differ substantially from those of Chelikowsky and Christensen et al.).

Another essential output from Chelikowsky's model is the possibility to predict the transition pressure and the high-pressure structure (rocksalt or β-Sn) on the basis of the bond length. In Fig. 5.9, the transition from zincblende to white tin (ZB–β-Sn) and from zincblende to rocksalt (ZB–RS) are indicated in an "ionicity-bond length" space taking into account the experimental data of $A^{I}B^{III}X_2^{VI}$ CP and $A^{II}B_2^{III}X_4^{VI}$ DC and DS compounds (see Table 5.4). Above the critical ionicity of 0.79, the zincblende

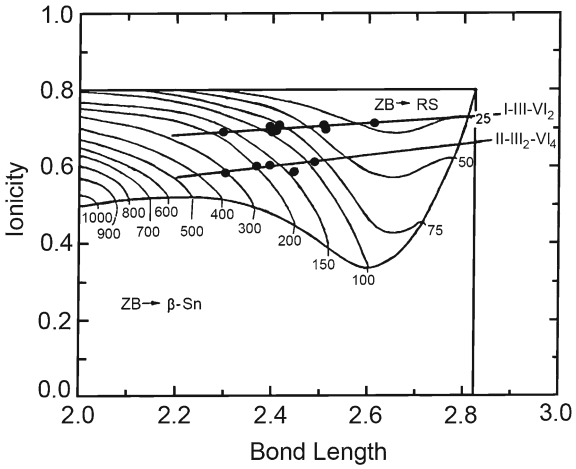

Fig. 5.9 Experimental data summarized in Table 5.4 for $A^{I}B^{III}X_2^{VI}$ and $A^{II}B_2^{III}X_4^{VI}$ compounds inserted in the high-pressure domains for diamond and ZB semiconductors calculated by Chelikowsky. Reprinted with permission from [21], V. V. Ursaki et al., *Phys. Rev. B* 59, 257 (1999). © 1999, American Physical Society

structure is not stable at normal pressure. Also, for bond lengths greater than 2.8 Å the zincblende structure cannot exist. As mentioned above, the theory is not applicable to compounds with bond length less than ~2.3Å. One can see that all $A^{I}B^{III}X_2^{VI}$ CP and $A^{II}B_2^{III}X_4^{VI}$ DC compounds lay in the ZB–RS domain. Thus, a transition to the rocksalt structure is expected.

Figure 5.9 also displays a contour plot of transition pressures to rocksalt phase predicted by Chelikowsky's model [41]. Table 5.5 presents a comparison between the experimental and the predicted high-pressure forms and transition pressure for $A^{I}B^{III}X_2^{VI}$ and $A^{II}B_2^{III}X_4^{VI}$ compounds. One can conclude that agreement between theory and experiment is rather satisfactory. However, the predicted transition pressures for the sulphides are overestimated, while for selenides are underestimated. One can notice the same tendency for zincblende $A^{II}X^{VI}$ compounds, when analyzing the data presented by Chelikowsky [41]. This behaviour can be accounted for by the fact that their calculations do not include explicit treatment of *d*-orbital effects.

A different approach has been used by Jayaraman et al. to give account for the different transition pressures from tetrahedral to octahedral coordination in $A^{I}B^{III}X_2^{VI}$ compounds [44]. These authors proposed an empirical rule to explain the different transition pressures on the basis of the ratio between the averaged cation and anion radii ratio, $\xi = r_A + r_B/2r_X$. Other size criteria, similar to Jayaraman's rule, have been proven to work satisfactory to predict the transition pressure in ternary compounds [45, 46]. However, Beister et al. [47] have challenged Jayaraman's rule based upon data on $LiInSe_2$, $CuInSe_2$ and $AgInSe_2$. These authors proposed the transition pressure should increase with the decreasing cation radius difference $|r_A - r_B|$. Errandonea et al. tried to apply this approach not only to $A^{I}B^{III}X_2^{VI}$ compounds but also

Table 5.4 Bond ionicity ($f^i_{AX,BX}$), bond length ($d_{AX,BX}$), crystal ionicity (f^i), average bond length (d), and the experimental transition pressure to the rocksalt-type structure, for ABX_2 and AB_2X_4 compounds. [21]

Compound	f^i_{AX}	f^i_{BX}	f^i	d_{AX}(Å)	d_{BX}(Å)	d(Å)	P_{NaCl}(GPa)
ABX_2							
$CuAlS_2$	0.813	0.561	0.687	2.374	2.219	2.297	15
$CuGaS_2$	0.816	0.561	0.689	2.340	2.255	2.298	16.5
$CuGaSe_2$	0.825	0.567	0.696	2.395	2.410	2.403	13.6
$CuInS_2$	0.808	0.569	0.689	2.310	2.490	2.400	9.6
$CuInSe_2$	0.817	0.572	0.695	2.440	2.580	2.510	7.1
$AgGaS_2$	0.849	0.559	0.704	2.575	2.255	2.415	15.0
$AgGaSe_2$	0.851	0.566	0.709	2.601	2.416	2.509	8.3
$AgInSe_2$	0.850	0.573	0.712	2.600	2.625	2.613	2.5
AB_2X_4							
$CdAl_2S_4$	0.685	0.561	0.602	2.532	2.255	2.395	14.0
					2.249		
$CdGa_2S_4$	0.685	0.561	0.602	2.435	2.372	2.368	15.0
					2.298		
$CdGa_2Se_4$	0.699	0.567	0.611	2.637	2.411	2.488	15.0
					2.416		
$ZnGa_2S_4$	0.623	0.561	0.582	2.303	2.328	2.201	22.0
					2.278		
$ZnGa_2Se_4$	0.630	0.567	0.588	2.455	2.416	2.429	18.0
					2.416		

to $A^{II}B^{III}_2X^{VI}_4$ [28]. Table 5.6 shows the transition pressures for different ABX_2 and AB_2X_4 compounds and the ionic radii of the elements A, B and X. Figure 5.10 shows the transition pressures as a function of the averaged cation to anion radii ratio. It can be observed that the transition pressure on these compounds can be rationalized using the ionic radius on cations and anions in a similar way than proposed by Jayaraman.

Most of the compounds of interest follow two different systematics in Fig. 5.10. One for those compounds with large cations ($1.35 > r_A + r_B > 1.15$) and another for the compounds with small cations ($r_A + r_B < 1.15$) [28]. In both cases, there is a tendency to the increase of the transition pressure with the increase of ξ. It is interesting to see that also spinel-structured AB_2X_4 compounds seem to follow the same systematics. It is important to note here that the fitting lines shown in Fig. 5.10 for each cation-size regime are dependent on the high-pressure points. Unfortunately, in the literature there are few data available for ξ values from 0.35 to 0.4, which make the systematic here proposed only valid to make back-of-the-envelope estimations for transition pressures in compounds not studied upon compression yet. Regarding the criterion proposed by Beister et al., it is clear from Table 5.2 that no possible correlation could be established between the transition pressures and cation radius difference $|r_A - r_B|$ [28].

Table 5.5 Comparison between theoretically predicted transition pressures (in GPa) to rocksalt-type structure and their experimental values for $A^{I}B^{III}X_2^{VI}$ and $A^{II}B_2^{III}X_4^{VI}$ compounds. After [21]

Compound	Theory	Experiment
ABX_2		
$CuAlS_2$	17.0	15.0
$CuGaS_2$	17.0	16.5
$CuGaSe_2$	8.0	13.6
$CuInS_2$	9.5	9.6
$CuInSe_2$	3.7	7.1
$AgGaS_2$	8.0	15.0
$AgGaSe_2$	4.0	8.3
$AgInSe_2$	2.4	2.5
AB_2X_4		
$CdAl_2S_4$	15.0	14.0
$CdGa_2S_4$	20.0	15.0
$CdGa_2Se_4$	9.0	15.0
$ZnGa_2S_4$	30.0	22.0
$ZnGa_2Se_4$	13.0	18.0

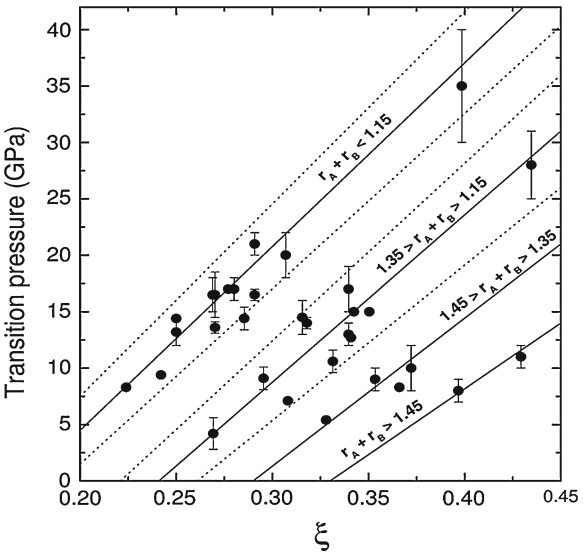

Fig. 5.10 Transition pressures of different ABX_2 and AB_2X_4 compounds as a function of $\xi = (r_A + r_B)/2r_X$. The solid lines estimate the transition pressure of different compounds, the *dotted lines* give the deviation from the estimated value. The data plotted correspond to those shown in Table 5.6. After [28]

Several high-pressure works have claimed that intermediate phases with a disorder intermediate between the DC and the DR structures should be found [20–22]. In particular, a two stage process has been suggested: (i) a first stage where cation disorder should occur without disorder of vacancies; and (ii) a second stage of disor-

Table 5.6 Transition pressures, P_T, and ionic radii of different sphalerite-related semiconductors

Compound	Structure	r_A	r_B	r_X	ξ	$\mid r_A - r_B \mid$	P_T(GPa)
$CuAlTe_2$	CP	0.60	0.39	2.21	0.2239	0.21	8.3
$CuGaTe_2$	CP	0.60	0.47	2.21	0.2421	0.13	9.4
$CuAlSe_2$	CP	0.60	0.39	1.98	0.2500	0.21	13.2
$ZnAl2Se_4$	DC	0.60	0.39	1.98	0.2500	0.21	14.4
$CuAlS_2$	CP	0.60	0.39	1.84	0.2690	0.21	16.5
$CuGaSe_2$	CP	0.60	0.47	1.98	0.2702	0.13	13.6
$ZnGa_2Se_4$	DS	0.60	0.47	1.98	0.2702	0.13	16.5
$ZnAl_{1.2}Ga_{0.8}S_4$	CP	0.60	0.42	1.84	0.2771	0.18	17.0
CuGaSSe	CP	0.60	0.47	1.91	0.2801	0.13	17.0
$MnGa_2Se_4$	DC	0.66	0.47	1.98	0.2854	0.19	13.0
$CuGaS_2$	CP	0.6	0.47	1.84	0.2907	0.13	16.5
$ZnGa_2S_4$	DS	0.60	0.47	1.84	0.2907	0.13	21.0
$ZnAl_2S_4$	Spinel	0.60	0.53	1.84	0.3070	0.07	20.0
$MgAl_2O_4$	Spinel	0.57	0.53	1.38	0.3985	0.04	35.0
$CuInTe_2$	CP	0.60	0.62	2.21	0.2692	0.02	4.2
$CdAl_2Se_4$	DC	0.78	0.39	1.98	0.2955	0.39	9.1
$CuInSe_2$	CP	0.60	0.62	1.98	0.3081	0.02	7.1
$CdGa_2Se_4$	DC	0.78	0.47	1.98	0.3156	0.31	16.0
$CdAl_2S_4$	DC	0.78	0.39	1.84	0.3179	0.39	14.0
$CuInS_2$	CP	0.60	0.62	1.84	0.3315	0.02	9.6
$CuIr_2S_4$	Spinel	0.57	0.68	1.84	0.3396	0.11	13.0
$CdGa_2S_4$	DC	0.78	0.47	1.84	0.3396	0.31	17.0
$HgAl_2Se_4$	DC	0.96	0.39	1.98	0.3409	0.57	12.7
$AgGaS_2$	CP	0.79	0.47	1.84	0.3424	0.32	15.0
$CuCrZrS_4$	Spinel	0.57	0.72	1.84	0.3505	0.15	15.0
Zn_2TiO_4	Inverse Spinel	0.60	0.60	1.38	0.4347	0	28.0
$AgGaTe_2$	CP	0.98	0.47	2.21	0.3320	0.51	5.4
$CdCr_2Se_4$	Spinel	0.78	0.62	1.98	0.3535	0.16	9.0
$AgGaSe_2$	CP	0.98	0.47	1.98	0.3661	0.51	8.3
$MgIn_2S_4$	Spinel	0.57	0.80	1.84	0.3723	0.23	10.5
$MnIn_2S_4$	Spinel	0.66	0.80	1.84	0.3967	0.14	8.0
$CdIn_2S_4$	Spinel	0.78	0.80	1.84	0.4293	0. 02	11.0

The factor $\xi = (r_A + r_B)/2r_X$ was calculated for each compound using the Shannon radii [48]. After [28]

der where both cations and vacancies should be mixed resulting in a DZ phase prior to the transition to the DR phase. The occurrence of possible intermediate phases between the DC and DR phases will be discussed in Sect. 5.4 regarding Raman scattering measurements at high pressures since XRD measurements at high pressures have provided no signature of the intermediate phases of disorder so far.

5.4 High-Pressure Raman Studies of AB_2S_4 OVCs

At ambient conditions, the vibrational properties of ternary AB_2X_4 OVCs have been mostly studied with Raman (R) and infrared (IR) spectroscopy. According to group theory [49], the DC structure (model 1) of $CdGa_2S_4$ should have 21 optical vibrational modes at Γ with the mechanical representation:

$$\Gamma = 3A \oplus 5B(\mathrm{R}, \mathrm{IR}) \oplus 5E(\mathrm{R}, \mathrm{IR}) \oplus B \oplus E \tag{5.1}$$

where A modes are non-polar modes, and B and E modes are polar modes, being E modes doubly degenerated. This results in a total of 13 Raman-active modes and 10 IR-active modes since one B and one E are acoustic modes. It is interesting to note that doubly degenerate E modes correspond to vibrations of atoms along the a and b axis; i.e., in the directions perpendicular to the c axis, while B modes correspond to vibrations of atoms along the c axis.

On the other hand, the DS structure of $ZnGa_2S_4$ (assuming it corresponds to model 2 of Table 5.2) should have 21 optical vibrational modes at Γ with the following representation:

$$\Gamma = 2A_1(\mathrm{R}) \oplus A_2 \oplus 2B_1(\mathrm{R}) \oplus 3B_2(\mathrm{R}, \mathrm{IR}) \oplus 5E(\mathrm{R}, \mathrm{IR}) \oplus B \oplus E \tag{5.2}$$

where B_2 and E are polar modes, being E modes doubly degenerated. This results in a total of 12 Raman-active modes and 8 IR-active modes ($3\ B_2 \oplus 5E$) because the A_2 mode is silent and one B_2 and one E are acoustic modes. Note that the same number of modes are expected for model 6 of the DS phase.

Finally, the DS structure of $HgAl_2S_4$ (assuming it corresponds to model 7 of Table. 5.2) should have 24 optical vibrational modes at Γ with the following representation:

$$\Gamma = 2A_1(\mathrm{R}) \oplus A_2 \oplus 2B_1(\mathrm{R}) \oplus 4B_2(\mathrm{R}, \mathrm{IR}) \oplus 6E(\mathrm{R}, \mathrm{IR}) \oplus B_2 \oplus E \tag{5.3}$$

where B_2 and E are polar modes, being E modes doubly degenerated. A total of 14 Raman-active modes and 10 IR-active modes are expected since one B_2 and one E modes are acoustic and the A_2 mode is silent.

In addition, two wavenumbers (either R or IR) should be observed for each B and E (B_2 and E modes) in the DC (DS) structure, due to the transversal-longitudinal optic (TO–LO) splitting of the polar modes. Consequently, taking into account the TO-LO splitting, up to 23, 20 and 22 Raman-active modes could be observed in the DC (model 1), DS (model 2), and DS (model 7) phases.

High-pressure studies of the lattice dynamics of OVCs have been usually performed using Raman spectroscopy. Raman spectroscopy is a very sensitive technique able to detect the occurrence of structural phase transitions at even smaller pressures than XRD measurements because Raman scattering is more sensitive to local structural changes than XRD, which usually detect large scale structural changes.

In addition, the careful study of the intensity of some specific Raman modes under compression can provide valuable information about the pressure-induced order-disorder effects which can be compared with the structural information described in Sect. 5.2. In this section we will concentrate on discussing Raman results for AB_2S_4 OVCs at high pressures paying special attention to the high-pressure Raman spectra of DC-$HgGa_2S_4$ as a matter of example.

Figure. 5.11a shows Raman spectra of DC-$HgGa_2S_4$ at selected pressures up to 20 GPa [50]. Above 20 GPa new modes (asterisks) appear in the Raman spectrum that add to the previous observed modes of the DC phase. The appearance of new modes suggests a phase transition to a structure with more Raman modes than the DC phase or a coexistence of a new phase with the original DC phase. The Raman spectrum of DC-$HgGa_2S_4$ is typical of DC and most DS compounds with the only exception that in DS compounds there is one *A* mode (the *A* mode of intermediate frequency, named A^2) that is lost. The Raman spectrum of DC-$HgGa_2S_4$ can be divided into three regions: (i) the low-frequency region below 200 cm^{-1}, (ii) the medium-frequency region between 200 and 300 cm^{-1}, and (iii) the high-frequency region above 300 cm^{-1}. For the DC phase, 16 Raman-active modes at ambient pressure have been observed. The *B* and *E* modes spread mainly along the three regions, while the non-polar *A* modes, that in the OVCs involve the different oscillations

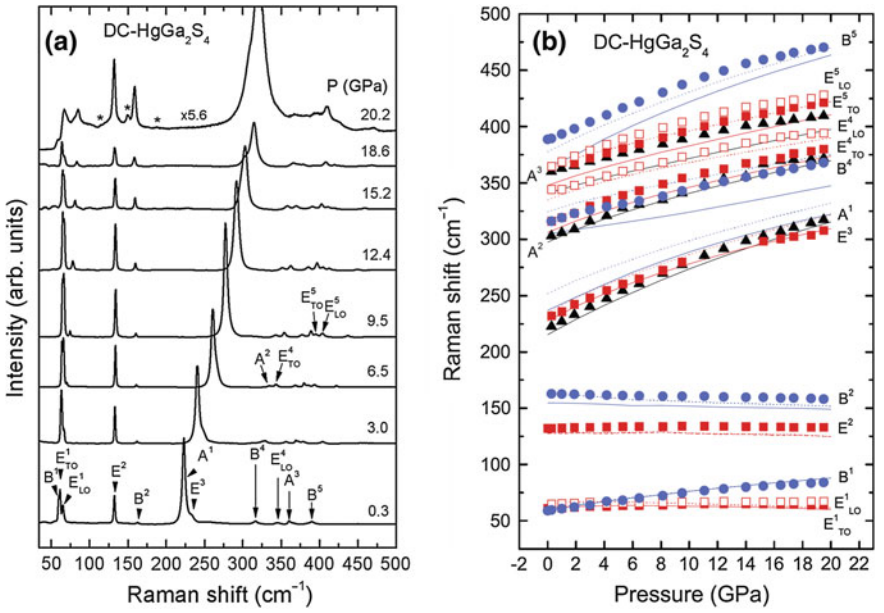

Fig. 5.11 **a** Raman spectra of DC-$HgGa_2S_4$ at selected pressures up to 20 GPa. The symmetry of the Raman-active modes is also shown. **b** Pressure dependence of the Raman-active modes of DC-$HgGa_2S_4$. Experimental values of *A*, B_{TO}/B_{LO} and E_{TO}/E_{LO} Raman modes are represented by *solid triangles* (*black*), solid/open circles (*blue*), and solid/open squares (*red*), respectively

of anions around vacancies, are located in the medium- and high-frequency regions. In general, the modes in the low- and medium-frequency regions are more intense than those in the high-frequency region. Furthermore, modes in the high-frequency region are considerably overlapped. The most intense peak of the Raman spectrum of DC-$HgGa_2S_4$, and also in all ternary OVCs with DC or DS structure is the A^1 mode. This mode is called the "breathing" mode since it is associated to the symmetric oscillation of the anions against the stoichiometric vacancy.

As regards the symmetry assignment of the Raman-active modes, it must be taken into account that DC and DS compounds are optically uniaxial crystals. This means that, except for incidence along the optical axis or at 90° from it, symmetry or character coupling is to be expected for Raman modes [51, 52]. Thus, one may observe E, B, LO, and TO quasimodes, resulting from the coupling of $E_{TO} + E_{LO}$, $B_{TO} + B_{LO}$, $E_{TO} + B_{TO}$, or $E_{LO} + B_{LO}$ modes. These couplings depend on the relative magnitude of polar (LO–TO) versus anisotropy (B–E) splitting for each B–E pair of modes. In particular, when Raman scattering is measured with laser incidence along the (111) plane, which is the direction perpendicular to the typical cleavage plane of OVCs we are not expected to observe pure E or B modes but quasimodes; therefore, the comparison of experimental data with theoretical data which provide pure E and B modes and pure TO and LO modes must be done with caution. In Fig. 5.11a the symmetries assigned to the different Raman modes in DC-$HgGa_2S_4$ on the basis of the comparison with theoretical data are shown [50].

Figure 5.11b shows the experimental pressure dependence of the Raman mode frequencies of DC-$HgGa_2S_4$ at selected pressures up to 20 GPa. The symmetries, frequencies, and the frequency pressure coefficients at zero-pressure are summarized in Table 5.7, where they are compared with the corresponding data in DC-$CdAl_2S_4$ and DC-$CdGa_2S_4$. Note that data reported for $CdAl_2S_4$ [30] and $CdGa_2S_4$ [53, 54] are in good agreement with those already published [20, 22, 27]. The Raman spectrum of DC-$HgGa_2S_4$ and its pressure dependence can be understood on the basis of its similarity to that of other ternary OVCs with DC or DS structure like $CdAl_2S_4$ and $CdGa_2S_4$. Both tetragonal DS and DC structures derive from the zincblende structure by a doubling of the unit cell along the *c* axis. This results in a folding of the X and W points of the Brillouin zone edge of the zincblende structure into the Γ point of these two tetragonal structures. Therefore, several Raman modes in the tetragonal DC and DS structures behave similarly to vibrational modes occurring at the X and W points of the cubic zincblende structure. With this in mind, the very small or even negative pressure coefficients of the low-frequency *E* and *B* modes can be understood assuming that the low-frequency E and B modes come from transverse acoustic (TA) and longitudinal acoustic (LA) modes, respectively, at the X and W points of the BZ of the zincblende structure [20, 27, 55]. A similar effect was observed in chalcopyrites like $CuGaS_2$ [56].

On the basis of the comparison of the Raman modes of DC and DS structures and those of the zincblende structure, it is possible to understand why the Raman modes of DS and DC structures located in the medium-frequency region exhibit the largest frequency pressure coefficients and why the modes of the high-frequency region exhibit a little bit smaller frequency pressure coefficients than the modes

Table 5.7 Symmetry, zero-pressure frequency, and frequency pressure coefficients of Raman-active modes in DC-$CdAl_2S_4$[30], DC-$CdGa_2S_4$ [53], and DC-$HgGa_2S_4$ [50]

DC-$CdAl_2S_4$			DC-$CdGa_2S_4$			DC-$HgGa_2S_4$		
Symmetry	ω_0 (cm^{-1})	$d\omega$/dP (cm^{-1}/GPa)	Symmetry	ω_0 (cm^{-1})	$d\omega$/dP (cm^{-1}/GPa)	Symmetry	ω_0 (cm^{-1})	$d\omega$/dP (cm^{-1}/GPa)
E^1(TO)	89(1)	0.4(1)	E^1(TO)	88(1)	0.2(1)	E^1(TO)	62(1)	0.16(3)
E^1(LO)	94(1)	0.14(3)	B^1	88(1)	1.0(1)	E^1(LO)	65(1)	0.10(1)
B^1	96(1)	1.2(1)	E^2	139(1)	0.2(1)	B^1	61(1)	1.3(1)
E^2	185(1)	0.4(1)	B^2(TO)	162(1)	−0.5(1)	E^2	133(1)	0.04(2)
B^1	203(1)	0.3(1)	B^2(LO)	168(1)	−0.3(1)	B^2	163(1)	-0.2(1)
A^1	215(1)	6.1(2)	A^1	224(1)	5.8(2)	A^1	220(1)	7.0(1)
E^3(TO)	258(2)	4.9(2)	E^3	247(1)	5.0(2)	E^3	230(2)	6.3(1)
E^3(TO)	264(2)	4.7(2)	B^1	264(2)	5.0(2)	A^2	300(2)	5.1(1)
B^3	297(2)	4.5(2)	A^2	317(1)	3.6(2)	B^3		
A^2	315(3)	4.1(3)	E^4	328(2)	2.8(1)	B^4(TO)	316(3)	3.0(1)
A^3	374(2)	2.7(2)	B^4	328(2)	3.8(2)	B^4(LO)	316(3)	3.0(1)
	409(2)	1.4(2)	A^3	355(2)	3.4(1)	E^4(TO/LO)	315(4)/341(3)	4.9(3)/3.9(2)
E^4	425(2)	5.0(1)	E^5(TO)	366(3)	3.9(2)	A^3	358(2)	3.7(1)
B^4	435(2)	5.0(2)	B^5(TO)	368(3)	2.7(2)	E^5(TO)	360(3)	4.3(2)
$E^5 + 5^5$ (TO)	450(3)	6.6(2)	E^5(LO)	369(4)	4.2(2)	E^5(LO)	364(3)	3.2(2)
$E^5 + 5^5$ (LO)	501(3)	4.6(2)	B^5(LO)	396(4)	4.9(2)	B^5	387(4)	6.1(3)

of the medium-frequency region. The explanation is that modes of the medium-frequency and high-frequency regions can be considered to be analogs of the TO and LO modes in the zincblende structure, where TO modes exhibit usually larger pressure coefficients than LO modes; a signature of the decrease of the ionicity of the compound with increasing pressure [57, 58].

As already commented, new Raman modes appear above 18 GPa in $HgGa_2S_4$ [50]. In order to resolve whether there is only one or two phases above 18 GPa the authors increased pressure to 22 GPa and checked if the phase transition proceeded further showing the decrease of the peaks assigned to the original DC phase. Since this effect was not observed till 22 GPa they decreased pressure to almost ambient pressure and noted that the same Raman features were observed at low pressures; thus indicating a new metastably phase present near ambient conditions. Figure 5.12 shows the comparison of the Raman spectra around 3 GPa during the first upstroke and after the first upstroke (second upstroke). It can be observed that the new peaks appearing during the first upstroke above 18 GPa are still observed after decreasing pressure to almost ambient pressure. Furthermore, a close comparison of the linewidth of the Raman peaks during the first and second upstroke revealed that some peaks get broadened while others do not. The negligible broadening of several Raman modes suggests that no stress is present in the recovered sample and that the broadening of several modes, like the most intense *A* mode and the high-frequency modes can be attributed to the fact that the recovered sample corresponds to the DS phase rather than to the original DC phase. This is similar to what has been found in $ZnGa_2Se_4$ [24] and in $CdGa_2Se_4$ [25]. In summary, this result indicates that above 18 GPa the original DC

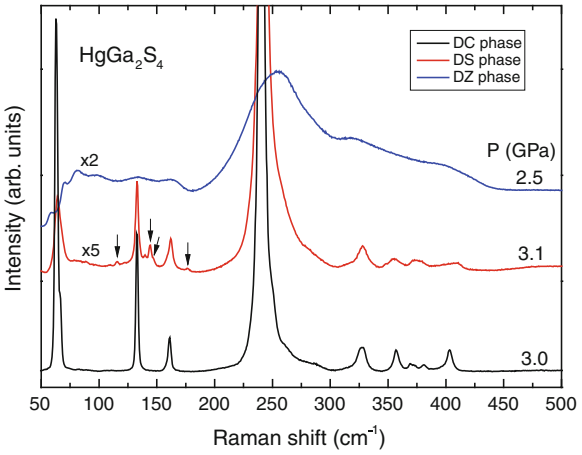

Fig. 5.12 Comparison of the Raman spectra of the DC-, DS- and DZ-$HgGa_2S_4$ at different pressures during the first, second, and third upstrokes at pressures of 3.0, 3.1 and 2.5 GPa, respectively. *Arrows* indicate the new Raman modes observed in the DS phase with respect to those observed in the DC phase

sample undergoes an irreversible phase transition to an intermediate phase between the DC and DR structure which has the DS structure [50].

It can be noted that several models for the DS phase (models 3, 4, 5, 7, 8 and 9 in Table 5.2) have a total or partial occupation of the vacancy site and therefore should exhibit one extra mode with respect to the DC phase (they must exhibit one B_2 and one E mode more but one A mode less). Therefore, the high-pressure phase of DC-$HgGa_2S_4$ above 18 GPa was tentatively attributed to model 7 on the basis of the probability of disorder from the ordered DC (model 1) phase [50]. The appearance of this model in $HgGa_2S_4$ at high pressures was justified because Hg is a rather large A^{II} cation compared to Ga (B^{III} cation) therefore the interchange of cations Hg and Ga at the same cation plane can be difficult and this impedes the model 6 to be formed. This is the opposite case to $ZnGa_2S_4$ where polytype 6 is the assumed DS phase occurring at ambient conditions due to the easy of interchange of Zn and Ga atoms with similar size. Consequently the second more probable polytype to be formed is polytype 7 where disorder is given by interchange of Ga cations with vacancies in the same cation plane. It is noteworthy that DS (model 7) is also the structure found in $HgAl_2S_4$ at ambient conditions [16, 31]. Therefore, the same argument can be used to justify the formation of this model instead of the DS (model 6) in this compound.

Vilaplana et al. characterized the pressure dependence of the vibrational properties of the new DS phase in $HgGa_2S_4$ up to 25 GPa (see Fig. 5.13a) [50]. The Raman modes of the DS phase (model 7) were observed till 23 GPa because of the transition to the DR phase above this pressure. On decreasing pressure till almost ambient pressure the Raman spectrum of the DS phase is not recovered, thus indicating that the DS to DR phase transition is not reversible. Instead, Vilaplana et al. observed a Raman spectrum with broad bands which compare with the narrow Raman modes of the DC and DS phases (see Fig. 5.12). The Raman spectrum of the recovered sample is rather continuous and looks like a one-phonon density of states of the zincblende phase. Clearly, the Raman spectrum on downstroke cannot be attributed to the DR phase, which is Raman inactive, but also it cannot correspond to the initial DC phase. Since the DR phase is a totally disordered phase and assuming that the initial order of the DC structure cannot be recovered without providing thermal energy to the system, the Raman spectrum on downstroke was tentatively attributed to the totally disordered zincblende phase (DZ), as it was done in a previous high-pressure work of $CdGa_2Se_4$ [25]. This result is also in agreement with results of many authors that have observed the DZ phase on decreasing pressure in several defect chalcopyrites [22, 29, 33].

The pressure dependence of the Raman modes in the DZ phase of $HgGa_2S_4$ were measured on increasing pressure during a third upstroke till 18.4 GPa (see Fig. 5.13b). Above this pressure the Raman spectrum disappears suggesting that the sample transited again to the DR phase. Furthermore, the same Raman spectrum of the DZ phase was recovered on decreasing pressure from the DR phase, thus showing the reversibility of the DZ to DR phase transition. This reversibility is expected because both structures are fully cation-vacancy disordered. In general, it was found that the maximum values of the pressure coefficients are smaller in the DZ phase than in the DC and DS phases, so it can be concluded that pressure coefficients

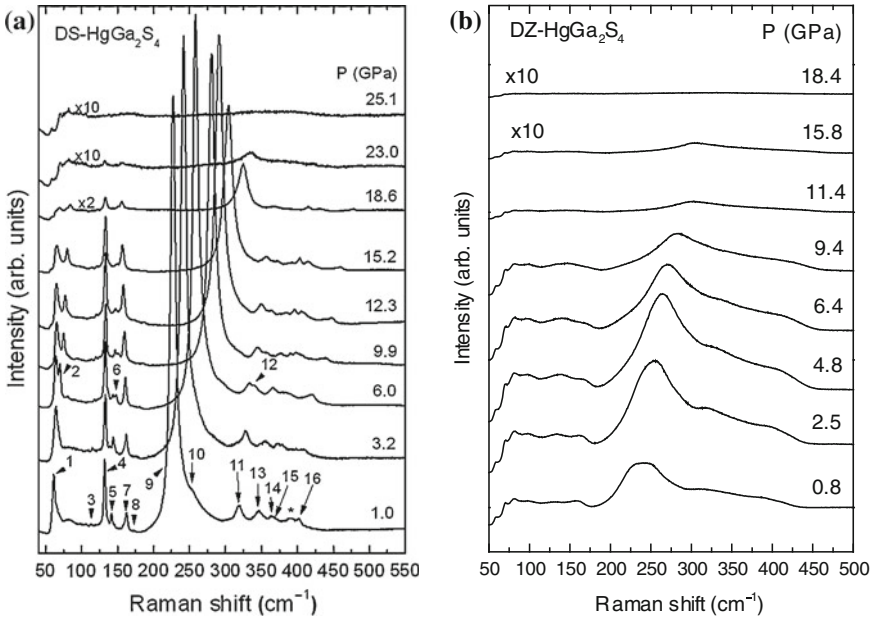

Fig. 5.13 **a** Room-temperature Raman spectra of DS-$HgGa_2S_4$ up to 25.1 GPa. **b** Room-temperature Raman spectra of DZ-$HgGa_2S_4$ up to 18.4 GPa

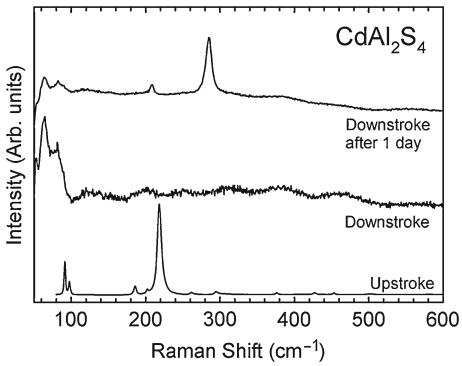

Fig. 5.14 Room-temperature Raman spectra of DC-$CdAl_2S_4$ at 1 atm before and after being pressurized to 25 GPa. Raman spectra on upstroke (*bottom*) and downstroke (*middle*) are completely different. Furthermore, the Raman spectrum on downstroke after one day (*top*) showed strong Raman peaks consistent with the recrystallization of an spinel phase

have decreased as disorder has increased in $HgGa_2S_4$, as it was already observed in $CdGa_2Se_4$ [25].

In summary, high-pressure Raman scattering results of DC-$HgGa_2S_4$ provide clear evidence of the intermediate stages of disorder in ternary OVCs. It can be concluded that experimental results till now suggest that the DC to DR phase transition occurs via a single disorder stage through the DS structure but no evidence has been found of other intermediate DCA or DZ phases prior to the DR phase yet. A possible reason to explain the lack of observation of the intermediate DCA and DZ phases is that

these very disordered phases could have a smaller stability region than DC and DS phases with respect to the DR phase; i.e., that the phase transition pressure of the DCA or DZ phase to the DR phase is smaller than that of the DC and DS phases. Note that the phase transition pressure from the DZ to the DR phase in $HgGa_2S_4$ is 18 GPa while that of the DS-to-DR phase is 24 GPa. Therefore, it is not possible to observe the DZ phase above 23–24 GPa in $HgGa_2S_4$ because at these pressures the DZ phase is likely to be not a stable structure with respect to the DR phase.

Finally, we present in Fig. 5.14 Raman scattering spectra of $CdAl_2S_4$ at ambient pressure before and after pressurization to 25 GPa. It is noted that the spectrum after downstroke is clearly different to that of the DZ phase observed in $HgGa_2S_4$ and it can be attributed to the spinel phase already present in $ZnAl_2S_4$ at ambient conditions. These results are in good agreement with the observation of the spinel phase in $CdAl_2S_4$ and other ternary sulphides on decreasing pressure from high pressures and high temperature [59–61] but contradict high-pressure XRD measurements of Meenakshi et al. [29]. Therefore, the study of the pressure behaviour of $CdAl_2S_4$ will be extended in a future work [30].

5.5 Conclusions

In this chapter we have reviewed the effects of pressure in the structural, mechanical, and lattice-dynamical properties of ternary sulphur-based ordered-vacancy compounds. High-pressure X-ray diffraction measurements in tetragonal OVCs have shown that there is an anisotropy in the axial compression being the *a* axis more compressible than the *c* one. Therefore, OVCs with DC and DS structure tend with pressure to values of *c/a* ratio close to 2 which are typical of some OVCs with DS structure.

High-pressure Raman scattering measurements have shown that different vibrational modes can be observed in OVCs with different structures, like DC or DS. The vibrational modes of tetragonal ternary OVCs are related to those in the zincblende structure and can be analysed by the folding method to explain the vibrational frequencies and their pressure dependence. Raman measurements evidence the pressure-induced phase transitions to the DR and DZ phases found by XRD measurements in several cases. However, this seems not to be the case of $CdAl_2S_4$ whose behaviour under pressure deserves a closer attention since this compound may show a behaviour intermediate between those of spinel-type and defect chalcopyrite AB_2X_4 compounds.

The behaviour of different sulphur-based compounds under pressure is summarized and the pressure-induced phase transitions either from the DC or DS phases to the DR phase are described and compared to those of their parent materials, the zincblende-type *AX* and the chalcopyrite-type ABX_2 compounds. In particular, the pressure-induced transformation of the DC structure to the DR phase through an intermediate DS structure has been exemplified. Furthermore, we have shown that after the transformation of OVCs to the DR phase, where there is a total cation-vacancy

disorder, the cation and vacancy order cannot be recovered; therefore, OVCs return to the tetrahedrally-coordinated DZ structure. It has been shown that the DZ to DR phase transition is fully reversible since both phases are totally disordered phases. It must be stressed that the occurrence of intermediate phases between DS and DR phases, like the possible DCA or DZ phases proposed in Table 5.2, are still to be proved experimentally. The pressure-induced phase transitions here described seem to be different in $CdAl_2S_4$. In this respect, we have to note that $CdAl_2S_4$ seems to be a special case, like $ZnAl_2S_4$ which can show different phases as will be commented in another chapter of this book. We hope the results here reviewed will help to trigger new studies to further elucidate the effects of pressure on the properties of OVCs.

Acknowledgments This study was supported by the Spanish government MEC under project MAT2010-21270-C04-04, by MALTA Consolider Ingenio 2010 project (CSD2007-00045), by Generalitat Valenciana under project GVA-ACOMP-2013-012 and by the Vicerrectorado de Investigación y Desarrollo of the Universidad Politécnica de Valencia (UPV2011-0914 PAID-05-11 and UPV2011-0966 PAID-06-11).

References

1. MacKinnon A (1985) Tables of numerical data and functional relationships in science and technology, vol. 17. Springer-Verlag, Berlin, p. 124
2. Georgobiani AN, Radautsan SI, Tiginyanu IM (1985) Wide-gap $A(II)B(III)_2C(VI)_4$ semiconductors—optical and photoelectric properties, and potential applications (review). Sov Phys Sem USSR 19:121–132
3. Bernard JE, Zunger A (1988) Ordered-vacancy compound semiconductors: pseudocubic $CdIn_2Se_4$. Phys Rev B 37:6835–6856
4. Jiang X, Lambrecht WRL (2004) Electronic band structure of ordered vacancy defect chalcopyrite compounds with formula $II\text{-}III_2\text{-}VI_4$. Phys Rev B 69:035201(8)
5. Binsma JJM, Galing LJ, Bloem J (1981) Order-disorder behaviour and tetragonal distortion of chalcopyrite compounds. Phys Stat Sol A 63:595–603
6. Zunger A (1987) Order-disorder transformation in ternary tetrahedral semiconductors. Appl Phys Lett 50:164–166
7. Rincón C (1992) Order–disorder transition in ternary chalcopyrite compounds and pseudobinary alloys. Phys Rev B 45:12716–12719
8. Garbato L, Ledda F, Rucci A (1987) Structural distortions and polymorphic behavior in ABC_2 and AB_2C_4 tetrahedral compounds. Prog Cryst Growth Charact 15:1–41 and references therein
9. Tiginyanu IM, Ursaki VV, Fulga VN (1989) Order-disorder phase transition in the cation sublattice of $ZnGa_2Se_4$. Sov Phys Semicond 23:1069–1070
10. Dietrich M, Unterricker S, Deicher M, Burchard A, Magerle R, Pfeiffer W, Forkel-Wirth D, Tiginyanu IM, Moldovyan NA (1996) Quadrupole interaction in defect chalcopyrite semiconductors studied by PAC. Cryst Res Technol 31(S2):853–856
11. Dietrich M, Unterricker S, Deicher M, Burchard A, Magerle R, Pfeiffer W, Forkel-Wirth D, Tiginyanu IM, Moldovyan NA (1996) PAC Investigation of ordered vacancy semiconductors of type $A^{II}B_2^{III}C_4^{VI}$. Hyperfine Interact C 1:242–245
12. Alonso-Gutiérrez P, Sanjuán ML, Morón MC (2009) Thermally activated catión ordering in $Zn_{0.5}Mn_{0.5}Ga_2Se_4$ single crystals studied by Raman scattering. Phys Status Solidi C 6:1182–1186
13. Caldera D, Morocoima M, Quintero M, Rincon C, Casanova R, Grima P (2011) On the crystal structure of the defective ternary compound $ZnGa_2Se_4$. Solid State Commun 151:212–215

14. Hahn H, Frank G, Klingler W, Stoerger AD, Stoerger G (1955) Über ternare chalcogenide des aluminiums, galliums und indiums mit zink, cadmium und quecksilber. Z Anorg Allgem Chemie 279:241–270
15. Guseinov GG, Kerimova TG, Nani RK (1980) The refinement of crystal-structure of $CdGa_2S_4$. Izvestiya Akademii Nauk Azerbaidzhanskoi SSR seriya Fisiko-Teknischeskikh i Matemticcheskikh Nauk 4:59–61
16. Schwer H, Kraemer V (1990) The crystal structure of $CdAl_2S_4$, $HgAl_2S_4$, and $HgGa_2S_4$. Z Kristall 190:103–110
17. Carpenter GB, Wu P, Gao YM, Wold A (1989) Redetermination of crystal structure of zinc thiogallate. Mater Res Bull 24:1077–1082
18. Lowe-Ma CK, Vanderah TA (1991) Structure of $ZnGa_2S_4$, a defect sphalerite derivative. Acta Cryst C 47:919–924
19. Gastaldi L, Simeone MG, Viticoli S (1985) Cation ordering and crystal structures in AGa_2X_4 compounds ($CoGa_2S_4$, $CdGa_2S_4$, $CdGa_2Se_4$, $HgGa_2Se_4$, $HgGa_2Te_4$). Solid State Commun. 55: 605–607 and referencies therein; Agostinelli E, Gastaldi L, Viticoli S (1985) Crystallographic and magnetic investigations on cobalt gallium sulfides: α-$CoGa_2S_4$ and γ-$CoGa_2S_4$. J Phys Chem Solids 46:1345–1349
20. Burlakov II, Raptis YS, Ursaki VV, Anastassakis E (1997) Order-disorder phase transition in $CdAl_2S_4$ under hydrostatic pressure. Solid State Commun 101:377–381
21. Ursaki VV, Burkalov II, Tiginyanu IM, Raptis YS, Anastassakis E, Aneda A (1999) Phase transitions in defect chalcopyrite compounds under hydrostatic pressure. Phys Rev B 59:257–268
22. Meenakshi S, Vijyakumar V, Godwal BK, Eifler A, Orgzall I, Tkachev S, Hochheimer HD (2006) High pressure X-ray diffraction study of $CdAl_2Se_4$ and Raman study of AAl_2Se_4 (A = Hg, Zn) and $CdAl_2X_4$ (X = Se, S). J Phys Chem Solids 67:1660–1667
23. Eifler A, Hecht JD, Lippold G, Riede V, Grill W, Krauss G, Krämer V (1999) Combined infrared and Raman study of the optical phonons of defect chalcopyrite single crystals. Physica B 263–264:806–808
24. Eifler A, Krauss G, Riede V, Krämer V, Grill W (2005) Optical phonon modes and structure of $ZnGa_2Se_4$ and $ZnGa_2S_4$. J Phys Chem Solids 66:2052–2057
25. Gomis O, Vilaplana R, Manjón FJ, Pérez-González E, López-Solano J, Rodríguez-Hernández P, Muñoz A, Errandonea D, Ruiz-Fuertes J, Segura A, Santamaría-Pérez D, Tiginyanu IM, Ursaki VV (2012) High-pressure optical and vibrational properties of $CdGa_2Se_4$: order–disorder processes in adamantine compounds. J Appl Phys 111:013518 (15)
26. Manjón FJ, Gomis O, Vilaplana R, Sans JA, Ortiz HM (2013) Order–disorder processes in adamantine ternary ordered-vacancy compounds. Phys Stat Sol B 250: 1496-1504
27. Mitani T, Onari S, Allakhverdiev K, Gashimzade F, Kerimova T (2001) Raman scattering in $CdGa_2S_4$ under pressure. Phys Stat Sol B 223:287–291
28. Errandonea D, Kumar RS, Manjón FJ, Ursaki VV, Tiginyanu IM (2008) High-pressure x-ray diffraction study on the structure and phase transitions of defect-stannite $ZnGa_2Se_4$ and defect-chalcopyrite $CdGa_2S_4$. J Appl Phys 104:063524(9)
29. Meenakshi S, Vijyakumar V, Eifler A, Hochheimer HD (2010) Pressure-induced phase transition in defect chalcopyrites $HgAl_2Se_4$ and $CdAl_2S_4$. J Phys Chem Solids 71:832–835
30. Sans JA (2013), to be published
31. Santamaría-Pérez D (2013), to be published
32. Gomis O, Santamaría-Pérez D, Vilaplana R, Luna R, Sans JA, Manjón FJ, Errandonea D, Pérez-González E, Rodríguez-Hernández P, Muñoz A, Tiginyanu IM, Ursaki VV (2013) Structural and elastic properties of defect chalcopyrite HgGa2S4 under high pressure. J Alloys and Comp doi:10.1016/j.jallcom.2013.08.123
33. Grzechnik A, Ursaki VV, Syassen K, Loa I, Tiginyanu IM, Handfland M (2001) Pressure-induced phase transitions in cadmium thiogallate $CdGa_2Se_4$. J Solid State Chem 160:205–211
34. Marquina J, Power Ch, Grima P, Morocoima M, Quintero M, Couzinet B, Chervin JC, Munsch P, González J (2006) Crystallographic properties of the $MnGa_2Se_4$ compound under high pressure. J Appl Phys 100:093513(6)

35. Hanada T (1998) Neutron and electron diffraction studies of $ZnGa_2Se_4$. Physica B 241–243:373–375
36. Ackland GJ (2001) High-pressure phases of group IV and III-V semiconductors. Rep Prog Phys 64:483–516
37. Mujica A, Rubio A, Muñoz A, Needs RJ (2003) High-pressure phases in group-IV, III-V, and II-VI compounds. Rev Mod Phys 75:863–912
38. Bovornratanaraks T, Saengsuwan V, Yoodee K, McMahon MI, Hejni C, Ruffolo D (2010) High pressure orthorhombic structure of $CuInSe_2$. J Phys Condens Matter 22:355801(4)
39. Xue HT, Tang FL, Lu WJ, Feng YD, Wang ZM, Wang Y (2013) First-principles investigatioin of structural phase transitions and electronic properties of $CuGaSe_2$ up to 100 GPa. Comp Mat Sci 67:21–26
40. Chelikovsky JR, Burdett JK (1986) Ionicity and the structural stability of solids. Phys Rev Lett 56:961–964
41. Chelikowsky JR (1987) High-pressure phase transitions in diamond and zinc-blende semiconductors. Phys Rev B 35:1174–1180
42. Ozolins V, Zunger A (1999) Theory of systematic absence of NaCl-Type (β-Sn-Type) high pressure phases in covalent (Ionic) semiconductors. Phys Rev Lett 82:767–770
43. Christensen NE, Satrathy S, Pawlowska Z (1987) Bonding and ionicity in semiconductors. Phys Rev B 36:1032–1050
44. Jayaraman A, Dernier PD, Kasper HM, Maines RG (1977) Pressure induced phase transformations in some I-III-IV2 semiconductors. High Temp High Press 9:97–102
45. Serghiou G, Reichmann HJ, Boehler R (1997) Size criterion for amorphization of molecular ionic solids. Phys Rev B 55:14765–14769
46. Errandonea D, Manjón FJ, Somayazulu M, Hausermann D (2004) Effects of pressure on the local atomic structure of $CaWO_4$ and $YLiF_4$: mechanism of the scheelite-to-wolframite and scheelite-to-fergusonite transitions. J Solid State Chem 177:1087–1097
47. Beister HJ, Ves S, Honle W, Syassen K, Kuhn G (1991) Structural phase transitions and optical absorption of $LiInSe_2$ under pressure. Phys Rev B 43:9635–9642
48. Shannon RD (1976) Revised effective ionic-radii and systematic studies of interatomic distances in halides and chalcogenides. Acta Crystallogr Sect A Cryst Phys Diffr Theor Gen Crystallogr 32:751–767
49. Kroumova E, Aroyo MI, Perez-Mato JM, Kirov A, Capillas C, Ivantchev S, Wondratschek H (2003) Bilbao crystallographic server : useful databases and tools for phase-transition studies. Phase Transitions 76:155–170
50. Vilaplana R, Robledillo M, Gomis O, Sans JA, Manjón FJ, Pérez-González E, Rodríguez-Hernández P, Muñoz A, Tiginyanu IM, Ursaki VV (2013) Vibrational study of $HgGa_2S_4$ under high pressure. J Appl Phys 113:093512(10)
51. Loudon R (1964) Raman effect in crystals. Adv Phys 13:423
52. Alonso-Gutiérrez P, Sanjuán ML (2008) Ordinary and extraordinary phonons and photons: Raman study of anisotropy effects in the polar modes of $MnGa_2Se_4$. Phys Rev B 78:045212(9)
53. Luna R (2013), to be published
54. Allakverdiev KR (2001) Pressure induced phase transitions in GaSe-, $TlGaSe_2$-, and $CdGa_2S_4$-type crystals. Frontiers of high pressure research II: application of high pressure to low-dimensional novel electronic materials. Kluwer, Amsterdam, pp. 99–118
55. Klotz S, Besson JM, Braden M, Karch K, Pavone P, Strauch D, Marshall WG (1997) Pressure induced frequency shifts of transverse acoustic phonons in germanium to 9.7 GPa. Phys Rev Lett 79:1313–1316
56. González J, Fernandez BJ, Besson JM, Gauthier M, Polian A (1992) High-pressure behavior of Raman modes in $CuGaS_2$. Phys Rev B 46:15092–15101
57. Anastasakis E, Cardona M (1998) High pressure in semiconductor physics, vol 2. Academic, New York, p. 152 and references therein
58. Sanjurjo JA, López-Cruz E, Vogl P, Cardona M (1983) Dependence on volume of the phonon frequencies and the ir effective charges of several III-V semiconductors. Phys Rev B 28:4579–4584 and references therein

59. Range KJ, Becker W, Weiss A (1968) Uber Hochdruckphasen des $CdAl_2S_4$, $HgAl_2S_4$, $ZnAl_2Se_4$, $CdAl_2Se_4$, und $HgAl_2Se_4$ mit Spinell-struktur. Z Naturforschg 23b:1009–1009
60. Range KJ (1971) Hochdruckuntersuchungen and ternarën Chalkogeniden mit tetraedrisch koordinierten Kationen. Chem Zeitung 95:3–11
61. Kaempfer M, Neuhaus A (1972) Drucktransformationen von $ZnGa_2S_4$, $CdGa_2S_4$ un $HgGa_2S_4$. Chemie-Ing Techn 44:946–946

Chapter 6
AB_2Se_4 Ordered-Vacancy Compounds at High Pressures

Óscar Gomis and Francisco Javier Manjón

Abstract In this chapter, an overview of the effects of pressure on the crystalline structure and physical properties of selenium-based ordered-vacancy compounds of the $A^{II}B_2^{III}X_4^{VI}$ family is presented. Recent X-ray diffraction, Raman spectroscopy, and optical absorption studies are presented with a main focus on the discussion of pressure-induced phase transitions and their related order-disorder processes.

Keywords Defect chalcopyrite · Thiogallate · Defect stannite · Defect famatinite · Pseudocubic · High pressure · X-ray diffraction · Lattice dynamics · Optical absorption · Phase transitions

6.1 Introduction

Many compounds of the type $A^{II}B_2^{III}X_4^{VI}$, with A^{II} and B^{III} being divalent and trivalent metals, respectively, and X^{VI} = Se, crystallize at ambient conditions in tetragonal structures derived from the diamond or zincblende (space group (S.G.) F-43m, No. 216, Z = 2) structure. These structures contain both A and B cations in tetrahedral coordination so they have an unbalanced number of cations and anions which leads to the appearance of vacancies in these structures. In most cases the vacancies are located in fixed Wyckoff positions of the unit cell so these compounds are called adamantine ordered-vacancy compounds (OVCs). In particular, $A^{II}B_2^{III}Se_4$

Ó. Gomis (✉)
Centro de Tecnologías Físicas: Acústica, Materiales y Astrofísica, MALTA Consolider Team, Universitat Politècnica de València, 46022 València, Spain
e-mail: osgohi@fis.upv.es

F. J. Manjón
Instituto de Diseño para la Fabricación y Producción Automatizada, MALTA Consolider Team, Universitat Politècnica de Valencia, 46022 València, Spain
e-mail: fjmanjon@fis.upv.es

F. J. Manjón et al. (eds.), *Pressure-Induced Phase Transitions in AB_2X_4 Chalcogenide Compounds*, Springer Series in Materials Science 189,
DOI: 10.1007/978-3-642-40367-5_6,

compounds crystallize at ambient conditions in tetragonal structures which are similar to those of $A^{II}B_2^{III}S_4$ compounds reviewed in Chap. 5. The only known exception among selenides is that of compounds with B = Cr that curiously crystallize in the spinel structure, whose behaviour under pressure has been already reviewed in Chap. 3 devoted to thiospinels and selenospinels.

As already commented, adamantine OVCs constitute a class of semiconductors that exhibit extraordinary and unusual properties. In particular, adamantine OVCs have important applications in optoelectronics, solar cells, and non-linear optics that have attracted considerable attention in the last thirty years [1–4]. The main difference between the optical nonlinear applications of sulfur-based and selenium-based ternary OVCs is due to their different direct bandgap. Thus, selenium-based compounds with a direct bandgap till 2.5 eV operate in the green-red-NIR range, sulfur-based compounds with a direct bandgap above 3 eV can operate also in the UV and blue region.

The behaviour under pressure of sulfur-based OVCs has been reviewed in Chap. 5. In particular, Table 5.2 summarizes the different structures that could be expected in ternary OVCs depending of the degree of cation-vacancy disorder. From now on, we will refer to the different models of the structures reported in that table. In particular, the AB_2Se_4 family typically crystallize in one of three tetragonal structures: (i) the defect chalcopyrite (DC) structure with space group (S.G.) I-4, No. 82, (ii) the defect stannite (DS) structure, also known as defect famatinite, with S.G. I-42m, No. 121, and (iii) the ordered pseudocubic (PC) structure with S.G. P-42m, No. 111. In particular, if we consider the different structures of DC, DS and PC phases shown in Table 5.2, most of the AB_2Se_4 OVCs ($CdAl_2Se_4$, $HgAl_2Se_4$, $CdGa_2Se_4$, $HgGa_2Se_4$, $MnGa_2Se_4$) crystallize in the ordered DC structure (model 1) (Fig. 6.1a). $ZnAl_2Se_4$ and $ZnGa_2Se_4$ tend to crystallize in the DS structure (model 6 of Chap. 5 (Fig. 6.1b)) if the temperature is decreased too fast during the growth process [5, 6]. Finally, $CdIn_2Se_4$ tend to crystallize in the ordered PC structure (model 1) (Fig. 6.1c). As mentioned in Chap. 5, no sulfur-based compound is known to crystallize in the PC structure since $CdIn_2S_4$, $MgIn_2S_4$, $MnIn_2S_4$, and $HgIn_2S_4$ crystallize in the spinel structure.

We have to note that the usual way to describe the atomic positions in the DC structure followed till now in the Inorganic Chemistry Structural Database (ICSD) assumes that in AB_2X_4 compounds *A* atoms occupy *2a* Wyckoff sites, *B* atoms occupy *2b* and *2c* Wyckoff sites, while vacancies (*V*) occupy *2d* sites. However, $ZnGa_2Se_4$ can crystallize either in the DC or DS (model 6) structures depending on the growth conditions. Therefore, it is convenient for the comparison of both structures to adopt the convention that, in the DC structure of $ZnGa_2Se_4$, Ga (*B*) atoms occupy *2a* and *2c* Wyckoff sites while vacancies and Zn (*A*) atoms occupy *2b* and *2d* Wyckoff sites, respectively [see Fig. 6.1a]. In this way, a disorder of cations at *2c* and *2d* sites leads to the model 6 of the nine possible polytypes of the DS phase discussed in several works [7–10] and summarized in Chap. 5. In model 6 of the DS structure, Ga atoms at *2a* sites and vacancies at *2b* sites remain ordered while Ga and Zn atoms at *2c* and *2d* sites mix together resulting in a fractional occupation (1/2Zn + 1/2Ga) of the *4d* Wyckoff sites of the DS phase (see Fig. 6.1b). In this context, we must note that

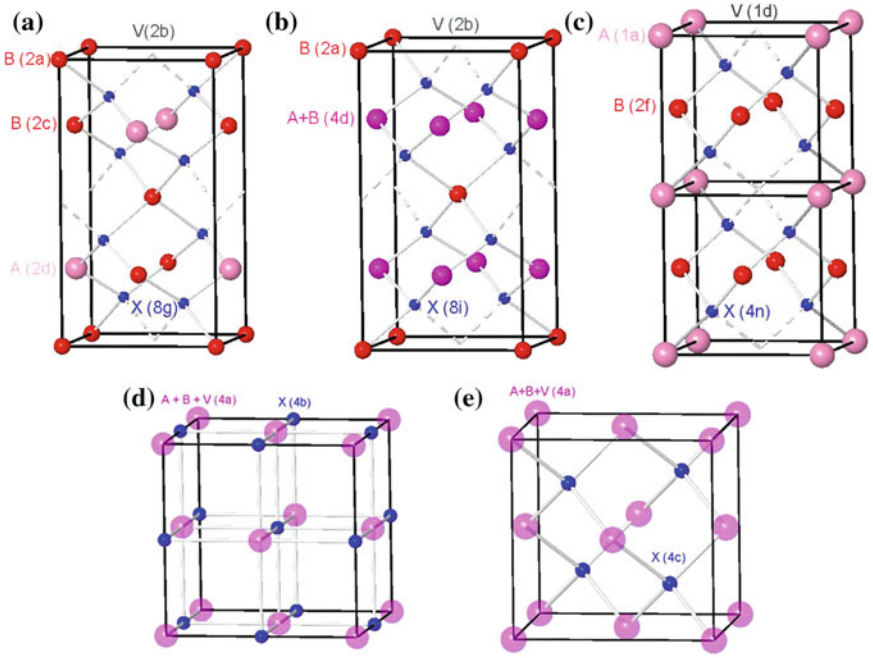

Fig. 6.1 Details of the structure of: **a** ordered defect chalcopyrite (DC) $ZnGa_2Se_4$ and $CdGa_2Se_4$, **b** defect stannite (DS) $ZnGa_2Se_4$ (model 6 of Table 5.2 in Chap. 5), **c** pseudocubic (PS) $CdIn_2Se_4$, **d** defect rocksalt (DR) structure, and **e** defect zincblende (DZ) structure. *Big pink* atoms are *A* cations, *medium red* atoms are *B* cations, and *small dark* atoms are *X*(Se) anions. To distinguish between non-equivalent atoms in the DC and DS structures the Wyckoff sites are given in parenthesis

the two descriptions proposed for the DC phase are equivalent and only a translation of the origin and a rotation of the unit cell is needed to go from one to the other. However, this translation and rotation of the unit cell origin leads to different *x*, *y*, and *z* values of anions (Se atoms in our case) in the unit cell that occupy general *8g* (*x,y,z*) Wyckoff positions.

In this chapter we are going to review the high-pressure studies performed on selenium-based OVCs of DC and DS structure with a special emphasis in their high-pressure phase transitions. Unfortunately, no high-pressure study has been performed in PC-$CdIn_2Se_4$ except at high temperatures [11]. Section 6.2 is devoted to review the pressure dependence of the volume and lattice parameters of ternary OVCs obtained by means of x-ray diffraction (XRD) measurements. Section 6.3 summarizes the pressure-induced phase transitions observed by XRD measurements in selenium-based OVCs. Section 6.4 deals with high-pressure Raman scattering measurements and also the phase transitions observed with this technique. Section 6.5 will cover high-pressure optical absorption measurements. Finally, Sect. 6.6 will summarize the main conclusions of this work.

6.2 Isothermal Compression of AB_2Se_4 OVCs: X-ray Diffraction Studies

The pressure dependence of the lattice parameters and the unit cell volume has been studied by means of X-ray diffraction measurements in several selenium-based ternary OVCs: $ZnGa_2Se_4$ [12], $CdGa_2Se_4$ [13], $HgGa_2Se_4$ [14], $MnGa_2Se_4$ [16], $CdAl_2Se_4$ [17], and $HgAl_2Se_4$ [18]. High-pressure powder XRD measurements in the above compounds show that the diffraction patterns can be indexed with the low-pressure tetragonal structure until it occurs a pressure-induced phase transition to a disordered rocksalt (DR) structure (Fig. 6.1d) which will be commented in the Sect. 6.3.

XRD and neutron diffraction measurements show that $ZnGa_2Se_4$ crystallizes in model 6 of the DS structure [19–21] when temperature is decreased too fast during crystal growth [5, 6], while the other OVCs crystallize in the ordered DC structure (model 1) at ambient conditions. As a matter of example, Fig. 6.2 shows the evolution of the XRD patterns of DS-$ZnGa_2Se_4$ under pressure. The structural parameters of DC-$CdGa_2Se_4$ [22] and DS-$ZnGa_2Se_4$ [12] at room pressure are summarized in Tables 6.1 and 6.2.

Figure 6.3 shows the pressure dependence of the unit cell volume for several AB_2Se_4 compounds. Fits to the volume versus pressure data with a third-order Birch-Murnaghan equation of state (EOS) [23] gives information on the zero-pressure volume, bulk modulus, and its pressure derivative denoted as V_0, B_0, and B_0' respectively. The values of B_0 and B_0' for several AB_2Se_4 and AB_2S_4 compounds has been summarized in Table 6.3.

We note that larger values of the bulk modulus at zero pressure are expected for sulfide-based OVCs than for selenide-based OVCs due to the larger ionic radio of selenium in comparison to that of sulphur. On the other hand, it is also expected the decrease of the bulk modulus of AGa_2Se_4 compounds on the increase of the ionic radius of the A cation in the series (A = Zn, Cd, Hg) and also on the increase of the ionic radius of the B cation in HgB_2Se_4 compounds in the series (B = Al, Ga). However, the values of B_0 and B_0' reported in Table 6.3 do not always agree with the expected results when comparing data from different compounds and experiments. There are at least two reasons for the above discrepancy. The first one is that the values of B_0 and B_0' are strongly correlated in the way that the increment of one implies the decrement of the other one. The second reason is that the value of B_0 depends on the hydrostatic conditions of the XRD experiment. In this sense, previous works have shown an overestimation of B_0 under non-hydrostatic conditions [14, 26–30]. These two facts make difficult in practice to compare results of B_0 obtained in different experiments by different authors. This difficulty becomes important when the difference between B_0 values is not very large.

Considerable information can be obtained from the study of the pressure dependence of the lattice parameters and unit cell volume in OVCs. Figure 6.4 shows the pressure dependence of the lattice parameters for DS-$ZnGa_2Se_4$ and DC-$CdGa_2Se_4$ from data taken from [12, 13], respectively. An estimation of the axial

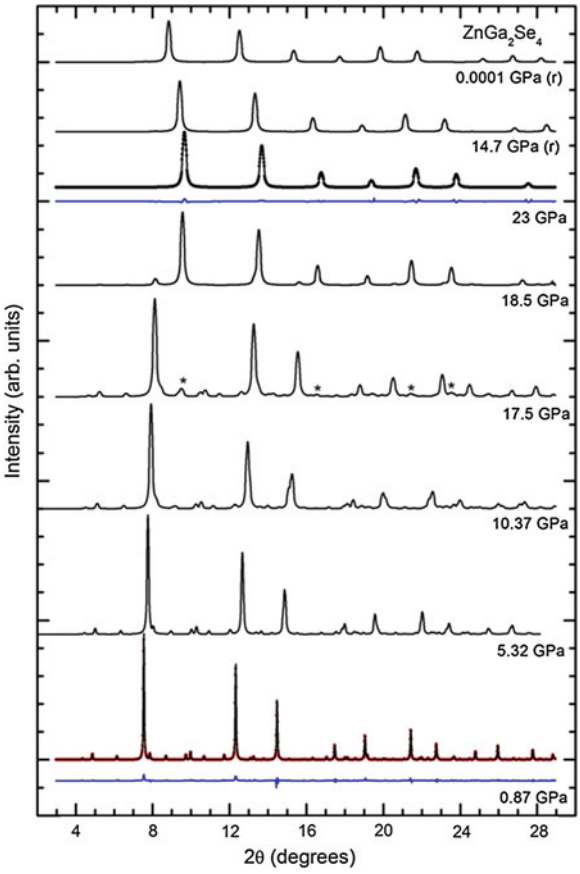

Fig. 6.2 Evolution of the X-ray diffraction patterns of DS-$ZnGa_2Se_4$ under pressure. The stars show peaks corresponding to the high pressure DR phase. At 0.87 and 23 GPa the collected pattern (*dots*) is shown together with the refined patters (*solid line*) and the residuals of the refinement. These two patterns illustrate the quality of the refinements obtained for the low- and high-pressure phases

compressibilities for the a and c axes at zero pressure, defined as $k_x = \frac{-1}{x}\frac{\partial x}{\partial P}$, from a fit of the pressure dependence of the lattice parameters to a Murnaghan EOS [31] has been carried out for the different DC and DS compounds studied by XRD under pressure in the literature. The results are summarized in Table 6.3. It can be observed that in all cases there is an anisotropy in the axial compression being the a axis more compressible than the c one.

Finally, we want to analyze the evolution of the c/a ratio with pressure in selenium-based OVCs since the tetragonal distortion, $\delta = 2-c/a$, could give information of the behavior of the sample with pressure. Figure 6.5 shows the pressure dependence of the c/a ratio versus pressure for DS-$ZnGa_2Se_4$, DC-$CdGa_2Se_4$, and DC-$MnGa_2Se_4$.

Table 6.1 Atomic positions and site occupancy factor (SOF) for DC-$CdGa_2Se_4$ at ambient pressure taken from [13]

Atom	Site	x	y	z	SOF
Ga	2*a*	0	0	0	1
Vacancy	2*b*	0	0	1/2	0
Ga	2*c*	0	1/2	1/4	1
Cd	2*d*	0	1/2	3/4	1
Se	8*g*	0.2475	0.2702	0.113	1

Defect-chalcopyrite structure, space group: I-4, z = 2 with $a = 5.700(1)$ Å, and $c = 10.805(2)$ Å

Table 6.2 Atomic positions and site occupancy factor (SOF) for DS-$ZnGa_2Se_4$ at ambient pressure taken from [12]

Atom	Site	x	y	z	SOF
Ga	2*a*	0	0	0	1
Vacancy	2*b*	0	0	1/2	0
Ga	4*d*	0	1/2	1/4	0.5
Zn	4*d*	0	1/2	1/4	0.5
Se	8*i*	0.264(8)	0.264(8)	0.117(4)	1

Defect-stannite structure, space group: I-42m, z = 2, with $a = 5.512$ Å, and $c = 10.963$ Å

For DS-$ZnGa_2Se_4$, the *c/a* ratio increases from 1.99 at ambient pressure to 2.00 at 18 GPa. On the other hand, the *c/a* ratio in DC-$CdGa_2Se_4$ increases from 1.87 at ambient pressure to 1.93 at 18 GPa. Similarly, the *c/a* ratio in DC-$MnGa_2Se_4$ increases from 1.895 at ambient pressure to about 1.96 at 12 GPa. Therefore, in general a pressure-induced increase of the *c/a* ratio both in sulfur- and selenium-based ternary OVCs is observed. Note that this general behaviour is observed despite the different *c/a* ratios at ambient pressure of the different compounds.

As commented in Chap. 5, it is noteworthy that AGa_2X_4 compounds (A = Mn, Zn, Cd, Hg; X = S, Se) with tetragonal DC structure and DC-$HgAl_2Se_4$ have *c/a* values at ambient pressure below 1.90 [13, 14, 16, 18, 32], while those with tetragonal DS structure (model 6 in Chap. 5), which have already some cation disorder, have *c/a* ratios above 1.97 at ambient pressure [12, 33]. Curiously, this is not the case of DS-$HgAl_2S_4$ which crystallizes in the DS phase (model 7) and with *c/a* ratio near 1.85 [34]. In this respect, a *c/a* ratio at ambient pressure very close to 2, or equivalently a very small tetragonal distortion of the DC phase, was considered up to now as a measure of complete cation disorder [22, 32]; however, the case of DS-$HgAl_2S_4$ points to the possibility that this empirical rule to measure cation disorder could be wrong. Further work in this compound is needed to clarify this subject.

The above considerations seem to indicate that A and B cations showing similar ionic radius, like Zn and Ga in $ZnGa_2S_4$ and $ZnGa_2Se_4$, are in compounds which tend to crystallize in the DS phase (model 6) with a certain cation disorder and a *c/a* ratio near 2. A similar situation occurs for Cd and In in $CdIn_2Se_4$ since it crystallizes in the PC phase with a *c/a* ratio near 1. However, A and B cations showing different ionic radius are mostly in compounds that tend to crystallize in the ordered DC structure

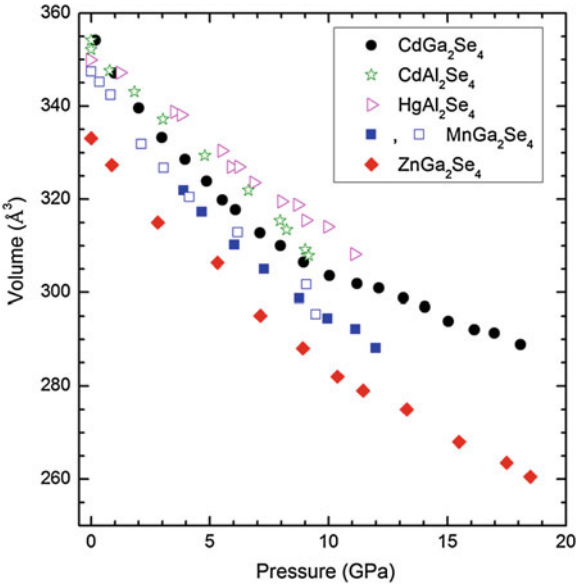

Fig. 6.3 Unit cell volume as a function of pressure for different AB_2Se_4 compounds. Data for $ZnGa_2Se_4$, $CdGa_2Se_4$, $CdAl_2Se_4$, $HgAl_2Se_4$, $MnGa_2Se_4$, and are taken from [12, 13, 16–18], respectively. For the case of $MnGa_2Se_4$ *open* (*solid*) *squares* refer to experiments carried out with methanol–ethanol (neon) as pressure transmitting medium

Table 6.3 Axial compressibilities of a (κ_a) and c (κ_c) lattice parameters at ambient pressure of sulphur- and selenium-based ternary OVCs

Compound	κ_a (10^{-3} GPa^{-1})	κ_c (10^{-3} GPa^{-1})	B_0 (GPa)	B_0'	PTM	Ref.
DS-$ZnGa_2Se_4$	7.3(5)	6.3(5)	47(2)	3.9(3)	silicone oil	[12]
DC-$MnGa_2Se_4$	8.3	6.6	44(2)	3.8(4)	methanol–ethanol, neon, and silicone oil	[16]
DC-$CdAl_2Se_4$	–	–	52.1	4	methanol–ethanol	[17]
DC-$CdGa_2Se_4$	12.5(9)	8.3(6)	41.5(2)	5(1)	methanol–ethanol	[13]
DC-$HgAl_2Se_4$	5(1)	–	66(1.5)	4	paraffin oil	[18]
DC-$HgGa_2Se_4$	9(2)	5(1)	52(2)	4	MgO	[14]
	9.2(6)	7.1(7)	39(2)	5.2(4)	methanol–ethanol	
DC-$CdGa_2S_4$	5.9(8)	4.5(7)	64(2)	4.1(3)	silicone oil	[12]
DC-$CdAl_2S_4$	–	–	44.6(1)	4	methanol–ethanol	[18]
DS-$HgAl_2S_4$	8.6(7)	6.3(5)	39(1)	6.0(4)	methanol–ethanol	[24]
DC-$HgGa_2S_4$	7.6(6)	5.3(8)	48.4(3)	4	methanol–ethanol	[25]

The bulk modulus (B_0), and its pressure derivative (B_0') at ambient pressure for the DC or DS phases are also given along with the pressure transmitting medium (PTM) used during the experiment. When axial compressibilities have not been reported in the original work we have estimated their values and uncertainties from data given in the corresponding reference

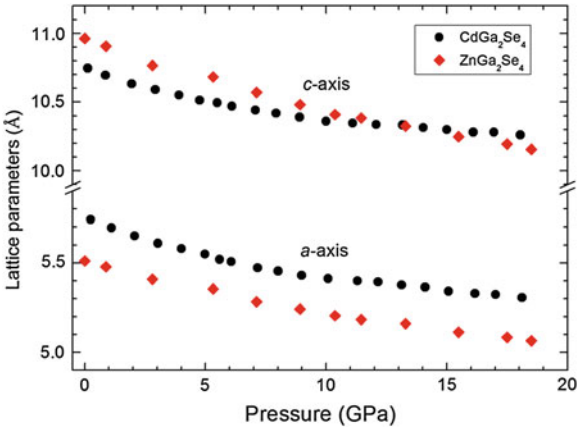

Fig. 6.4 Evolution of the lattice parameters with pressure for DC-$CdGa_2Se_4$ and DS-$ZnGa_2Se_4$

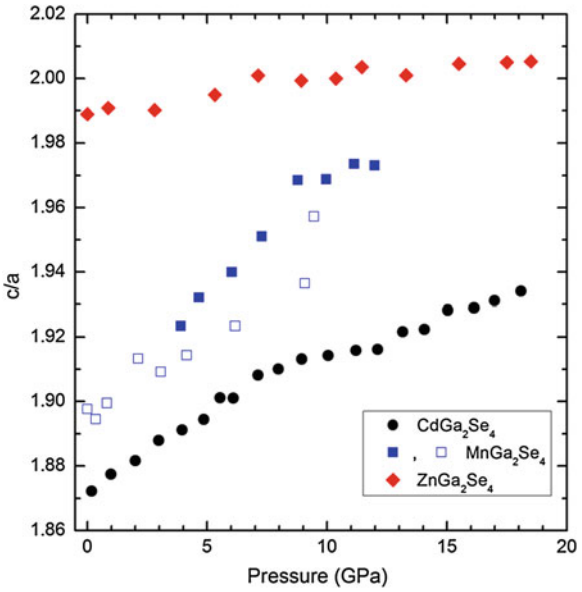

Fig. 6.5 Evolution of the *c/a* ratio as a function of pressure for $ZnGa_2Se_4$, $CdGa_2Se_4$, and $MnGa_2Se_4$. Data are taken from [12, 13, 16], respectively. For the case of $MnGa_2Se_4$ *open* (*solid*) *squares* refer to experiments carried out with methanol–ethanol (neon) as pressure transmitting medium

with a small *c/a* ratio. Finally, A and B cations showing very different ionic radius, like Hg and Al in $HgAl_2S_4$, are in compounds that tend to crystallize in the DS phase (model 7) also with a small *c/a* ratio. This behavior is also observed in ABX_2 compounds with chalcopyrite structure because those with similar A and B cations

tend to show a larger *c/a* ratio and to exhibit a temperature-induced cation disorder. This disorder results in a phase transition to the disordered zincblende (DZ) phase prior to melting, while those with very different A and B cations show a smaller *c/a* ratio and no tendency to disorder on increasing temperature [35]. Therefore, the presented results show that DC and DS structures evolve to a more symmetrical structure with increasing pressure that seems to be compatible with an increase of the cation disorder as pressure increases.

6.3 Pressure-Induced Phase Transitions in Adamantine OVCs

As previously commented, in the high-pressure XRD studies published for AB_2Se_4 compounds a pressure-induced phase transition from the DC phase towards the disordered rocksalt (DR) structure (S.G. Fm-3m, No. 225, $Z = 1$) has been found. In this structure, all cations are octahedrally-coordinated and the three cations and vacancies mix in the same Wyckoff (*4a*) site (see Fig. 6.1d). In Chap. 5, it was commented that some authors proposed that, since the DC to DR or DS to DR phase transition is an order–disorder phase transition, the disorder process should proceed in two stages with some intermediate phases between both DC (or DS) and DR phases which would result in the transformation to the DZ structure prior to the transition to the DR phase [17, 36, 37]. This disorder process would proceed then in the same way as on increasing temperature where there is a transformation of the DC or DS phases to the DZ structure prior to melting [31, 38]. In the DZ structure of ternary OVCs, all cations are tetrahedrally-coordinated to anions and the three cations and vacancies mix in the same Wyckoff *4a* site (see Fig. 6.1e). Curiously, none of the XRD studies already published has reported any intermediate structure.

In DS-$ZnGa_2Se_4$ the DR phase is observed above 15.5 GPa (see Fig. 6.2) [12]. The low and high-pressure phases of DS-$ZnGa_2Se_4$ coexist from 15.5 to 18.5 GPa and the high-pressure phase remains stable up to 23 GPa [12]. In general, the transition to the DR phase in OVCs takes place at pressures that depend on the compound and the experimental conditions. A summary of transition pressures to the DR phase in DC and DS compounds obtained from XRD measurements is given for comparison in the second column of Table 6.4. As far as the DR structure is concerned, Table 6.4 summarizes the relative volume variation in % at the DC/DS to DR transition pressure. In all ternary OVCs, it is found that the transition from the low-pressure tetragonal phase to the high-pressure DR phase is a first-order phase transition with a discontinuity in the volume which seems to be slightly larger for selenium-based compounds than for sulphur-based compounds. Table 6.4 also summarizes the values of B_0 and B_0' parameters for the high-pressure DR phase in the few cases when has been reported. In all cases, the B_0 values for the DR phase are greater than those corresponding to the initial tetragonal DC or DS phase, thus showing that the high-pressure DR phase is less compressible than the low-pressure DC or DS phase.

Table 6.4 Transition pressure (P_t) to the DR phase for different AB_2Se_4 compounds with the DC or DS structure at ambient conditions

Compound	P_t (GPa)	ΔV (%)	B_0 (GPa)	B_0'	PTM	Ref.
DS-$ZnGa_2Se_4$	15.5	−4.6	50(2)	4	silicone oil	[12]
DC-$MnGa_2Se_4$	12		56(5)	2.0(6)	methanol–ethanol, neon, and silicone oil	[16]
DC-$CdAl_2Se_4$	9.1	−10	–	–	methanol–ethanol	[17]
DC-$CdGa_2Se_4$	21.4	−6(1)	–	–	methanol–ethanol	[13]
DC-$HgAl_2Se_4$	13	−2.1	–	–	paraffin oil	[18]
DC-$HgGa_2Se_4$	17.2	−2.2[a]	–	–	MgO	[14]
DC-$CdAl_2S_4$	9,15	−7	66.4(1.4)	4	methanol–ethanol	[18]
DC-$CdGa_2S_4$	17	−5	–	–	silicone oil	[12]
DS-$HgAl_2S_4$	21				methanol–ethanol	[24]
DC-$HgGa_2S_4$	22				methanol–ethanol	[39]

[a] Value estimated at 16.2 GPa

The relative volume variation at the phase transition pressure, the bulk modulus (B_0), and its pressure derivative (B_0') at ambient pressure for the DR phase of the compounds are also given. The used pressure transmitting medium is provided. In some cases the estimation has not been possible from experimental data. Data for AB_2S_4 compounds are also given for comparison

Once the DS and DC samples have been transformed to the DR structure, several works have reported XRD measurements on downstroke. In many cases, a metastable DZ structure has been found near ambient pressure [13, 14, 17, 18]. On the other hand, in the case of DS-$ZnGa_2Se_4$ and DC-$MnGa_2Se_4$ the DR structure has been found on downstroke up to the lowest pressure reached in those experiments which was 1 atm and 3.5 GPa, respectively [12, 16]. For DC-$HgGa_2Se_4$, it has been found that if recovered samples with the DZ phase at low pressure are thermally annealed a tetragonal structure similar the original ones can be recrystallized [14]. These results are similar to those of AB_2S_4 compounds (reviewed in Chap. 5) and suggest that the order–disorder phase transition is not reversible; i.e., once cations and vacancies are mixed the order of cations and vacancies cannot be recovered on decreasing pressure unless additional energy (by thermal annealing) is supplied. This means that the cation-vacancy disorder of the octahedrally-coordinated DR phase transforms into the cation-vacancy disorder of the tetrahedrally-coordinated DZ phase on decreasing pressure. Note that in some works the DR phase has been metastably recovered at ambient conditions if there is a fast decrease of pressure.

We must note that old studies in both sulphur- and selenium-based ternary OVCs subjected at high pressures and high temperatures have reported a phase transition to the DR structure on increasing pressure and to the DZ phase on decreasing pressure [11, 40–43]. Furthermore, other structures have been found in those studies after a high-pressure and high-temperature treatment in OVCs, like the spinel structure; so it is possible that also other structures obtained from spinels at high pressures, and reviewed in the first chapters of this book, or those obtained from chalcopyrites at high pressures and temperatures, like the octahedrally-coordinated α-$NaFeO_2$ structure, could be found in ternary OVCs at high pressures and high temperatures [43].

6.4 High-Pressure Raman Studies of AB_2Se_4 OVCs

As commented in Chap. 5, the vibrational properties of ternary OVCs of the AB_2X_4 family have been mostly studied with Raman (R) and infrared (IR) spectroscopy. However, all high-pressure studies of the lattice dynamics of OVCs have been performed using Raman spectroscopy. Raman studies under pressure in selenium-based ternary OVCs have been carried out for $CdGa_2Se_4$ [9, 37, 44], $ZnGa_2Se_4$ [37, 45, 47], $HgGa_2Se_4$ [46], $CdAl_2Se_4$ [17, 48], $HgAl_2Se_4$ [17], and $ZnAl_2Se_4$ [17]. In this section, we will concentrate on discussing these Raman results for OVCs of the AB_2Se_4 family at high pressures paying special attention to the high-pressure Raman spectra of $ZnGa_2Se_4$ in the DS and DC phases, and DC-$CdGa_2Se_4$ as a matter of example.

As commented in Chap. 5, the DC structure of $CdGa_2Se_4$ or $ZnGa_2Se_4$ should have 21 optical vibrational modes at Γ with the mechanical representation according to group theory [49]:

$$\Gamma = 3A(\mathrm{R}) \oplus 5B(\mathrm{R, IR}) \oplus 5E(\mathrm{R, IR}) \oplus B \oplus E \tag{6.1}$$

where A modes are non-polar modes, and B and E modes are polar modes, E modes being doubly degenerated. This results in a total of 13 Raman-active (R) modes ($3A \oplus 5B \oplus 5E$) and 10 IR-active (IR) modes ($5B \oplus 5E$) since one B and one E are acoustic modes. It is interesting to note that doubly degenerate E modes correspond to vibrations of atoms along the a and b axis; i.e., in the directions perpendicular to the c axis, B modes correspond to vibrations of atoms along the c axis, and A modes correspond to vibrations of anions around the vacancies.

On the other hand, the DS structure of $ZnGa_2Se_4$ (assuming it corresponds to model 6 in Chap. 5) should have 21 optical vibrational modes at Γ with the following representation:

$$\Gamma = 2A_1(\mathrm{R}) \oplus A_2 \oplus 2B_1(\mathrm{R}) \oplus 3B_2(\mathrm{R, IR}) \oplus 5E\ (\mathrm{R, IR}) \oplus B \oplus E \tag{6.2}$$

where B_2 and E are polar modes, E modes being doubly degenerated. This results in a total of 12 Raman-active modes ($2A_1 \oplus 2B_1 \oplus 3B_2 \oplus 5E$) because the A_2 mode is silent, and 8 IR-active modes ($3B_2 \oplus 5E$) since one B_2 and one E are acoustic modes. The same number of Raman and IR modes will be observed if the DS structure corresponds to polytypes of models 1 and 2 where the *2b* sites are vacant [9, 10].

In addition, two different wavenumbers (R or IR) should be observed for polar mode in the DC or DS structures due to the transversal–longitudinal optic (TO–LO) splitting. Consequently, taking into account the TO–LO splitting, up to twenty-three Raman-active modes could be observed in the DC phase while twenty modes should be observed in the DS phase (models 1, 2, and 6 in Chap. 5). Note that two additional Raman modes should be observed for the models 3–5 and 7–9 of the DS phase due to the occupancy of the *2b* site [9, 10].

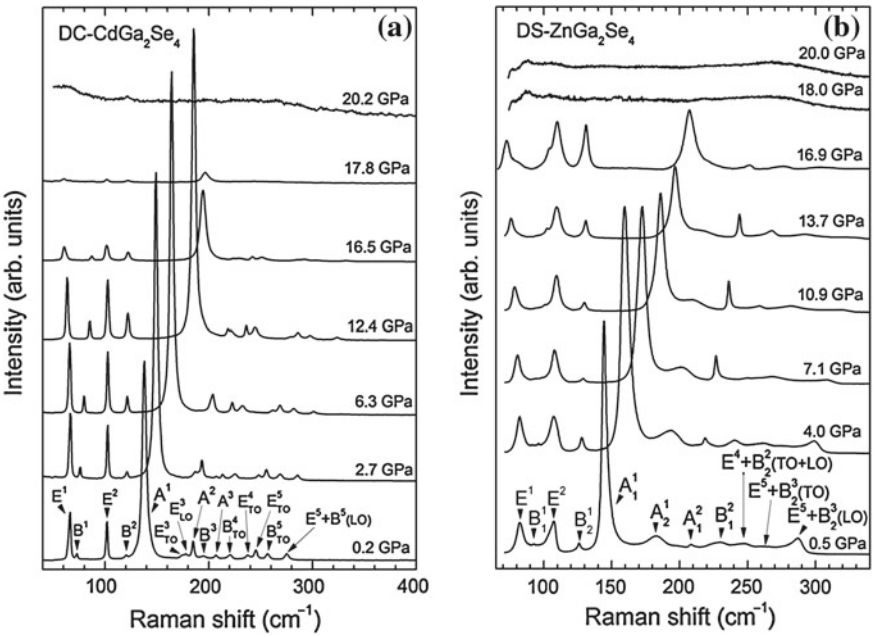

Fig. 6.6 **a** Room-temperature Raman spectra of DC-$CdGa_2Se_4$ at different pressures. The different symmetries of the Raman modes are indicated at 0.2 GPa. **b** Room-temperature Raman spectra of DS-$ZnGa_2Se_4$ at different pressures. The different symmetries of the Raman modes are indicated at 0.5 GPa

Figure 6.6a and b show the Raman spectra of DC-$CdGa_2Se_4$ and DS-$ZnGa_2Se_4$ at selected pressures up to 20 GPa. The Raman-active modes of the DC phase in $CdGa_2Se_4$ can be followed till 17.8 GPa [9]. Similarly, the Raman-active modes of the DS phase in $ZnGa_2Se_4$ can be followed till 16.9 GPa in good agreement with already published results [37]. Above 17.8 and 16.9 GPa both DC-$CdGa_2Se_4$ and DS-$ZnGa_2Se_4$ samples undergo a phase transition to a Raman-inactive phase. These Raman spectra evidence the phase transition towards the DR phase which was already observed in XRD measurements above 21.4 and 15.5 GPa for DC-$CdGa_2Se_4$ and DS-$ZnGa_2Se_4$, respectively [12, 13]. We note that the transition pressure from the DS to the DR structure found by XRD for $ZnGa_2Se_4$ is slightly lower than that found by Raman scattering measurements. This could be explained by the fact that in XRD experiments silicon oil was used as the pressure transmitting medium and a loss of hydrostaticity at high pressure could cause a decrease on the transition pressure. In any case, in the XRD experiments the DR structure only becomes the main phase at pressures equal or greater than 18.5 GPa.

The Raman spectrum of DS-$ZnGa_2Se_4$ is typical of a DS compound corresponding to models 1, 2 and 6. The most significant feature is that it shows less Raman modes than DC compounds and in particular there is one *A* mode less (the *A* mode of intermediate frequency, named A^2) [50]. On the other hand, the Raman

spectrum of DC-$CdGa_2Se_4$ is typical of DC compounds as shown in Chap. 5 for DC-$HgGa_2S_4$. The Raman spectra of both DS-$ZnGa_2Se_4$ and DC-$CdGa_2Se_4$ can be divided into three regions: (i) the low-frequency region below 130 cm^{-1}, (ii) the medium-frequency region between 130 and 200 cm^{-1}, and (iii) the high-frequency region above 200 cm^{-1}. For DS-$ZnGa_2Se_4$ and DC-$CdGa_2Se_4$, 11 and 15 Raman-active modes have been observed at low pressures, respectively. In both OVCs the B and E modes spread mainly along the three regions, while the non-polar A modes, that in the OVCs involve the different oscillations of anions around vacancies, are located in the medium- and high-frequency regions. In general, the Raman modes of the low- and medium-frequency regions are more intense than those of the high-frequency region. In particular, the most intense peak of the Raman spectrum of DS-$ZnGa_2Se_4$ (DC-$ZnGa_2Se_4$ and DC-$CdGa_2Se_4$) is the $A_1^1(A^1)$ mode. This mode is called the "breathing" mode since it is associated to the symmetric oscillation of the anions against the stoichiometric vacancy in both DS and DC structures.

Table 6.5 summarizes the zero-pressure frequencies and the frequency pressure coefficients of the first-order Raman-active modes together with the symmetry assignment of the different Raman modes for DS-$ZnGa_2Se_4$, DC-$ZnGa_2Se_4$, and DC-$CdGa_2Se_4$ taken from [9, 45] which are similar to those reported in other works. For the assignment of the symmetries of the Raman-active modes we have taken into account that DC and DS compounds are optically uniaxial crystals. As commented in Chap. 5, this means that, except for incidence along the optical axis or at 90° from it, symmetry or character coupling can be expected for Raman modes [51, 52].

Raman frequencies and symmetry assignments at room pressure in DS-$ZnGa_2Se_4$ in [50] are in general in good agreement with those of [37, 53]. However, there are several differences. In particular, the silent A_2^1 mode in [50] was previously assigned to the E^3 mode in [37]. On the other hand, authors in [53] assigned to B^1 and B^2 modes the Raman B_2^1 and B_1^2 modes in [50]. For the case of DC-$ZnGa_2Se_4$, the Raman frequencies in [50] are in good agreement with those of [8, 37]. The differences are that the modes attributed to $E^4 + B^4$ (TO), $E^4 + B^4$ (LO), and $E^5 + B^5$ (LO), were previously assigned to the B^4 (TO), E^4 (TO + LO), and B^5 (TO + LO), respectively in [8]. In the case of DC-$CdGa_2Se_4$, a good agreement is found for the Raman frequencies and pressure coefficients reported in the literature [9, 37]. The only difference for the Raman mode assignments is that authors in [9] assigned the E^5 (TO) mode to the mode previously assigned to the $E^5 + B^5$ (TO) mode in [37].

Table 6.5 allows one to compare the frequencies of the different Raman modes between the DS and DC structures of the same AB_2Se_4 compound ($ZnGa_2Se_4$) and between two different DC compounds with different *A* cation ($ZnGa_2Se_4$ and $CdGa_2Se_4$). In the case of $ZnGa_2Se_4$ it can be seen that the mode frequencies are very similar between DC and DS phases. For the case of the $ZnGa_2Se_4$ and $CdGa_2Se_4$ compounds it results that the DC-$ZnGa_2Se_4$ has mode frequencies greater than those of DC-$CdGa_2Se_4$. This is because the Cd atom is heavier than the Zn one and many mode frequencies are in many cases inversely proportional to the square root of the mass or reduced mass of the atoms under vibration.

A comparison of the mode frequencies at ambient pressure of $ZnGa_2Se_4$ (shown in Table 6.5) with those of $ZnAl_2Se_4$ [17]; i.e., between two ZnB_2Se_4 compounds

Table 6.5 Symmetry, zero-pressure frequency, and frequency pressure coefficients of Raman-active modes in DS-$ZnGa_2Se_4$, DC-$ZnGa_2Se_4$, and DC-$CdGa_2Se_4$

DS-$ZnGa_2Se_4$ [45]			DC-$ZnGa_2Se_4$ [45]			DC-$CdGa_2Se_4$[9]		
Symmetry	ω_0 (cm^{-1})	$d\omega/dP$ (cm^{-1}/GPa)	Symmetry	ω_0 (cm^{-1})	$d\omega/dP$ (cm^{-1}/GPa)	Symmetry	ω_0 (cm^{-1})	$d\omega/dP$ (cm^{-1}/GPa)
E^1	82.6	0.00	E^1	82.0	−0.009	E^1	66	0.11
B_1^1	92.7	0.88	B^1	91.9	0.90	B^1	73	1.30
E^2	106.9	0.19	E^2	105.8	0.28	E^2	102	0.20
B_2^1	126.0	0.51	B^2	125.1	0.63	B^2	120	0.22
A_1^1	142.8	4.3	A^1	141.9	4.53	A^1	137	5.05
A_2^1 (silent)	182.6	2.71	A^2	188.4	3.38	E^3 (TO)	173	5.31
A_1^2	208.3	2.57	E^3	194.7	5.43	E^3 (LO)	177	4.52
E^3	196		A^3	207.9	3.03	A^2	184	3.63
B_1^2	229.3	2.76	B^3	229.2	2.77	B^3	194	5.10
$E^4 + B_2^2$ (TO)	243.4	3.54	$E^4 + B^4$ (TO)	239.3	4.33	A^3	206	2.92
$E^4 + B_2^2$ (LO)	243.4	3.54	$E^4 + B^4$ (LO)	244.2	4.39	B^4 (TO)	220	1.98
$E^5 + B_2^3$ (TO)	260.4	4.31	$E^5 + B^5$ (TO)	259.0	5.30	E^4 (TO)	237	4.49
$E^5 + B_2^3$ (LO)	285.7	3.41	$E^5 + B^5$ (LO)	281.3	3.83	E^5 (TO)	244	4.49
						B^5 (TO)	257	4.80
						$E^5 + B^5$ (LO)	274	4.90

Data are taken from [9, 45] (in brackets)

with B = (Al, Ga) shows that $ZnAl_2Se_4$ has greater Raman mode frequencies than $ZnGa_2Se_4$ as expected because of the smaller mass of the Al atom in comparison with that of the Ga atom. The same tendency is found when comparing Raman mode frequencies of $CdGa_2Se_4$ [9, 37] with those of $CdAl_2Se_4$ [48]. A similar comparison can be made between the Raman frequencies of selenium-based and sulfur-based compounds. In particular, the Raman mode frequencies for DC-$CdGa_2Se_4$ are smaller than those for DC-$CdGa_2S_4$ due to the larger mass of Se than that of S. The different Raman mode frequencies upon the change of anion is particularly clearly observed in the comparison of the frequencies of the A modes in ternary OVCs since these modes only involve the vibrations of the anions with respect to the vacancy. On the other hand, the changes in Raman mode frequencies upon the change of the cation are a little more difficult to discuss, but it is clear that A cations affect strongly the frequencies of the Raman modes of the low-frequency region, while *B* cations seem to affect more the frequencies of Raman modes in the medium- and high-frequency region [54].

As regards the pressure coefficients of the Raman modes in selenium-based ternary OVCs, Table 6.5 shows that they are similar to those previously found in sulfur-based ternary OVCs reviewed in Chap. 5. Moreover, as explained in Chap. 5, the pressure coefficients of the different first-order Raman-active modes can be explained because both tetragonal DS and DC structures derive from the zincblende structure by a doubling of the unit cell along the *c* axis. This results in a folding of the X and W points of the Brillouin zone edge of the zincblende structure into the Γ point of these two tetragonal structures [55, 56]. Therefore, several Raman modes in the tetragonal DC and DS structures behave similarly to vibrational modes occurring at the X and W points of the cubic zincblende structure. Consequently, the very small or even negative pressure coefficients of the low-frequency E and B modes can be understood by assuming that the low-frequency E and B modes come from transverse acoustic (TA) and longitudinal acoustic (LA) modes, respectively, at the X and W points of the BZ of the zincblende structure [9, 35, 55–57]. A similar effect was observed in chalcopyrites, like $CuGaS_2$ [58], and in sulfur-based defect chalcopyrites as reviewed in Chap. 5. Similarly to sulfur-based OVCs, the medium-frequency region exhibits the largest frequency pressure coefficients and the modes of the high-frequency region exhibit a little bit smaller frequency pressure coefficients than the modes of the medium-frequency region. The explanation is that modes of the medium-frequency and high-frequency regions can be considered to be analogs of the TO and LO modes in the zincblende structure, where TO modes exhibit usually larger pressure coefficients than LO modes; a signature of the decrease of the ionicity of the compound with increasing pressure.

Now, we want to address the question regarding the existence of an intermediate phase between the DC (or DS) phase and the DR phase from the point of view of high-pressure Raman scattering measurements. Most of the measurements in selenium-based OVCs have not reported evidence of any intermediate phase neither of DZ structure nor any other. Note that several possible disordered structures between the DC and DS phases and the DZ phase, like the disordered CuAu-like (DCA) structure have been proposed [9, 10]. In this context, a progressive

pressure-induced phase transition from the DC structure to the DS structure was proposed in DC-$CdGa_2Se_4$ prior to the DR phase [9]. Similarly, a DS phase has been recently shown to occur at high pressures in DC-$HgGa_2Se_4$ between the DS and DR phases [46]. Finally, it must be stressed that Raman scattering measurements in DS-$ZnGa_2Se_4$, DC-$ZnGa_2Se_4$, DC-$CdGa_2Se_4$ and DC-$HgGa_2Se_4$ have also evidenced that on decreasing pressure from the DR phase the samples do not return to the original DS or DC phase but to a disordered phase [9, 45, 46] which is consistent with the DZ phase observed by XRD on downstroke [13, 14]. Furthermore, Raman scattering measurements in DZ-$ZnGa_2Se_4$, DZ-$CdGa_2Se_4$ and DZ-$HgGa_2Se_4$ under pressure have found that the DZ phase undergoes a phase transition to the DR phase at similar or even slightly smaller pressures than those of the original DC phase and that on decreasing pressure the sample returns to the DZ phase. This result indicates that the DC-to-DZ transition is not observed prior to the transition to the DR phase and that the DZ-to-DR phase transition is completely reversible since there is no change of disorder in the cation sublattice at the phase transition pressure [9, 45, 46]. As can be observed, the Raman spectra of the DZ phase at different pressures in the three AGa_2Se_4 (A = Zn,Ga,Hg) compounds are very similar to those reported in Chap. 5 for DZ-$HgGa_2S_4$.

6.5 High-Pressure Optical Absorption Studies of AB_2Se_4 OVCs

The optical properties of ternary AB_2Se_4 OVCs under high pressure have been studied recently by means of optical absorption spectroscopy for the particular case of DC-$MnGa_2Se_4$ [59], DC-$CdGa_2Se_4$ and DC-$HgGa_2Se_4$ [9, 60]. Therefore, in this section we will concentrate on discussing optical absorption results for AB_2Se_4 OVCs at high pressures paying special attention to the optical absorption of DC-$CdGa_2Se_4$ as a matter of example because similar results have been obtained for DC-$CdGa_2Se_4$ and DC-$HgGa_2Se_4$ [60].

DC-$MnGa_2Se_4$, DC-$CdGa_2Se_4$ and DC-$HgGa_2Se_4$ are semiconductors with a direct bandgap energy at ambient pressure [9, 59–64]. Figure 6.7 shows the evolution of the bandgap energy as a function of pressure for DC-$CdGa_2Se_4$ in two different upstrokes. In the first one, pressure was increased up to 22 GPa and the original tetragonal phase fully suffered a transition to the DR phase. Unfortunately, dark linear defects appear on the sample above 14 GPa which lead to strong scattering and prevent the correct measurement of the optical absorption edge above 16 GPa [9]. During the first upstroke it can be observed that the direct bandgap energy increases with a pressure coefficient of 36 ± 4 meV/GPa at low pressures, while at pressures above 11 GPa the bandgap energy decreases with a pressure coefficient of -26 ± 3 meV/GPa. It can be also observed that the experimental direct bandgap energy of DC-$CdGa_2Se_4$ has a strong non-linear pressure dependence up to 6–8 GPa resulting in a negative shift above 10 GPa. The non-linear behavior of the direct bandgap energy at low pressures is a general feature common to all OVCs due to a conduction band anticrossing at the Γ point of the Brillouin zone caused by the

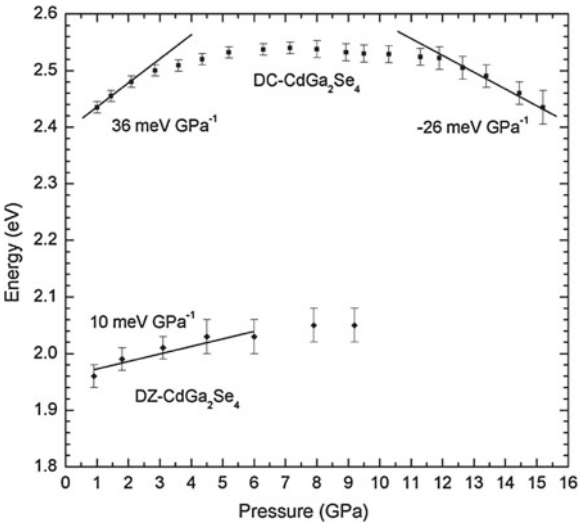

Fig. 6.7 Evolution of the bandgap energy with pressure in DC-$CdGa_2Se_4$. Squares correspond to experimental values for the DC phase while diamonds correspond to experimental values for the DZ phase. Values of pressure coefficients of the direct bandgap at room pressure and at high pressure are also shown

presence of ordered vacancies in adamantine OVCs and the doubling of the unit cell along the *c* axis with respect to the zincblende structure [60]. On the other hand, a comparison of bandgap energy measurements with ab initio theoretical calculations (to be commented in Chap. 7), which do not include disorder, show that the strong non-linear decrease of the direct bandgap energy above 8 GPa in DC-$CdGa_2Se_4$ could be compatible with the increase of cation disorder and the consequent gradual phase transition from the DC to the DS structure. This DC to DS phase transition has been proposed to be prior to the phase transition to the opaque DR structure, as already commented in Sect. 6.4.

After $CdGa_2Se_4$ was fully transformed into the DR phase, pressure was decreased slowly down to 1 GPa [9]. The evolution of the bandgap energy of $CdGa_2Se_4$ during a second upstroke is plotted in Fig. 6.7. As can be observed, the bandgap energy decreases more than 0.4 eV at 1 GPa when comparing with the first upstroke. In addition, the pressure coefficient at zero pressure for the second upstroke is of 10 ± 2 meV/GPa, which is a value about four times smaller than that obtained during the first upstroke. A strong decrease of the direct bandgap energy in going from the ordered chalcopyrite structure to the DZ structure has been found in several chalcopyrite-type compounds [65]. Besides, a similar but smaller decrease of the bandgap was also experimentally found in $CdGa_2Te_4$ where the disorder at cation sites causes the decrease of the bandgap energy from 1.5 eV in the ordered DC structure to 1.4 eV in the DZ phase [3]. Therefore, the strong decrease of the direct bandgap in $CdGa_2Se_4$ on downstroke has been interpreted as an evidence of the formation

of the DZ phase due to the non-reversibility of the pressure-induced order-disorder processes in DC-$CdGa_2Se_4$ [9]. These results obtained with optical absorption experiments under pressure are in agreement with XRD and Raman experiments under pressure carried out with AB_2Se_4 compounds and it is expected that similar results will be obtained when optical absorption studies at high pressures are performed in AB_2S_4 compounds.

6.6 Conclusions

In this chapter the high-pressure studies performed in OVCs of the AB_2Se_4 family with DS and DC structures have been reviewed with a special emphasis in their high-pressure phase transitions, which are compared to those of their parent semiconductors, the OVCs of the AB_2S_4 family, the binary zincblende-type AX compounds, and the ternary chalcopyrite-type ABX_2 compounds.

High-pressure x-ray diffraction measurements in tetragonal OVCs have shown that in both sulfur- and selenium-based ternary OVCs there is an anisotropy in the axial compression being the *a* axis more compressible than the *c* one. Therefore, OVCs with DC structure tend with pressure to values of *c/a* ratio typical of OVCs with DS structure. Expectations regarding the value of the bulk modulus in sulphur- and selenium-based AB_2X_4 compounds are still under debate. Selenium-based OVCs show a similar pressure behaviour than sulphur-based OVCs and both undergo a phase transition to the DR structure on increasing pressure at room temperature that leads to the DZ structure on decreasing pressure. However, other phases have been found after a high-pressure and high-temperature treatment and they need to be explored further.

High-pressure Raman scattering measurements have shown that different vibrational modes can be observed in OVCs with different structures, like DC or DS. Similarly to the case of ternary chalcopyrite-type ABX_2 compounds, the vibrational modes of tetragonal sulphur- and selenium-based ternary OVCs of the AB_2X_4 family are related to those in the zincblende structure and can be analysed by the folding method to explain the vibrational frequencies and their pressure dependence. Raman measurements evidence the pressure–induced phase transitions to the DR and DZ phases found by XRD measurements. Since high-pressure Raman measurements are easier to perform and analyze than high-pressure XRD measurements (which in many cases require the use of synchrotron sources), Raman studies have evidenced the behaviour of the DC, DS and DZ phases in several sulphur- and selenium-based OVCs and have confirmed the irreversibility of the order-disorder phase transitions taking place in OVCs. Only the DZ to DR phase transition is completely reversible since there is no change of disorder in the cation sublattice between these two structures.

Finally, high-pressure optical absorption measurements is selenium-based OVCs show clearly that the direct bandgap of ternary OVCs shows a non-linear pressure dependence because of the special character of their conduction bands and that there

is a decrease of the direct bandgap of ternary OVCs as disorder increases. This last behaviour is similar to that found previously in ABX_2 chalcopyrites. We hope that the present comprehensive work will stimulate further research of the interesting properties of OVCs of the AB_2X_4 family, specially at high pressures.

Acknowledgments This study was supported by the Spanish government MEC under project MAT2010-21270-C04-04, by MALTA Consolider Ingenio 2010 project CSD2007-00045, by Generalitat Valenciana under project GVA-ACOMP-2013-012 and by the Vicerrectorado de Investigacin y Desarrollo of the Universidad Politcnica de Valencia (UPV2011-0914 PAID-05-11 and UPV2011-0966 PAID-06-11).

References

1. MacKinnon A (1985) Tables of numerical data and functional relationships in science and technology, vol 17. Springer-Verlag, Berlin, pp 124
2. Gorgonians AN, Radautsan SI, Tiginyanu IM (1985) Wide-gap A(II)B $(III)_2$ C $(VI)_4$ semiconductors—optical and photoelectric properties, and potential applications (review). Sov Phys Sem USSR 19:121–132
3. Bernard JE, Zunger A (1988) Ordered-vacancy compound semiconductors: pseudocubic $CdIn_2$ Se_4. Phys Rev B 37:6835–6856
4. Jiang X, Lambrecht WRL (2004) Electronic band structure of ordered vacancy defect chalcopyrite compounds with formula II-III_2-VI_4. Phys Rev B 69:035201(8)
5. Alonso-Gutiérrez P, Sanjuán ML, Morón MC (2009) Thermally activated catión ordering in $Zn_{0.5}$ $Mn_{0.5}Ga_2Se_4$ single crystals studied by Raman scattering. Phys. Status Solidi c 6:1182–1186
6. Caldera D, Morocoima M, Quintero M, Rincon C, Casanova R, Grima P (2011) On the crystal structure of the defective ternary compound $ZnGa_2Se_4$. Solid State Commun 151:212–215
7. Eifler A, Hecht JD, Lippold G, Riede V, Grill W, Krauss G, Krämer V (1999) Combined infrared and Raman study of the optical phonons of defect chalcopyrite single crystals. Physica B 263–264:806–808
8. Eifler A, Krauss G, Riede V, Krämer V, Grill W (2005) Optical phonon modes and structure of $ZnGa_2Se_4$ and $ZnGa_2S_4$. J Phys Chem Solids 66:2052–2057
9. Gomis O, Vilaplana R, Manjón FJ, Pérez-González E, López-Solano J, Rodríguez-Hernández P, Muñoz A, Errandonea D, Ruiz-Fuertes J, Segura A, Santamaría-Pérez D, Tiginyanu IM, Ursaki VV (2012) High-pressure optical and vibrational properties of $CdGa_2Se_4$: order–disorder processes in adamantine compounds. J Appl Phys 111:013518(15)
10. Manjón FJ, Gomis O, Vilaplana R, Sans JA, Ortiz HM (2013) Order-disorder processes in adamantine ternary ordered-vacancy compounds. Phys Stat Sol b 250:1496–1504
11. Range KJ, Becker W, Weiss A (1969) Das Verhalten von $CdIn_2$ Se_4 bei hohen Drucken. Z Naturforschg 24b:1654–1655
12. Errandonea D, Kumar RS, Manjón FJ, Ursaki VV, Tiginyanu IM (2008) High-pressure X-ray diffraction study on the structure and phase transitions of defect-stannite $ZnGa_2$ Se_4 and defect-chalcopyrite $CdGa_2$ S_4. J Appl Phys 104:063524(9)
13. Grzechnik A, Ursaki VV, Syassen K, Loa I, Tiginyanu IM, Handfland M (2001) Pressure-induced phase transitions in cadmium thiogallate $CdGa_2$ Se_4. J Solid State Chem 160:205–211
14. Gomis O, Vilaplana R, Manjón FJ, Santamaría-Pérez D, Ruíz-Fuertes J, Errandonea D, Pérez-González E, López-Solano J, Rodríguez-Hernández P, Muñoz A, Tiginyanu IM, Ursaki VV (2013) High-pressure study of the structural and elastic properties of defect-chalcopyrite $HgGa_2Se_4$. J Appl Phys 113:073510(10)

15. Gomis O, Vilaplana R, Manjón FJ, Santamaría-Pérez D, Errandonea D, Pérez-González E, López-Solano J, Rodríguez-Hernández P, Muñoz A, Tiginyanu IM, Ursakif VV (2013) Crystal structure of $HgGa_2Se_4$ under compression. Materials Research Bulletin 48:2128–2133
16. Marquina J, Power Ch, Grima P, Morocoima M, Quintero M, Couzinet B, Chervin JC, Munsch P, González J (2006) Crystallographic properties of the $MnGa_2Se_4$ compound under high pressure. J Appl Phys 100:093513(6)
17. Meenakshi S, Vijyakumar V, Godwal BK, Eifler A, Orgzall I, Tkachev S, Hochheimer HD (2006) High pressure X-ray diffraction study of $CdAl_2Se_4$ and Raman study of AAl_2Se_4 (A = Hg, Zn) and $CdAl_2X_4$ (X = Se, S). J Phys Chem Solids 67:1660–1667
18. Meenakshi S, Vijyakumar V, Eifler A, Hochheimer HD (2010) Pressure-induced phase transition in defect chalcopyrites $HgAl_2Se_4$ and $CdAl_2S_4$. J Phys Chem Solids 71:832–835
19. Hanada T (1998) Neutron and electron diffraction studies of $ZnGa_2Se_4$. Physica B 241–243:373–375
20. Morón MC, Hull S (2003) Order-disorder phase transition in $Zn_{1-x}Mn_xGa_2Se_4$: long-range order parameter versus x. Phys Rev B 67:125208(7)
21. Morón MC, Hull S (2005) Effect of magnetic dilution in $Zn_{1-x}Mn_xGa_2Se_4$ ($0 < x < 0.5$). J Appl Phys 98:013904(6)
22. Gastaldi L, Simeone MG, Viticoli S (1985) Cation ordering and crystal structures in AGa_2X_4 compounds ($CoGa_2S_4$, $CdGa_2S_4$, $CdGa_2Se_4$, $HgGa_2Se_4$, $HgGa_2Te_4$). Solid State Commun 55:605–607
23. Birch F (1978) Finite strain isotherm and velocities for single-crystal and polycrystalline NaCl at high pressures and 300 K. J Geophys Res 83:1257–1268
24. Santamaría-Pérez D, Gomis O, Dziubek K, Errandonea D, Manjón FJ, Sans JA, Vilaplana R, Muñoz A, Rodríguez-Hernández P, Ursaki VV, Tiginyanu IM, to be submitted
25. Gomis O, Santamaría-Pérez D, Vilaplana R, Luna R, Sans JA, Manjón FJ, Errandonea D, Pérez-González E, Rodríguez-Hernández P, Muñoz A, Tiginyanu IM, Ursaki VV (2013) Structural and elastic properties of defect chalcopyrite $HgGa_2S_4$ under high pressure. J Alloy & Comp, doi:10.1016/j.jallcom.2013.08.123
26. Liu HZ, Ding Y, Somayazulu M, Qian J, Shu J, Häusermann D, Mao HK (2005) Rietveld refinement study of the pressure dependence of the internal structural parameter u in the wurtzite phase of ZnO. Phys Rev B 71:212103(4)
27. Liu HZ, Hu JZ, Shu JF, Häusermann D, Mao HK (2004) Lack of the critical pressure for weakening of size-induced stiffness in 3C–SiC nanocrystals under hydrostatic compression. Appl Phys Lett 85:1973–1975
28. Ruiz-Fuertes J, Errandonea D, Lacomba-Perales R, Segura A, González J, Rodríguez F, Manjón FJ, Ray S, Rodríguez-Hernández P, Muñoz A, Zhu Z, Tu CY (2010) High-pressure structural phase transitions in $CuWO_4$. Phys Rev B 81:224115(10)
29. Santamaría-Pérez D, Gracia L, Garbarino G, Beltrán A, Chulia-Jordan R, Gomis O, Errandonea D, Ferrer-Roca Ch, Martínez-García D, Segura A (2011) High-pressure study of the behavior of mineral barite by X-ray diffraction. Phys Rev B 84:054102(8)
30. Gomis O, Sans JA, Lacomba-Perales R, Errandonea D, Meng Y, Chervin JC, Polian A (2012) Complex high-pressure polymorphism of barium tungstate. Phys Rev B 86:054121(10)
31. Frogley MD, Sly JL, Dunstan DJ (1998) Pressure dependence of the direct band gap in tetrahedral semiconductors. Phys Rev B 58:12579–12582
32. Garbato L, Ledda F, Rucci A (1987) Structural distortions and polymorphic behavior in ABC_2 and AB_2C_4 tetrahedral compounds. Prog Cryst Growth Charact 15:1–41
33. Lowe-Ma CK, Vanderah TA (1991) Structure of $ZnGa_2S_4$, a defect sphalerite derivative. Acta Cryst C 47:919–924
34. Schwer H, Kraemer V (1990) The crystal structure of $CdAl_2S_4$, $HgAl_2S_4$, and $HgGa_2S_4$. Z Kristall 190:103–110
35. Binsma JJM, Galing LJ, Bloem J (1981) Order–disorder behaviour and tetragonal distortion of chalcopyrite compounds. Phys Stat Sol a 63:595–603
36. Burlakov II, Raptis YS, Ursaki VV, Anastassakis E (1997) Order–disorder phase ransition in $CdAl_2S_4$ under hydrostatic pressure. Solid State Commun 101:377–381

37. Ursaki VV, Burkalov II, Tiginyanu IM, Raptis YS, Anastassakis E, Aneda A (1999) Phase transitions in defect chalcopyrite compounds under hydrostatic pressure. Phys Rev B 59:257–268
38. Tiginyanu IM, Ursaki VV, Fulga VN (1989) Order–disorder phase transition in the cation sublattice of $ZnGa_2Se_4$. Sov Phys Semicond 23:1069–1070
39. Luna R (2013) to be published
40. Range KJ, Becker W, Weiss A (1968) Uber Hochdruckphasen des $CdAl_2S_4$, $HgAl_2S_4$, $ZnAl_2Se_4$, $CdAl_2Se_4$, und $HgAl_2Se_4$ mit Spinell-struktur. Z Naturforschg 23b:1009–1009
41. Range KJ, Becker W, Weiss A (1968) Uber Hochdruckphasen des $CdIn_2Te_4$, und $HgIn_2Te_4$ mit NaCl-Struktur. Z Naturforschg 23b:1261–1261
42. Becker W, Range KJ, Weiss A (1968) Uber das Verhalten von $ZnIn_2Te_4$, $CdGa_2Se_4$ und $ZnGa_2Se_4$ bei hohen Drucken. Z Naturforschg 23b:1545–1545
43. Range KJ (1971) Hochdruckuntersuchungen and ternarën Chalkogeniden mit tetraedrisch koordinierten Kationen. Chem Zeitung 95:3–11
44. Mitani T, Naitou T, Matsuishi K, Onari S, Allakhverdiev K, Gashimzade F, Kerimova T (2003) Raman scattering in $CdGa_2Se_4$ under pressure. Phys stat sol b 235:321–325
45. Vilaplana R, Gomis O, Pérez-Gonzalez E, Ortiz HM, Manjón FJ, Rodríguez-Hernández P, Muńoz A, Alonso-Gutiérrez P, Sanjuán ML, Ursaki VV, Tiginyanu IM (2013) High-pressure Raman scattering study of defect chalcopyrite and defect stannite ZnGa2Se4. J Appl Phys 113(10):233501
46. Vilaplana R, Gomis O, Manjón FJ, Ortiz HM, Pérez-Gonzalez E, López-Solano J, Rodríguez-Hernández P, Muñoz A, Errandonea D, Ursaki VV, Tiginyanu IM (2013) Lattice dynamics study of $HgGa_2Se_4$ at high pressures. J Phys Chem C 117:15773–15781
47. Allakhverdiev K, Gashimzade F, Kerimova T, Mitani T, Naitou T, Matsuishi T, Onaric S (2003) Raman scattering under pressure in $ZnGa_2Se_4$. J Phys Chem Solids 64:1597–1601
48. Tiginyanu IM, Ursaki VV, Manjón FJ, Tezlevan VE (2003) Raman scattering study of pressure-induced phase transitions in $A^{II}B_2^{III}C_4^{VI}$ defect chalcopyrites and spinels. J Phys Chem Solids 64:1603–1607
49. Kroumova E, Aroyo MI, Perez-Mato JM, Kirov A, Capillas C, Ivantchev S, Wondratschek H (2003) Bilbao crystallographic server: useful databases and tools for phase-transition studies. Phase Transitions 76:155–170
50. Vilaplana R, Gomis O, Pérez-González E, Ortiz HM, Manjón FJ, Rodríguez-Hernández P, Muñoz A, Alonso-Gutiérrez P, Sanjuán ML, Ursaki VV, Tiginyanu IM (2013) Thermally activated cation ordering in $ZnGa_2Se_4$ single crystals studied by Raman scattering, optical absorption, and ab initio calculations. J Phys Condens Matter 25(11):165802
51. Loudon R (1964) Raman effect in crystals. Adv Phys 13:423
52. Alonso-Gutiérrez P, Sanjuán ML (2008) Ordinary and extraordinary phonons and photons: Raman study of anisotropy effects in the polar modes of $MnGa_2Se_4$. Phys Rev B 78:045212(9)
53. Alonso-Gutiérrez P (2009) Estudio mediante espectroscopía Raman de la serie de semiconductores tetraédricos $Zn_{1-x}Mn_xGa_2Se_4$, Colección de Estudios de Física, Ph.D. Thesis, vol 78. Prensas Universitarias de Zaragoza, Zaragoza
54. Tiginyanu IM, Lottici PP, Razzetti C, Gennari S (1993) Effects of the cations on the Raman spectra of sulphur defect chalcopyrites. Jpn J Appl Phys 32 (Suppl. 32–33):561–563
55. Miller A, MacKinnon A, Weaire D (1981) Beyond the binaries-the chalcopyrite and related semiconductors. Solid State Phys 36:119–175
56. Alonso-Gutiérrez P, Sanjuán ML (2007) Fermi resonance in the Raman spectrum of the Se-vacancy breathing mode of $MnGa_2Se_4$. Phys Rev B 76:165203(7)
57. Klotz S, Besson JM, Braden M, Karch K, Pavone P, Strauch D, Marshall WG (1997) Pressure induced frequency shifts of transverse acoustic phonons in germanium to 9.7 GPa. Phys Rev Lett 79:1313–1316
58. González J, Fernández BJ, Besson JM, Gauthier M, Polian A (1992) High-pressure behavior of Raman modes in $CuGaS_2$. Phys Rev B 46:15092–15101

59. Gonzalez J, Rico R, Calderón E, Quintero M, Morocoima M (1999) Absorption edge of $MnGa_2Se_4$ single crystals under hydrostatic pressure. Phys Stat Sol b 211:45–49
60. Manjón FJ, Gomis O, Rodríguez-Hernández P, Pérez-González E, Muñoz A, Errandonea D, Ruiz-Fuertes J, Segura A, Fuentes-Cabrera M, Tiginyanu IM, Ursaki VV (2010) Nonlinear pressure dependence of the direct band gap in adamantine ordered-vacancy compounds. Phys Rev B 81:195201(7)
61. Bacewicz R, Lottici PP, Razetti C (1979) Raman scattering of the ordered-vacancy compound $CdGa_2Se_4$. J Phys C Solid State 12:3603–3614
62. Sosovska SM, Yurchenko OM, Romanyuk YE, Olekseyuk ID, Parasyuk OV (2006) Phase diagram of the $CdGa_2Se_4$–Bi_2Se_3 system and growth of $CdGa_2Se_4$ single crystals. J Alloys and Comp 417:127–130
63. Kim CD, Cho TS, Kim WT (1987) Temperature-dependence of the energy gaps in $CdGa_2Se_4$ and $CdGa_2Se_4$—Co^{2+} single crystals. Solid State Commun 63:871–872
64. Kim WT, Cho GJ, Kim CS, Kim CD (1991) Impurity optical absorption of $HgGa_2Se_4 : Co^{2+}$ single crystals. Phys Rev B 43:14265–14267
65. Roa L, Chervin JC, Chevy A, Davila M, Grima P, González J (1996) Optical absorption and Raman scattering measurements in $CuAlSe_2$ at high pressure. Phys Stat Sol b 198:99–104

Chapter 7
Theoretical Ab Initio Calculations in Ordered-Vacancy Compounds at High Pressures

A. Muñoz and M. Fuentes-Cabrera

Abstract Ab initio calculations within the Density Funtional Theory and the Density Functional Perturbation Theory of the defect chalcopyrite, defect stannite and pseudo-cubic chalcopyrite structures of AB_2X_4 (X = S and Se) compounds are reported. The electronic, dynamical, and elastic properties under hydrostatic pressures are reviewed and discussed in relation with pressure-induced order-disorder phase transitions. Finally, as a matter of example, we present new results of a *first-principles* study of the pressure dependence of several properties for the pseudo-cubic chalcopyrite structure of $CdIn_2Se_4$. We found that the generalized Born stability criteria are violated above 11 GPa, thus PC-$CdIn_2Se_4$ becomes mechanically unstable. Furthermore, we found a phonon dynamical instability around 18 GPa; thus showing that PC-$CdIn_2Se_4$ becomes unstable at high pressures not only from the static but also from the dynamical point of view.

Keywords Ab initio · High pressure · Defect chalcopyrite · Defect stannite · Defect famatinite · Pseudocubic chalcopyrite · Electronic · Dynamical · Elastic properties

7.1 Introduction

Ordered-vacancy compounds (OVCs) of the $A^{II}B_2^{III}X_4^{VI}$ family are semiconducting materials with potential applications in nonlinear optical and photovoltaic devices. OVCs crystallize in several tetragonal structures (defect chalcopyrite, defect stannite, and pseudocubic structure) derived from the zinc-blende structure. These structures

A. Muñoz (✉)
Departamento de Física Fundamental II, Instituto de Materiales y Nanotecnología, Universidad de La Laguna, La Laguna, Tenerife, Spain
e-mail: amunoz@ull.edu.es

M. Fuentes-Cabrera
Center for Nanophase Materials Science, Computer Science and Mathematics Division, Oak Ridge National Laboratory, Oak Ridge, Tennessee 37831, USA
e-mail: fuentescabma@ornl.gov

F. J. Manjón et al. (eds.), *Pressure-Induced Phase Transitions in AB_2X_4 Chalcogenide Compounds*, Springer Series in Materials Science 189,
DOI: 10.1007/978-3-642-40367-5_7,

can be considered as tetrahedrally coordinated if one assumes that they contain an ordered array of stoichiometric vacancies (□) that compensate the smaller number of cations (A and B) with respect to anions (X). In this way, these compounds can be also formulated as $\square A^{II}B_2^{III}X_4^{VI}$. The effect of the stoichiometric vacancies on the electronic and stability properties of these compounds has been the subject of several theoretical studies.

This chapter will focus on the theoretical studies from ab initio methods of the structural, electronic, elastic, and dynamical properties of these compounds under hydrostatic pressure. We will review the high-pressure studies already published for sulphur- and selenium-based OVCs with defect chalcopyrite and defect stannite structures. Furthermore, we will provide, as a matter of example, some new results for $CdIn_2Se_4$ with pseudocubic structure in order to show how the theoretical methods can be used to study and to predict the dynamical and elastic properties since no high-pressure experimental results are available for this compound to our knowledge.

7.2 Theoretical Background

The state-of-the-art in computational materials science uses the ability of quantum mechanics to predict the total energy of a system of nuclei and electrons. In this respect, ab initio calculation techniques only require as input data the atomic number and the chemical composition of the material. With this input it is possible to calculate a variety of properties (electronic, elastic, thermal, vibrational) of any material of interest. In what follows, we give a general introduction to these techniques by focusing on how they have been applied to the study of structural, electronic, dynamical, and elastic properties of $A^{II}B_2^{III}X_4^{VI}$ chalcopyrite compounds under hydrostatic pressure.

The Density Functional Theory (DFT) is an ab initio technique that allows the study and prediction of the electronic and structural properties of a material by minimizing its total energy with respect to the nuclear and electronic coordinates. The fundamental variable in this theory is the electronic charge density of the system. The theorem of Hohenberg and Kohn [1] and the seminal work of Khon and Sham [2] are the basis of this theory since they establish that the total energy, E(V), of the ground state of a system is an unique functional of the charge density (and therefore of volume, V), and that this functional is a global (not local) minimum of energy for the correct ground state density. A review on DFT applications can be found in reference [3]. The main approximation in DFT is related to the way in which the contribution to the energy from the effects of the exchange–correlation interactions between electrons is described. The Local Density Approximation (LDA) and the Generalized Gradient Approximation (GGA) are the most popular descriptions currently used [4].

Mujica et al. [5] have reviewed how DFT is applied to the study of the high-pressure phases of many semiconductor compounds. Two different strategies are used to identify the lowest-enthalpy phase of a material as a function of applied pressure.

One strategy consists on minimizing, for a selected set of volumes, the total energy as function of the structural external and internal parameters. It is important to note that pressure, P(V), is a function of volume which is obtained within the DFT formalism at the same time, but independently, as total energy, E(V). The values of pressure (as well others derivatives of the energy) are obtained from the stress theorem [6] which allows also to compute the enthalpy, $H = E + PV$. In the other strategy, the enthalpy is directly minimized at constant pressure. Both strategies provide values for energy, volume, and pressure from where the equation of state (EOS) for a selected structure can be obtained. These techniques, however, have important limitations, the most important one being the existence of many local minima in the configuration space. Many strategies are adopted to overcome this limitation in order to study the high-pressure phases of many materials. For instance, some techniques search the structure of a material at a selected pressure avoiding the imposition of special symmetries, other techniques employ a random search [7], and others employ evolutionary and genetic algorithms [8].

The lattice dynamics of a material and its behavior under high pressure can be analyzed by DFT or by the Density Functional Perturbation Theory (DFPT) [9]. DFPT requires the calculation of the ground state charge density and its linear response to external excitations. This permits, among other interesting quantities, to obtain the elastic properties and the phonon dispersion along the whole Brillouin zone. In particular, this technique is interesting for the study of phonons in polar materials, which are more complex from the theoretical point of view, since the long range of the Coulomb interactions gives rise to a macroscopic electric field, and phonons in polar materials are coupled to this macroscopic electric field. This effect is reflected in the appearance in polar materials of different values for the frequencies of the transversal optic (TO) and the longitudinal optic (LO) phonons at the zone center (Γ point) of the Brillouin zone; i.e., the so-called LO–TO splitting. This splitting can be calculated by means of the Born effective charge tensor Z* and the electronic dielectric constant ε_∞. To take these two variables into account for the calculation of the LO–TO splitting, DFPT requires the study of the electron density response to an homogeneous electric field allowing to obtain the LO–TO splitting near the Γ point (along the [100] or [010] and [001] directions in OVCs).

Phonon frequencies can be also calculated from energy differences using DFT instead of DFPT. In DFT, phonon frequencies are obtained producing small finite displacements of a few atoms in a periodic crystal at equilibrium. In this methodology, one begins with the equilibrium structure at a certain pressure and produces a distortion by displacing a single atom by a small amount U_0 (typically 0.2 Å in OVCs). The atomic forces that result from this distortion are then computed, and the ratio of these forces and U_0 gives one complete row of the force-constants matrix. Subsequently, symmetry operations are applied to these rows to produce the complete matrix. Within the harmonic approximation, this method is exact, yet anharmonic effects are avoided by averaging the results with displacements $+U_0$ and $-U_0$. This approach, named the frozen-phonon approach or direct method, permits to calculate a phonon vibration at a selected wave vector, q [10, 11]. In this method, the study of phonons in polar materials is not straightforward, as in DFPT, because the non-

analytic term related with the electric field is not included in the dynamical matrix at the Γ point, so only frequencies of TO modes are obtained; i.e., the LO-TO splitting is not provided. However, the LO–TO splitting can be obtained a posteriori if the Born effective charge tensor and the macroscopic dielectric constant are calculated from ab initio. In summary, the direct method approach can be used for the calculation of the phonon dispersion but is limited by the size of the system under study when the size of the supercell increases. Its advantage relies on how easy it is to implement.

Since Raman and infrared spectra provide information of phonon frequencies at the Γ point, these frequencies can be computed either with DFPT or with the direct method approach. The study of the vibrational spectra of the material under pressure can provide many interesting properties of the compound under study. For example, the presence of soft modes could be related with phase transitions [9]. Furthermore, using simple models to describe the electron–phonon interactions it is possible to calculate the temperature dependence of the electronic band gap [12].

Elastic constants are interesting to know the elastic or mechanical properties of materials. The elastic properties provide, not only information concerning the strength of the material, they also provide important insight into the interatomic potentials, EOS, and other elastic quantities (Young modulus, shear modulus, etc.) which are interesting for material engineering. The pressure behavior of the elastic constants of a material in a certain structure gives information concerning the mechanical stability of that material under pressure and its possible relation with the structural transformations. These constants can be viewed as force constants associated to a homogeneous strain applied to the material. In fact, the calculation of the elastic constants is performed by studying the response of the periodic system to a microscopic distortion. In order to obtain the elastic constants from ab initio methods, again DFPT is used to calculate the elastic constants tensor.

7.3 Structural Considerations

As already commented, $A^{II}B_2^{III}X_4^{VI}$ compounds (with A and B divalent and trivalent metals, respectively and X = S, Se) known as ordered vacancy compounds crystallize in different tetragonal structures deriving from the zinc-blende structure. In fact, they are variants of the tetrahedrally-bonded tetragonal chalcopyrite structure which is common to materials of chemical composition $A^{II}B^{IV}X_2^{V}$ and $A^{I}B^{III}X_2^{VI}$. Different crystal structures with slightly different ordering of the cations and vacancies as well as order–disorder transition phases exist in this type of compounds. Excellent works related with these materials can be found in the review of Georgobiani et al. [13] and in the paper of Bernard and Zunger [14].

OVCs of the $A^{II}B_2^{III}X_4^{VI}$ family crystallize in three different tetragonal phases: the defect chalcopyrite (DC) structure (space group I-4, No. 82), also known as thiogallate structure, the defect stannite (DS) structure, also known as defect famatinite, (space group I-42m, No. 121), and the ordered pseudo-cubic structure (PC) (space group P-42m, No. 111). The DC and DS structures are defective-like

chalcopyrite structures with different degrees of cation disorder which have seven atoms and one vacancy per unit cell. If the vacancy is considered as an atom, them each atom is surrounded by four neighbors in a tetrahedral-like environment. For details and pictures of all these structures we refer the readers to the two previous chapters of this book.

7.4 Electronic Band Structure and Optical Properties

As already commented, $A^{II}B_2^{III}X_4^{VI}$ materials are interesting for nonlinear frequency conversion applications and nonlinear optical devices and some of them have been proposed for phase change memories to replace actual flash memories. The reduction of the cubic T_d symmetry in zinc-blende-type crystals to the tetragonal symmetry D_{2d} in chalcopyrite-type and defect chalcopyrite-type crystals is the origin of birefringent behavior and the reason for the nonlinear properties of these semiconductors [14]. Thus, their electronic band structures and their evolution under pressure have been the subject of numerous experimental and theoretical studies. It is well known that DFT systematically underestimates the band gap and that different exchange-correlation functional provides different values of the band gap, yet the pressure evolution and the symmetry of the band gap are usually well described [15]. As the theoretical techniques improved, many OVCs of the $A^{II}B_2^{III}X_4^{VI}$ family have been studied and their electronic properties have been compared to experiments when possible. In what follows, we briefly describe some of the most interesting studies on the electronic properties of these compounds.

One of the earliest theoretical studies on the electronic properties is that of Baldereschi et al. [16]. In 1977, they used a pseudopotential method to investigate the electronic properties of PC-$CdIn_2Se_4$. The character and value of the calculated band gap were in agreement with previous experiments, yet an intra-valence gap was found. In 1988, Bernard and Zunger [14] used an all-electron potential-variation mixed-basis approach to investigate the structure and electronic properties of the same material. This study revealed that the vacancy has associated with it lone-pair Se dangling orbitals which are oriented in different directions and form a disperse band occupying the uppermost part of the valence band. However, unlike Baldereschi et al. [16], an intra-valence gap was not found. Subsequently, Marinelli et al. [17] using DFT-LDA and norm-conserving pseudopotentials studied the PC and spinel (space group Fd-3m, No. 227) structures of $CdIn_2Se_4$ at equilibrium pressure. For the PC structure, they did not find an intra-valence gap, either.

Of the theoretical studies, the most comprehensive ones are those of Jiang and Lambrecht [18] and Mishra and Ganguli [19]. They studied the materials $A^{II}B_2^{III}X_4^{VI}$ (A = Zn, Cd, Hg; B = Al, Ga, In; X = S, Se, Te) and AAl_2Se_4 (A = Ag, Cu, Cd, Zn), respectively. Noteworthy, Jiang and Lambrecht [18] used an empirical correction for the band gaps that improved the agreement with experimental data. This work reports the band structure and the band gap of many compounds with DC

structure and the authors examined the chemical trends for the bands gaps and the relations with the possible nonlinear optical applications.

DC-$CdAl_2Se_4$ was studied by Fuentes Cabrera and Sankey [20], using total energy pseudopotential calculations with the LDA functional parametrized by Perdew and Zunger [21], and the GGA functional in the Perdew and Wang approximation [22] for the exchange correlation potential. They studied the DC and the spinel phases and showed that the DC phase has a direct gap while the spinel phase has an indirect gap. Using a Generalized Density Functional Theory (GDFT) correction [23], the calculated band gap of the DC phase was found in excellent agreement with experiments. These authors also showed that DC and spinel structures have practically the same energy when the LDA functional is used, whereas the DC phase is more stable than the spinel structure, as is experimentally found, when the GGA functional is used. Recently, Ourani et al. have studied the same compound by means of the full potential linearized augmented plane waves (FP-LAPW) [24]. Using the Engel-Vosko GGA functional (EV-GGA) [25], they found a direct band gap very close to the 3.07 eV experimental band gap. Verma et al. [26] analyzed the pressure and temperature evolution of direct and indirect band gaps of this compound, using FP-LAPW method, and considering the effect of employing different exchange-correlation functionals (LDA [20], Perdew–Burke–Ernzenhoff (GGA-PBE) [27], and GGA and the EV-GGA [25]). Calculations with EV-GGA were found to reproduce well the value of the experimental band gap.

The electronic and optical properties of $ZnAl_2Se_4$ have been reported by Verma et al. [28] calculated with the FP-LAPW method and two different functionals for the exchange-correlation potential (GGA-PBE [27] and EV-GGA [25]). They concluded that $ZnAl_2Se_4$ is a direct wide band gap material and that both the direct and indirect band gaps increase with pressure. The optical properties were also reported showing a considerable anisotropy.

The trends of the band gap pressure coefficients of the family compounds $ZnGa_2X_4$ (X = S, Se, Te) have been studied by Jiang et al. [29] using the LDA functional to describe the exchange-correlation potential with the pseudopotential plane wave method. They found that DC and DS phases have different band gaps. Ouahrani et al. [30] have made a study of the AAl_2Se_4 compounds (A = Zn, Cd, and Hg) within the DFT and the GW quasi-particle approximation to correct the DFT band gap underestimation, with emphasis in the influence between nonlinear optical properties and the iconicity degree.

Singh et al. investigated the electronic and optical properties of DC-$HgAl_2Se_4$ using the FP-LAPW method with LDA, GGA, GGA-PBE, and EV-GGA exchange-correlation functionals [31]. They also included the spin-orbit coupling in the calculations and showed that this reproduces the structural parameters better than EV-GGA. However, EV-GGA gives a band gap in excellent agreement with experimental results. The real and imaginary part of the dielectric function was also reported, showing considerable anisotropy of optical properties. Similarly, Reshak et al. investigated DC-$HgGa_2S_4$ with the FP-LAPW method and different exchange correlation functionals (LDA, GGA, and EVGGA) to study the band gap [32]. Once again, it was

found that EV-GGA functional gives a direct band gap of 2.84 eV in good agreement with the experiments.

Lavrentyev et al. performed ab initio calculations and X-ray photoelectron spectroscopy, to study DC-$CdGa_2S_4$ and DC-$CdGa_2Se_4$ compounds [33–35]. They reported a direct band gap in $CdGa_2Se_4$ and the real and imaginary part of the electronic dielectric function that evidence considerable anisotropy. For $CdGa_2S_4$, employing an ab initio full Multiple scattering code, they obtained the theoretical form of the X-ray absorption spectra and the density of states which reveals how the form of the edge of conduction band is determined mainly by Ga *s*-states.

Fuentes-Cabrera et al. investigated the dependence of the band-gap with pressure of DC-$CdGa_2S_4$ and DC-$CdGa_2Se_4$ without the inclusion of disorder in the structure [36]. The band gap showed a parabolic behavior: as the pressure increased, the band gap reached a maximum and then it started to decrease. The strong nonlinear pressure dependence of the optical band gap in DC-$CdGa_2Se_4$ and DC-$HgGa_2Se_4$ and other OVCs was studied experimentally and theoretically (with DFT calculations using the GGA-PBE functional) by Manjón et al. [37]. The strong nonlinear behavior of the direct band gap was found to be due to a band anti-crossing at the Γ point caused by the presence of ordered stoichiometric vacancies in OVCs. Therefore, it was proposed that this nonlinear behavior of the direct band gap is a general characteristic of the adamantine-type OVCs of the $B_2^{III}X_3^{VI}$ and $A^{II}B_2^{III}X_4^{VI}$ families. A similar experimental and theoretical study of the pressure dependence of the band gap was performed by Gomis et al. in DC-$CdGa_2Se_4$ [38]. The dependence of the band gap under pressure showed a parabolic behavior as in [36]. However, the experimental and the theoretical dependence showed a disagreement at high pressures. This was interpreted as an indication that order–disorder transitions (not considered in calculations) were taking place. That is, it was argued that as the order-disorder transitions consisting of cation or cation-vacancy disorder were not accounted for by theory (since in these calculations the structures remained always ordered with cations and vacancies at fixed positions), so they were the reason for the disagreement between theory and experiment.

In both references [14] and [16], it was suggested that the stoichiometric vacancies play a determinant role on the structural properties of these materials. This would explain why for some of these compounds it is, generally, impossible to determine unequivocally whether they are in an ordered stannite (or famatinite) or in a defect chalcopyrite structure at room temperature. In this respect, Bernard and Zunger [14] discussed a number of possible order–disorder transitions, and even identified two stages of disordering. These disordering transitions are discussed in the next section.

7.5 Vibrational Properties Under Hydrostatic Pressure

Some empirical methods can be also employed in the study of the dynamical properties of materials. Lattice dynamical calculations of DC-AGa_2X_4 (A = Cd, Hg; X = S, Se) compounds were performed by Ohrendorf et al. using a short-range

force model; i.e., an empirical model [39]. The work discusses the problems related with the long range interactions, and how the force parameters, used in the study of vibrational properties, are affected. In what follows, we will concentrate only in the theoretical ab initio studies of the vibrational properties.

The primitive unit cell of tetragonal DC and DS structures contains one formula unit, i.e., 7 atoms. As commented in the two previous chapters, there are 21 normal modes of vibration, of which 3 are acoustic and 18 are optical modes. According to group theory, the irreducible representations of phonon modes at the Γ point for the DC structure are:

$$\Gamma: \quad 3A(\mathrm{R}) \ \oplus \ 6B(\mathrm{R},\mathrm{IR}) \ \oplus \ 6E(\mathrm{R},\mathrm{IR})$$

where R means that the mode is Raman active and IR that it is infrared active. The A modes are non-polar, and the B and E (doubly degenerated) are polar modes. This results in 13 Raman-active modes ($3A \oplus 5B \oplus 5E$), 10 IR-active modes ($5B \oplus 5E$), and 3 acoustic modes ($B \oplus E$). On the other hand, the ordered DS structure (model 1 in Table 5.2) has also 21 phonon modes at the Γ zone center point with the following mechanical representation:

$$\Gamma: \quad 2A_1(\mathrm{R}) \ \oplus \ A_2(\mathrm{R},\mathrm{IR}) \oplus 2B_1(\mathrm{R}) \oplus 4B_2(\mathrm{R},\mathrm{IR}) \ \oplus \ 6E(\mathrm{R},\mathrm{IR})$$

where B_2 and E are polar modes. This gives 12 Raman-active modes ($2A_1 \oplus 2\ B_1 \oplus 3B_2 \oplus 5E$), 8 IR-active modes ($3B_2 \ \oplus 5E$), 3 acoustic modes ($B_2$ and E), and one silent mode A_2. Since polar modes have a LO–TO splitting, this means that the DC structure has 23 Raman-active modes and the DS structure has 20 Raman-active modes.

In 1988, Bernard and Zunger suggested that the vacancies play a determinant role in the structural properties of $A^{II}B_2^{III}X_4^{VI}$ OVCs [14]. In particular, they discussed a number of possible order–disorder transitions and proposed two stages of disordering upon increasing temperature. In the first stage, the two cations A and B mutually substitute for one another; in the second stage, the two cations and the vacancy disorder mutually. Such transitions would explain why for some of these compounds it is generally unequivocally impossible to determine whether they are in an ordered stannite (or famatinite) or in a defect chalcopyrite structure at room temperature.

In 1999, Ursaki et al. used Raman spectroscopy under hydrostatic pressure to investigate the compounds AGa_2X_4 (A = Cd, Zn; X = S, Se) [40]. The compounds with Cd crystallize in the DC structure, whereas those with Zn crystallize in the DS structure (model 6 in Table 5.2 with partial disorder in the cation sublattice). Ursaki et al. proposed that all these compounds undergo the two stages of pressure-induced disordering already proposed by Bernard and Zunger for temperature-induced disordering. They suggested that in the DC compounds the first stage involved a disordering among the Cd and Ga cations (thus leading to the DS structure as commented in [41]). This stage could also occur for the compounds with the DS structure having model 6 in Table 5.2 and [41], where Zn and Ga atoms are already partially disordered, if one considers that both Zn and Ga atoms can become totally disordered to

give the DS structure (model 2 in Table 5.2 and [41]. The first stage of disordering was proposed to be characterized by the tetragonal distortion of the initial structures. In the second stage of disordering, vacancies are involved in the disordering with cations giving rise to a disordered zinc-blende (DZ) structure prior to the phase transition to the Raman-inactive disordered rocksalt (DR) structure. Unfortunately, Raman spectra of the DZ phase have not been found prior to the transition from either DC or DS compounds to the DR phase yet. Therefore, the existence of these two stages of pressure-induced disorder have been recently questioned by the group of Manjón et al. in several papers which support only the existence of the first stage of disorder and the direct transition from the DS structures to the DR phase [38, 42, 43].

In 2001, Fuentes-Cabrera used DFT-LDA calculations to investigate the Raman spectra under hydrostatic pressure of the compounds DC-$CdGa_2X_4$ (X = S, Se) [36]. The LO–TO splitting was not taken into account in this study. The results were subsequently fitted to the polynomial, i.e. $\omega = \omega_0 + aP + bP^2$, where ω is frequency and P is pressure; this is the same polynomial considered by Ursaki et al. [40]. A good agreement was found in the comparison of the experimental and theoretical Raman frequencies at different pressures. This was also true even for the A and E modes, whose changes in width were considered as the signals for the first stage of pressure-induced phase transitions. The agreement of the frequencies at different pressures was surprising because in the theoretical calculations the structures were not disordered at all, whereas Ursaki et al. suggested several order–disorder transitions caused by the two-stages of disordering proposed by Bernard and Zunger. This data along with the theoretical dependence of the band gap with pressure [36] offer one more piece of the puzzle, and could be compared with future experimental studies to settle the argument of whether order–disordering transitions were or not taking place under hydrostatic pressure.

In a subsequent study, Gomis et al. measured and calculated, using ab initio techniques, the optical and vibrational spectra of DC-$CdGa_2Se_4$ under pressure [38]. Raman scattering measurements complemented with the lattice dynamics calculations allowed to assign and to discuss the symmetries of the Raman-active modes up to 22 GPa. In general, a good agreement between experimental and theoretical phonon frequencies was found along the whole pressure range.

Vilaplana et al. performed recently experiments and ab initio DFPT calculations to evaluate the vibrational properties of DC-$ZnGa_2Se_4$, DS-$ZnGa_2Se_4$, DC-$HgGa_2Se_4$, and DC-$HgGa_2S_4$ under pressure [42–44]. Pure B and E modes with TO and LO splitting were obtained which could be compared to experimental values. Tables 7.1, 7.2 show the experimental and theoretical Raman mode frequencies of Raman-active optical modes and the pressure coefficients for DC-$HgGa_2Se_4$ and DC-$HgGa_2S_4$, respectively. Figures 7.1 and 7.2 show the theoretical and experimental Raman-active modes as function of pressure of DS and DC phases of $ZnGa_2Se_4$ respectively. It must be noted that the theoretical DS structure was calculated with the 4d sites occupied by Ga (model 1 in Table 5.2 and [41]) to be compared with the experimental DS structure where Zn and Ga are mixed in 4d sites (model 6 in Table 5.2 and [41]) because of the computationally expensive task of performing calculations of disordered phases

Table 7.1 Experimental and theoretical Raman mode frequencies and their pressure coefficients in DC-HgG_2Se_4 at zero pressure using $\omega(P) = \omega_0 + a_1 P + a_2 P^2$

Mode symmetry	ω_0[a] [cm^{-1}]	a_1^a [$cm^{-1}GPa^{-1}$]	$a_2^a \times 100$ [$cm^{-1}GPa^{-2}$]	ω_0^b [cm^{-1}]	a_1^b [$cm^{-1}GPa^{-1}$]	$a_2^b \times 100$ [$cm^{-1}GPa^{-2}$]
E^1_{TO}	51.1	0.30	−2.3	49.1	0.26	−2.9
E^1_{LO}				53.0	−0.02	−2.2
B^1_{TO}	54.7	1.50	−2.1	49.9	1.73	−2.7
B^1_{LO}				50.9	1.60	−2.3
E^2_{TO}	100.1	0.03	−0.8	94.9	−0.13	
E^2_{LO}				95.0	−0.13	
B^2_{TO}	119.5	0.07	5.9	116.0	−0.10	
B^2_{LO}				119.3	−0.26	
A^1	139.2	4.72	−7.3	126.8	4.53	−5.1
E^3_{TO}	157.8	4.66	−8.5	143.8	4.65	−7.2
E^3_{LO}				150.9	4.54	−6.7
B^3_{TO}	176.4	4.72	−10.6	161.2	4.55	−6.6
B^3_{LO}				169.1	4.86	−7.4
A^2	182.6	4.45	−18.0	165.4	4.00	−6.5
A^3	205.4	2.86	−3.6	185.0	2.97	−2.6
B^4_{TO}	216.3	2.01	0.4	198.6	2.04	0.5
B^4_{LO}				213.9	1.91	−0.2
E^4_{TO}	235.8	4.17	−7.6	215.9	4.71	−7.5
E^4_{LO}				224.8	4.43	−6.4
E^5_{TO}	242.8	4.47	−9.7	232.3	3.61	−3.7
E^5_{LO}	271.5	2.54	−2.85	249.9	3.48	−4.7
B^5_{TO}	272.3	4.90	−5.94	240.4	6.60	−10.3
B^5_{LO}	288.4	3.08	−0.92	252.7	6.07	−9.0

[a] Experimental Raman data
[b] Theoretical calculations

with ab initio techniques. These results are a clear example of how the ab initio calculations can help to identify the different Raman modes and the reasonable agreement between the theoretical data and the experimental results.

7.6 Elastic Properties Under Pressure

The study of the elastic properties of ternary chalcopyrite compounds with ab initio methods was also applied to $A^{II}B_2^{III}X_4^{VI}$ compounds. It must be noted that very few ab initio theoretical studies of elastic properties are available for these materials.

Compounds crystallizing in the DC (I-4) structure belong to the tetragonal Laue group TII. This Laue group contains all crystals with 4, −4 and 4/*m* point groups. In this group there are seven independent elastic constants which are:

Table 7.2 Experimental (exp.) and calculated (th.) Raman-mode frequencies at room pressure and their pressure coefficients in DC-$HgGa_2S_4$ as obtained from fits to the data using ($\omega = \omega_0 + aP$) or ($\omega = \omega_0 + aP + bP^2$) equations

Mode symmetry (th.)	ω_0 (th.) (cm^{-1})	a (th.) ($cm^{-1}GPa^{-1}$)	b (th.) × 100 ($cm^{-1}GPa^{-2}$)	Mode symmetry (exp.)	ω_0 (exp.) (cm^{-1})	a (exp.) ($cm^{-1}GPa^{-1}$)	b (exp.) × 100 ($cm^{-1}GPa^{-2}$)
E^1(TO)	64(1)	−0.14(3)		E^1(TO)	62(1)	0.16(3)	
E^1(LO)	68(1)	−0.3(1)		E^1(LO)	65(1)	0.10(1)	
B^1(TO)	61(1)	1.4(1)		B^1(TO)	61(1)	1.3(5)	
B^1(LO)	62(1)	1.3(1)		B^1(LO)			
E^2(TO)	128(1)	−0.14(4)		E^2(TO)	133(1)	0.04(2)	
E^2(LO)	129(1)	−0.16(3)		E^2(LO)			
B^2(TO)	155(1)	−0.3(1)		B^2(TO)	163(1)	−0.2(1)	
B^2(LO)	162(1)	−0.5(1)		B^2(LO)			
A^1	216(2)	6.6(3)	−8(2)	A^1	220(1)	7.0(1)	−10(2)
E^3(TO)	229(2)	6.0(3)	−10(3)	E^3(TO)	230(2)	6.3(1)	−12(2)
E^3(LO)	236(2)	5.9(3)	−8(2)	E^3(LO)			
B^3(TO)	237(2)	6.1(3)	−9(2)	B^3(TO)			
B^3(LO)	253(2)	5.2(3)	−7(2)	B^3(LO)			
A^2	299(2)	5.0(3)	−7(2)	A^2	300(2)	5.1(1)	−7(1)
B^4(TO)	305(2)	1.8(1)	1.9(1)	B^4(TO)	316(3)	3.0(1)	−2(1)
B^4(LO)	326(2)	3.1(2)	−3(1)	B^4(LO)			
E^4(TO)	307(2)	4.6(2)	−6(2)	E^4(TO)	315(4)	4.9(3)	−7(1)
E^4(LO)	336(2)	3.8(2)	−6(2)	E^4(LO)	341(3)	3.9(2)	−6(1)
A^3	342(2)	3.3(2)	−3(1)	A^3	358(2)	3.7(1)	−6(1)
E^5(TO)	349(2)	3.8(2)	−4(1)	E^5(TO)	360(3)	4.3(2)	−6(1)
E^5(LO)	362(2)	4.0(2)	−5(1)	E^5(LO)	364(3)	3.2(2)	−10(2)
B^5(TO)	364(2)	6.7(3)	−8(2)	B^5(TO)	387(4)	6.1(3)	−9(2)
B^5(LO)	378(2)	6.0(3)	−7(2)	B^5(LO)			

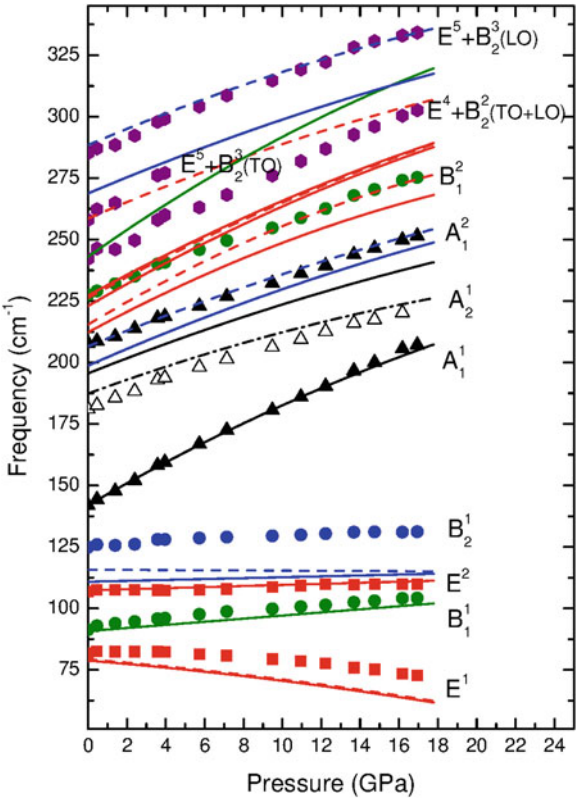

Fig. 7.1 Pressure dependence of the experimental (*symbols*) and calculated (*lines*) vibrational modes in DS-$ZnGa_2Se_4$

C_{11}, C_{12}, C_{13}, C_{33}, C_{44}, C_{66}, and C_{16} [45]. On the other hand, the DS (I-42m) and PC (P-42m) structures belong to the tetragonal Laue group TI, which contains all crystals with 422, 4*mm*, $-42m$ and 4/*mmm* point groups. In this group there are six independent second-order elastic constants which are: C'_{11}, C'_{12}, C'_{13}, C'_{33}, C'_{44}, and C'_{66} [45]. It is possible to transform the seven components C_{ij} of the elastic tensor of a TII crystal into the six components C'_{ij} of the elastic tensor of a TI crystal. For that purpose it is necessary to make C'_{16} equal to zero by means of a rotation around the z axis [46].

Gomis et al. recently performed a theoretical study of the elastic properties of DC-$HgGa_2Se_4$ under pressure [47], using the pseudopotential plane wave method with the GGA PBEsol [48] functional to describe the exchange correlation energy. Table 7.3 shows the set of seven elastic constants C_{ij} obtained at zero pressure together with the two sets of six C'_{ij} obtained after applying the corresponding rotations. The table also includes previous theoretical results for the seven C_{ij} elastic constants of DC-$CdGa_2Se_4$ and DC-$CdGa_2S_4$ [49].

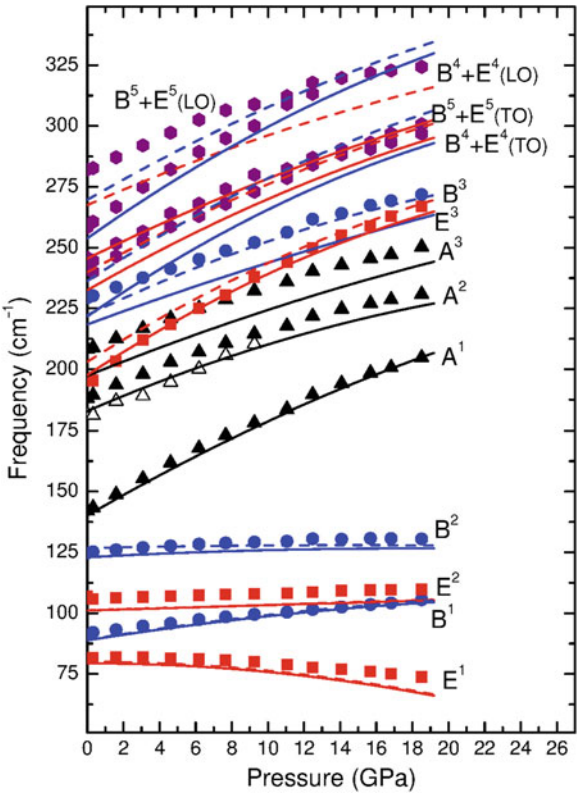

Fig. 7.2 Pressure dependence of the experimental (*symbols*) and calculated (*lines*) vibrational modes in DC-$ZnGa_2Se_4$

From the elastic constants it is possible to obtain, using standard formulas, the bulk modulus, B, and the shear modulus, G, for the tetragonal Laue group TI. Three different approximations are used in order to calculate the bulk and shear modulus, they are know as the Voigt [50], Reuss [51] and Hill [52] approximations, labeled with subscripts *V*, *R*, and *H*, respectively, defined by the following equations:

$$B_V = \frac{2C_{11} + C_{33} + 2C_{12} + 4C_{13}}{9} \tag{7.1}$$

$$B_R = \frac{1}{2S_{11} + S_{33} + 2S_{12} + 4S_{13}} \tag{7.2}$$

$$B_H = \frac{B_V + B_R}{2} \tag{7.3}$$

Table 7.3 The C_{ij} elastic constants (in GPa) for DC-$HgGa_2Se_4$

	DC-$HgGa_2Se_4$	DC-$CdGa_2Se_4$[a]	DC-$CdGa_2S_4$[a]
C_{11}	54.2	52.5	61.8
C_{12}	24.3	20.4	24.7
C_{13}	31.2	38.8	35.7
C_{33}	55.5	60.0	50.0
C_{44}	29.9	31.6	33.9
C_{66}	26.2	16.0	27.0
C_{16}	−0.3	−1.9	−2.7
C'_{11}	54.2[b], 65.5[c]		
C'_{12}	24.3[b], 13.0[c]		
C'_{13}	31.2[b], 31.2[c]		
C'_{33}	55.5[b], 55.5[c]		
C'_{44}	29.9[b], 29.9[c]		
C'_{66}	26.2[b], 14.9[c]		
B_V, B_R, B_H	37.5, 37.2, 37.4	36.1[d]	58.4[d]
G_V, G_R, G_H	22.3, 18.8, 20.6		
Y_V, Y_R, Y_H	55.9, 48.4, 52.2		
ν_V, ν_R, ν_H	0.25, 0.28, 0.27		
$B_V/G_V, B_R/G_R, B_H/G_H$	1.68, 1.98, 1.81		
A	1.75[c], 0.57[d]		

The set of elastic C'_{ij} constants (after rotation for two different angles) are also given. The elastic moduli B, G, and Y (in GPa) and Possion's ratio (ν) are given in the Voigt, Reuss and Hill approximations. The B/G ratio and the shear anisotropy factor (A) are also given

[a] C_{ij} data from [48]

[b,c] Rotation angle of $\phi_\kappa = 0.76°$ and $\phi_\gamma = 45.76°$, respectively

[d] Obtained for B_R a value 40.6 GPa from the C_{ij} data from [48]

$$G_V = \frac{2C_{11} + C_{33} - C_{12} - 2C_{13} + 6C_{44} + 3C_{66}}{15} \tag{7.4}$$

$$G_R = \frac{15}{8S_{11} + 4S_{33} - 4S_{12} - 8S_{13} + 6S_{44} + 3S_{66}} \tag{7.5}$$

$$G_H = \frac{G_V + G_R}{2} \tag{7.6}$$

where S_{ij} are the components of the elastic compliance tensor (the inverse of the elastic constants tensor).

Other interesting elastic quantities are the Young modulus (Y) and the Poisson's ratio (ν) defined by:

$$Y_Z = \frac{9B_Z G_Z}{G_Z + 3B_Z} \tag{7.7}$$

$$\nu_Z = \frac{1}{2}\left(\frac{3B_Z - 2G_Z}{3B_Z + G_Z}\right) \tag{7.8}$$

where the subscript Z refers to the symbols V, R, and H, respectively. Table 7.3 reports the values obtained of the B, G, and Y for DC-$HgGa_2Se_4$ at zero pressure in the three approximations. The bulk modulus $B_H = 37.4$ GPa is in very good agreement with the value of $B_0 = 36.0$ GPa obtained from a third order Birch-Murnaghan EOS [53].

Table 7.3 includes the values of the ratio between the bulk and shear modulus, B/G, and the shear anisotropy factor A. According to the Pugh criterion [54], a B/G value above 1.75 indicates a tendency for ductility; otherwise, the material behaves in a brittle manner. The value of B/G = 1.81 indicates that the material should behave in a ductile manner. The shear anisotropy factor A for the tetragonal cell is defined as $A = 2C_{66}/(C_{11} - C_{12})$. If A is equal to one, no anisotropy exists. On the other hand, the more this parameter differs from one, the more elastically anisotropic is the crystalline structure. In this case the material shows an anisotropic behavior.

As mentioned previously, the elastic constants allow the study of the mechanical stability of the system. A lattice is mechanically stable only if the elastic energy change associated with an arbitrary deformation given by small strains is positive for any small deformation [55]. It means that the principal minors of the determinant with elements C_{ij} are all positive [56]. This is known as the Born stability criteria. For the case of a tetragonal crystal with six C_{ij} elastic constants, the mechanical stability at zero pressure requires that:

$$C_{11} > 0, \quad C_{44} > 0, \quad C_{66} > 0, \quad C_{11} - C_{12} > 0 \tag{7.9}$$

and

$$C_{11}C_{33} + C_{12}C_{33} - 2C_{13}^2 > 0 \tag{7.10}$$

DC-$HgGa_2Se_4$ at zero pressure satisfies the Born stability criteria and the crystal is mechanically stable at zero pressure [47]. Similarly, Ma et al. obtained the seven theoretical elastic constants at equilibrium pressure of DC-$CdGa_2S_4$ and DC-$CdGa_2Se_4$ using the pseudopotential plane wave method and the GGA approximation to describe the exchange correlation potential [49]. They concluded that also both compounds are mechanically stable at zero pressure.

To analyze the mechanical stability of a structure at high pressure it is necessary to study the evolution of the elastic constants as pressure increases and modify the Born stability criteria. The generalized Born stability criteria valid for the tetragonal crystal under an external hydrostatic pressure P take the form [56]:

$$C_{11} - P > 0, \quad C_{44} - P > 0, \quad C_{66} - P > 0, \tag{7.11}$$

$$C_{11} - C_{12} - 2P > 0 \tag{7.12}$$

$$(C_{33} - P)(C_{11} + C_{12}) - 2(C_{13} + P)^2 > 0 \tag{7.13}$$

The study of the mechanical stability of DC-$HgGa_2Se_4$ under pressure by Gomis et al. [47] concluded that the tetragonal phase becomes mechanically unstable beyond

Table 7.4 Theoretical and experimental cell parameters and Wyckoff positions of PC-$CdIn_2Se_4$ at zero pressure

	Theory			Experiment [58]		
a (Å)	5.7763			5.8151		
c (Å)	5.9042			5.80		
Wyckoff positions	x	y	z	X	y	z
Cd *(1a)*	0	0	0	0	0	0
In *(2f)*	0.5	0	0.5	0.5	0	0.5
Se *(4n)*	0.2776	0.2776	0.2281	0.2707	0.2707	0.230

13.3 GPa. Experimentally, this pressure is consistent with the pressure at which dark linear effects appear in optical absorption experiments.

7.7 Theoretical Study of $CdIn_2Se_4$ in the Pseudo-Cubic Phase

In order to illustrate how ab initio methods allow the study of OVCs in a predictive way, we present a theoretical study of PC-$CdIn_2Se_4$ under pressure [57]. This material has not been studied experimentally under pressure. Structural studies on polytypes of $CdIn_2Se_4$ have been reported by Ivaschchenko et al. [58], that include the tetragonal PC phase at zero pressure.

In the tetragonal PC structure, the primitive unit cell contains one formula unit; i.e., 7 atoms. Cd atoms are located at *2a* Wickoff positions, In atoms at *2f* positions, and Se atoms at *4n* positions (x, y, z) with x = y. Therefore, in this structure there are there are two free lattice parameters (a = b, c) and two internal atomic positions of Se atoms (see Table 7.4). Alternatively, the PC phase is characterized by one external parameter *c/a*, and two internal parameters, x and z.

Total-energy ab initio simulations have been performed within DFT framework as implemented in the Vienna ab initio simulation package (VASP) [59, 60] (and references therein). The program performs ab initio structural calculations with the plane-wave pseudo-potential method. The set of plane waves employed extended up to a kinetic energy cutoff of 370 eV in order to achieve highly converged results within the projector-augmented-wave (PAW) scheme [60, 61]. The PAW method takes into account the full nodal character of the all-electron charge density distribution in the core region. The exchange-correlation energy was treated with the GGA-PBEsol functional [48]. It is well known that the GGA approach typically underestimates the cohesion energy [5] (in turn producing an overestimation of the equilibrium volume). We used dense special point grids appropriate to the structure considered to sample the Brillouin zone (BZ), thus ensuring a high convergence of 1–2 meV per formula unit in the total energy of each structure as well as an accurate calculation of the forces on the atoms. At each selected volume, the structures were fully relaxed through the calculation of the forces on atoms and the stress tensor [5]. It means that

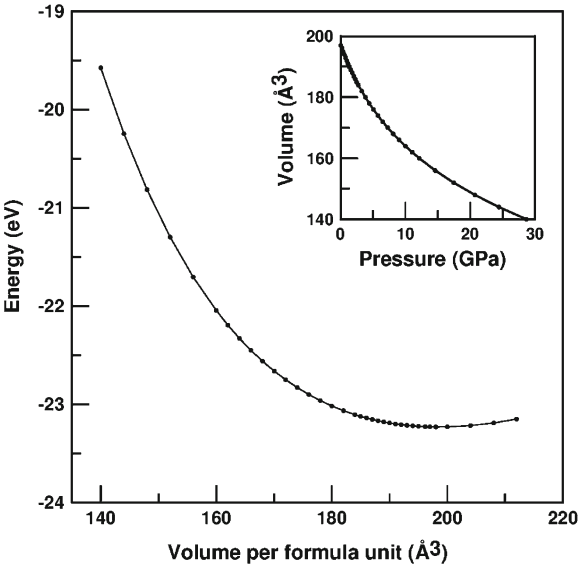

Fig. 7.3 Theoretical E(V) and V(P) data for PC-$CdIn_2Se_4$

for a select volume, V, we obtain the theoretical E(V) and P(V) at the same time but independently. The equilibrium volume, V_0, corresponds to the relaxed theoretical equilibrium (the V with lower E and P = 0) configuration. The forces were smaller than 0.006 eV/Å, and the deviation of the stress tensor, from a diagonal hydrostatic form was less than 0.1 GPa in all the relaxed volumes.

Table 7.4 reports the calculated structural parameters at equilibrium, except for the typical overestimation of the GGA approach the theoretical results compare quite well with the available experimental parameters. Figure 7.3 shows the calculated energy versus volume data, the inset also shows the calculated evolution of volume with increasing pressure. These data are fitted with a Birch–Murnaghan 4th order EOS [53]. Values of bulk modulus and pressure derivatives are $B_0 = 33.2$ GPa, $B'_0 = 4.7$ and $B''_0 = 0.4 \times 10^{-3}$. Figure 7.4 shows the pressure evolution of the calculated lattice parameters and *c/a* ratio. The axial compressibility for *a* and *c* axes at zero pressure are calculated as $\kappa_x = \frac{-1}{x}\frac{\partial x}{\partial p}$. We obtain $\kappa_a = 5.7 \times 10^{-3}\,\mathrm{GPa}^{-1}$, and $\kappa_c = 9.9 \times 10^{-3}\,\mathrm{GPa}^{-1}$, these values show an anisotropic compressibility, being *c* the most compressible axis according to our calculations.

Lattice-dynamics calculations of phonon modes were performed at the zone center (Γ point) of the BZ with the direct force-constant approach without the inclusion of electric field effects [10]. These calculations provide information about the symmetry of the modes and their polarization vectors, and allow us to identify the irreducible representations and the character of the phonon modes at the Γ point.

According to group theory, the PC structure of $CdIn_2Se_4$ has 21 phonon modes at Γ with the mechanical representation [41]:

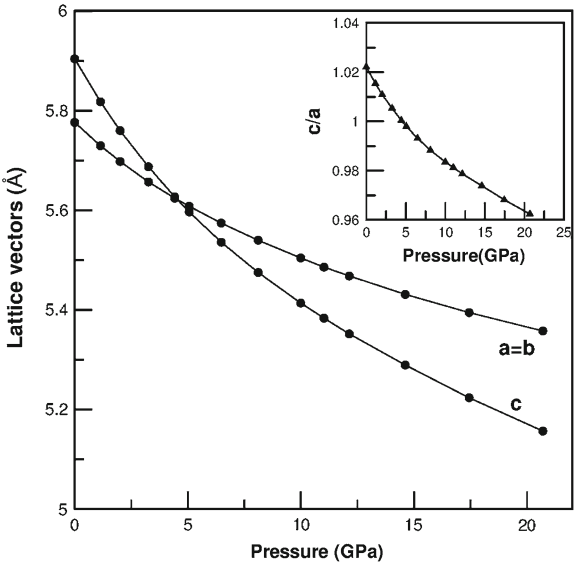

Fig. 7.4 Pressure dependence of the theoretical lattice paremeters a, c and *c/a* of PC-$CdIn_2Se_4$

$$\Gamma = 2A_1(\mathrm{R}) \oplus 2A_2 \oplus B_1(\mathrm{R}) \oplus 4B_2(\mathrm{R, IR}) \oplus 6E(\mathrm{R, IR})$$

where A_1 and B_1 are non-polar modes, A_2 are silent modes, and B_2 and E are polar modes, being E modes doubly degenerated. This results in a total of 16 Raman-active modes ($2A_1 \oplus B_1 \oplus 3B_2 \oplus 5E$) and 13 IR-active modes ($3B_2 \oplus 5E$) since one B_2 and one E are acoustic modes. Table 7.5 summarizes the symmetries of the phonons along with their frequencies and pressure derivatives. The results were subsequently fitted to the polynomial $\omega(P) = \omega_0 + \mathrm{a} \cdot P + \mathrm{b} \cdot P^2$, where P is the pressure, ω_0 is the zero pressure frequency, and a and b are the first-order and second-order pressure coefficients. Figure 7.5 shows the total Phonon density of states (DOS) and the projected phonon density of states (PDOS) for each atom. The modes are located in two frequency regions, one from 0–120 cm^{-1}, and the other from 130–230 cm^{-1}, clearly separated by a phonon-gap. The main contribution to vibrations above 130 cm^{-1} comes from the Se atom, due to the lower mass of this atom. Figure 7.6 shows the pressure evolution of the calculated phonon modes. A dynamical instability appears around 18 GPa because both the silent A_2 mode and the E mode with lowest frequency become negative. The softening of these modes could be the fingerprint of a phase transition around that pressure which is similar to the phase transition pressures found in other OVCs of the AB_2X_4 family (see Chaps. 5 and 6 of this book).

We include the effect of the electric field in our calculations by means of the Born-effective charge tensor, and the dielectric constant calculated from ab initio. As already commented, this procedure allows us to include the non-analytical term at the Γ point and to calculate the LO–TO splitting of the polar modes B_2 and E.

Table 7.5 Theoretical frequencies of Raman, Infrared and silent modes and pressure coefficients of PC-$CdIn_2Se_4$ as obtained from fits to the data using $\omega = \omega_0 + aP + bP^2$ equation

Mode symmetry	ω_0 (cm^{-1})	a ($cm^{-1}GPa^{-1}$)	b ($cm^{-1}GPa^{-2}$)
E(RI)	49.50	−0.77[a]	−0.051[a]
A_2	52.10	−1.24[b]	−0.043[b]
B_2(RI)	65.75	−0.26	−0.017
E (RI)	77.92	−0.41	0.005
A_1 (R)	138.50	4.78	−0.044
B_2 (RI)	160.05	3.86	−0.058
E (RI)	175.80	3.20	−0.024
E (RI)	179.17	4.53	−0.066
A_1 (R)	183.33	3.58	−0.053
B_1 (R)	183.33	3.32	−0.033
E (RI)	206.05	4.39	−0.058
A_2	206.22	4.15	−0.052
B_2 (RI)	210.89	2.89	−0.029

[a] Fit up to 18 GPa
[b] Fit up to 14 GPa

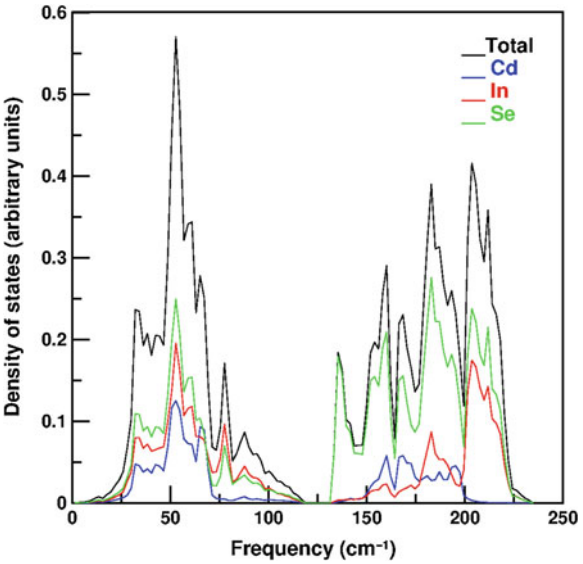

Fig. 7.5 Calculated phonon total density of states (DOS) and atom projected DOS of PC-$CdIn_2Se_4$

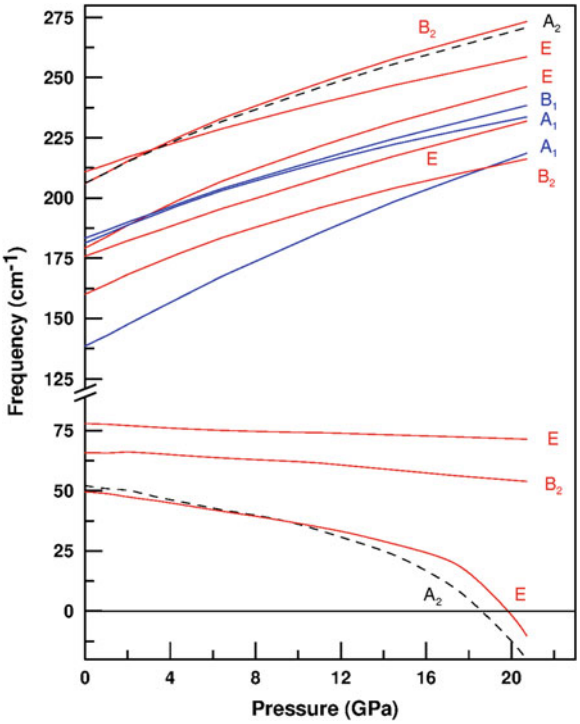

Fig. 7.6 Pressure dependence of the theoretical Raman, IR and silent modes of PC-$CdIn_2Se_4$

Figure 7.7 displays the phonon dispersion at zero pressure of PC-$CdIn_2Se_4$, showing the LO–TO splitting of the different modes at the Γ point.

Finally, we have studied the elastic properties of PC-$CdIn_2Se_4$. As already commented, the PC structure has six independent second-order elastic constants which are: C_{11}, C_{12}, C_{13}, C_{33}, C_{44}, and C_{66}. Table 7.6 reports the calculated values of the C_{ij} elastic constants as well as the shear modulus, G, the Young modulus, Y, the Poisson's ratio (ν), and other calculated elastic parameters (see (7.1–7.8)). We obtain a bulk modulus of 34.5 GPa, a shear modulus G_v of 18.76 GPa and a Young modulus Y_v of 47.7 GPa. Note that the reported B_v bulk modulus obtained from the elastic constants 34.8 GPa, agrees with the B obtained from the Birch–Murnaghan 4th EOS fit [53], this gives confidence to our elastic constants calculation. The ratio between bulk modulus and shear modulus (B/G = 1.86) indicates that the compound is ductile according to the Pugh criteria. The shear anisotropy factor (A = 3.6) is clearly different of one, thus indicating a clear anisotropy of this compound.

At zero pressure the Born stability criteria are fulfilled for PC-$CdIn_2Se_4$and the crystal is mechanically stable. Figure 7.8 shows the pressure evolution of the C_{ij} elastic constants. C_{11}, C_{12}, C_{33}, and C_{13} increase monotonically as pressure increase, whereas C_{44} and C_{66} increase with pressure up to 10 and 5 GPa, respectively, and then

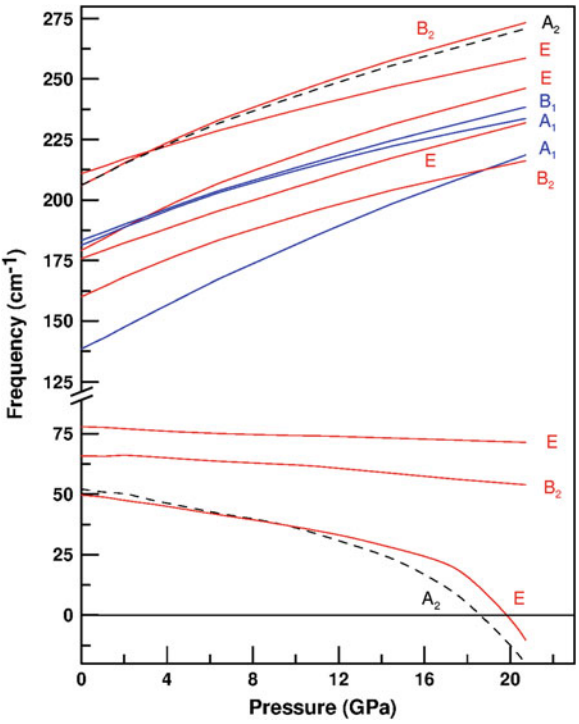

Fig. 7.7 Theoretical phonon dispersion at zero pressure for PC-$CdIn_2Se_4$ (LO-TO splitting at Γ point is included)

decrease as pressure increase. These results allow us to study the mechanical stability under pressure. The generalized Born criteria of this compound under pressure are represented in Fig. 7.9. It is clear that above 11 GPa two of the generalized Born criteria, defined by (7.12) and (7.13), are violated; therefore, the system becomes mechanically unstable above this pressure. This pressure is similar to the pressure for which the calculated elastic constant C_{44} begins to decrease, but lower than the pressure at which the dynamic instability appears. It remains to be checked experimentally if the different pressures for mechanic and dynamic instability of PC-$CdIn_2Se_4$ could be related to the occurrence of phase transitions and to the appearance of dark linear defects which are precursors of the phase transition to an opaque metallic phase as the DR phase observed in several OVCs.

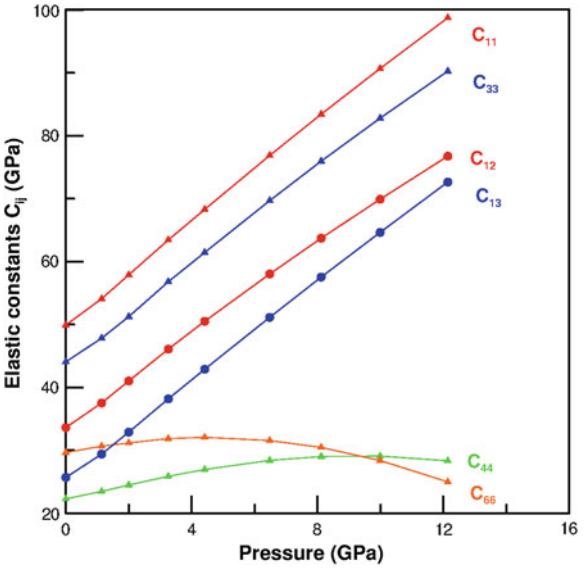

Fig. 7.8 Calculated pressure evolution of the C_{ij} elastic constants of PC-$CdIn_2Se_4$

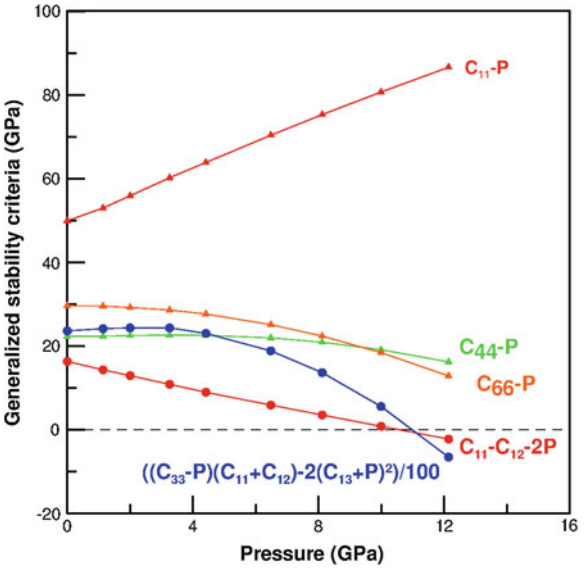

Fig. 7.9 Generalized Born stability criteria as function of pressure for PC-$CdIn_2Se_4$

Table 7.6 Elastic constants C_{ij} (in GPa) for PC-$CdIn_2Se_4$. Bulk (B_v), shear (G_v), and Young (Y_v) moduli (in GPa), Poisson's ratio (ν_v), B_v/G_v ratio, and shear anisotropy factor (A_v) are also given in the Voigt approximation

C_{11}	C_{33}	C_{44}	C_{66}	C_{12}	C_{13}	B_v	G_v	E_v	ν_v	B_v/G_v	A_v
49.9	44.1	22.3	29.6	33.6	25.7	34.5	18.8	47.7	0.27	1.86	3.64

7.8 Conclusions

In this chapter we have made an overview of the electronic, elastic, and vibrational properties of the OVCs of the AB_2X_4 (X = S, Se) family under pressure from a theoretical point of view. *First principles* (also known as ab initio) calculations are a powerful complement to experimental results. These studies can predict many properties of the materials under extreme conditions that sometimes are not available from experiments. Although theoretical studies are scarce, e.g. there is no work published on OVCs with X = Te, they may help to elucidate some controversy on the structural, electronic, elastic, and vibrational properties under pressure. We also presented a theoretical study of the pseudo-cubic $CdIn_2Se_4$ under pressure, where no experimental data under pressure are available. We hope this overview will encourage further studies that cover the lack of data on OVCs under pressure.

References

1. Hohenberg P, Kohn W (1964) Inhomogenous electron gas. Phys Rev 136:B864–B871
2. Kohn W, Sham LJ (1965) Self-consistent equations including exchange and correlation effects. Phys Rev 140:A1133–A1138
3. Payne MC, Teter MP, Allan DC, Arias TA, Joannopoulos JD (1992) Iterative minimization techniques for ab initio total-energy calculations: molecular dynamics and conjugate gradients. Rev Mod Phys 64:1045–1097
4. Martin RM (2004) Electronic structure: basic theory and practical methods. Cambridge University Press, New York
5. Mujica A, Rubio A, Muñoz A, Needs RJ (2003) High pressure phase of group-IV, III-V, and II-VI compounds. Rev Mod Phys 75:863–912
6. Nielsen OH, Martin RM (1983) First-principles calculations of stress. Phys Rev Lett 50:697–700
7. Pickard CJ, Needs RJ (2011) Ab initio random structure searching. J Phys:Condens Matter 23: 053201(23)
8. Oganov A, Ma YM, Lyakhov AO, Valle M, Gatti C (2010) Evolutionary crystal structure prediction as a method for the discovery of minerals and materials, in theoretical and computational methods in mineral physics: geophysical applications. In: Wentzcovitch R, Stixrude L (eds) Reviews in mineralogy & geochemistry, vol 71. New York, McGraw-Hill, pp 271–298
9. Baroni S, de Gironcoli S, Dal Corso A, Gianozzi P (2001) Phonons and related crystal properties from density-functional perturbation theory. Rev Mod Phys 73:515(48)
10. Parlinski K (1999) Calculation of phonon dispersion curves by the direct method. In: Johnson MR, Kearley GJ, Buttner HG (eds) Neutrons and numerical methods-n(2)m. AIP conference proceedings, vol 479. New Yorks, AIP, pp 121–126

11. Alfe D (2009) PHON: a program to calculate phonons using the small displacement method. Comp Phys Commun 180:2622–2633
12. Bhosale J, Ramdas AK, Burger A, Muñoz A, Romero AH, Cardona M, Lauck R, Kremer RK (2012) Temperature dependence of band gaps in semiconductors:electron–phonon interaction. Phys Rev B 86:195208(10)
13. Georgobiani AN, Radaustan SI, Tiginyanu IM (1985) Wide-gap $A(II)B(III)_2C(VI)_4$ semiconductors—optical and photoelectric properties, and potential applications (review). Sov Phys Sem (USSR) 19:121–132
14. Bernard JE, Zunger A (1988) Ordered-vacancy-compound semiconductors:pseudocubic $CdIn_2Se_4$. Phys Rev B 37:6835–6856
15. Fahy S, Chang KJ, Louie SG, Cohen ML (1987) Pressure coefficients of band-gaps of diamond. Phys Rev B 35:5856–5859
16. Baldereschi A, Meloni F, Aymerich F, Mula G (1977) Electronic properties of defect-Zincblende semiconductor $CdIn_2Se_4$. Solid State Commun 21:113–116
17. Marinelli M, Depascale T, Meloni F, Mula G, Serra M, Baroni S (1989) Theoretical-study of cubic versus tetragonal structures of defect Zincblende semiconductors—$CdIn_2Se_4$. Phys Rev B 40:1725–1731
18. Jiang XS, Lambrecht WRL (2004) Electronic band structure of ordered vacancy defect chalcopyrite compounds with formula $II\text{-}III_2\text{-}VI_4$. Phys Rev B 69:035201(8)
19. Mishra S, Ganguli B (2011) Electronic and structural properties of a Al_2Se_4 (A=Ag, Cu, Cd, Zn) chalcopyrite semiconductors. J Solid State Chem 184:1614–1621
20. Fuentes-Cabrera M, Sankey OF (2001) Theoretical study of the ordered-vacancy semiconducting compound $CdAl_2Se_4$. J Phys: Condens Matter 13:1669–1684
21. Perdew JP, Zunger A (1981) Self-interaction correction to density-functional approximations for many-electron systems. Phys Rev B 23:5048–5079
22. Perdew JP (1991) Generalized gradient approximations for exchange and correlation—a look backward and forward. Physica B 172:1–6
23. Fritsche L, Gu YM (1993) Band gaps in a generalized density-functional theory. Phys Rev B 48:4250–4258
24. Ouahrani T, Reshak AH, Khenata R, Amrani B, Mebrouki M, Otero-de-la-Roza A, Luana V (2010) Ab-initio study of the structural, linear and nonlinear optical properties of $CdAl_2Se_4$ defect-chalcopyrite. J Solid State Chem 183:46–51
25. Engel E, Vosko SH (1993) Exact exchange-only potentials and the virial relation as microscopic criteria for generalized gradient approximations. Phys Rev B 47:13164–13174
26. Verma UP, Singh P, Jensen P (2012) Pressure and temperature induced structural, electronic and thermal properties of $CdAl_2Se_4$. Solid State Commun 152:624–629
27. Perdew JP, Burke K, Ernzerhof M (1996) Generalized gradient approximation made simple. Phys Rev Lett 77:3865–3868
28. Verma UP, Singh P, Jensen P (2011) A study of the electronic, optical and thermal properties for $ZnAl_2Se_4$ using the FP-LAPW method. Phys Stat Solidi B 248:1682–1689
29. Jiang X-S, Yan Y-C, Yuan S-M, Mi S, Niu Z-G, Lian J-Q (2010) Trends in the band-gap pressure coefficients and bulk moduli in different structures of $ZnGa_2S_4$, $ZnGa_2Se_4$, and $ZnGa_2Te_4$. Chin Phys B 19:107104(7)
30. Ouahrani T, Khenata R, Lasri B, Reshak AH, Bouhemadou A, Bin-Omran S (2012) First and second harmonic generation of the XAl_2Se_4 (X = Zn, Cd, Hg) defect chalcopyrite compounds. Physica B 407:3760–3766
31. Singh P, Verma UP, Jensen P (2011) Electronic and optical properties of defect chalcopyrite $HgAl_2Se_4$. J Phys Chem Solids 72:1414–1418
32. Reshak AH, Khenata R, Kityk IV, Plucinski KJ, Auluck S (2009) X-ray photoelectron spectrum and electronic properties of a noncentrosymmetric chalcopyrite compound $HgGa_2S_4$: LDA, GGA, and EV-GGA. J Phys Chem B 113:5803–5808
33. Lavrentyev AA, Gabrelian BV, Dubeiko VA, Nikiforov IY, Rehr JJ (2002) Experimental and theoretical X-ray K spectra of sulfur of zincblende-based compounds $AgGaS_2 - CdGa_2S_4 - InPS_4$. J Phys Chem Solids 63:227–231

34. Lavrentyev AA, Gabrelian BV, Nikiforov IY, Rehr JJ, Ankudinov AL (2003) Ab initio calculations of the electron structure of the compounds $AgGaS_2$, $CdGa_2S_4$, $InPS_4$. J Phys Chem Solids 64:1251–1255
35. Lavrentyev AA, Gabrelian BV, Nikiforov IY, Parasyuk OV, Khyzhun OY (2009) Electronic structure of cadmium selenogallate $CdGa_2Se_4$ as studied using ab initio calculations and X-ray photoelectron spectroscopy. J Alloys Comp 481:28–34
36. Fuentes-Cabrera M (2001) Ab initio study of the vibrational and electronic properties of $CdGa_2S_4$ and $CdGa_2Se_4$ under pressure. J Phys: Condens Matter 13:10117–10124
37. Manjón FJ, Gomis O, Rodríguez-Hernández P, Pérez-González E, Muñoz A, Errandonea D, Ruiz-Fuertes J, Segura A, Fuentes-Cabrera M, Tiginyanu IM, and Ursaki VV (2010) Nonlinear pressure dependence of the direct band gap in adamantine ordered-vacancy compounds. Phys Rev B 81:195201(7)
38. Gomis O, Vilaplana R, Manjón FJ, Pérez-González E, López-Solano J, Rodríguez-Hernández P, Muñoz A, Errandonea D, Ruiz-Fuertes J, Segura A, Santamaría-Pérez D, Tiginyanu IM, Ursaki VV (2012) High-pressure optical and vibrational properties of $CdGa_2Se_4$: order–disorder processes in adamantine compounds. J Appl Phys 111:013518(15)
39. Ohrendorf FW, Haeuseler H (1995) Lattice dynamical calculations on compounds crystallizing in a Thiogallate-type structure. J Solid State Chem 114:442–450
40. Ursaki VV, Burlakov II, Tiginyanu IM, Raptis YS, Anastassakis E, Anedda A (1999) Phase transitions in defect chalcopyrite compounds under hydrostatic pressure. Phys Rev B 59:257–268
41. Manjón FJ, Gomis O, Vilaplana R, Sans JA, Ortiz HM (2013) Order–disorder processes in adamantine ternary ordered-vacancy compounds. Phys Stat Sol B (in press). doi:10.1002/pssb.201248596
42. Vilaplana R, Robledillo M, Gomis O, Sans JA, Manjón FJ, Pérez-González E, Rodríguez-Hernández E, Muñoz A, Tiginyanu IM, Ursaki VV (2013) Vibrational study of $HgGa_2S_4$ under high pressure. J Appl Phys 113:093512(10)
43. Vilaplana R, Gomis O, Manjón FJ, Ortiz H, Pérez-González E, Ortiz HM, Rodríguez-Hernández P, Muñoz A, Errandonea D, Ursaki VV, Tiginyanu IM (2013) Lattice dynamics study of $HgGa_2Se_4$ at high pressures (to be published)
44. Vilaplana R, Gomis O, Pérez-González E, Ortiz HM, Manjón FJ, Rodríguez-Hernández P, Muñoz A, Alonso-Gutiérrez P, Sanjuán ML, Ursaki VV, Tiginyanu IM (2013) Thermally activated cation ordering in $ZnGa_2Se_4$ single crystals studied by Raman scattering, optical absorption, and ab initio calculations. J Phys: Condens Matt 25:165802(11)
45. Nye JF (1957) Physical properties of crystals: their representation by tensors and matrices. Oxford University Press, Oxford
46. Farley JM, Saunders GA, Chung DY (1973) Elastic-constants of strontium molybdate. J Phys C: Solid State Phys 6:2010–2019
47. Gomis O, Vilaplana R, Manjón FJ, Santamaría-Perez D, Errandonea D, Pérez-González E, López-Solano J, Rodríguez-Hernández P, Muñoz A, Tiginyanu IM, Ursaki VV (2013) High-pressure study of the structural and elastic properties of defect-chalcopyrite $HgGa_2Se_4$. J Appl Phys 113:073510(10)
48. Perdew JP, Ruzsinszky A, Csonka GI, Vydrov OA, Scuseria GE, Constantin LA, Zhou X, Burke K (2008) Restoring the density-gradient expansion for exchange in solids and surfaces. Phys Rev Lett 100:136406(4)
49. Ma S-H, Jiao Z-Y, Zhang X-Z (2012) Structural, elastic, electronic, and optical properties of defect-chalcopyrite structure $CdGa_2X_4$ (X = S, Se) compounds. J Matt Sci 47:3849–3854
50. Voigt W (1928) Lehrbuch der Kristallphysics. Teubner, Leipzig
51. Reuss A, Anew Z (1929) Account of the liquid limit of mixed crystals on the basis of the plasticity condition for single crystal. Angew Math Mech 9:49–58
52. Hill R (1952) The elastic behavior of a crystalline aggregate. Proc Phys Soc London, Sect A 65:349–355
53. Birch F (1947) Finite elastic strain of cubic crystals. Phys Rev 71:809–824

54. Pugh SF (9154) Relations between the elastic moduli and the plastic properties of polycrystalline pure metals. Philos Mag 45:823–843
55. Born M, K'un H (1954) Dynamical theory of crystal lattices. Oxford UniversityPress, Oxford
56. Wallace DC (1972) Thermodynamics of crystals. Wiley, New York
57. Muñoz A, Rodriguez-Hernández P (2o13) Theoretical Ab Initio Calculations in Ordered Vacancy Compounds at High Pressures. In: Manjon FJ, Tiginyanu IM, UrsakiVV (ed) Pressure-Induced Phase Transitions in AB_2X_4 Chalcogenides Compounds, Springer Series in Materials Science, Springer-Verlag Berlin Heidelberg
58. Ivaschchenko IA, Aksel'rud LG, Olekseyuk ID, Zmii OF (2004) Ukrains'kii Khimicheskii Zhurnal (Russian Edition) 70:67–71
59. Kresse G, Furthmuller J (1996) Efficient iterative schemes for ab initio total-energy calculations using a plane-wave basis set. Phys Rev B 54:11169–11186
60. Kresse G, Joubert D (1999) From ultrasoft pseudopotentials to the projector augmented-wave method. Phys Rev B 59:1758–1775
61. Blochl PE (1994) Projector augmented-wave method. Phys Rev B 50:17953–17979

Part III
AB_2X_4 Chalcogenide Compounds with Other Types of Structures

Chapter 8
AB_2X_4 Compounds with Other Types of Structures at High Pressures

V. V. Ursaki and I. M. Tiginyanu

Abstract Phase transitions in $A^{II}B_2^{III}X_4^{VI}$ compounds with initial structures different from cubic spinel or tetragonal chalcopyrites and stannites are analyzed in this chapter on the instance of layered $A^{II}InGaS_4$ crystals with Cd, Zn, and Mg as A^{II} cations as well as on the instance of the Zn–Al–S system which provides an initial wurtzite structure in addition to the spinel structure. Apart from that, it is shown that even the behavior of the $ZnAl_2S_4$ with spinel structure under pressure is different from that of $M^{II}In_2S_4$ (M = Cd, Mg, Mn) spinel in the sense that a reversible transition to a structure similar to that of calcium ferrite ($CaFe_2O_4$) occurs instead of a phase transition to a variant of NaCl-type structure. It is also shown that quaternary solid solutions $ZnAl_{2(1-x)}Ga_{2x}S_4$ obtained by adding gallium atoms to the system demonstrate a systematics of phase transitions different from that inherent to $A^{II}B_2^{III}X_4^{VI}$ compounds with chalcopyrite, stannite, and spinel structure.

Keywords Hydrostatic pressure · Phase transition · Wurtzite · Spinel · Layered compounds · Rocksalt-type structure · Solid solution · Raman scattering · Phonon spectrum

8.1 A Comparison of Pressure Induced Phase Transitions in Wutrzite and Spinel Phases of the $ZnAl_2S_4$ Compound

$ZnAl_2S_4$ is a very interesting material for the purpose of investigating phase transitions in ternary compounds, since it can be obtained in different structural modifi-

V. V. Ursaki (✉)
Institute of Applied Physics, Academy of Sciences of Moldova, Chisinau, Moldova
e-mail: ursaki@yahoo.com

I. M. Tiginyanu
Institute of Electronic Engineering and Nanotechnologies, Academy of Sciences of Moldova, Chisinau, Moldova
e-mail: tiginyanu@gmail.com

F. J. Manjón et al. (eds.), *Pressure-Induced Phase Transitions in AB_2X_4 Chalcogenide Compounds*, Springer Series in Materials Science 189,
DOI: 10.1007/978-3-642-40367-5_8,

cations, depending on growth temperature [1–4]. Three phases exist in the region of low growth temperatures (700–900 °C), namely, the spinel structure (α-phase), the wurtzite-type structure with a statistical distribution of the cations, called *w*-phase, and the layered structure with a hexagonal lattice, called the *L*- or γ′-phase. At high growth temperatures (1050–1100 °C) an orthorhombic β-phase and a rhombohedral γ-phase can be obtained. Furthermore, quaternary solid solutions $ZnAl_{2(1-x)}Ga_{2x}S_4$ (obtained by adding gallium atoms to the Zn–Al–S system) crystallize in a defect chalcopyrite (DC) structure [5]. In this chapter the results of a structural study of (α- and *w*-type phases of) $ZnAl_2S_4$ under hydrostatic pressure up to 300 kbar are presented.

α- and *w*-phase $ZnAl_2S_4$ crystals were grown by the chemical transport method, with iodine used as transport agent. For the α-phase, the temperatures at the charge and growth zones were 850 and 750 °C, respectively. The spinel structure of the single crystals was confirmed through X-ray analysis, with a lattice parameter of 10.01 Å [6]; *w*-phase crystals were obtained when the growing temperature was 50 °C lower than that for α-phase. Two types of *w*-$ZnAl_2S_4$ crystals were grown, one with full stoichiometry and a second one with about 10 % of the Zn atoms substituted by Cd atoms. According to the X-ray analysis, both types of *w*-$ZnAl_2S_4$ crystals possess a random distribution of cations and stoichiometric vacancies among the possible tetrahedral sites of the lattice, with unit cell parameters a = 3.76 and c = 6.15 Å [3].

There are five Raman active modes (A_{1g}, E_g, $3T_{2g}$) in the normal spinel structure. Figure 8.1a shows the unpolarized Raman spectra of α-$ZnAl_2S_4$ at various pressures.

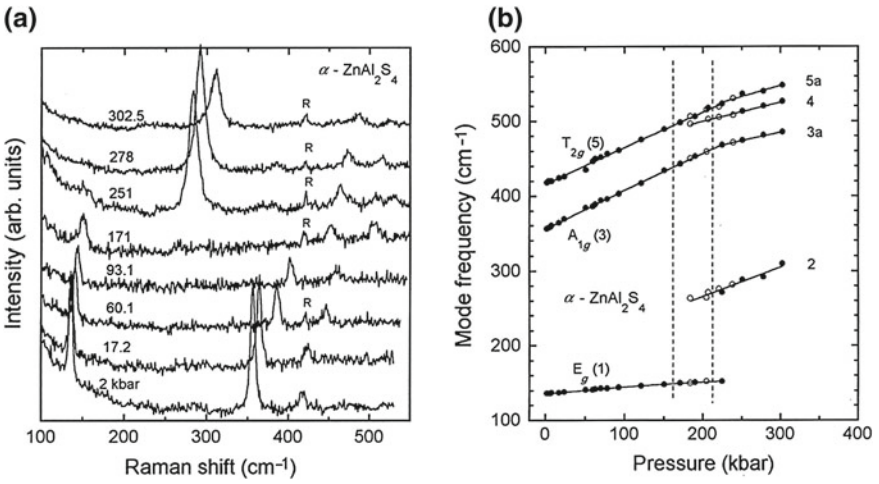

Fig. 8.1 **a** Unpolarized Raman spectra of α-$ZnAl_2S_4$ at various pressures and room temperature. R corresponds to sapphire *Raman line*. **b** Pressure dependence of Raman-active modes. *Full* and *open circles* correspond to up- and down-stroke of the pressure, respectively. Numbers in parentheses correspond to spinel structure, those without parentheses to calcium ferrite structure. Reprinted with permission from Ursaki et al. [6]. © 1998, APEX/JJAP

Table 8.1 Pressure dependence of Raman-active phonon frequencies of α-$ZnAl_2S_4$

Band number	ω_0	a	b	$1/\omega_0(d\omega/dP)$
1	133	1.05	−1.35	7.9
2	185	3.93	–	21.2
3	353	5.45	−1.80	15.4
3a	414	2.26	–	5.6
4	446	2.54	–	5.7
5	413	4.99	−1.02	12.1
5a	466	2.61	–	5.6

The parameter ω_0 is in units of cm^{-1}, a is in units of $10^{-1}\cdot cm^{-1}\cdot kbar^{-1}$, b in units of $10^{-4}\cdot cm^{-1}\cdot kbar^{-2}$, and $(1/\omega_0)$ $(d\omega/dP)$ in units of $10^{-4}\cdot kbar^{-1}$

Only three Raman-active modes (E_g, A_{1g} and T_{2g}) are observed under ambient conditions at 133, 353 and 413 cm^{-1}, respectively. The assignments of these modes are based on previously published polarization data at zero pressure [7].

Figure 8.1b illustrates the Raman shifts as a function of pressure. A monotonous shift to higher frequencies is a characteristic of all modes observed. The linear and quadratic pressure coefficients of Raman shifts obtained from a least-squares fit are listed in Table 8.1 together with their relative slopes $(1/\omega_0)(d\omega/dP)$ which are related to the mode Grüneisen parameters γ through $\gamma = (1/\beta)(1/\omega_o)(d\omega/dP)$, being β the bulk modulus.

The intensity of all modes was found to decrease with pressure (Fig. 8.2a, inset). A significant transformation of the Raman spectrum may be noticed at the critical pressure $P_c = 230$ kbar. The disappearance of the E_g band (#1, Figs. 8.1, 8.2) and

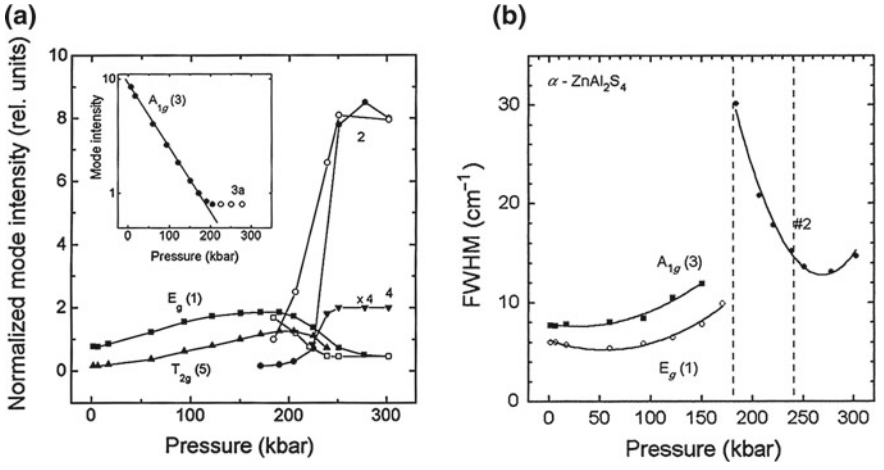

Fig. 8.2 **a** Scattering intensity (normalized to that of A_{1g} mode) for some of α-$ZnAl_2S_4$ modes as a function of pressure. The inset shows how the pressure of 230 kbar is determined. Full symbols correspond to increasing pressure, open symbols are for decreasing pressure. **b** FWHM as a function of pressure. Reprinted with permission from Ursaki et al. [6]. © 1998, APEX/JJAP

the emergence of two new bands (#2, #4, Fig. 8.1), is very dramatic. The behaviour of the mode intensities normalized to the intensity of the A_{1g} (3) peak is shown in Fig. 8.2a. The decrease in the intensity of the spinel mode is accompanied by an enhancement of modes #2 and #4, the former being the dominant one. On the downstroke change of the pressure, all new modes exhibit a hysteresis and disappear completely at 180 kbar. As the pressure is completely released, the initial Raman spectrum is fully recovered.

Significant changes occur in the Raman spectrum at 230 kbar; this critical pressure was established from the extrapolation to zero of the A_{1g} mode intensity (Fig. 8.2, inset). One should note that $MgAl_2O_4$ which crystallizes in the perfect spinel structure undergoes, at pressures above 250 kbar, a phase transition to a high-pressure phase with a structure similar to that of calcium ferrite (see X-ray powder diffraction data of [8]). The calcium ferrite ($CaFe_2O_4$) structure belongs to the D_{2h}^{16} (Pnam) space group and is the most dense structure among all known crystalline materials with the AB_2O_4 stoichiometry, the A^{2+} ions being located in eight-coordinated sites and the B^{3+} ions in octahedral sites. Its unit cell consists of four formula units. According to group theory, one should expect four types of Raman active modes (A_g, B_{1g}, B_{2g}, B_{3g}) and three types of IR active modes (B_{1u}, B_{2u}, B_{3u}). On the basis of correlation between the Raman active modes of the two point groups (O_h and D_{2h}) one finds that the spinel modes A_{1g} and E_g go over to A_g and $2A_g$ modes respectively, and the T_{2g} modes go over to the $B_{1g} + B_{2g} + B_{3g}$ modes. The parallel behaviour of the new mode #2 and the spinel E_g (1) mode in the pressure up- and downstrokes allows us to assume that the mode #2 is of A_g symmetry. Two additional new modes, namely #4 and 5a, exhibit similar behaviour; they correlate to the T_{2g} (5) spinel mode and as such they should have $B_{(1,2,3)g}$ symmetry. As to the mode #3a, its symmetry is A_g since it originates from the A_{1g} (3) spinel mode. Therefore, we infer that α-$ZnAl_2S_4$ undergoes a phase transition to the $CaFe_2O_4$ structure.

Taking into account the similarity of the unit cell parameters for $w - ZnAl_2S_4$ with the random distribution of cations, and w-ZnS (a = 3.811 and c = 6.234 Å) [9], one can conclude that these materials belong to the same space group C_{6v}^4. The $w-ZnAl_2S_4$ lattice contains 1/2 formula units in the primitive unit cell. Group theory then predicts $\Gamma = 2A_1 + 2E_1 + 2E_2 + 2B_1$, for the k = 0 modes. The acoustic modes are $A_1 + E_1$, while the B_1 modes are silent. According to this reduction, the first-order Raman spectrum consists of four Raman-active optical modes, namely $A_1 + E_1 + 2E_2$. The polar E_1 and A_1 modes exhibit LO–TO splitting. Therefore, the total number of peaks expected in the Raman spectrum is six. However at the microscopic level, each randomly distributed cation and stoichiometric vacancy occupy certain tetrahedral sites; hence, a number of additional local-type modes may be presented in the spectrum. Figure 8.3 shows the Stokes Raman spectra of undoped and Cd-doped w-$ZnAl_2S_4$ crystals for various pressures up to about 120 kbar. Unlike in undoped crystals, the defect-induced second-order broad Raman bands are absent in Cd-doped crystals. This indicates that addition of Cd atoms in w-$ZnAl_2S_4$ leads to a considerable increase of the crystal quality.

Apart from six modes assigned as R1–R6 (R for random) and assumed to be characteristic of the random distribution of cations, a number of additional local-type

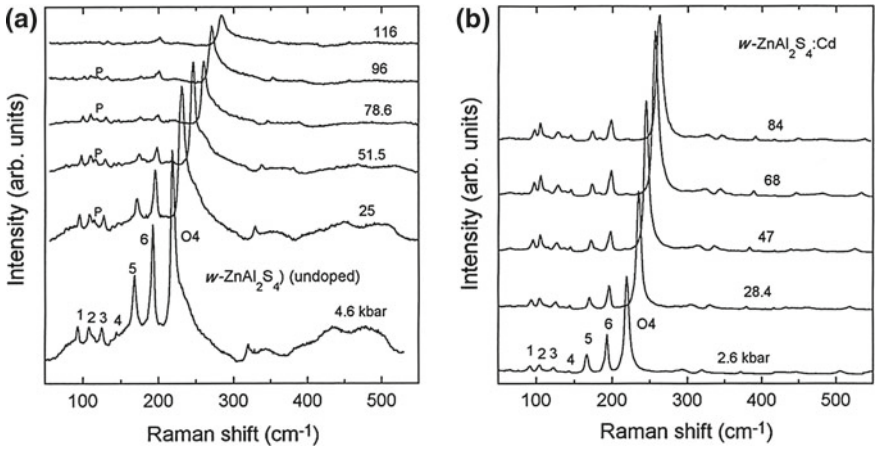

Fig. 8.3 Raman spectra of undoped (**a**) and Cd doped (**b**) $w-ZnAl_2S_4$ crystals at various pressures and room temperature. P is a *laser plasma line*. 1–6 correspond to R1–R6 random distribution modes and O4 is an ordered distribution mode. Reprinted with permission from Ursaki et al. [6]. © 1998, APEX/JJAP

modes are present in the spectrum. These are very similar to the modes inherent to defect-chalcopyrite $ZnAl_2S_4$ [5] where the stoichiometric vacancies and cations are strictly ordered. The pressure behaviour of the most intense O4 of these modes (O for ordered) is analogous to the so-called "breathing"mode which is caused by symmetric oscillations of anions surrounding the vacancy in defect-chalcopyrite $CdAl_2S_4$ [10].

In order to analyze the pressure behaviour of the various modes in Fig. 8.3, a multiple-band fitting of the spectra was used. The mode frequencies were found to increase with increasing pressure. The shifts as a function of pressure are shown in Fig. 8.4. The linear and quadratic pressure coefficients of the Raman shifts are the same for both Cd-doped and undoped crystals and listed in Table 8.2 together with their relative slopes $(1/\omega_0)(d\omega/dP)$.

As pressure increases up to 60–70 kbar, the intensity of local-type modes in Cd-doped w-$ZnAl_2S_4$ increases. Beyond this pressure, the intensities start to decrease sharply (see, for instance, mode O4 in Fig. 8.5a). At the same time the R-modes decrease in intensity, when normalized to O4 mode, up to the pressure of about 60 kbar. This behaviour is an indication that some ordering of cations takes place at ~60 kbar. It is noted that in the case of complete ordering of cations we obtain the β-phase, which can be regarded as having a wurtzite-derivative structure; in the latter, the anions are arranged in hexagonal close packing, whereas Zn and Al atoms and vacancies are distributed in an ordered manner over tetrahedral sites. The decrease of mode intensities beyond 60 kbar in Cd-doped crystals is attributed to lattice deformations prior to the high-pressure phase transition, as confirmed by the pressure dependence of full width at half maximum (FWHM) of the Raman modes (see O4 mode in Fig. 8.5b). As the pressure increases up to 60 kbar, the O4 mode exhibits a slight decrease of FWHM, whereas the FWHM increases for $P > 60$ kbar.

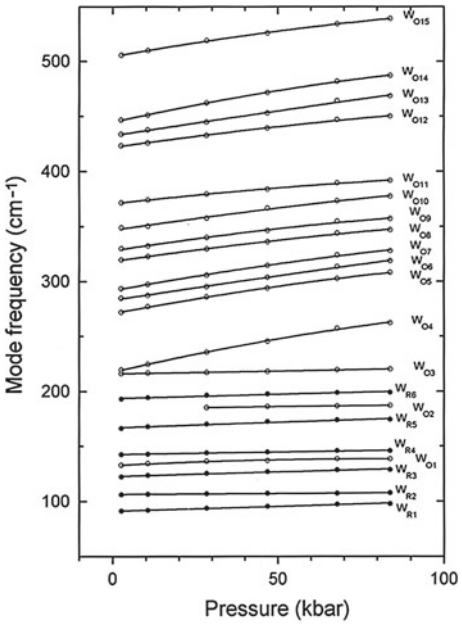

Fig. 8.4 Pressure dependence of the Raman-active modes of *w*-$ZnAl_2S_4$. Full (*open*) circles correspond to R (O) modes. *Solid lines* are quadratic fits. Reprinted with permission from Ursaki et al. [6]. © 1998, APEX/JJAP

At about 90 kbar the Raman signal disappears completely and irreversibly in Cd-doped *w*-$ZnAl_2S_4$ (see Fig. 8.5a for the O4 mode). This change with increasing pressure is attributed to a phase transition to a high-pressure structure with sixfold coordination, probably of rocksalt-type. Moreover, some changes in the crystal structure are initiated already at 60 kbar.

It should be noted that the critical pressure for the phase transition to the Raman-inactive phase is different in undoped and Cd-doped *w*-$ZnAl_2S_4$ crystals (130 and 90 kbar, respectively, see O4 mode in Fig. 8.5a). Therefore, one can conclude that Cd atoms tend to stabilize the wurtzite structure. The Raman signal in both cases is recovered only below 10 kbar and the shape of the spectrum is different.

The Raman spectrum of undoped *w*-$ZnAl_2S_4$ which was recovered below 10 kbar, was not the same as the initial one, and exhibited distinct signs of amorphization. Such a pressure-induced amorphization process has been previously observed in tetrahedrally bonded materials [11, 12]. It has been established, that amorphization occurs if the pressure is released in certain temperature interval. Above this interval the initial crystal structure is recovered. Pressure release below this interval leads to quenching of the high-pressure phase. In this case amorphization from the quenched high-pressure phase occurs when the temperature is elevated at low pressure. In the case of *w*-$ZnAl_2S_4$ the room temperature is inside of the critical temperature interval for amorphization. Thus, an amorphous phase of *w*-$ZnAl_2S_4$ is obtained when pressure is released at room temperature. The degree of amorphization depends on how far from the point of phase transition to the Raman-inactive phase has the pressure been increased (see Fig. 8.6a. If the maximum pressure reached is $P_{max} =$

Table 8.2 Pressure dependence of Raman-active phonon frequencies of *w*-type $ZnAl_2S_4$

Mode	ω_0	*a*	*b*	$1/\omega_0(d\omega/dP)$
R1	91	0.85	–	9.4
R2	106	0.16	–	1.5
R3	123	0.80	–	6.5
R4	143	0.43	–	3.0
R5	167	0.99	–	5.9
R6	194	0.74	–	3.8
O1	133	1.50	−9.69	11.3
O2	184	0.61	−2.51	3.3
O3	216	0.49	–	2.3
O4	217	6.88	−17.50	31.7
O5	271	5.67	−15.04	20.9
O6	283	4.49	−2.43	15.9
O7	292	5.50	−13.04	18.8
O8	318	4.45	−11.60	14.0
O9	328	4.68	−14.33	14.3
O10	347	4.37	−8.20	12.6
O11	371	3.34	−9.61	9.0
O12	422	4.10	−8.45	9.7
O13	432	4.64	−2.39	10.7
O14	444	6.82	−19.86	15.4
O15	504	5.33	−14.17	10.6

The units are as in Table 8.1

130 kbar, the features of the initial crystalline structure are fully recovered upon releasing pressure. If $P_{max} \geq 150$ kbar full amorphization is observed. An analogous behaviour was observed in ZB III-V compounds [13, 14]. It was shown that the amount of amorphous phase produced increases with P_{max}, by analogy to the increase observed as the dose increases in heavy ion-implanted GaAs [13]. Furthermore, the long-range order observed in GaP samples after pressure release has been shown to depend on P_{max} [14].

Figure 8.6b illustrates the Raman spectra of Cd-doped $w-ZnAl_2S_4$ after pressure release, for two different values of P_{max}. For $P_{max} = 100$ kbar we have a mixture of two phases. The Raman spectrum also exhibits a new peak (S, for spinel) besides the ones characterizing the *w*-phase. The position of this new peak is very close to the E_g mode in α-$ZnAl_2S_4$ (see Fig. 8.1). One can conclude that there is a mixture of α- and *w*-phases. For $P_{max} = 110$ kbar the peaks characteristic of the *w*-phase disappear after pressure release, the remaining peak presumably originating from the α-phase.

Figure 8.7a shows the Raman spectra of *w*-$ZnAl_2S_4$:Cd at various pressures, after the initial release. As shown in Fig. 8.7b, there is a monotonous shift to higher frequencies for four wurtzite modes and one S mode (S). The linear pressure coefficients of these Raman shifts, obtained from a least-squares fit, are listed in Table 8.3 together with their relative slopes $(1/\omega_0)(d\omega/dP)$.

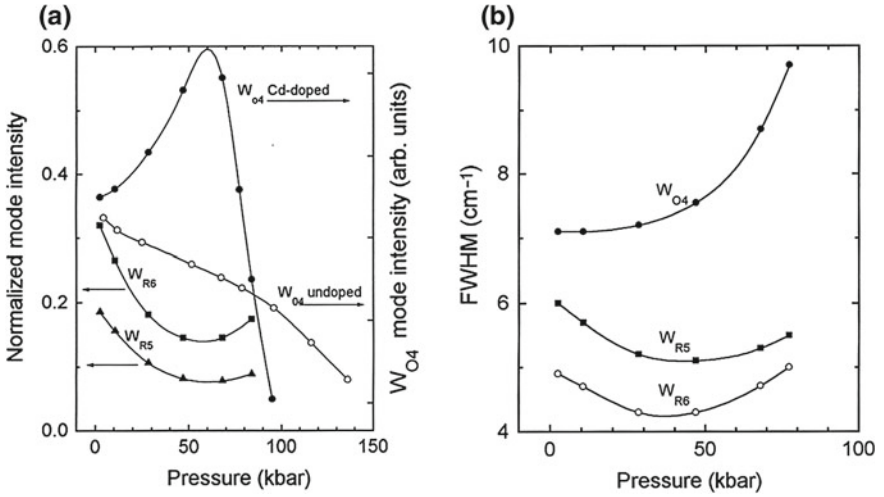

Fig. 8.5 **a** Pressure dependence of the intensity of the O4 mode (217 cm^{-1} at P = 0, intensity axis on the *right-hand side*) for Cd-doped and undoped crystals, and normalized intensities for the Cd-doped R5 and R6 modes relative to that of Cd-doped O4 mode. **b** FWHM for the Cd-doped O4, R5, and R6 modes as a function of pressure. Reprinted with permission from Ursaki et al. [6]. © 1998, APEX/JJAP

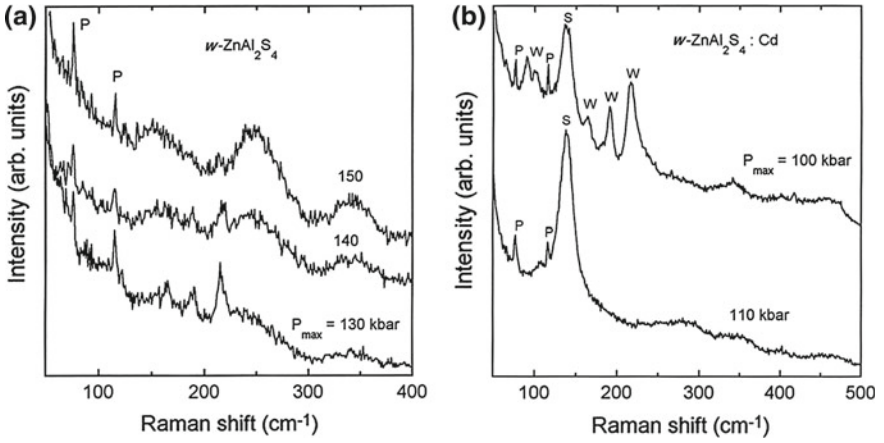

Fig. 8.6 **a** Raman spectra of undoped *w*-$ZnAl_2S_4$ after pressure release, for P_{max} = 130, 140, and 150 kbar. **b** Raman spectra of Cd-doped *w*-$ZnAl_2S_4$ after pressure release, P_{max} = 100, 110 kbar. P are laser plasma lines. Reprinted with permission from Ursaki et al. [6]. © 1998, APEX/JJAP

There are some differences in the behaviour of the S (Fig. 8.6b) and E_g (1) modes (Fig. 8.1b), owing to the very defective type of the α-phase obtained after pressure release (probably its structure is quasi-crystalline). Furthermore, the pressure dependence of S-mode intensity and FWHM differs from that of the E_g (1) mode. The

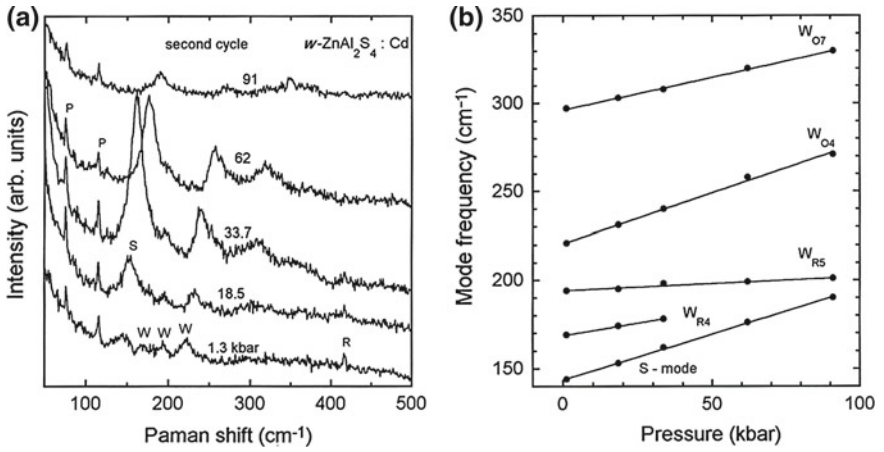

Fig. 8.7 **a** Raman spectra of Cd-doped $w - ZnAl_2S_4$ after pressure release, during the second pressure cycle. R is a sapphire Raman line, and P are laser plasma lines. **b** Pressure dependence for some of modes, including the new S-mode during the second pressure cycle. *Solid lines* are linear fits. Reprinted with permission from Ursaki et al. [6]. © 1998, APEX/JJAP

Table 8.3 Pressure dependence of Raman-active phonon frequencies of Cd-doped w-$ZnAl_2S_4$ during a second pressure cycle

Mode	ω_0	a	$1/\omega_0(d\omega/dP)$
S-type	144	5.13	35.63
R5	169	2.78	16.45
R6	194	0.78	4.02
O4	221	5.67	25.65
O7	296	3.73	12.60

The units are as in Table 8.1

parameters for the first and second pressure cycle for w-modes are different as well. Namely, the R-modes become more sensitive to the pressure [larger $(1/\omega_0)$ $(d\omega/dP)$], while the O-modes become less sensitive to the pressure [smaller $(1/\omega_0)$ $(d\omega/dP)$]. The increasing of the S-mode intensity and decreasing of FWHM for $P \leq 40$ kbar suggests that a recrystallization process of the destroyed α-phase takes place at intermediate pressures. The behaviour of the S-mode for $P \geq 50$ kbar differs from that of the E_g (1) mode in the single crystal α-phase. The latter is stable for $P \leq 230$ kbar where a phase transition to the new phase occurs, as mentioned above, while the *S*-mode disappears near 100 kbar, indicating a phase transition to some Raman-inactive phase. In order to clarify the nature of this phase transition, an X-ray analysis under pressure is needed. It is noted that a similar difference in the properties of crystalline and decompressed material has been observed in GaN [15] and explained by invoking nanocrystal structures.

Finally, for P ≥ 130 kbar the behaviour of the Cd-doped *w*-$ZnAl_2S_4$ is similar to that of the undoped *w*-$ZnAl_2S_4$, in the sense that amorphization sets in after pressure release.

8.2 Raman Scattering Study of Pressure Induced Phase Transitions in $ZnAl_{2(1-x)}Ga_{2x}S_4$ Solid Solutions

Although the quaternary solid solutions $ZnAl_{2(1-x)}Ga_{2x}S_4$ (obtained by adding gallium atoms to the Zn–Al–S system) crystallize in a defect chalcopyrite (DC) structure, the trends of pressure induced phase transitions at high concentrations of Al differ from those observed in compounds with DC structure, namely, a new phase supposed to be of layered-type is produced instead of a rocksalt-type structure. A Raman scattering (RS) study of $ZnAl_{2(1-x)}Ga_{2x}S_4$ crystals for three values of X (namely 0.1; 0.2 and 0.4) was undertaken under hydrostatic pressure up to 300 kbar [16].

Figure 8.8 presents for comparison the RS spectra of $ZnAl_{2(1-x)}Ga_{2x}S_4$ for two values of X (0.1 and 0.4) as well as the spectra of $ZnGa_2S_4$ and $CdAl_2S_4$ at ambient pressure. It was observed that the RS spectrum of $ZnAl_{2(1-x)}Ga_{2x}S_4$ for X = 0.2 is similar to that for X = 0.1.

One can observe from Fig. 8.8 that the RS spectra of $CdAl_2S_4$ and $ZnAl_{2(1-x)}Ga_{2x}S_4$ for X = 0.1 and 0.4 are similar in the high frequency region, except for some broadening of the bands and the shift of the band around 500 cm^{-1} towards low frequency in $ZnAl_{2(1-x)}Ga_{2x}S_4$ with increasing of X value. The broadening of bands was assumed to disordering in cation sublattice with increasing of X [17]. The position of the most high frequency band is determined by the III group cation [5] being equal to 400 cm^{-1} in $ZnGa_2S_4$ and 500 cm^{-1} in $CdAl_2S_4$. So, that the shift

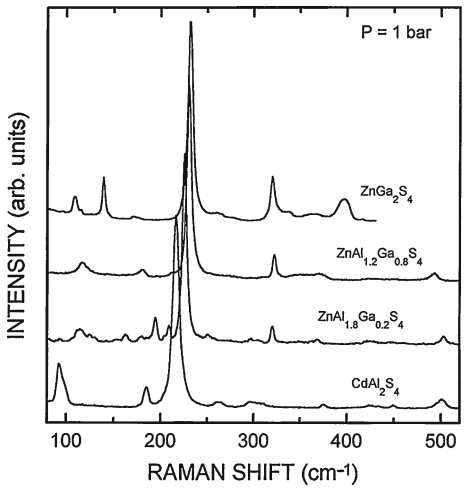

Fig. 8.8 RS spectra of $ZnAl_{2(1-x)}Ga_{2x}S_4$ for two values of X (0.1 and 0.4); $ZnGa_2S_4$; and $CdAl_2S_4$ at ambient pressure

of this mode towards low frequencies in $ZnAl_{2(1-x)}Ga_{2x}S_4$ with increasing of X is expected.

In the low frequency region the spectra of $ZnAl_{2(1-x)}Ga_{2x}S_4$ for X = 0.1 and 0.4 are different. The spectrum of $ZnAl_{1.2}Ga_{0.8}S_4$ is similar to that of $CdAl_2S_4$ and $ZnGa_2S_4$. While two new bands assigned as #2a and #3a as well as other bands of low intensity emerged in the spectrum of $ZnAl_{1.8}Ga_{0.2}S_4$. Therefore, one can conclude that high concentration of Ga leads to the stabilization of DC-type structure. For the low values of X the structure differs from usual DC one.

Figure 8.9 shows the RS spectra of $ZnAl_{2(1-x)}Ga_{2x}S_4$ for X = 0.1, 0.2 and 0.4 for various pressures up to 170 kbar. The mode frequencies were found to increase with increasing pressure. The shifts as a function of pressure are shown in Figs. 8.10a, b for X = 0.4 and 0.1, respectively. The behaviour of the modes with pressure for X = 0.2 is identical to that for X = 0.1. Solid lines on these figures represent polynomial fits of the form $\omega = \omega_0 + aP + bP^2$.

$ZnAl_{2(1-x)}Ga_{2x}S_4$ with the high value of X (X = 0.4) forms a more stable system. As the pressure increases the intensity of all bands decreases (for instance, see mode #5 in Fig. 8.11). The rate of decrease differs from mode to mode. Thus, the E modes at 120 (#1) and 180 cm^{-1} (#3) and also the A^3 mode (#10) at 370 cm^{-1} increase in intensity up to pressures $\approx$ 120 kbar when normalized to the intensity of the A^1 mode (Fig. 8.11). On the other hand the absolute intensity of the modes near 500 cm^{-1} (#14, 15) and the more essential the A^2 mode (#8) at 320 cm^{-1} drop faster than the low frequency modes. At the pressure above 120 kbar the intensity of the modes starts to decrease drastically more and the RS signal disappears completely and irreversibly at pressures around 170 kbar (see Fig. 8.11 for A^1 mode). The disappearance of the RS signal in the $ZnAl_{2(1-x)}Ga_{2x}S_4$ with pressure increase, as in the case of other $A^{II}B_2^{III}C_4^{VI}$ compounds, is attributed to a phase transition from adamantine structure

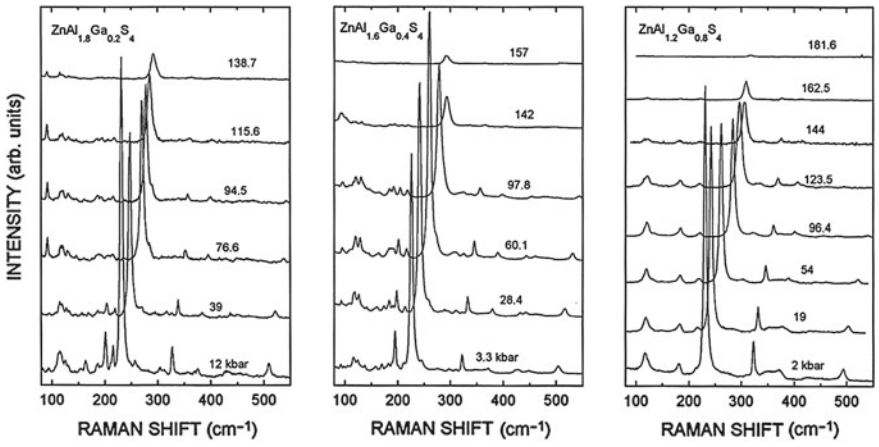

Fig. 8.9 Unpolarized Raman spectra of $ZnAl_{2(1-x)}Ga_{2x}S_4$ (X = 0.1, 0.2, and 0.4) at various pressures

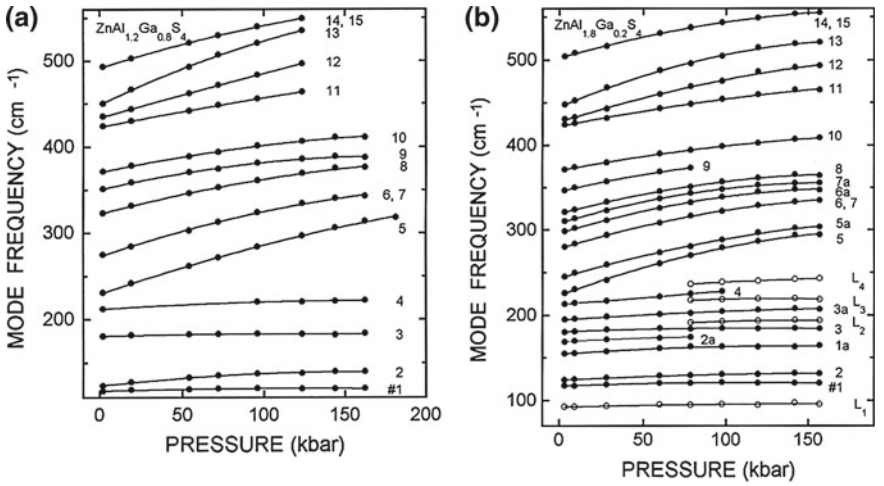

Fig. 8.10 Pressure dependence of the Raman active modes for X = 0.4 (**a**) and X = 0.1 (**b**). *Solid lines* are quadratic fits. Reprinted with permission from Ursaki et al. [16]. © 1998, Institute of Physics

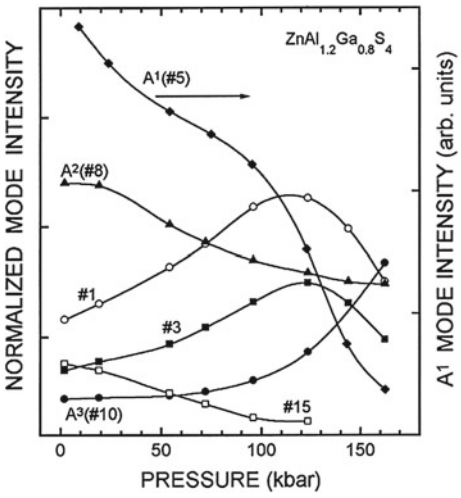

Fig. 8.11 *Right-hand side* intensity axis: pressure dependence of the intensity of the A^1 (5) mode for $ZnAl_{1.2}Ga_{0.8}S_4$ crystals. Left-hand side axis: normalized intensities, relative to A^1, of various modes. Reprinted with permission from Ursaki et al. [16]. © 1998, Institute of Physics

of fourfold atomic coordination to a high pressure structure with sixfold coordination of rocksalt-type.

The structural evolution of $ZnAl_{2(1-x)}Ga_{2x}S_4$ with low values of X (X = 0.1) is analyzed in Fig. 8.12 which shows the absolute intensity of A^1 (#5) mode and the intensity of other modes normalized to the intensity of this mode. One can see the sharp decreasing of the intensity of untypical for DC modes (see, for example, #2a and 3a modes) up to the pressure around of 70 kbar. One can conclude that the structure tends to the more stable one of typical DC. But some other processes simultaneously

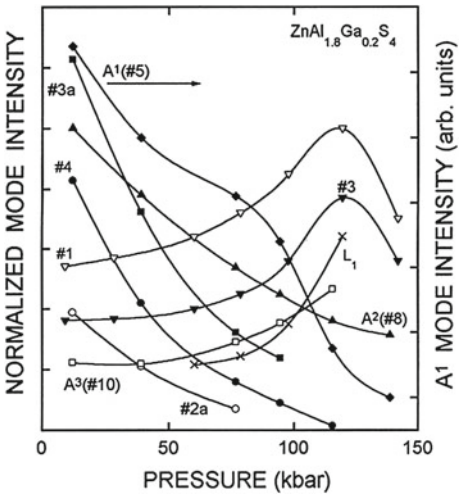

Fig. 8.12 *Right-hand side* intensity axis: pressure dependence of the intensity of the A^1 (5) mode for $ZnAl_{1.8}Ga_{0.2}S_4$ crystals. *Left-hand side* axis: normalized intensities, relative to A^1, of various modes. Reprinted with permission from Ursaki et al. [16]. © 1998, Institute of Physics

occur. First of all, the relative decreasing of the A^2 (#8) mode and increasing of A^3 (#10) mode intensity is an indicative of disordering in the cation sublattice, like in the case of high values of X. The more essential is the emergency at the pressure 70 kbar of new L_1 and other modes assigned as $L_1 \div L_4$ in Fig. 8.10b. These modes indicate the appearance of new phase coexisting with DC one in the pressure interval of $70 \div 150$ kbar.

Raman signal disappears completely at the pressure around 150 kbar (for instance, see mode A^1 (#5) in Fig. 8.12). The later is like in the case of high values of *X* an indicative of phase transition to Raman-inactive phase rocksalt-type. It is to be noted that the higher is the *X* value the higher is the point of pressure of phase transition to rocksalt-type structure, being equal to 150, 160 and 170 for $X = 0.1$, 0.2 and 0.4, respectively. This phase transition is irreversible. The RS signal is not recovered when pressure is released up to the pressure lower than 10 kbar. At pressures lower than 10 kbar the RS signal is recovered but its shape is different for different values of *X* (see Fig. 8.13a). In the spectrum of $ZnAl_{1.2}Ga_{0.8}S_4$ the more intensive A^1 mode of DC structure is present along with a series of broad bands inherent for amorphous phase. As mentioned above the pressure-induced amorphization was observed in other $A^{II}B_2^{III}C_4^{VI}$ compounds as well as in $ZnAl_2S_4$ of wurtzite type.

The spectrum of $ZnAl_{1.6}Ga_{0.4}S_4$ is dominated by the S peak observed earlier in decompressed *w*-$ZnAl_2S_4$ doped by Cd and supposed to be characteristic for strong destroyed spinel phase. Beside this the amorphous bands are also present in the spectrum. In the spectrum of $ZnAl_{1.2}Ga_{0.8}S_4$ after pressure release the more intensive are three broad bands. Namely, S band, whose position coincides with E_g mode of spinel phase, DC band coinciding with A^1 mode of DC structure and L band located near the L_6 mode of the structure coexisting with DC one in the pressure interval of $70 \div 150$ kbar as mentioned above. The broadness of these bands is caused by heavily destroyed, probable of quasi-crystalline type, structure. So, this

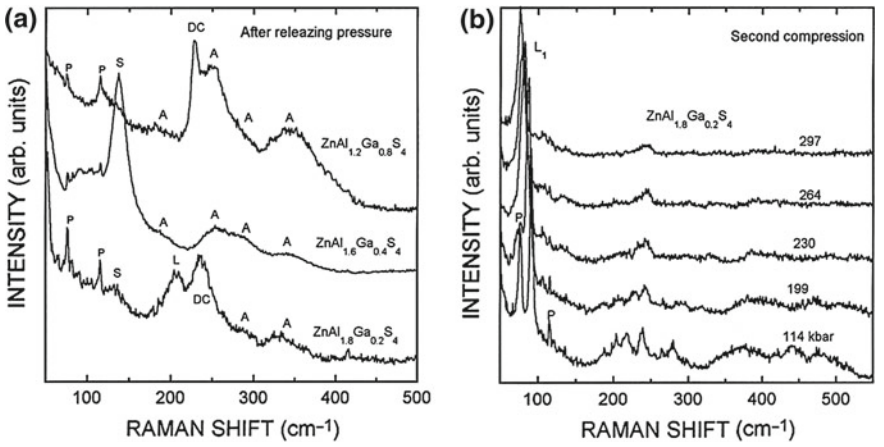

Fig. 8.13 **a** Raman spectra of the decompressed $ZnAl_{2(1-x)}Ga_{2x}S_4$ with different X-values. **b** Raman spectra of $ZnAl_{1.8}Ga_{0.2}S_4$ at various pressures during the second pressure cycle. Reprinted with permission from Ursaki et al. [16]. © 1998, Institute of Physics

decompressed material seems to consist of three quasi-crystalline phases, despite low intensity amorphous bands are also observed.

Now, if this mixture of phases is subjected to a second compression the L-phase is recrystallized (see Fig. 8.13b) and this structure is stable up to the pressure of around 300 kbar (it was the highest pressure achieved in this experiment). The intensity increase of the more intensive L_1 mode up to the pressure of 120 kbar is followed by its decrease above this point of pressure (as shown in Fig. 8.14a). In downstroke

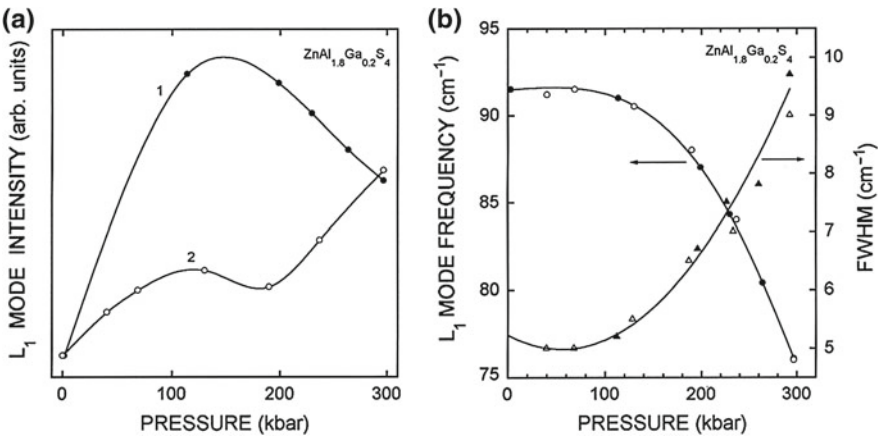

Fig. 8.14 **a** Pressure dependence of the L_1 mode intensity for $ZnAl_{1.8}Ga_{0.2}S_4$ on upstroke (1) and downstroke (2) change of pressure. **b** L_1 mode frequency and FWHM for $ZnAl_{1.8}Ga_{0.2}S_4$ as a function of pressure. Full (*open*) circles and triangles are for upstroke (*downstroke*) of pressure. Reprinted with permission from Ursaki et al. [16]. © 1998, Institute of Physics

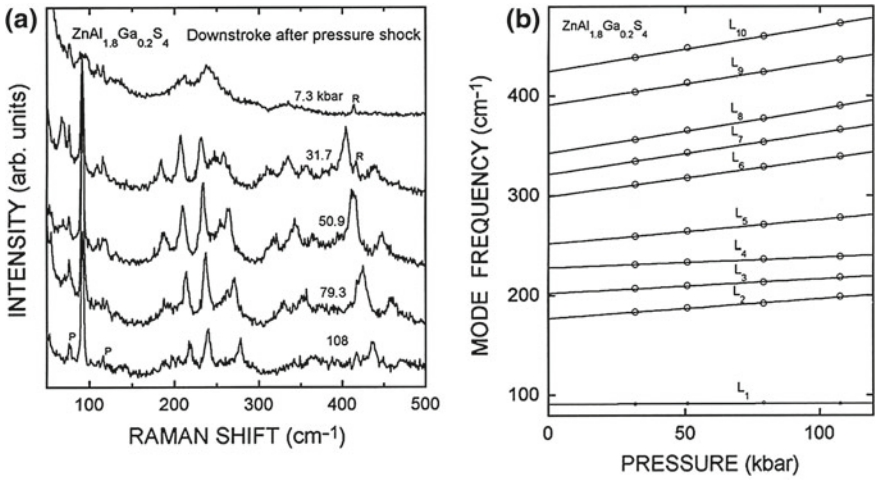

Fig. 8.15 **a** Raman spectra of $ZnAl_{1.8}Ga_{0.2}S_4$ on downstroke of pressure after a pressure shock to 108 kbar. **b** Pressure dependence of the Raman-active modes. *Solid lines* are linear fits. Reprinted with permission from Ursaki et al. [16]. © 1998, Institute of Physics

of pressure some hysteresis is observed. At the same pressure of around 120 kbar the FWHM of L_1 mode starts to increase and its frequency starts to decrease (see Fig. 8.14b) indicating the soft character of this mode and initiation of the new phase transition [18].

A direct phase transition from DC $ZnAl_{1.8}Ga_{0.2}S_4$ to L-phase takes place if the crystal is subjected to a pressure shock by increasing pressure from ambient pressure to 100 kbar. Figure 8.15 shows the RS spectra of $ZnAl_{1.8}Ga_{0.2}S_4$ in downstroke after the pressure shock to 108 kbar (a), and the shift of Raman modes (b). As the pressure decreases the intensity of the bands slightly increases. At pressures lower than 10 kbar the shape of the RS spectrum is identical to that obtained after decompression from rocksalt-type phase (compare Figs. 8.15a and 8.13a).

The different behaviour of the material when the pressure is increased slowly and quickly in 4:1 methanol–ethanol solution can be explained in terms of the influence of the rate of pressure increase upon the hydrostatic conditions. The rapid compression seems to produce more nearly hydrostatic conditions than the slow one [19].

Therefore, the addition of Ga atoms to the $ZnAl_2S_4$ system leads to the crystallization in DC structure instead of spinel one. The higher is the X value in the solid solutions $ZnAl_{2(1-x)}Ga_{2x}S_4$ the more stable is the DC structure and the higher is the pressure of transition to Raman-inactive phase. At high values of X ($X \geq 0.4$) the behaviour of the solid solutions under hydrostatic pressure is similar to other tetrahedrally coordinated compounds: an order-disorder phase transition takes place before the transition to Raman-inactive phase. At low X-values ($X \leq 0.2$) simultaneously with the disordering a new phase coexisting with the DC one up to the transition to rocksalt-type structure is formed. The path of phase transformations is dependent

on the composition and on the rate of pressure increase. A direct phase transition from the DC structure to the above mentioned new phase takes place if the crystal is subjected to a sharp increase of pressure up to 10 GPa instead of a gradual one. This phase is stable up to the pressure of more than 30 GPa [20].

8.3 Raman Scattering Study of Layered $AInGaS_4$ (A = Zn, Cd, Mg) Compounds Under Hydrostatic Pressure

$CdInGaS_4$, $ZnInGaS_4$ and $MgInGaS_4$ are layered semiconducting compounds with band gap energies 2.81, 2.92 and 2.57 eV respectively [21, 22]. The crystal structure of the compounds under consideration is based on a close packing of the chalcogen atoms, the cation coordination being both tetrahedral and octahedral [21]. In $CdInGaS_4$, $ZnInGaS_4$ and $MgInGaS_4$ the cations form flat nets of filled tetrahedra and octahedra. These nets are grouped in packs with ion-covalent chemical bonds inside them. The weak coupling between layers is believed to reflect the action of Van der Waals force between neighboring packs. The behavior of the optical lattice vibrations of $CdInGaS_4$, $ZnInGaS_4$ and $MgInGaS_4$ under pressure up to 160 kbar is discussed in this subchapter [23, 24].

Figure 8.16 illustrates the Raman spectra of as-grown $CdInGaS_4$, $ZnInGaS_4$ and $MgInGaS_4$single crystals at normal conditions (T = 300 K and P = 1 bar). The spectra appear to be similar, although the spectrum of $MgInGaS_4$ is rather smeared. The quite high similarity is observed for modes with frequencies above 180 cm^{-1}. This part of spectrum is believed to correspond to intralayer modes and is sensitive

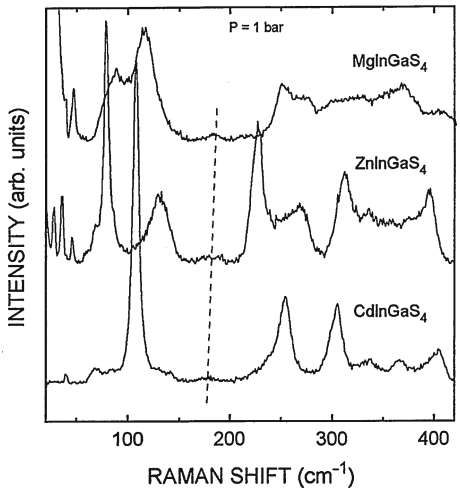

Fig. 8.16 Unpolarized Raman spectra of $A^{II}InGaS_4$ compounds at room pressure and temperature

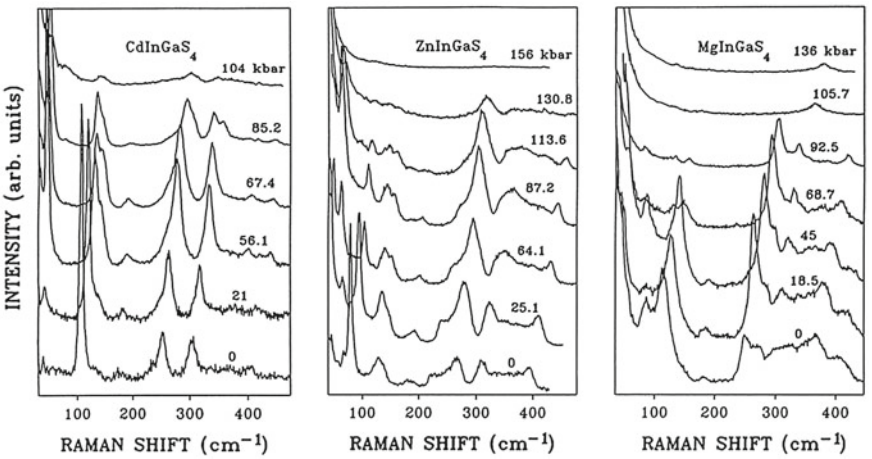

Fig. 8.17 Raman spectra of $A^{II}InGaS_4$ compounds at various pressures and room temperature

only to the composition. The part of spectrum below 180 cm^{-1} is different for each compound, and this reflects their different layered structure. The existence of narrow and intense lines in the low-frequency region is inherent to layered materials. These acusto-derived rigid-layer (RL) modes [25] are responsible for interlayer vibrations. The number of modes should be related to the number of non-equivalent layers in the primitive unit cell.

Figure 8.17 shows the Raman spectra of $CdInGaS_4$, $ZnInGaS_4$ and $MgInGaS_4$ single crystals under various hydrostatic pressures. The increase of Raman intensity in all com-pounds is followed by its sharp decrease at pressures above 70–90 kbar (see e.g. Figs. 8.18 and 8.19). In $CdInGaS_4$ and $ZnInGaS_4$ changes of the low-frequency modes ($n < 100\ cm^{-1}$) can be observed around 30 kbar, including the disappearance of some modes, e.g. #4 and 5, with simultaneous emergence of new nearly modes (#4a and 5a), and enhancement of mode #3 (see Fig. 8.18). One might also infer a sharp decrease of modes #1 and 2, which are difficult to observe because of their superposition with the Rayleigh tail. It is worth noting that in $MgInGaS_4$ an analogous behaviour near 30 kbar was not observed, with the exception of an intensity decrease in half of the modes at 50 kbar (Fig. 8.19). From the same analysis we also see in two of the compounds ($CdInGaS_4$ and $ZnInGaS_4$) intensification of most of the bands (e.g #4a and 10 in Fig. 8.17) as well as the decrease of the other two modes, e.g. #3 and 5a, in $ZnInGaS_4$.

In Table 8.4 a common numbering of the modes observed in all three compounds is used, based on the similarity of their Raman spectra. The decrease of Raman intensity at 70–90 kbar in all compounds is accompanied by the emergence of a new Raman mode in the high frequency region (labelled by SP in Table 8.4). After reaching the 110 kbar for $CdInGaS_4$ and 150 kbar for $ZnInGaS_4$, the Raman signal disappeared completely in both materials; these critical values are designed by P_c.

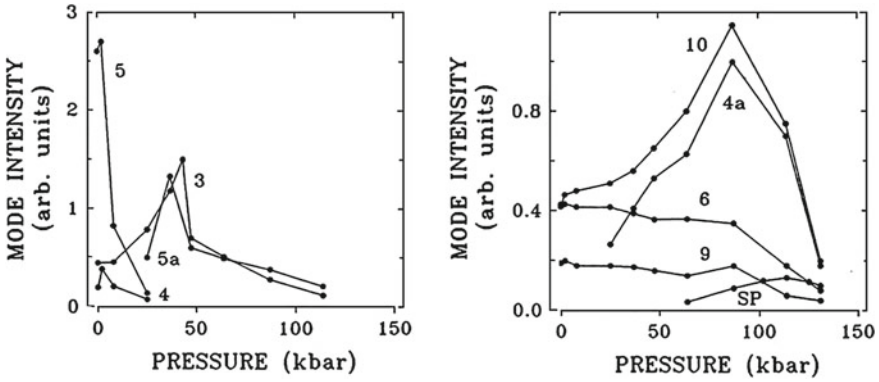

Fig. 8.18 Pressure dependence of the intensity of Raman modes in $ZnInGaS_4$

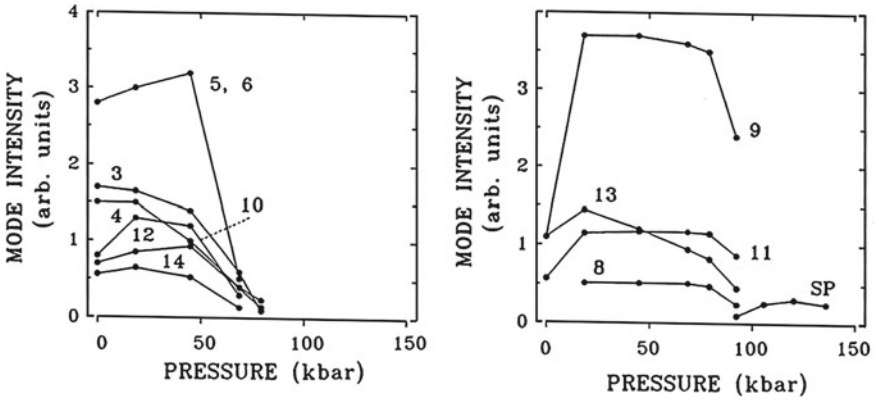

Fig. 8.19 Pressure dependence of the intensity of Raman modes in $MgInGaS_4$

On the contrary, the Raman signal in $MgInGaS_4$ did not disappear up to the maximum pressure applied, hence one could not find the P_c value for this material.

Before reaching P_c, the samples were measured under gradual pressure decrease, and the following was observed: In $CdInGaS_4$ and $ZnInGaS_4$ the downstroke of pressure, starting from 80 and 130 kbar, respectively, revealed a recovery of the Raman spectrum, though with a weak hysteresis. When we tried to repeat the downstroke measurements, starting from the corresponding P_c values we observed a different picture: The Raman spectrum in $CdInGaS_4$ was not recovered up to the ambient pressure, whereas in $ZnInGaS_4$ the spectrum was recovered around 50 kbar. As for $MgInGaS_4$, the high pressure spectrum remained unchanged, i.e. the new band (SP) continued to exist even after releasing the pressure.

Figure 8.20 illustrates the pressure dependence of Raman-active mode frequencies when the pressure is increased; this shift is rather weak for the low-frequency modes. The mode shift parameters are summarized in Table 8.4.

Table 8.4 Raman-active optical phonon frequencies (in cm^{-1}) and their shift parameter k (in 10^{-3} $kbar^{-1}$) for the layered $A^{II}InGaS_4$ compounds

Mode number	$CdInGaS_4$		$ZnInGaS_4$		$MgInGaS_4$	
	ω_0	a	ω_0	a	ω_0	a
1	17[a]	–	19	–		
2	27[a]	–	33	–	35	–
3	37	4.81	41	2.17	41	5.02
4	62	3.00	62	0.97	83	−0.01
4a			60	0.28		
5	105	2.92	77	1.81	97	4.53
5a	116	1.91	83	3.23		
6	131	1.31	127	1.15	114	4.17
7			137	1.43		
8	175	1.45	183	1.64	178	1.62
9	237	1.59	226	2.32	249	2.40
10	250	1.90	268	1.36	266	2.36
11	304	1.40	309	1.27	299	1.33
SP	328	0.97	316	1.69	296	2.06
12	331	1.27	333	1.75	331	1.63
13	356	1.74	357	1.76	336	1.51
14	401	1.32	393	1.37	405	1.04

The [a] frequencies are from [27]

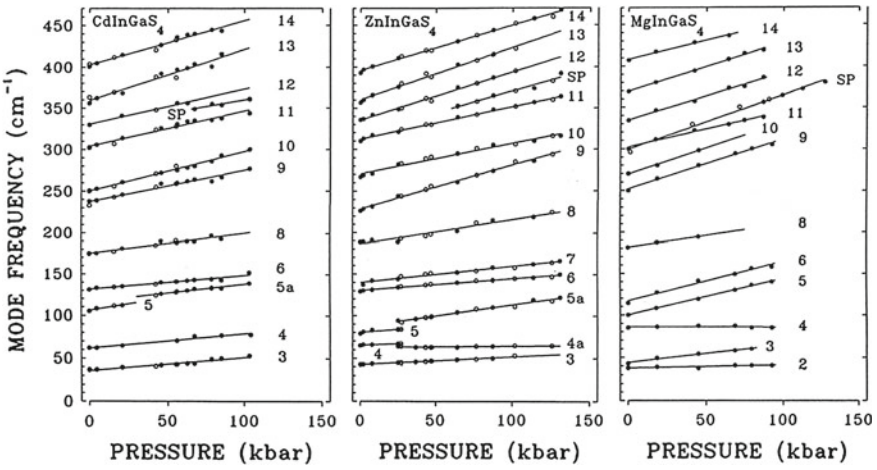

Fig. 8.20 Pressure dependence of Raman active mode frequencies in $A^{II}InGaS_4$ compounds. Full lines are linear fits. Full (*open*) circles correspond to upstroke (*downstroke*) of pressure

One can define four characteristic pressure values: 30, 50 kbar, P_{sp} (pressure at which the SP mode appears) and P_c. Each one corresponds to certain structural transformation. The latter two values are different for each compound.

Near 30 kbar in $CdInGaS_4$ and $ZnInGaS_4$, a strong transformation of the low-frequency part of spectrum was observed, caused mainly by the cation redistribution accompanied by partial filling of interlayer voids. In $MgInGaS_4$ no transformations at 30 kbar were observed. This allows one to suggest that there is sufficient cation disorder with partial filling of interlayer voids already at normal conditions. This assumption is supported by the absence of any narrow and intense band in the low-frequency region, like the mode #5 in $CdInGaS_4$ and $ZnInGaS_4$.

The second spectrum transformation, observed in all three compounds, occurs at 50 kbar and is accompanied by mode intensity changes in the high-frequency part of the spectrum, i.e. decrease for some modes and increase for some others. This fact may be caused by redistribution of cations on tetrahedral and octahedral voids inside the packet, which indicates the beginning of a lattice structure transformation, as it will be discussed below. These processes follow different procedures in each compound, but they have many common features.

In the middle pressure interval (70–90 kbar) a decrease of intensity of the last modes begins. In this range of pressures, 70 kbar for $CdInGaS_4$ and 90 kbar for $MgInGaS_4$, or a little earlier (65 kbar for $ZnInGaS_4$) the appearance and subsequent intensification of a new mode (SP) is observed. Its frequency value referred to zero pressure is given in Table 8.4. It is interesting to notice its unique place in the frequency space. In all three materials it appears between modes #11 and 12 and is accompanied by the disappearance of mode #12. In $CdInGaS_4$ and $ZnInGaS_4$ this new mode coexists with the regular modes in the interval 70–90 kbar for the first and 65–130 kbar for the second compound, whereas for $MgInGaS_4$ the changes are more sharp, the appearance of SP mode occurring simultaneous with the disappearance of other modes.

In the process of analyzing these results, it was taken into account that $ZnIn_2S_4$, a material with analogous crystal structure, under high pressure crystallizes in the spinel structure [26]. The transition to spinel structure is one of the most probable for layered compounds with tetrahedral and octahedral cation coordination [21]. It was assumed that the new mode (SP) is related to the spines structure, being sufficient intense [23, 24]. Concerning the transformation of mode #12 with A symmetry [27] into the SP mode, two possible ways were proposed for this to occur: first, the mode #12 goes over the A_g mode of the spinel structure (without symmetry change) and second, it goes over to the T_{2g} mode of the spinel structure. In favor of the latter is the close value of its frequency in all three compounds to the T_{2g} mode frequency of corresponding spinals, e.g. 311 cm^{-1} for $CdIn_2S_4$ [28], 315 cm^{-1} for $ZnIn_2S_4$ [29] and 314 cm^{-1} for $MgIn_2S_4$ [30]. As to the other spinel modes, there are some difficulties in their detection, a consequence of coexistence of both phases (layered and spinel) in the pressure interval.

The disappearance of Raman signals in $CdInGaS_4$ and $ZnInGaS_4$ at $P > P_c$ can be explained by taking into account the possibility of a phase transition to Raman-inactive phase, which is characteristic of cubic structures under pressure. As a rule this Raman-inactive phase correspond to the rocksalt-type structure [31]; however, it could be a high-pressure defective spinel structure as that found in $CdIn_2S_4$, $MgIn_2S_4$ and $MnIn_2S_4$ [32] and described in Chap. 3.

It is worth noticing that $P_c(CdInGaS_4) < P_c(ZnInGaS_4)$, which indicates that the zinc spinel is more stable under pressure than the cadmium spinel. The weaker stability of the latter is connected to a higher ability of its cations (Cd and In) for mutual substitution which, in turn, leads to relaxation of the normal spinel structure. It is to be noted, that in $CdIn_2S_4$ the analogous phase transition to the Raman-inactive phase was observed at $P \approx 120$ kbar, which is very close to P_c of $CdInGaS_4$, taking into account the initial perfect spinel structure in the first case.

Gradual release of pressure, starting from $P < P_c$, in $CdInGaS_4$ and $ZnInGaS_4$ reveals recovery of the layered structure, though in a slightly disordered form. It is to be noted that the SP mode in $CdIn_2S_4$ disappeared at 50 kbar, in accordance with the assumption about the onset of structural transformation in the upstroke of pressure run. When reducing the pressure, starting from $P > P_c$, the layered phase was recovered only in $ZnInGaS_4$with a large hysteresis (recovery commenced at 50 kbar). The substitution of Cd by Zn seems to favour the recovery of the initial layered structure. It was mentioned above that $MgInGaS_4$ is characterized by a rather sharp and irreversible phase transition under pressure from the layered to the spinel phase. No phase transition to the Raman-inactive phase was observed in this case up to 150 kbar, but it is reasonable to expect such transition to take place at higher pressure.

8.4 Conclusions

The Zn-Al-S system, including quaternary solid solutions $ZnAl_{2(1-x)}Ga_{2x}S_4$ obtained by adding gallium atoms to the system, demonstrate a systematics of phase transitions different from that inherent to $A^{II}B_2^{III}X_4^{VI}$ compounds with chalcopyrite, stannite, and spinel structure.

While thioindates and oxide $A^{II}B_2^{III}X_4^{VI}$ compounds are grown predominantly in spinel structure, $ZnAl_2S_4$ compound is produced in two modifications: wurtzite and spinel. The behavior of the $ZnAl_2S_4$ spinel under pressure is different from that of $M^{II}In_2S_4$ (M = Cd, Mg, Mn) and oxide spinels. While the experiments in $M^{II}In_2S_4$ evidence a phase transition to a disordered NaCl-type structure or to an ordered double-NaCl structure of the $LiTiO_2$ or $LiVO_2$-type under hydrostatic pressure, another behavior was observed in $ZnAl_2S_4$ spinel. The changes in the phonon spectrum of this compound at high pressures were attributed to a reversible phase transition to a denser high-pressure phase, having similar structure to that of calcium ferrite.

The changes introduced by hydrostatic pressure in $ZnAl_{2(1-x)}Ga_{2x}S_4$ solid solutions with a high Ga content are also different from those observed in compounds with DC structure, namely, a new phase supposed to be of layered-type is produced instead of a rocksalt-type structure. On the other hand, similarly to most of tetragonal and cubic $A^{II}B_2^{III}C_4^{VI}$ compounds, a phase transition to rocksalt-type structure was found to occur in wurtzite-type $ZnAl_2S_4$ as well as in layered $CdInGaS_4$, $ZnInGaS_4$ and $MgInGaS_4$ compounds. This phase transition in layered compounds is preceded

by cation redistribution accompanied by partial filling of interlayer voids, and in intermediate phase transition to a spinel structure.

Therefore, phase transitions in layered compounds and spinels are still far from being rationalized. Moreover, the issue of pressure induced phase transitions in $A^{II}B_2^{III}X_4^{VI}$ compounds with orthorhombic structure such as $M^{II}Ga_2(S, Se)_4$ compounds with M^{II} = Mg, Pb, Sr, Eu, Yb and Ca remains absolutely unexplored. We believe that investigation of these materials under high pressure would give a significant contribution to the construction of generalized phase diagrams for the different compounds and the understanding of the systematics of pressure-driven phase transitions of materials.

References

1. Hills ME, Harris DC, Lowe-Ma CK (1987) Zinc aluminium sulfide:electron paramagnetic resonance spectroscopy and anfrared transmittance. J Phys Chem Solids 48:501–507
2. Berthold HJ, Köhler K (1981) Prepärative und röndgenographische untersuchugen über das system AL_2 S_3-ZnS (Temperaturderich 800–1080 °C). Z Anorg Allg Chem 475:45–49
3. Kaifuku KT, Aksenov I, Sato K (1995) Green photoluminescence from α-phase $ZnAl_2S_4$'. Jap J Appl Phys 34:3073–3074
4. Moldovyan NA, Markus MN, Radautsan SI (1989) Layered $ZnAl_2S_4$ single crystals. Dokl Akad Nauk USSR 304:151–155
5. Tiginyanu IM, Lotttici PP, Razzetti C, Gennari S (1993) Effects of the cations on the Raman spectra of sulfur defect chalcopyrites. Jap J Appl Phys 32(Suppl. 32–3):561–564
6. Ursaki VV, Burlakov II, Tiginyanu IM, Raptis Y, Anastassakis E, Aksenov I, Sato K (1998) Pressure-induced phase transitions in spinel and wurtzite phases of $ZnAl_2S_4$. Jap J Appl Phys 37:135–140
7. Kulikova OV, Moldovyan NA, Popov SM, Radautsan SI, Siminel AV (1993) Optical absorption and Raman scattering of $ZnAl_2S_4$ spinel-type semiconductor. Jap J App Phys 32(Suppl. 32–3):586–589
8. Irifune T, Fujino K, Ohtani E (1991) A new high-pressure form of $MgAl_2O_4$. Nature (UK) 349(6308):409
9. Wyskoff RWJ (1963) Crystal structure, 2nd edn, vol 1. Wiley, New York, p 112
10. Burlakov II, Raptis Y, Ursaki VV, Anastassakis E, Tiginyanu IM (1997) Order-disorder phase transition in $CdAl_2$ S_4 under hydrostatic pressure. Sol State Commun 101:377–381
11. Tsuji K, Katayama Y, Koyama N, Yamamoto Y, Chen J-Q, Imai M (1993) Amorphization from quenched high-pressure phase in tetrahedrally bonded materials. J Non-Cryst Solids 156–158:540–543
12. Tsuji K, Katayama Y, Yamamoto Y, Kanda H, Nosaka H (1995) Amorphization from the quenched high-pressure phase in tetrahedrally bonded materials'. J Phys Chem Solids 56:559–562
13. Vohra YK, Xia H, Ruoff AL (1990) Optical reflectivity and amorphization of GaAs during decompression from megabar pressures. Appl Phys Lett 57:2666–2671
14. Itie JP, Polian A, Jauberthie-carillon C, Dartyge E, Fontanie A, Tolentino H, Tourillon G (1989) High-pressure phase transition in gallium phosphide. An X-ray-absorption spectroscopy study. Phys Rev B 40:9707–9714
15. Perlin P, Jauberthie-Carillon C, Itie JP, Miguel AS, Grzegory I, Polian A (1992) Raman scattering and X-ray absorption spectroscopy in gallium nitride under high pressure. Phys Rev B 45:83–89

16. Ursaki VV, Burlakov II, Tiginyanu IM, Raptis Y, Anastassakis E, Anedda A (1998) Phase transitions in defect chalcopyrite $ZnAl_{2(1-x)}\,Ga_{2x}S_4$ at high pressure. Inst Phys Conf Series 152:605–608
17. Moldovyan NA, Radautsan SI, Tiginyanu IM (1991) Raman scattering spectra of $ZnAl_{2(1-x)}\,Ga_{2x}\,S_4$ single crystals. Fizi Tekn Poluprov 25:2038–2039
18. Anastassakis E, Pinczuk A, Berstein E, Polllack FH, Cardona M (1970) Effect of static uniaxial stress on the Raman spectrum of silicon. Sol State Commun 8:133–138
19. Hu JZ, Black DR, Spain IL (1984) GaP at ultrahigh pressure. Sol State Commun 51:285–287
20. Ursaki VV, Burlakov II, Tiginyanu IM, Raptis YS, Anastassakis E, Anedda A, Corpino R (2000) Phase transitions induced by hydrostatic pressure in II-III_2 VI_4. Jap J Appl Phys 39(Suppl. 39–1):143–145
21. Moldovyan NA, Pyshnaya NB, Radautsan SI (1993) New multinary layered chalcogenides with octahedral and tetrahedral cation coordination. Jap J Appl Phys 32(Suppl. 32–3):781–784
22. Ando Sh, Endo S, Nakanishi H, Toyoda T, Irie T (1993) Optical properties of $Zn_X\,Cd_{1-X}\,InGaS_4$ system. Jap J Appl Phys 32(Suppl. 32–3):501–504
23. Tiginyanu IM, Raptis YS, Ursaki VV, Anastassakis E, Burlakov II (1996) Pressure induced phase transition in $MgInGaS_4$. Cryst Res Technol 31:777–780
24. Anastassakis E, Raptis YS, Ando Sh, Erie T, Ursaki VV, Tiginyanu IM, Radautsan SI, Burlakov II (1996) Raman scattering study of $ZnInGaS_4$ and $CdInGaS_4$ under hydrostatic pressure $MgInGaS_4$. Cryst Res Technol 31:365–368
25. Vinogradov EA, Zhizhin GN, Melnik NN, Subbotin SI, Panfilov VV, Allakhverdiev KR, Babaev SS, Zhitar VF (1980) Raman scattering in ε-GaSe and $ZnIn_2\,S_4$ single crystals under pressure. Phys Stat Sol B 99:215–221
26. Donica FG, Radautsan SI, Kiosse GA, Semiletov SA, Donica TV, Mustya IG (1971) Crystal structure of two-packets polytype of $ZnIn_2\,S_4$(II). Sov Phys Crystall 16:190–195
27. Abbasov AN, Allakhverdiev KR, Mekhtiev TR, Nani RKh (1981) Raman scattering in $CdInGaS_4$ single crystals. Sov Phys Sol State 23:370–374
28. Damaskin IA, Zenchenco VP, Pyshkin SL, Radautsan SI, Tiginyanu IM, Tezlevan VE, Fulga VM (1990) Raman scattering cpectra of $CdIn_2\,S_4$ compound with different ordering in the cation sublattice. Dokl Akad Nauk USSR 315:1365–1367
29. Unger WK, Farnworth B, Irwin JC (1978) Raman and infrared spectra of $CdIn_2\,S_4$ and $ZnIn_2\,S_4$. Sol State Commun 25:913–915
30. Anedda A, Berger G, Bogiovani G, Mura A (1990) Optical spectra and cation ordering in $MgIn_2\,S_4$. In: Proceeding 8th international conference on ternary and multinary compounds, Kishinev, pp 301–305
31. Beister HJ, Ves S, Honle W, Syassen K, Kuhn G (1991) Structural phase transitions and optical absorption of $LiInS\,E_2$ under pressure. Physi Rev B 43:9635–9642
32. Santamaría-Pérez D, Amboage M, Manjón FJ, Errandonea D, Muñoz D, Rodríguez-Hernández P, Mujica A, Radescu S, Ursaki VV, Tiginyanu IM (1992) Crystal chemistry of $CdIn_2\,S_4$, $MgIn_2\,S_4$, and $MnIn_2\,S_4$ thiospinels under high pressure. J Phys Chem C 116:14078–14087

Chapter 9
Epilogue

Francisco Javier Manjón, Ion Tiginyanu and Veaceslav Ursaki

The present book has reviewed the main experimental and theoretical results obtained in the study of $A^{II}B_2^{III}X_4^{VI}$ chalcogenide compounds at high pressures to date, paying special attention to the pressure-induced phase transitions.

The first part of the book is devoted to spinels and spinel-related compounds. In this section, it has been shown that experimental and theoretical studies have understood in general the evolution of the structural, mechanical, vibrational, and electronic properties of spinels and their related structures under high pressures. However, the bulk modulus of thiospinels, seems not to be intermediate between that of oxospinels and selenospinels. This question merits further studies. On the other hand, spinels tend to crystallize with different degrees of cation inversion depending on the crystal growth conditions. In this respect, there is a lack of calculations of many disordered spinel structures because they are difficult to perform and experimental studies at high pressures with samples containing different degrees of disorder are scarce. Finally, it must be stressed that despite the considerable number of high-pressure studies performed in spinels there is still a lack of a systematics that allows us to understand the relatively large number of high-pressure post-spinel phases. In particular, recent results in thiospinels under pressure have shown that the post-spinel phase in thiospinels is a disordered structure with the same space group than spinel, but with cations and vacancies mixing at the same Wyckoff sites. This result establishes a bridge between the structure and properties of spinel-related compounds

F. J. Manjón (✉)
Instituto de Diseño para la Fabricación y Producción Automatizada, MALTA Consolider Team, Universitat Politècnica de València, 46022 València, Spain
e-mail: fjmanjon@fis.upv.es

I. Tiginyanu
Academy of Sciences of Moldova, Chisinau, Moldova
e-mail: tiginyanu@asm.md

V. Ursaki
Institute of Applied Physics, Chisinau, Moldova
e-mail: ursaki@yahoo.com

F. J. Manjón et al. (eds.), *Pressure-Induced Phase Transitions in AB_2X_4 Chalcogenide Compounds*, Springer Series in Materials Science 189,
DOI: 10.1007/978-3-642-40367-5_9, © Springer-Verlag Berlin Heidelberg 2014

and those of ordered-vacancy compounds (OVCs) since evidences the occurrence of a pressure-induced order–disorder phase transition in spinel-related compounds as well as in OVCs.

The second part of the book is devoted to tetrahedrally-coordinated adamantine-type OVCs. In this section, it has been shown that the combination of experimental and theoretical studies have allowed us to understand in general the evolution of the structural, mechanical, vibrational, and electronic properties of OVCs under high pressures. In particular, OVCs feature strong non-linear pressure dependencies of electronic and vibrational properties that have been understood thanks to the combination of experimental and theoretical techniques. Unfortunately, OVCs can crystallize in different structures with different degrees of cation or cation-vacancy disorder depending on the crystal growth conditions. Furthemore, they undergo pressure-induced phase transitions to disordered structures where cations and vacancies get mixed at the same cation sites. Thus, OVCs feature pressure-induced order-disorder transitions as well as temperature-induced order-disorder transitions, being the latter known for many years. Since calculations of disordered phases are difficult, there is a lack of theoretical calculations of disordered structures in OVCs either at different pressures or temperatures. Finally, we have to stress that recent high-pressure studies in defect chalcopyrite $CdAl_2S_4$ have shown that on decreasing pressure from 25 GPa it undergoes a phase transition to the spinel structure. In fact, theoretical calculations show that the defect chalcopyrite structure is stable only at negative pressures (or equivalently at high temperatures). This result again establishes a bridge between spinel-related materials and OVCs that merits further exploration.

The third part of the book is devoted to compounds crystallizing in structures not related to those of spinel or to those of OVCs, e.g. layered materials. In $ZnAl_2S_4$ a phase transition to the $CaFe_2O_4$ phase (rocksalt type) is suggested from Raman scattering measurements for spinel-type (wurtzite-type). Similarly, layered structures of $CdInGaS_4$, $ZnInGaS_4$ and $MgInGaS_4$ are suggested to undergo a pressure-induced phase transition likely to the spinel structure. However, these studies are far from completed because no X-ray diffraction experiments at high pressures nor theoretical studies have been performed to verify these hypotheses. New high-pressure studies in the family of sulphide-based AB_2X_4 compounds are needed to fully understand the relationship between the spinel, layered, and ordered-vacancy related structures of the AB_2X_4 family.

In summary, the studies performed in $A^{II}B^{III}_2X^{VI}_4$ chalcogenide compounds under high pressures have helped us to understand the properties of these compounds and the relationship between their properties and their structures which can have profound implications in many fields. These studies have shown that the understanding and control of their properties require a precise control of the growth conditions. Theoretical treatment of disordered phases is needed to further understand the properties of these complex materials featuring a considerable degree of cation or cation-vacancy disorder. Furthermore, there is still a lack of a systematics which allows us to understand the high-pressure phases of $A^{II}B^{III}_2X^{VI}_4$ compounds, in particular of spinels with their Geophysical implications. We hope the present book will stimulate further studies in these interesting materials.

Index

F. J. Manjon et al. (eds.), *Pressure-Induced Phase Transitions in AB_2X_4 Chalcogenide Compounds*, Springer Series in Materials Science 189,
DOI: 10.1007/978-3-642-40367-5, © Springer-Verlag Berlin Heidelberg 2014